

The Pennsylvania State University

The Graduate School

**EXPLORING ADDITIVE MANUFACTURING FOR COOLING DESIGNS**

A Dissertation in

Mechanical Engineering

by

Alexander J. Wildgoose

© 2023 Alexander J. Wildgoose

Submitted in Partial Fulfillment  
of the Requirements  
for the Degree of

Doctor of Philosophy

May 2023

The dissertation of Alexander Wildgoose was reviewed and approved by the following:

Karen A. Thole  
Distinguished Professor of Mechanical Engineering  
Dissertation Advisor  
Chair of Committee

Stephen P. Lynch  
Associate Professor of Mechanical Engineering

Allison M. Beese  
Associate Professor of Materials Science and Engineering and Mechanical Engineering

Edward W. Reutzel  
Head of the Laser Process Technology Department at Penn State Applied Research Laboratory  
Associate Professor of Engineering Science and Mechanics

Mary I. Frecker  
Department Head of Mechanical Engineering  
Professor of Mechanical Engineering

## ABSTRACT

The opportunities for additive manufacturing (AM) methods to create novel cooling schemes has garnered significant attention by the heat transfer community, in particular the gas turbine field. Using AM to fabricate complicated gas turbine parts under load, such as blades and vanes, is challenging in high temperature environments due to creep strength relative to traditionally casted components. Instead, the additive process allows for the rapid prototyping of advanced cooling components, such as vanes and blades, during the component development phase because of the added design freedom relative to cast components. To unlock the full potential of metal AM for rapid prototyping of advance cooling schemes, such as vanes, a better understanding of the impact the build process has on the build quality and cooling performance of internal features (cooling passages) and external features (film cooling holes and airfoil shape) are essential. The work in this dissertation explores the impact AM build considerations have on the cooling performance and geometric tolerances of internal passages as well as the external build quality of an engine relevant turbine guide vane.

A multitude of cooling channel coupons were fabricated using AM with varying build directions, locations on the build plate, channel sizes, cross-sectional channel shapes, and wall thicknesses. Geometric tolerances and surface roughness of the cooling passages were analyzed using computed tomography scanning. The roughness, specifically the arithmetic mean roughness, of the internal passages exponentially increases at build directions from  $60^\circ$  to  $0^\circ$  (horizontal). Increasing the radial distance of the cooling passage from the laser source led to a 35% increase in roughness when moving the part from a radial distance of 0 mm to 145 mm. The arithmetic mean surface roughness did not change with channel size for build directions between  $90^\circ$  and  $45^\circ$ . Changes to the cross-sectional shape of a channel caused nonuniformity in roughness between surfaces as a result of differences in wall thickness. At wall thicknesses below 0.6 mm the surface roughness of the cooling passage increases, which is an important factor to consider since internal passages in turbine components contain a wide range of wall thicknesses. The surface roughness varied by 10% from part to part for multiple cooling passages printed on a build plate with the same radial location, build direction, and design intent.

Surface roughness impacts the overall cooling performance of internal passages. To quantify these effects, an experimental rig was used to characterize the pressure loss and convective heat transfer performance of the various cooling coupons fabricated. Surface roughness was found to be linked to the friction factor of the coupons. Similar to roughness, the friction factor nonlinearly increased at build directions below  $60^\circ$ , while Nusselt number peaked between  $30^\circ$  and  $45^\circ$ .

Increasing the radial distance of a part from the laser source caused an increase to the friction factor and Nusselt number. The difference in cooling performance for cooling coupons printed multiple times at a shared radial build location of 112.5 mm was 18% for friction factor and 5% for Nusselt number.

Changes to the cross-sectional shape of a channel caused differences in secondary flows to have as much as a 31% difference in friction factor and 13% difference in Nusselt number. As a result of the difference in surface roughness between channel shapes, there was no difference in scaling friction factor or Nusselt number when using the characteristic length scale of square root of cross-sectional area compared to hydraulic diameter.

Using the cooling performance results from the different build considerations, a correlation was created that reduced the error in predicting friction factor and Nusselt number by half compared to correlations in literature. Using the created correlation, friction factor is able to be predicted within a maximum error of 25% and Nusselt number to within a maximum error of 39% regardless of changes to material or AM build parameters.

The build quality of more complicated curved surfaces, specifically the external features of a vane (film cooling holes and airfoil shape) was characterized using a combination of CT scanning and optical profilometry. More specifically, an engine scale vane was fabricated at different build directions, locations on the build plate, and layer thicknesses. The differences in local surface orientations of a vane airfoil can result in variations in surface quality (as much as a 300% difference in surface roughness) between the suction side and pressure side. Orientating the geometric leading edge of the vane to a 120° build direction results in the lowest amount of surface quality variation between the pressure side and suction side. At the same 120° leading edge orientation, the first-row film cooling holes were found to be closest to their design intent relative to other vane orientations. Surface roughness increased 39% at the leading edge of a vane airfoil when increasing the radial location of 75 mm to 112.5 mm. Changes to the layer thickness from 80 microns to 40 microns increased the surface roughness of the pressure side and suction side. The work completed as part of this dissertation provides the foundational component design and AM build considerations needed for the AM process to be used as rapid prototyping in the development of advanced cooling designs, such as gas turbine components.

## TABLE OF CONTENTS

List of Figures .....	viii
List of Tables .....	xiii
Nomenclature .....	xiv
Greek.....	xv
Subscripts.....	xvi
Acknowledgements.....	xvii
1 Introduction.....	1
1.1 Using AM in the Rapid Development of Gas Turbine Components.....	1
1.2 Laser Powder Bed Fusion.....	3
1.3 Surface Roughness and Deformation .....	5
1.4 Research Objectives .....	6
1.5 Outline of Dissertation .....	7
2 Impact of Additive Manufacturing on Internal Cooling Channels with Varying Diameters and Build Directions.....	9
2.1 Abstract .....	9
2.2 Introduction .....	9
2.3 Literature Review .....	10
2.4 Description of Test Coupons.....	11
2.5 Geometric Channel Shapes.....	14
2.6 Geometric Tolerances.....	17
2.7 Roughness Evaluation .....	22
2.8 Channel Performance Measurements .....	24
2.9 Experimental Uncertainty.....	25
2.10 Friction Factor Evaluation.....	26
2.11 Heat Transfer Evaluation.....	28
2.12 Conclusion.....	33
3 Heat Transfer and Pressure Loss of Additively Manufactured Internal Cooling Channels with Various Shapes .....	35
3.1 Abstract .....	35

3.2 Introduction .....	35
3.3 Literature Review .....	36
3.4 Description of Test Coupons .....	37
3.5 Characterization of Channel Shapes.....	40
3.6 Roughness Quantities .....	47
3.7 Channel Performance Measurements .....	48
3.8 Experimental Uncertainty.....	49
3.9 Computational Fluid Dynamics Simulations.....	50
3.10 Pressure Loss Measurements.....	50
3.11 Heat Transfer Evaluation.....	54
3.12 Conclusion.....	61
<b>4 Roughness Related to Cooling Performance of Channels Made Through Additive Manufacturing .....</b>	<b>63</b>
4.1 Abstract .....	63
4.2 Introduction .....	63
4.3 Literature Review .....	64
4.4 Description of Test Coupons .....	66
4.5 Geometry Characterization.....	70
4.6 Roughness Characterization .....	71
4.7 Channel Performance Measurements .....	73
4.8 Experimental Uncertainty.....	74
4.9 Pressure Loss Measurements.....	75
4.10 Heat Transfer Measurements.....	77
4.11 Pressure Loss Correlation.....	80
4.12 Heat Transfer Correlation.....	87
4.13 Conclusion.....	91
<b>5 Impacts of The Additive Manufacturing Process on The Roughness of Engine Scale Vanes and Cooling Channels .....</b>	<b>93</b>
5.1 Abstract .....	93
5.2 Introduction .....	93
5.3 Literature Review .....	94
5.4 Description of Samples .....	95
5.5 Influence of Wall Thickness on Roughness .....	100
5.6 Effect of Build Direction on Vane Roughness .....	104
5.7 Impact of Build Location on Roughness .....	107

5.8 Effect of Layer Thickness and Machine Type .....	110
5.9 Conclusion.....	114
6 Variability in Additively Manufactured Turbine Cooling Features.....	116
6.1 Abstract .....	116
6.2 Introduction .....	116
6.3 Causes for Geometric Variation of Additively Manufactured Components .....	117
6.4 Progress in Using AM to Manufacture Turbine Cooling Features.....	118
6.5 Roughness and Geometry Variability of Simple Channels due to Build Plate Location	122
6.6 Part-to-part Variability of Features on Turbine Components due to Build Plate Location	126
6.7 Pressure loss and Heat transfer resulting from Build Plate Location .....	131
6.8 Conclusion.....	136
7 Conclusions.....	138
7.1 Influence of the AM process on the build quality of internal cooling passages.....	138
7.2 Pressure loss and Convective Heat Transfer relationships of AM cooling schemes.....	140
7.3 Impact of the AM process on the Build Quality of External features of Turbine Parts ..	141
7.4 Recommendations for Future Work .....	142
References.....	144
Appendix A: Uncertainty Analysis .....	154

## LIST OF FIGURES

Figure 1-1 Diaphragm of gas turbine blade with a variety of external cooling (a) and internal cooling (b) features [5].	3
Figure 1-2 Schematic of a general PBF process showing the substrate, energy source, component, powder, and re-coater blade/roller.	4
Figure 1-3 Range of roughness types experienced in AM parts which are impacted by design consideration and the AM process [12–16].	5
Figure 2-1 CAD schematic of overall coupon dimensions used for experimental testing.	14
Figure 2-2 Coupon support structures generated over the five build directions.	14
Figure 2-3 Distribution of measured diameters from CT scans of a 1 mm coupon at 0°, 45°, and 90°.	15
Figure 2-4 3 $\sigma$ deviations of calculated diameter for each of the coupons over a range of build directions.	16
Figure 2-5 Distribution of measured diameters from CT scans of a 0.75 mm, 1mm, and 1.25 mm coupon at a 45° build direction.	17
Figure 2-6 Deviation of channel diameter from design intent across multiple build directions.	17
Figure 2-7 Physical definitions of concentricity (a) and total runout (b).	18
Figure 2-8 Axial slices of a 1 mm channel built at 0° (a), 30° (b), 45° (c), 60° (d), and 90° (e) showing the impact of build direction on the geometric deformation of a circular cross-section.	19
Figure 2-9 Impact of build direction on the circularity of the 0.75 mm, 1 mm, and 1.25 mm coupons.	20
Figure 2-10 0.75 mm (a), 1 mm (b), and 1.25 mm (c) circular channel cross-sections at a 45° build direction.	21
Figure 2-11 Impact of build direction on the concentricity of the 0.75 mm, 1 mm, and 1.25 mm coupons.	22
Figure 2-12 Impact of build direction on the normalized total runout, Total runout/Dh, of the 0.75 mm, 1 mm, and 1.25 mm coupons.	22
Figure 2-13 Averaged arithmetic mean roughness measured from CT scan data of circular channels.	24
Figure 2-14 Schematic of experimental rig used for pressure loss and heat transfer measurements.	25
Figure 2-15 Cylindrical channel friction factor data of coupons with varying diameters and build directions, along with benchmark data from Stimpson et al. [33].	27



Figure 2-16 Sandgrain roughness calculated using equation (2-3) compared with measured arithmetic mean roughness of coupons. ....	28
Figure 2-17 Cylindrical channel Nusselt number data with benchmark results from Stimpson et al. [33]. ....	30
Figure 2-18 Nusselt number of the 0.75C45, 1.00C45, 1.25C45 coupons with Stimpson et al. [30] correlation calculated using measured friction factor.....	31
Figure 2-19 Nusselt number and friction factor augmentations over a range of Reynolds numbers. ....	32
Figure 2-20 Friction factor augmentation of coupons across multiple build directions at a shared Reynolds number of 20,000. ....	33
Figure 2-21 Nusselt number augmentation of coupons across multiple build directions at a shared Reynolds number of 20,000. ....	33
Figure 3-1. Schematic of coupon dimensions used for experimental testing.....	40
Figure 3-2. Distribution of hydraulic diameter along with design intent calculated from CT scans of the different channel shapes.....	42
Figure 3-3. $3\sigma$ deviations of hydraulic diameter (a), perimeter (b), and cross-sectional area (c) of the different channel shapes. ....	43
Figure 3-4. Axial slices of channel shapes (circle (a), hexagon (b), pentagon (c), ellipse (d), diamond (e), square (f), rectangle (g), trapezoid (h), and triangle (i) sharing a constant design intent perimeter of 4.79 mm fabricated at the 90° build direction. ....	44
Figure 3-5. Arithmetic mean roughness, $R_a$ , from CT scan data of multiple surfaces among the different channel shapes which are at the same surface orientation as Figure 4(a-i). ....	46
Figure 3-6. Area average arithmetic mean roughness of the different channel shape surfaces weighted by the design intent surface area.....	48
Figure 3-7. Experimental rig used for static pressure drop and bulk convection coefficient measurements. ....	49
Figure 3-8. Friction factor data over a range of Reynolds numbers calculated using hydraulic diameter with benchmark data from Stimpson et al. [30] and smooth noncircular data compiled by Duan et al. [50]......	53
Figure 3-9. Friction factor data over a range of Reynolds numbers calculated using square root of cross-sectional area with benchmark data from Stimpson et al. [30] and smooth noncircular data compiled by Duan et al. [50]. ....	54
Figure 3-10. Nusselt number data calculated using hydraulic diameter as the characteristic length scale along with numerical data and benchmark results from Stimpson et al. [30]. ....	56

Figure 3-11. Nusselt number data calculated using square root of cross-sectional area as the characteristic length scale along with numerical data and benchmark results from Stimpson et al. [30]. .....	57
Figure 3-12. Nondimensionalized temperature contours with secondary flow vectors of the triangle, trapezoid, square, and pentagon channel shapes. ....	60
Figure 3-13. Nusselt number and friction factor augmented by a hydraulically smooth channel for the different channel shapes over a range of fully turbulent Reynolds numbers.....	61
Figure 3-14. Nusselt number and friction factor of channel shapes augmented by the Nusselt number and friction factor of the circular channel shape at the same Reynolds number. ....	61
Figure 4-1 Coupons spanning a range of build directions and diameters fabricated at three distinct radial locations from the four laser EOS M400-4 machine.....	69
Figure 4-2 Schematic of overall coupon dimensions used for experimental testing. ....	69
Figure 4-3 Deviation from design intent hydraulic diameter of circular and teardrop channels at a range of build directions.....	71
Figure 4-4 Arithmetic mean roughness (a) and relative roughness (Ra/Dh) (b) of samples for a range of diameters at different build directions and radial build locations. ....	73
Figure 4-5 Schematic of experimental rig used to measure pressure loss and heat transfer.....	74
Figure 4-6 Friction factor of coupons from Table 4 1 built over a wide range of build directions, build locations, and diameters. ....	76
Figure 4-7 Friction factor augmented by the friction factor of a hydraulically smooth channel at a Reynolds number of 20,000 for the samples in Table 4 1.....	77
Figure 4-8 Nusselt number of samples (with a variety of build directions, locations, and diameters) from Table 4 1 covering a range of turbulent Reynolds numbers. ....	79
Figure 4-9 Nusselt augmentation of samples fabricated at a variety of build directions and diameters at R1, R2, and R3 at a shared Reynolds number of 20,000.....	80
Figure 4-10 Comparison of correlation length and density parameters to sandgrain roughness for the samples in Table 4-2.....	83
Figure 4-11 Experimental friction factor compared to friction factor predicted using the correlations in Table 4 3 of the datasets in Table 4 2.....	85
Figure 4-12 Comparison of friction factor correlations of select samples from Table 4 2. ....	87
Figure 4-13 Experimental Nusselt number of samples from Table 4 2 compared with the predicted Nusselt number using the experimental friction factor and friction factor predicted using equation (4-3). ....	90

Figure 4-14 Comparison of Nusselt number prediction using equation (4-4) and the Nusselt number correlation from Stimpson et al. [10].	91
Figure 5-1. Schematic of vertically oriented sample with square internal cooling channels at different wall thicknesses fabricated close to the center of the build plate.	99
Figure 5-2. Leading edge NExT vane [97] samples that were fabricated at three different radii from the laser source and contain two different wall thicknesses between the interior and exterior of the leading edge.	99
Figure 5-3. NExT vane airfoils without external and internal cooling fabricated across multiple build directions.	99
Figure 5-4. Schematic of vertically oriented internal cooling square channel samples fabricated on an EOS M280-1 at different radii from the center of the single laser source.	100
Figure 5-5. Build layout of chess piece samples fabricated on different machines using different layer thicknesses.	100
Figure 5-6. Arithmetic mean roughness (6a) and mean roughness depth (6b) of internal wall thickness sample measured from CT scan data of the 6 and 12 o'clock surface orientations.	103
Figure 5-7. Arithmetic mean roughness measured using CT scan data of the different wall thickness and build location leading edge NExT vanes samples fabricated on the EOS M290-1 in a 40 micron layer thickness, seen in Figure 5-2.	104
Figure 5-8. Arithmetic mean roughness measured using an optical profilometer across the pressure side, suction side, and leading edge NExT vane airfoils printed at 0° (8a), 60° (8b), 90° (8c), and 120° (8d) on an EOS M290-1 at a 40 micron layer thickness.	107
Figure 5-9. Build plate contour of average arithmetic mean roughness measured using CT scan data from the four internal surfaces of the square cooling channel.	109
Figure 5-10. Build plate contour of the 3σ deviation of arithmetic mean roughness measured using CT scan data from the four internal surfaces of the square cooling channel.	110
Figure 5-11. Average of 88 arithmetic mean roughness values for each surface of the “chess piece” fabricated using two different single laser machines, two layer thickness, and a four laser machine.	113
Figure 5-12. Arithmetic mean roughness Arithmetic using an optical profilometer across the pressure side, suction side, and leading edge of the NExT vane airfoils fabricated at the 0° (12a) and 60° (12b) build direction using different AM machines, build locations, and layer thicknesses.	114

Figure 6-1 Quality of additively manufactured film cooling holes (a) (Stimpson et al., 2018), (b) (Snyder and Thole, 2019), (c) (Veley et al., 2022), (d) film cooling hole from this study highlighting the improvement in printability over several years.....	119
Figure 6-2 Computed Tomography scans highlighting the print quality of (a) film cooling holes, (b) pin fins from Ferster et al. (Ferster et al. , 2017), (c) ribs , and (d) cooling microchannels from Snyder et al. (Snyder et al., 2015). .....	120
Figure 6-3 Deviation from design intent hydraulic diameter of microchannels in literature at a variety of build directions (Stimpson et al., 2016c, 2016a; Kirsch et al., 2017; Dahmen et al., 2020b; Wildgoose et al., 2021b, 2022; Alexander J Wildgoose and Thole, 20 .....	122
Figure 6-4 Layout of build plate to evaluate the variability of cooling channels and cooled NExT vanes on an EOS M290-1.....	124
Figure 6-5 Average hydraulic diameter of square and hexagonal channels, built across two different build locations, measured from CT scans (a) along with each of the coupons $3\sigma$ (b) variation in hydraulic diameter.....	125
Figure 6-6 Arithmetic mean roughness from CT scan data of each surface for the square cooling channels (a) along with area average arithmetic mean roughness (b) of the same square channels weighted by the design intent surface area.....	126
Figure 6-7 Leading edge NExT vane that were fabricated at different build locations as well as the full NExT vane with highlighted first row film cooling holes fabricated at different build directions ( $300^\circ$ , $270^\circ$ , $240^\circ$ , $60^\circ$ , $90^\circ$ , $120^\circ$ ). .....	127
Figure 6-8 Arithmetic mean roughness measured from CT scan data of the different wall thickness and build location of the leading edge NExT vane samples seen in Figure 7. ....	129
Figure 6-9 CT scans of the mid span first row 7-7-7 film cooling hole at the pressure side of the NExT vane fabricated at six different build directions.....	131
Figure 6-10 Friction factor augmentation of square cooling channel samples across various Reynolds numbers (a) as well as friction factor augmentation of the channels at a Reynolds number of 20,000 and 30,000 (b). .....	133
Figure 6-11 Nusselt number augmentation of square cooling channel samples across various Reynolds numbers (a) as well as Nusselt number augmentation of the channels at a Reynolds number of 20,000 and 30,000 (b). .....	134
Figure 6-12 Friction factor and Nusselt number augmentation of cooling channels built at different build directions, channel cross-sections, laser parameters, and diameters at a $Re = 10,000$ . 135	
Figure A.1 Parameter percent contribution to the friction factor uncertainty.....	158
Figure A.2 Paramter percent contribution to the Nusselt number uncertainty.....	160

## LIST OF TABLES

Table 2-1 Geometric Specifications for Coupons.....	12
Table 2-2 Processing Parameters for AM Coupons.....	13
Table 3-1. Geometric Specifications for Coupons Sharing a Constant Perimeter ( $P_{des} = 4.79$ mm) .....	39
Table 3-2. Processing Parameters for AM Coupons.....	41
Table 4-1 Geometries for Coupons Built at a Variety of Build Directions, Diameters, and Locations as seen in Figure 4-1.....	68
Table 4-2 Samples used for comparing and generating friction factor and Nusselt number correlations .....	81
Table 4-3 Correlations for Predicting Friction Factor of the Samples in Table 4-2. ....	84
Table 4-4 Correlations for Predicting Heat Transfer of the Samples in Table 4-2. ....	89
Table A.1 Reynolds number Uncertainty of Square Sample ( $Re = 9.91E3$ ).....	156
Table A.2 Reynolds number Uncertainty of Square Sample ( $Re = 1.98E4$ ).....	156
Table A.3 Friction factor Uncertainty of Square Sample ( $Re = 9.91E3$ ).....	157
Table A.4 Friction factor Uncertainty of Square Sample ( $Re = 1.98E4$ ).....	157
Table A.5 Nusselt Number Uncertainty of Square Sample ( $Re = 9.90E3$ ).....	159
Table A.6 Nusselt Number Uncertainty of Square Sample ( $Re = 1.98E4$ ).....	160

## NOMENCLATURE

A	cross-sectional flow area
$A_c$	cross-sectional flow area
$A_f$	frontal projected area
$A_s$	surface area of internal channel
$A_w$	wetted frontal area
AM	additive manufacturing
CT	computed x-ray tomography
$D_h$	hydraulic diameter, $4A/p$
f	Darcy friction factor, $f = \Delta P \frac{D_h}{L} \frac{2}{\rho u^2}$
$f_0$	friction factor of smooth channel ( $K_s = 0$ ) calculated from Colebrook equation
h	convective heat transfer coefficient, $h = \frac{Q_{in,heater} - \sum Q_{loss}}{A_s \Delta T_{lm}}$
$K_s$	sandgrain roughness
k	thermal conductivity
L	channel length
LE	leading edge
Nu	Nusselt number, $hD_h/k_{air}$
$Nu_0$	Nusselt number of smooth channel ( $K_s = 0$ ) calculated from Gnielinski correlation
$Nu_{D_h}$	Nusselt number calculated using $D_h$ as characteristic length, $hD_h/k_{air}$
$Nu_{\sqrt{A_c}}$	Nusselt number calculated using $\sqrt{A_c}$ as characteristic length, $h\sqrt{A_c}/k_{air}$
p	channel perimeter
P	static pressure
PS	pressure side
Pr	Prandtl number
r	radial distance from laser source
$R_a$	arithmetic mean roughness, $R_a = \frac{1}{n} \sum_{i=1}^n  z_{surf} - z_{ref} $
$R_q$	root mean square roughness, $R_q = \sqrt{\frac{1}{n} \sum_{i=1}^n (z_{surf} - z_{ref})^2}$

$R_z$	mean roughness depth, $R_z = \frac{1}{5} \sum_{i=1}^5 (z_{\max} - z_{\min})_i$
$R_{sk}$	skewness, $R_{sk} = \frac{1}{nR_q^3} \sum_{i=1}^n (z_{\text{surf}} - z_{\text{ref}})^3$
$R_{ku}$	kurtosis, $R_{ku} = \frac{1}{nR_q^4} \sum_{i=1}^n (z_{\text{surf}} - z_{\text{ref}})^4$
$R_t$	total height roughness
$Re$	Reynolds number, $uD_h/\nu$
$Re_{\sqrt{A_c}}$	Reynolds number calculated using $\sqrt{A_c}$ as characteristic length, $u\sqrt{A_c}/\nu$
$Re_{D_h}$	Reynolds number calculated using $D_h$ as characteristic length, $uD_h/\nu$
$Ref$	product of Reynolds number and Darcy friction factor
$S$	channel pitch distance
$SS$	suction side
$t$	wall thickness
$T$	temperature
$T_{LM}$	log-mean temperature, $\Delta T_{LM} = \frac{(\Delta T_{in} - \Delta T_{out})}{\ln\left(\frac{T_s - T_{in}}{T_s - T_{out}}\right)}$
$u$	mass average velocity
$z_{\text{ref}}$	reference surface height
$z_{\text{surf}}$	roughness height
$z_{\text{max}}$	maximum roughness height from $z_{\text{ref}}$
$z_{\text{min}}$	minimum roughness height from $z_{\text{ref}}$

## Greek

$\Lambda_s$	Sigal and Danberg density parameter
$\lambda$	correlation length
$\rho$	fluid density
$\nu$	kinematic viscosity
$\sigma$	standard deviation

## Subscripts

actual	actual dimension calculated from CT Scan
circle	dataset of circular channel shape
des	design intent dimension
exp	value measured from experiments
in	inlet condition
meas	measured dimension from CT Scan
out	exit condition
pred	value predicted from a correlation
s	surface condition
w	wall condition



## ACKNOWLEDGEMENTS

This endeavor would not have been possible without the guidance and mentorship from my advisor, Karen Thole. I would like to express my gratitude toward having been given the opportunity to perform industry leading research and work alongside an individual of such renown. Since the start of my journey, she has provided me with countless opportunities and resources to learn about gas turbines. I am eternally grateful for these experiences.

This endeavor would not have been possible without the financial and technical support from Siemens Energy and the Department of Energy<sup>1</sup>. Specifically, I would like to thank Lieke Wang for his technical guidance and practical industry perspective.

I am very thankful to work alongside such an amazing hardworking team of permanent staff, current, and former graduate students at the Penn State START Lab. The size of the team has significantly increase since the start of my graduate career and I would like to thank everyone for making graduate school memorable and for allowing me to be part of the START family. I specifically want to thank the AM side of START, Emma Veley and Thomas Corbett, who provided a platform to share ideas and moral support during those long weekends and nights. The work in this dissertation and my growth as an engineer is a testament to our collaborative efforts.

The resources offered through the Pennsylvania State University, has been vital toward completing my degree. I would like to personally thank Pennsylvania State University CIMP-3D, specifically Corey Dickman, for the technical AM process guidance and for building my foundation of AM component design. The researchers at the Pennsylvania State University CQI, have been invaluable toward nondestructive CT scanning. The samples highlighted in this dissertation is a direct result of the collaboration between START and CQI. I specifically want to thank Whitney Yetter, Tim Stecko, and Sara Mueller for their technical CT scan knowledge.

Words cannot express my gratitude for the unconditional support of my family and friends throughout my graduate studies. This pursuit would not have been possible without my parents, brother, and extended family members. Jeg dedikerer denne afhandling til min mor. Jeg ville ønske du var her for at se dette.

---

<sup>1</sup> This paper is based upon work supported by the Department of Energy under Award Number DE-FE0031760. Disclaimer: “This report was prepared as an account of work sponsored by an agency of the United States Government. Neither the United States Government nor any agency thereof, nor any of their employees, makes any warranty, express or implied, or assumes any legal liability or responsibility for the accuracy, completeness, or usefulness of any information, apparatus, product, or process disclosed, or represents that its use would not infringe privately owned rights. Reference herein to any specific commercial product, process, or service by trade name, trademark, manufacturer, or otherwise does not necessarily constitute or imply its endorsement, recommendation, or favoring by the United States Government or any agency thereof. The views and opinions of authors expressed herein do not necessarily state or reflect those of the United States Government or any agency thereof.”

# 1 INTRODUCTION

Innovations in manufacturing methods and materials have evolved design complexity and cooling performance of cooling designs across multiple heat transfer applications. These advances in cooling designs have resulted in increasing operation efficiencies of gas turbine engines over the past several decades. As engine cores become smaller than their predecessors, the demand for scaling down components and improving convective heat transfer while still fabricating tight tolerance parts is likely to rise to meet future engine efficiencies. Recent manufacturing developments such as metal additive manufacturing (AM) provides a platform to develop designs and enable rapid prototyping that can continue to drive engine efficiencies higher. The design freedom and rapid manufacturing offered through AM makes it a prime manufacturing method for novel cooling passages and in the product development cycle of more complicated components such as those seen in gas turbines compared to traditional manufacturing methods such as investment casting.

The focus of this work is to investigate how the AM method can be leverage to fabricate advanced cooling schemes as well as highlight how the AM process impacts the build quality of more complicated component geometry, such as those seen in gas turbines. To fulfill this goal, research was conducted to: (i) better understand how choices during the AM process impacts the geometric quality and tolerances of cooling passages, (ii) investigate relationships between the cooling performance and overall print quality of cooling channels, and (ii) examine how build choices during the AM process impacts the part quality of more complicated components such as turbine vanes. The following section highlights the motivation for implementing the AM method in heat transfer applications then transitions to part quality characteristics inherent with the additive process.

## 1.1 Using AM in the Rapid Development of Gas Turbine Components

Gas Turbine manufacturers have relied on increasing operating temperatures of engines to improve the overall efficiency. As a consequence, operational temperatures are much higher than the melting point of the materials used [1]. To adapt, engineers have developed new materials and implemented complex cooling technologies. As much as 20% to 30% of air from the compressor is used for cooling which bypasses the combustor resulting in an inefficiency to the overall performance of the engine [2]. Decreasing the amount of cooling air increases thermal efficiencies but requires efficient cooling schemes.

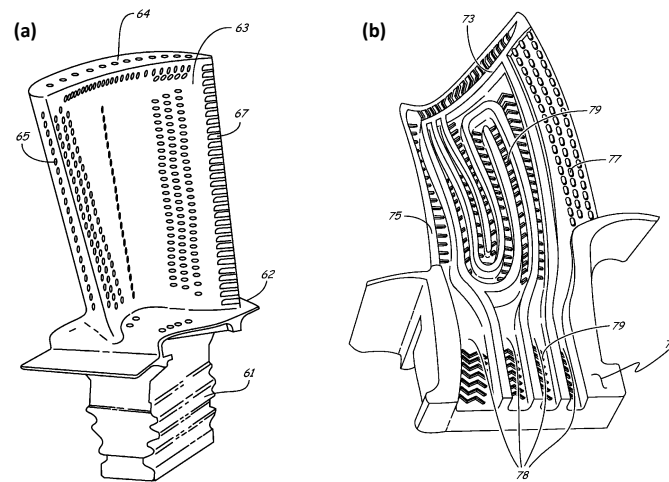
In an effort to improve turbine efficiency, aviation turbine designs have over time increased bypass ratios (air passing through the engine as compared to the air passing through the fan powered by the engine) to the point where the size of the outer casing is restricted. Consequently, engineers have pivoted to designing smaller engine cores to achieve the desired bypass ratio. As the engine core becomes smaller so do the cooling designs. Despite the challenge in manufacturing smaller designs, there are multiple benefits that come along with scaling down cooling designs. As cooling passages become smaller, such as cooling channel diameters less than 1 mm, a greater surface area to volume ratio is obtained resulting in the passage being able to respond faster to temperature fluctuations relative to larger sized passages. The ability to place cooling channels closer to the heat source leads to an increase in heat removal effectiveness. Additionally, the use of small cooling passages allows for multiple channel networks to be distributed within a part and provide a more uniform temperature profile. One of the challenges with implementing small scale cooling designs is being able to produce the geometry within the required tolerances while keeping cost low [3].

By leveraging the additive manufacturing platform, development time for turbine component testing and creation of complex cooling passages can be reduced relative to traditional investment casting methods used for intricate and multi-part gas turbine components. Additionally, the design freedom offered by AM allows for complex cooling geometries that would be challenging or impossible to produce using conventional methods. However, improvements in material development and process control are required for AM to be considered as the final-use parts in most commercial high load and high operating temperature (turbine) environments. Despite this, AM can be used at the product developmental level for complicated gas turbine components such as vanes and blades where experimental comparisons in efficiency can be performed on fast design iterations of cooling schemes and overall airfoil shape relative to traditional fabrication methods.

The complex cooling schemes of a typical gas turbine blade, seen in Figure 1-1, contains multiple serpentine passages with a variety of internal cooling (turbulators, impingement holes, pin fins) and external cooling (shower head holes and film cooling holes) features. The cooling features in Figure 1-1, are traditionally developed using a variety of complex casting processes. The additive process can bypass several of the tooling, core development, and wax pattern processes that are required for traditionally casted components [4]. The accelerated production timelines offered through AM come from the ability to verify and compare different cooling designs more rapidly compared to traditional manufacturing methods during the product development phase. Investigating the printability of the advanced cooling schemes within blades and vanes allows

future designers to alter geometry in order to produce favorable part tolerances; which can directly impact overall cooling performance.

Public literature is at an early stage for pressure loss and heat transfer relationships for components made using AM. As a result of the enhanced design space AM offers relative to casting, unique cooling geometries can be produced; however, designers need to account for the roughness and deformation that occurs in the AM process for the current printing technologies. By better understanding the influence of AM build considerations such as build direction and part locations, components can be manufactured more consistently from part to part and with higher cooling effectiveness compared to before.

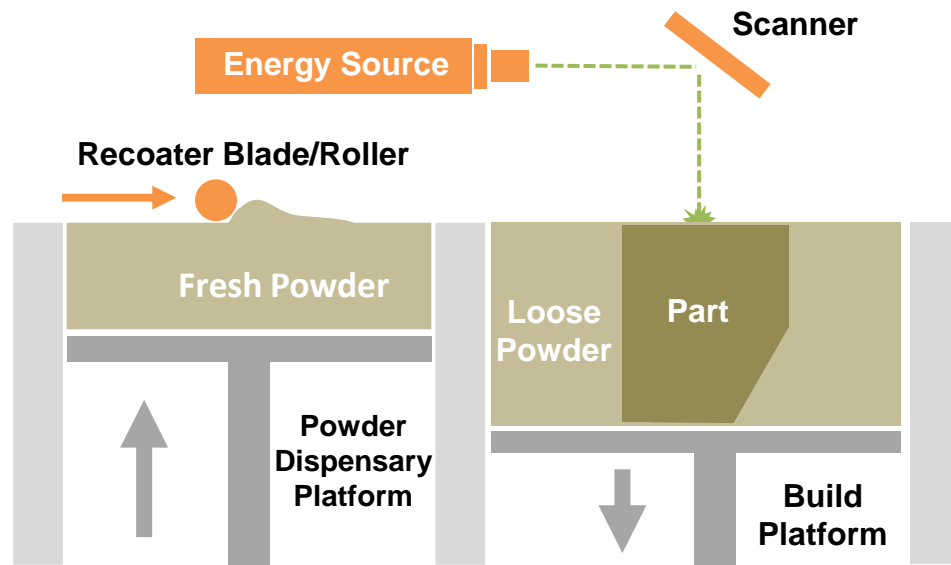


**Figure 1-1 Diaphragm of gas turbine blade with a variety of external cooling (a) and internal cooling (b) features [5].**

## 1.2 Laser Powder Bed Fusion

The use of metals for the fabrication of AM components is appealing to the energy and aerospace communities, in particular, due to the development of high temperature metal alloys, production of microscale features, high specific strength and stiffness relative to other non-metal materials, and desirable thermal properties. Of the seven categories of AM processes characterized by the American Society of Design and Materials group [6], metal 3D printing typically occurs through metal powder bed fusion techniques. Powder Bed Fusion is predominately used given its ability to resolve small features for true-scale components, material availability, surface morphology, post-processing methods, and cost relative to the other metal AM processes [7]. Powder bed fusion (PBF) processes are distinguished by the energy sources used [8] such as selective laser melting (SLM), electron beam melting (EBM), selective laser sintering (SLS), and direct metal laser sintering (DMLS). All samples studied in this proposal were fabricated using

metal AM, specifically DMLS. A typical PBF process is seen in Figure 1-1, where powder metal is selectively melted from an energy source (either electron beam or laser-based) that follows a profile outlined from the design intent digital model [8]. In more detail, the powder metal is melted by the energy source to form a liquid pool, also known as a melt pool, which then rapidly cools and solidifies. After the energy source has scanned a cross-sectional profile for a particular metal layer, the build platform is lowered to deposit another layer of powder using a re-coater blade or another device such as a roller. This process is then repeated until the component is built [9].



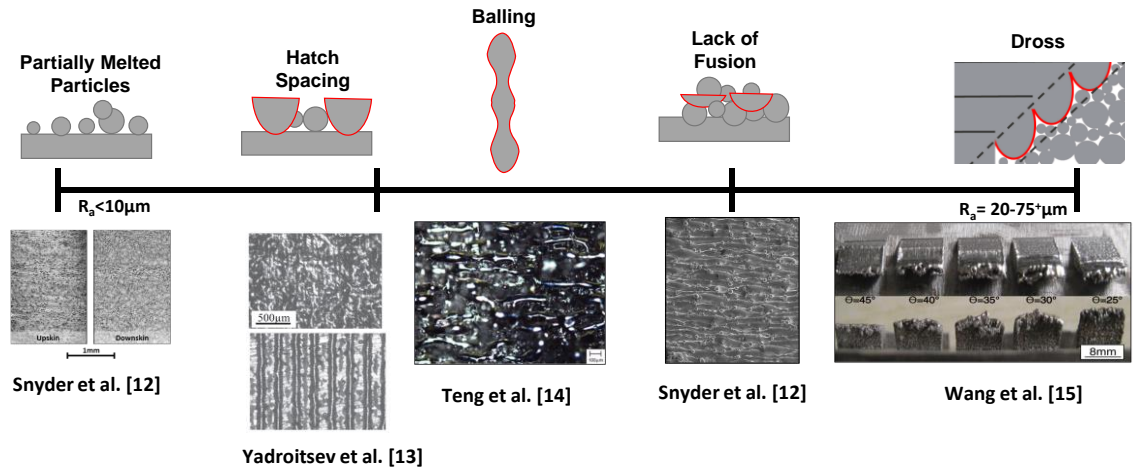
**Figure 1-2 Schematic of a general PBF process showing the substrate, energy source, component, powder, and re-coater blade/roller.**

A benefit in using the PBF process relative to most other metal AM processes is that unfused residual powder can be recycled and blended with virgin powder for a future build. However, it must be noted that the use of recycled powder can impact the repeatability and overall quality of an AM part [10]. After printing, post-processing techniques such as heat treatments are used to reduce residual thermal stresses that develop during the build to produce more favorable material properties and prevent further warpage that can occur when removing the part from the build plate [11]. After the parts have been heat treated, the parts are further post-processed by removing the components from the build plate as well as removing any support structures that were designed into the part for building purposes.

### 1.3 Surface Roughness and Deformation

A key characteristic of the DMLS process is the greater surface roughness relative to conventionally manufactured surfaces. The roughness elements experienced in internal DMLS channels can lead to significant protrusions into the flow causing high turbulent mixing leading to differences in pressure loss and convective heat transfer. In some cases the surface roughness can lead to favorable augmentations in heat transfer. In fact, the augmentation of heat transfer of simple AM channel shapes such as circular cross-sections can be similar to highly engineered cooling designs (such as convectional rib turbulators) made by non-AM methods [12].

A host of reasons exist as to why AM parts are inherently rough, including poor melt pool control, powder particles that are attracted to the melt pool during the process, and the stair stepping effect resulting from the layerwise process. Accordingly, there are a range of distinct surface roughness types present in AM that range in scale from small partially melted particles, which range between 20-60  $\mu\text{m}$ , to large dross formations illustrated in Figure 1-3. A general overview on the types of AM surface roughness includes partially melted particles, hatch spacing, balling, lack of fusion, and dross. All of these types of roughness in Figure 1-3 depend upon the process/design parameters and can even be tailored to enhance heat transfer [13].



**Figure 1-3 Range of roughness types experienced in AM parts which are impacted by design consideration and the AM process [12–16].**

Understanding the influences that cause the deviations and variations to surface morphology is important to understand the resulting impact to pressure loss and heat transfer augmentations. To fabricate AM components, common build considerations include the component build direction and placement on the substrate, powder removal, placement of support structures, and overall part

geometry. Several studies have investigated the impact of these factors on surface roughness. Design considerations such as the location of the component on the substrate can influence the deviation from design intent [17–20] which was shown by Kleszczynski et al. [17] to be attributed to the laser incidence angle. The work Oter et al. [19] and Sendino et al. [20] also observed that depending upon where the components are fabricated relative to the center of the substrate plate, various levels of surface roughness and deviations occur. A key consideration is the placement of support structures that add to conduction paths during the process directly impacting the thermal stresses and resulting warpage [21].

The work of Snyder et al. [22] and Mingear et al. [23] showed that internal channels can exhibit a range of deformations depending on different build directions. The resulting geometric deviations and surface roughness from changes to build direction influences the convective heat transfer and pressure loss of the internal passages. The effect of process parameters on internal surface morphology and impact to cooling performance is vital for heat transfer designers to understand so they can fabricate predictable cooling schemes.

#### **1.4 Research Objectives**

As additive manufacturing further develops there will be a paradigm shift in the process of advance product development, aimed particularly for complicated components with cooling passages as result of the added complexity offered by the design freedom of the growing AM technology compared to conventional manufacturing methods. However, until then, a basic understanding of general part tolerances and cooling performance relationships for cooling schemes and complicated components such as those seen in gas turbines made by AM needs to be better established. There are two main research objectives in this work: (i) determine the major impacts that the AM process has on the build quality and cooling performance of cooling passages and improve the capabilities of predicting pressure loss and heat transfer of AM cooling passages; and (ii) determine how the same AM process considerations impacts the geometry and tolerances of more complicated gas turbine components.

The first objective of this research is to improve the understanding of common AM build considerations (such as changes to part location on the build plate, build direction, and channel size) on the impact to surface roughness, pressure loss, and heat transfer of AM cooling schemes. By investigating both surface roughness and overall build quality of cooling passages, relationships to cooling performance can be explored to improve the capability in predicting pressure loss and heat transfer of AM cooling channels. The ability to predict cooling designs without the need for

experimental measurements is an important developmental design step toward the cooling design of a component made through AM.

The second objective of this research is to provide the foundational work toward fabricating complicated AM gas turbine components such as turbine guide vanes for rapid prototyping and experimental rig testing. Changes to a component geometry can impact the overall surface quality during the AM process, consequently even the most minute changes to surface roughness or tolerances of a turbine component can have a direct influence on the overall cooling effectiveness and efficiency. The work highlighted not only provides the major impacts the AM process can have on surface quality and deviation from design intent of guide vanes but also links similar build relationships to those found in cooling passages.

## **1.5 Outline of Dissertation**

This dissertation highlights five full research papers that are segmented into the central chapters of this dissertation. Four of the papers have undergone peer review in a conference or journal publication. The remaining paper is being submitted to Turbo Expo 2023 and the *Journal of Turbomachinery*.

Chapter 2 is a study presented at Turbo Expo 2020 and is published within the *Journal of Turbomachinery*. The work highlights the detailed impact of general AM build considerations such as build direction on the geometric tolerances, pressure loss, and heat transfer of cooling channels with a variety of diameters. The work found that heat transfer, in this case Nusselt number, does not always increase with increasing friction factor attributed to changes in build direction. Furthermore, build direction was found to be one of the primary factors toward differences in geometry and cooling performance.

Chapter 3 is a study presented during Turbo Expo 2022 and is published within the *Journal of Turbomachinery*. The study presents novel results on the convective heat transfer and pressure loss of different channel shapes and a comparative analysis on various characteristic length scales for scaling the overall cooling performance of the different channel shapes. Observations from the study showed that a combination of the shape of the channel and the internal surface roughness influences the convective mixing.

Chapter 4 is a study that is currently in review for Turbo Expo 2023 and the *Journal of Turbomachinery*. The study combines the results from previous Chapters and datasets from literature to develop an accurate correlation for pressure loss and convective heat transfer of AM channels. Due to the use of multiple roughness statistics in the proposed correlations, the



correlations can be applied to any circular channel regardless of changes to AM laser process parameters, build direction, channel size, and material.

Chapter 5 is a study presented at Turbo Expo 2022 and is published within the *Journal of Turbomachinery*. The study expands upon the effect of part geometry and build location on the surface quality of internal cooling channels. Furthermore, the work presents the first surface quality results of an engine relevant AM turbine vane (with no cooling features) printed at a variety of build directions in literature. The work also revealed the influence wall thickness can have on the surface quality of cooling channels and AM vane airfoils.

Chapter 6 is a study published within the *Journal of Global Power and Propulsion*. The study expanded upon the previous vane airfoil work by fabricating the same vanes with modern internal and external cooling features such as film cooling holes at various build directions. The work also showed the impact of part to part variation in pressure loss and convective heat transfer of cooling channels as well as the variation between parts of more complicated turbine vane geometries for a given build plate.

The final chapter of this dissertation, Chapter 7, outlines the main findings throughout each of the studies. Additionally, this chapter recommends future areas of work needed to further enhance the heat transfer and additive manufacturing community's understanding of using AM in gas turbines for rapid prototyping purposes.

## **2 Impact of Additive Manufacturing on Internal Cooling Channels with Varying Diameters and Build Directions<sup>2</sup>**

### **2.1 Abstract**

The use of additive manufacturing (AM) processes, such as direct metal laser sintering, provides the design freedom required to incorporate complex cooling schemes in gas turbine components. Additively manufactured turbine components have a range of cooling feature sizes and, because of the inherent three-dimensionality, a wide range of build angles. Previous studies have shown that AM build directions influence internal channel surface roughness that, in turn, augment heat transfer and pressure loss. This study investigates the impact of additive manufacturing on channel feature size and build direction relative to tolerance, surface roughness, pressure losses, and convective cooling. Multiple AM coupons were built from Inconel 718 consisting of channels with different diameters and a variety of build directions. An experimental rig was used to measure pressure drop to calculate friction factor and was used to impose a constant surface temperature boundary condition to collect Nusselt number over a range of Reynolds numbers. Significant variations in surface roughness and geometric deviations from the design intent were observed for distinct build directions and channel sizes. These differences led to notable impacts in friction factor and Nusselt number augmentations, which were a strong function of build angle.

### **2.2 Introduction**

Of the metal additive manufacturing (AM) processes, direct metal laser sintering (DMLS) has gained popularity among companies specializing in high temperature applications. The recent advancements in superalloy materials for DMLS are targeted towards difficult operating environments like those experienced by turbine components. The powerful design opportunities enabled by AM offer turbine designers the ability to incorporate complex cooling features within components.

While the design freedom is opened through AM, designers still need to keep in mind the build part that results from the process. The process chosen affects geometric tolerances, part shape, and surface roughness, which are important to internal cooling features. The challenge in removing surface roughness from additive parts with complex internal passages is constrained by the feature

---

<sup>2</sup> Wildgoose, A.J., Thole, K.A., Sanders, P., and Wang, L., 2021, "Impact of Additive Manufacturing on Internal Cooling Channels with Varying Diameters and Build Directions," *Journal of Turbomachinery*, vol. **137**(7), pp. 071003.

size. As-built surfaces exhibit large surface roughness that can be beneficial to convective heat transfer but comes coupled with increases in pressure losses.

Additively manufacturing a cooled turbine component results in many feature sizes being built with a range of local build directions. Consequently, it is imperative to understand how the intended design is affected by the build direction. Understanding these impacts allow designers to adjust their additive designs in strategic ways. For example, modifying the shape of a circular cooling channel to a geometry such as a teardrop shape allows the designer to compensate for the effects that gravity has on channel shape due to the build process. The unique goal of this study is to provide the designer with guidelines as to when build angle becomes important on particular features sizes.

### **2.3 Literature Review**

There are a multitude of process and design parameters that impact surface roughness in additively produced parts. It is well-known that build direction, the orientation of the external surface or streamwise channel axis relative to the surface of the substrate (i.e. build plate), has a significant contribution to surface roughness [17,18,24–29]. Many studies have investigated external surface roughness along multiple build directions. Ventola et al. [24] observed roughness on external surfaces increases from  $0^\circ$  to  $30^\circ$  then decreases from  $30^\circ$  to  $90^\circ$ . Additionally, similar surface roughness characteristics were observed on the external surfaces of samples fabricated by Tian et al. [28]. While these studies are thorough in their respective findings, a considerable amount of the studies have not characterized surface roughness and feature shape for internal channels.

Only a few studies have reported surface roughness measurements for internal channels [22,23,27,30]. Several of these studies have presented roughness measurements with a minimum of two different build directions. Mingear et al. [23], studied the effect of process parameters on vertical and horizontal orientations of internal channels with three varying diameters. Findings concluded that roughness decreases with diameter when channel axes are built parallel to the build plate (horizontal build direction,  $0^\circ$ ). Similarly, Stimpson et al. [30] observed that internal surface roughness decreases with diameter in rectangular channels fabricated at  $45^\circ$ . Snyder et al. [25] observed internal surface roughness for circular channels remains relatively similar between  $0^\circ$  and  $45^\circ$ . Pakkanen et al. [27] demonstrated that from  $60^\circ$  to  $90^\circ$ , upward and downward facing surfaces have similar roughness values. However, the sample diameters used in the study were between 5 mm and 10 mm, which are relatively large for implementation in turbine heat transfer applications.

Quantifying geometric tolerances and deviations from the design intent aids in understanding surface roughness and its impact on the pressure losses and convective cooling of

internal AM channels. Previous studies [22,27,31] give novel measurements for the magnitude of deformation of internal channels. Kamat et al. [31], developed an algorithm to predict channel shape deformation for diamond, circular, and ellipsoid shapes with diameters ranging from 4 mm to 12 mm built at 0°. Results indicated that the measured diameter for all channel shapes were larger than the design intent. These findings were similar to Snyder et al. [25], who additionally demonstrated that the distribution of deviation from design intent in circular channels built at 0°, 45°, and 90° were larger at 0° and 45° compared to 90°. Additionally, geometric tolerances such as concentricity were smallest at 90°. Many of these studies compare channels with less than three build directions that use diameters that are either held constant or have a range of above 4 mm. Few studies have investigated the geometric tolerances and deviations from design intent of multiple channel diameters below 4 mm built over a range of build directions.

Stimpson et al. [30], proposed a correlation for predicting Nusselt number in additive internal channels which was developed using rectangular channels built at 45°. Previous studies such as Parbat et al. [32], have shown reasonable agreement between the correlation and experimental results with channels built at the same 45° direction. Results to verify the correlation for nonrectangular channel shapes have not been thoroughly presented in literature.

A limited number of studies have experimentally measured the impact of surface roughness on the convection coefficients and pressure losses of AM internal channels built at a variety of build angles. Snyder et al. [25] provides the impact build direction has on the convective cooling and pressure loss performance of channels with a constant diameter built across three build directions. The study's results indicate that 45° channels contain larger convection coefficients compared to both horizontal and vertical orientations, which was attributed to roughness. As this study was limited to the 0°, 45°, and 90° build directions with a constant 0.5 mm channel diameter, the effects of build direction between 0° to 45° and 45° to 90° with varying channel diameters are unexplored.

The present study is unique because it aims to fill the gaps researchers currently have for additive channels in relating surface roughness, part tolerance, and geometric shape on the channel's pressure losses and cooling performance.

## **2.4 Description of Test Coupons**

To effectively understand the impact of build direction and channel size on pressure losses and convective cooling, multiple coupons consisting of a range of angular build directions and diameters were fabricated using DMLS in Penn State's Center for Innovative Materials Processing through Direct Digital Deposition (CIMP-3D) Lab. The design specifications of the fifteen coupons

used in this study are outlined in Table 2-1. Specifically, coupons were printed containing numerous channels with each having one of three different diameters. Each coupon was printed at a different build direction ranging from 0° to 90°. The build direction is defined as the angle between the streamwise axis of the channel relative to the surface of the substrate (i.e. build plate).

The design diameters (1.25 mm, 1 mm, and 0.75 mm) were chosen based upon a range of common diameters seen in additive internal cooling literature [25,30,32,33]. The naming convention of individual coupons, as shown in Table 2-1, provides information on the design diameter, circular channel shape, and build direction. Each coupon had the same 50.80 mm length, 26.42 mm width, and 3.05 mm height as shown in Figure 2-1. Indicated in Figure 2-1, the channel pitch spacing ( $S$ ) was designed so the fin efficiency between channels is greater than 95% to allow for the constant surface temperature boundary condition to be satisfied. The channel pitch spacing was also designed to minimize the effect of channel deformation attributed to placing channels in close proximity of one another. The number of channels in a coupon was varied between design diameters and is specified in Table 2-1.

**Table 2-1 Geometric Specifications for Coupons**

Coupon Name	$D_{h, \text{design}}$ [ $\mu\text{m}$ ]	Build Direction [degrees]	Number of Channels	$\frac{S_{\text{design}}}{D_{h, \text{design}}}$	$D_{h, \text{actual}}$ [ $\mu\text{m}$ ]	$\frac{p_{\text{actual}}}{p_{\text{design}}}$	$\frac{A_{\text{actual}}}{A_{\text{design}}}$	$\frac{L_{\text{actual}}}{D_{h, \text{actual}}}$
0.75C0	750	0	14			Failed to Print		
1.00C0	1000	0	12	1.660	794.1	1.051	0.832	62.1
1.25C0	1250	0	10	1.552	1076	1.025	0.880	45.8
0.75C30	750	30	14	1.840	668.4	0.987	0.879	73.8
1.00C30	1000	30	12	1.660	892.2	1.001	0.893	55.3
1.25C30	1250	30	10	1.552	1147	1.019	0.934	43.0
0.75C45	750	45	14	1.840	725.1	1.003	0.970	68.0
1.00C45	1000	45	12	1.660	987.7	1.020	1.007	49.9
1.25C45	1250	45	10	1.552	1230	1.016	1.000	40.1
0.75C60	750	60	14	1.840	774.6	1.044	1.078	63.6
1.00C60	1000	60	12	1.660	1031	1.041	1.073	47.8
1.25C60	1250	60	10	1.552	1310	1.016	1.113	37.6
0.75C90	750	90	14	1.840	808.1	1.083	1.166	61.0
1.00C90	1000	90	12	1.660	1055	1.061	1.120	46.7
1.25C90	1250	90	10	1.552	1327	1.086	1.153	37.1

Support structures varied across build directions as shown in Figure 2-2. Support structures were required to build the coupons due to overhanging external features such as flanges for use in experimental testing. The support generation of these coupons followed the same guidelines as described by Snyder et al. [25]. Using these guidelines, supports were generated on coupon surfaces angled less than 40° to the substrate. The coupons did not have any supports inside the channels.

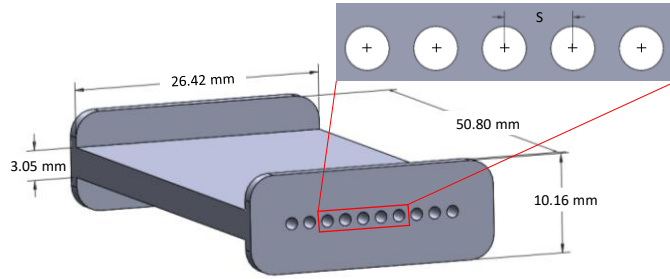
An EOS-M280 power bed fusion machine was used to manufacture all fifteen Inconel 718 (IN718) coupons with a 40-micron layer size. The IN718 powder supplied by EOS was sieved through a filter to a 40-micron nominal powder size. Coupons were grouped together to mitigate the difference in surface roughness between build locations on the substrate as observed by Kleszczynski et al. [17], Chen et al. [18], and Snyder et al. [22]. Furthermore, all coupons were angled 3° between the streamwise channel axis and re-coater blade direction as recommended by EOS [34].

Processing parameters have a significant impact on surface roughness and hence pressure loss and cooling performance [18,35–38]. The processing parameters used in this study, shown in Table 2-2, are recommended by EOS and kept constant between all coupons. Additionally, these recommended EOS parameters include wall contouring. Included in Table 2-2 is a calibration metric used to account for material shrinkage (material scaling) and a correction value to align the contour with respect to the CAD design (beam offset). These calibration parameters were calculated using the manufacturers procedures [34].

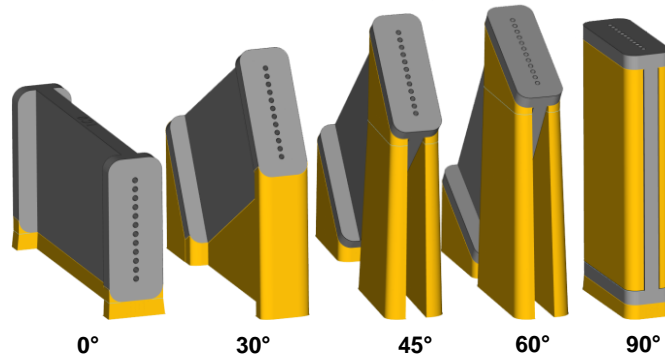
The coupons for this testing, while attached to the substrate, were solution annealed to remove residual stress as per recommended procedures for Inconel 718 [34]. After heat treatment, a wire electrical discharge machine was used to cut the coupons off the substrate and remove supports. Upon visual inspection, the 0.75C0 coupon channels were clogged with residual powder which could not be removed, as indicated in Table 2-1. The clogged channels demonstrate the challenge in additively manufacturing sub-millimeter channels.

**Table 2-2 Processing Parameters for AM Coupons**

Parameter	Value
Material	Inconel 718
Layer thickness	0.04 mm
Material setting	IN718 040 210 Performance
Material scaling X	0.366%
Material scaling Y	0.366%
Beam offset	0.106 mm



**Figure 2-1 CAD schematic of overall coupon dimensions used for experimental testing.**



**Figure 2-2 Coupon support structures generated over the five build directions.**

## 2.5 Geometric Channel Shapes

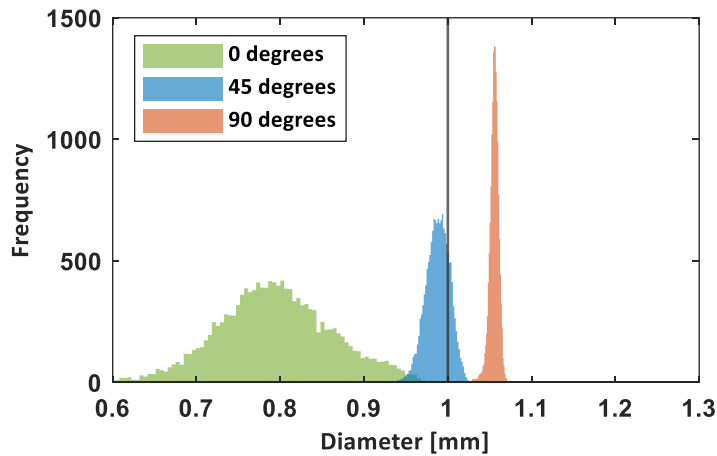
Assessing the as-built channel surface is essential in explaining differences between pressure loss and heat transfer augmentations when varying channel size and build direction. A non-destructive imaging method, computed x-ray tomography (CT Scan), was used to characterize the surface and geometric tolerances of the coupons. While optical profilometry provides better accuracy on surface roughness, it also requires line of sight access meaning that each coupon would essentially be destroyed. Stimpson et al. [10], noted that surface roughness measurements from CT scan data produce lower values compared to an optical profilometer. The CT scan accuracy of the spatial reconstruction of the coupons is influenced by the scanning resolution (i.e. voxel size). All coupons were CT scanned with a resolution of 35 microns using a GE v|tome|x L300 CT system. The volumetric measurements from the CT scan were examined using a commercial software that performs a surface determination based on gray-scale values from scans. The same software provides interpolation between voxels and is able to reduce the surface determination to 1/10<sup>th</sup> of the original voxel size [39].

Channel diameters were calculated following methods similar to Stimpson et al. [40]. After channel surfaces were determined, an in-house code was developed that used 1,200 image slices

along the axial length of the coupon to calculate hydraulic diameter. Channel perimeters were determined by summing the pixels along the border of a channel slice while the cross-sectional area was calculated by summing the pixels of the free space. The cross-sectional area and perimeter were then averaged between each channel and slice to determine a mean hydraulic diameter. All calculations used in this study are performed with the mean hydraulic diameter measured from CT scan data.

From Table 2-1, channel cross-sectional area varied greater from the design intent compared to channel perimeter. Both channel perimeter and cross-sectional area are closest to design intent at 45°. Results from Table 2-1 imply that channels fabricated at 90° contain channel perimeters and cross-sectional areas that are larger than design intent while channels fabricated closer to 0° become smaller than the design intent.

Shown in Figure 2-3 is the variation in the calculated hydraulic diameter for the 1 mm coupon at three build directions. There is significant deviation from the design diameter for the 0° and 90° build directions, while the 45° build direction is closest to the design diameter. For the 1 mm channel at 0°, 45°, and 90° build directions, the range of the diameters along with their 3σ deviation increased from 793.5±207 μm to 987.7±45 μm to 1055±19 μm, respectively.



**Figure 2-3 Distribution of measured diameters from CT scans of a 1 mm coupon at 0°, 45°, and 90°.**

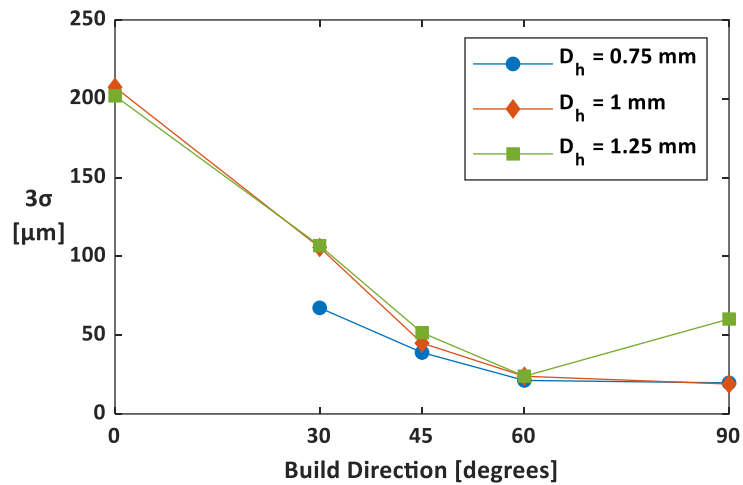
These results indicate the wide variation in hydraulic diameters for a channel at different build directions, particularly for the 0° build direction. The implications of these results are that tight tolerances are better held for vertical builds (90°) as opposed to horizontal builds (0°). Comparing the deviations of diameters between coupons over a range of build directions, shown in Figure 2-4, show similar tolerances can be achieved between 60° and 90°, regardless of diameter.



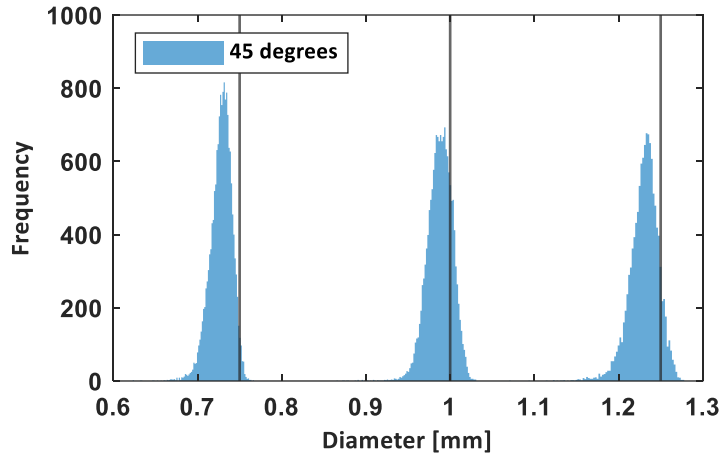
The distribution of diameters between 0° and 60° show a dramatic decrease in the spread. These results imply that with a horizontal build (0°) holding a particular tolerance is challenging at best. In turbine cooling applications, where tight tolerances are needed for specific coolant flows, it is not desirable to have a wide variety of channel dimensions.

Shown in Figure 2-5 is the variation that occurs for a single build direction of 45° for each of the three channel diameters. The three channel diameters and their 3σ deviations were 725.1±40 μm, 987.7±45 μm, and 1230±52 μm, respectively. Because the spread is nearly the same for each of the channel sizes, these results indicate that build direction has a major influence relative to the feature size.

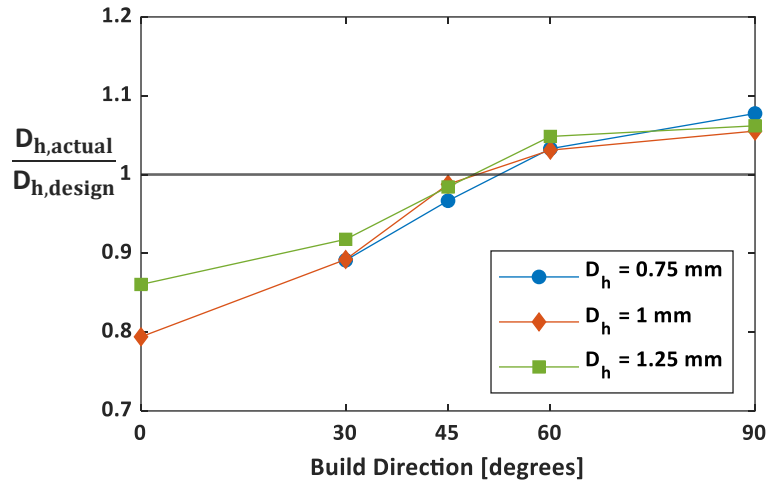
Shown in Figure 2-6 are the averaged hydraulic diameters normalized by the design intent for all of the coupons. The data in Figure 2-6 implies that diameter is larger than the design intent at angles above 60° while being lower than design intent at angles below 45°. Regardless of diameter size, the resulting diameter increases from 0° to 90°. The deviation in diameter from design intent for the 1 mm coupon is 21% at 0° compared to 6% at 90°.



**Figure 2-4 3σ deviations of calculated diameter for each of the coupons over a range of build directions.**



**Figure 2-5 Distribution of measured diameters from CT scans of a 0.75 mm, 1mm, and 1.25 mm coupon at a 45° build direction.**



**Figure 2-6 Deviation of channel diameter from design intent across multiple build directions.**

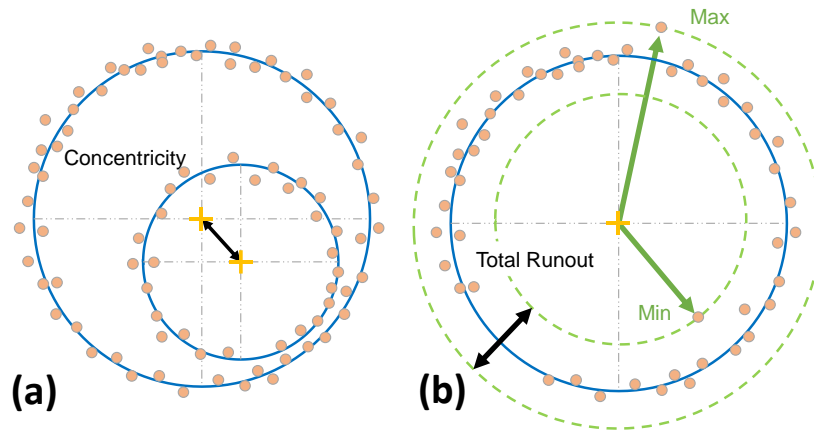
## 2.6 Geometric Tolerances

The benefit of deducing the pixel location along the perimeter is that it allows for the channel surface to be represented as a point cloud when calculating three-dimensional tolerances, such as concentricity, circularity, and runout. The concentricity of each coupon channel was calculated by taking the average distance between centroids of the slices. Shown in Figure 2-7(a), concentricity is a three-dimensional tolerance comparing the variation in centroids along the length of the channel. A concentricity value of zero infers that all centroid slices reside on the axial axis and represent a straight channel. As all coupons were designed with a circular cross-section,

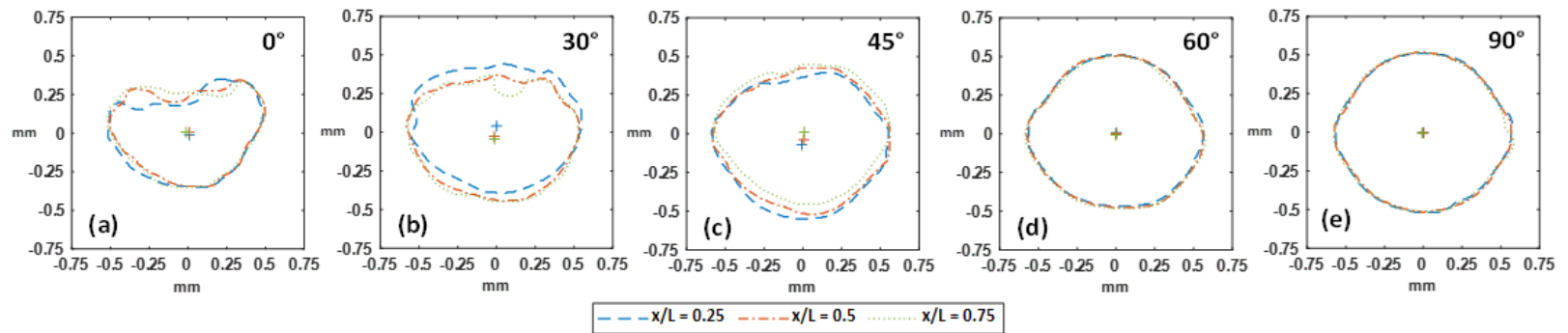
circularity, shown in equation (2-1), provides an indication to the amount of channel shape deviation from design intent. A circularity value of one, indicates channel shapes that meet the circular design intent.

$$\text{Circularity} = \frac{4\pi A}{p^2} \quad (2-1)$$

The circularity measurements reported in this study are averaged along the length of the coupon and were calculated using the filled cross-sectional area and perimeter of the slices. Total runout, visually shown in the Figure 2-7(b), combines both circularity and concentricity into a three-dimensional tolerance describing variation in straightness and circularity. The measurement of total runout requires defining an axis of rotation which was determined by averaging the location of all the centroid slices. The difference between the maximum and minimum distance from the surface to the axis of rotation along the entire length of the coupon was recorded as the total runout tolerance. A total runout value of zero represents perfectly cylindrical channels that are aligned in the streamwise direction. A comparison between channel shapes at three axial slices of the 1 mm coupon over a range of build directions are shown in Figure 2-8(a-e).



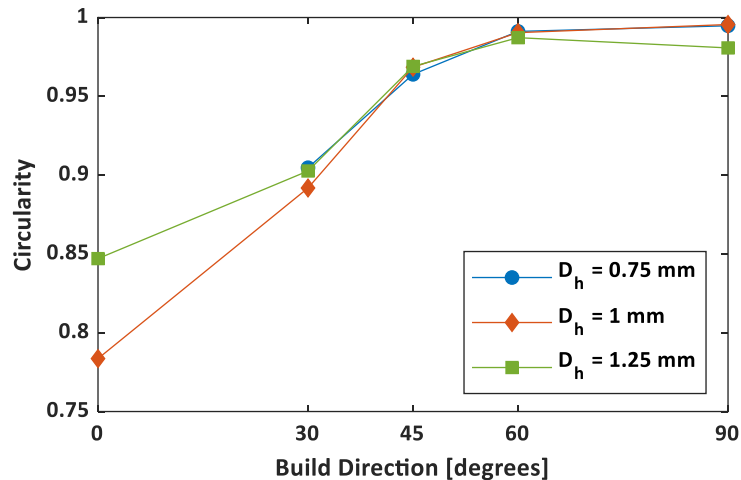
**Figure 2-7 Physical definitions of concentricity (a) and total runout (b).**



**Figure 2-8 Axial slices of a 1 mm channel built at 0° (a), 30° (b), 45° (c), 60° (d), and 90° (e) showing the impact of build direction on the geometric deformation of a circular cross-section.**

The results in Figure 2-8(a-e) reinforce the significant impact build direction has on channel deformation. Consistent with the results from Snyder et al. [25], channels fabricated at 90° are closest to their intended circular shape. In addition, the channel shape remains the same at each streamwise position. These findings for the 90° channel results from each build layer receiving a circular contour and not containing any preceding overhanging build layers.

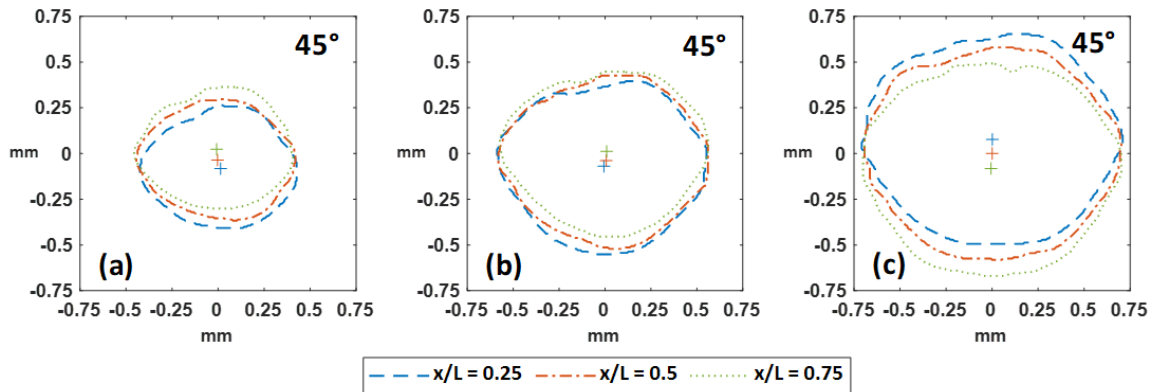
Channels built at orientations less than 60°, as shown in Figure 2-8(a-d), show clear deviations from the intended circular design with the downward facing surfaces exhibiting increasing flatness as the build angle decreases. Figure 2-8(a-c) show more deviations along the channel compared with Figure 2-8(d-e) as the build angle decreases, which is consistent with the wider spread in the hydraulic diameters for small build angles as shown in Figure 3 and Figure 4. Ealy et al. [41] presented similar results with circular channels displaying less deviation from design intent for channels built at 90°. The findings from Figure 2-8(a-e) are quantitatively shown when comparing circularity across various build directions as illustrated in Figure 2-9. As build direction decreases, the downward facing surface becomes increasingly exposed to unsintered powder which, in turn, becomes sintered to the top surface.



**Figure 2-9 Impact of build direction on the circularity of the 0.75 mm, 1 mm, and 1.25 mm coupons.**

Figure 2-9 also provides a guideline as to when geometric modifications are needed for a round channel design. For example, at build angles below 45°, slight modifications to the channel design can account for the deformation (non-circularity) that occurs during the build; however, as build angle decreases to 0° and 30°, more significant geometric modifications are needed in the design if circular channels are intended.

Channel modifications such as teardrop shapes from Snyder et al. [25] and Kamat et al. [31] aim to account for channel deformation attributed to build direction. Circularity between diameters exhibit changes only at build directions lower than  $30^\circ$ . Visually comparing circularity between diameters at  $45^\circ$ , in Figure 2-10, confirms that the amount of deformation is constant no matter the diameter at  $45^\circ$ .

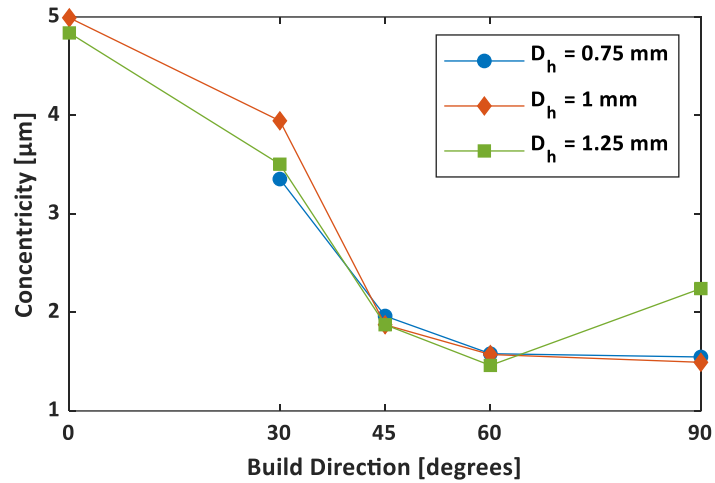


**Figure 2-10 0.75 mm (a), 1 mm (b), and 1.25 mm (c) circular channel cross-sections at a  $45^\circ$  build direction.**

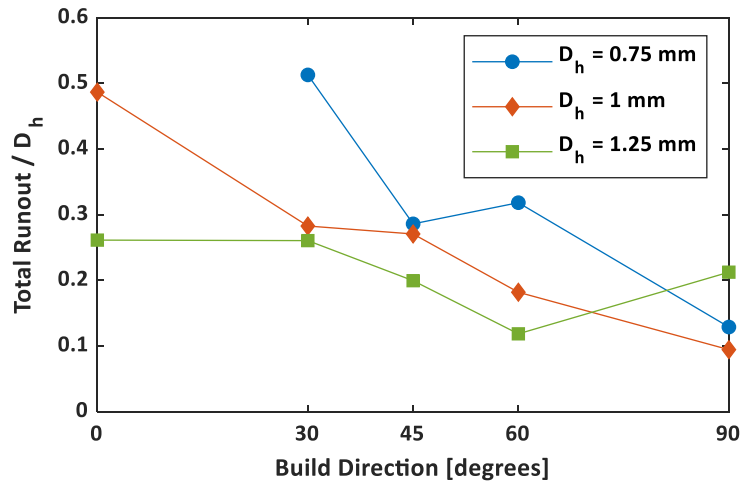
Investigating concentricity between build direction and channel diameter provides a tolerance describing channel straightness. Shown in Figure 2-11, concentricity decreases as build direction increases. This result is supported when comparing the differences in centroids along the axial length of a channel shown in Figure 2-8(a-e). The  $90^\circ$  channel centroids are grouped closer together compared to the other build directions such as the  $30^\circ$  centroids. These results are due to the  $90^\circ$  channel being built with no overhanging features.

Scaling the total runout by diameter removes the scale associated with varying diameters and provides an indication to the magnitude of total runout at a constant scale. Higher values of total runout/ $D_h$  indicate channels that are not uniformly positioned in the coupon. The results in Figure 2-12 imply that additively producing smaller channels lead to greater magnitudes of axial and surface deformations. Decreasing the build direction below  $90^\circ$  increases the runout due to the unsupported build layers on the downward facing surfaces, which is consistent with results in Figure 2-11. In Figure 2-12, the 0.75 mm  $60^\circ$  coupon has a larger total runout compared to its  $45^\circ$  counterpart. After further inspection of the 0.75C60 coupon, channels near the entrance of the coupon had a strikingly large difference between the mean centroid and channel surface. The deviation from design intent at the entrance of the 0.75C60 impacted the position of the mean centroid reference line which resulted in an increased total runout value. From CT scan results, the

1.25C90 coupon showed significant deviation and roughness compared to its 60° coupon equivalent. The authors believe that this effect is caused by the cooling rate of the sintered powder which was influenced by the design and placements of the support structures on the 0.75C60 and 1.25C90 coupon.



**Figure 2-11 Impact of build direction on the concentricity of the 0.75 mm, 1 mm, and 1.25 mm coupons.**



**Figure 2-12 Impact of build direction on the normalized total runout, Total runout/ $D_h$ , of the 0.75 mm, 1 mm, and 1.25 mm coupons.**

## 2.7 Roughness Evaluation

As previously discussed, CT scan data was used as a nondestructive determination for internal surface roughness. The arithmetic mean roughness ( $R_a$ ) was calculated using the axial

slices from CT scan data.  $R_a$  reflects the average surface deviation from a mean reference and its mathematical definition is given in equation (2-2).

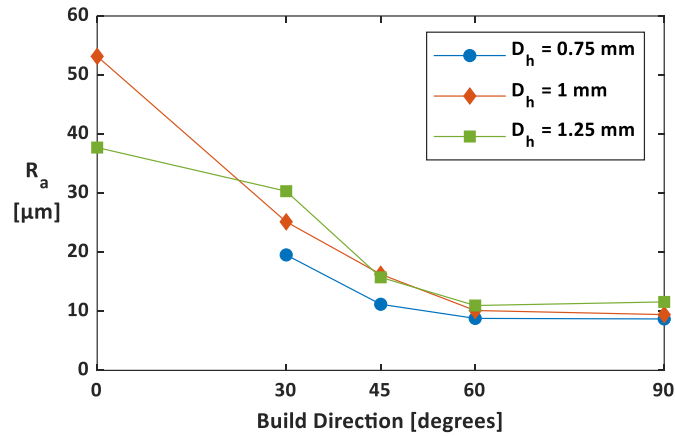
$$R_a = \frac{1}{n} \sum_{i=1}^n |z_{\text{surf}} - z_{\text{ref}}| \quad (2-2)$$

An in-house code was developed to measure the surface roughness using a method similar to Klingaa et al. [29]. Arithmetic mean roughness, equation (2), requires defining a mean reference line. The inherent curvature of the circular channel makes defining a reference line challenging. As such, an ellipsoid was fitted to each axial slice using a linear least square regression method to represent the reference line. Each of the axial slices contained its own fitted ellipsoid, resulting in a stack of 1,200 ellipsoids for a single channel. The smallest nominal distance between each pixel along the perimeter and the fitted ellipsoid was recorded as the nominal deviation. All roughness measurements were evaluated by averaging measurements of multiple channels in a coupon.

In agreement with previous studies [23,25], internal channel surface roughness decreases from  $0^\circ$  to  $90^\circ$  as demonstrated in Figure 2-13. Roughness levels found in this study are similar to values found in literature [18,22,26,27]. Uncertainties for these roughness values are the tolerances from the CT scan surface determination,  $\pm 3.5$  microns. Nearly the same roughness values occurred for all three channel diameters for a particular build direction. The agreement in the roughness values is expected since the same process was used; however, the implications of these results reinforce the importance of build angle on the roughness levels.

Results from Figure 2-13, give novel evidence that surface roughness is indistinguishable between  $60^\circ$  and  $90^\circ$  in small internal channels. This outcome is supported when comparing cross-sections of the 1 mm coupon at  $60^\circ$  and  $90^\circ$  in Figure 2-8(d-e). Below  $60^\circ$ , roughness values increase for all the geometries. Despite differences in nondimensional total runout, channels between  $60^\circ$  and  $90^\circ$  have similar surface roughness, concentricity, and circularity regardless of diameter.





**Figure 2-13 Averaged arithmetic mean roughness measured from CT scan data of circular channels.**

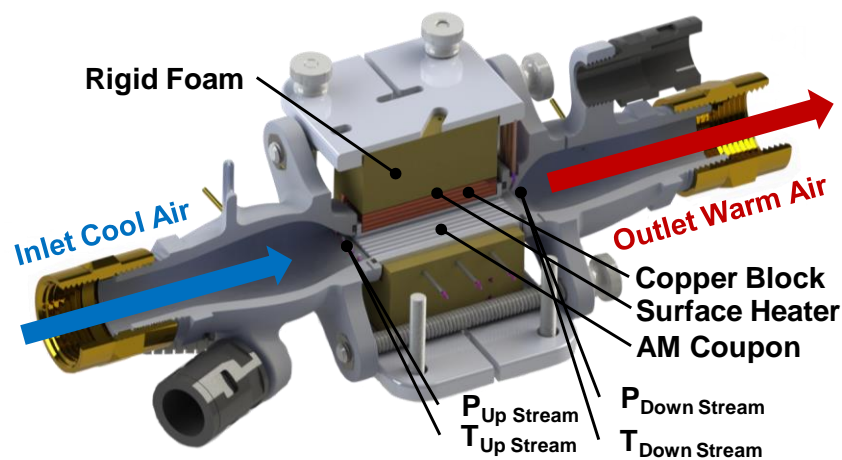
## 2.8 Channel Performance Measurements

An experimental rig was used to quantify coupon pressure losses and bulk convection coefficients over a range of Reynolds numbers. Both tests were performed on a rig designed similar to Snyder et al. [25] and Stimpson et al. [30] as shown in Figure 2-14. This particular rig has been described and previously benchmarked by several investigators [25,30].

Friction factors were calculated using a measured pressure drop and flowrate as well as coupon diameters from CT scan data. Since pressure taps were located both up and down stream of the coupon, loss coefficients were included in the pressure drop calculation. The inlet loss coefficients were calculated by evaluating an area ratio between the coupon channels and inlet plenum as described by Munson et al. [42]. The outlet loss coefficients were constant between all coupons with a value of one resulting from the sudden flow expansion. Mass flowrates were measured upstream with a laminar flow element coupled with temperature and pressure measurements.

Bulk convective heat transfer coefficients,  $h$ , were calculated using measured data from the same rig as that shown in Figure 2-14. A copper block was placed between a heater and the coupon surface to impose a constant channel surface temperature boundary condition. The method is described in further detail by Stimpson et al. [30]. A state-of-the-art thermal conductivity measurement device was used to determine the thermal properties of the additive IN718 material. The thermal conductivity value for IN718 was  $9.77 \pm 0.49$  W/mK at room temperature and was used for the coupon surface temperature analysis. This thermal conductivity value is similar to those reported in literature for Inconel 718 [43].

The heat transfer analysis included performing a one-dimensional conduction analysis using thermocouples inside the copper block, shown in Figure 2-14, to calculate the surface temperature of the coupon channel. Conduction losses in the plenums and foam material were accounted for in the heat transfer measurements. These conduction losses were less than 1% of the total power supplied by the heaters at high and low Reynolds numbers. An energy balance was performed between the amount of heat transferred into the air,  $Q_{\text{air}}$ , as it passed through the coupon and the amount of heat supplied by the heaters,  $Q_{\text{heaters}}$ . Theoretically, the amount of heat added to the system from the heaters minus that of the conduction losses should equal the amount of heat transferred to the air. The energy balance is an independent check comparing the difference between the amount of heat transferred into the air,  $Q_{\text{air}}$ , to the amount of heat supplied by the heaters with conduction losses. This energy balance was smaller than 6% across all Reynolds numbers tested for every coupon.



**Figure 2-14 Schematic of experimental rig used for pressure loss and heat transfer measurements.**

## 2.9 Experimental Uncertainty

Pressure drop and diameter were the main contributors to friction factor uncertainty. Uncertainty was calculated using the propagation of uncertainty method described by Figliola et al. [44]. The uncertainty in friction factor at high Reynolds numbers was 3% while for low Reynolds numbers it was 4%. The uncertainty in Reynolds number was between 4.5% and 7%. Exit thermocouple measurements and diameter were the main contributors to uncertainty in Nusselt number. The Nusselt number uncertainty was less than 7%.

## 2.10 Friction Factor Evaluation

Friction factors were quantified for each coupon over a range of Reynolds numbers (Re) as seen in Figure 2-15. Pressure drop measurements for the friction factors were collected in the incompressible flow regime at Mach numbers less than 0.2. Prior to measuring the pressure drop across the rough coupons, a benchmark test was conducted using a smooth coupon, which is also shown in Figure 2-15 to agree with a well-accepted correlation.

For the AM coupons, Figure 2-15 shows that there is a large range of friction factors that result from the different build angles and different channel diameters. Similar to previous literature [25,30,33], the transitional Reynolds number decreases with increasing roughness as shown in Figure 2-15 for the low Reynolds numbers. The transition Reynolds numbers can be seen with the 0.75C90 coupon which enters the transitional flow regime at a Re = 2,000 compared to the 0.75C30 coupon which starts its transition at a Re = 1,000.

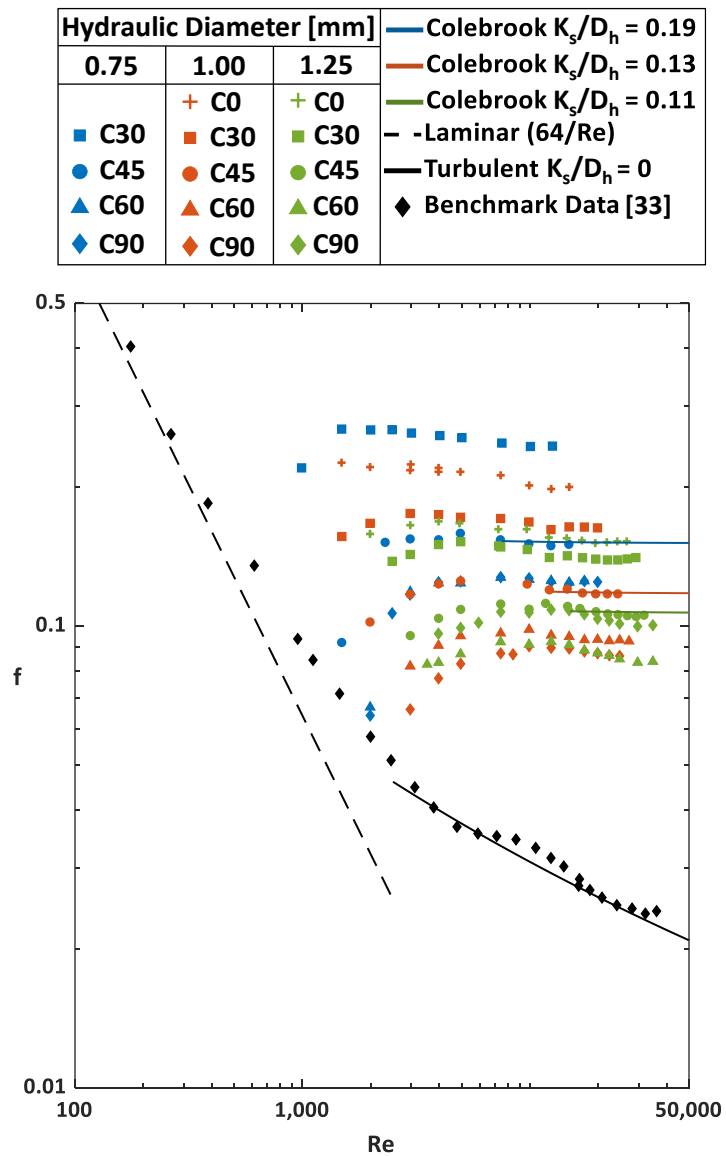
The data in Figure 2-15 shows that the highest friction factors occur at the lowest build direction, 0°. This highest friction factor result is consistent with the highest relative roughness levels ( $K_s/D_h$ ) also occurring for the lower build angles, Figure 2-13, as well as the most distorted channel shapes, Figure 2-8(a-e). Figure 2-15 also shows that for each of the channel diameters of 0.75 mm and 1.00 mm, the 60° and 90° data collapse to the same curve, respectively. However, the 0.75 mm channel size has overall higher friction factors than the 1.00 mm channel size since the roughness magnitudes are nearly the same, but with the subsequent roughness-to-diameter ratio being highest for the smallest channel.

The 1.25C45, 1.00C45, and 0.75C45 coupon friction factor values in Figure 2-15 are also displayed with their relative roughness values,  $K_s/D_h$ , which were calculated using the Colebrook correlation, equation (2-3), for each of the coupons in the fully turbulent regime. Relative roughness is an indication of the effect that a particular roughness morphology has on pressure loss.

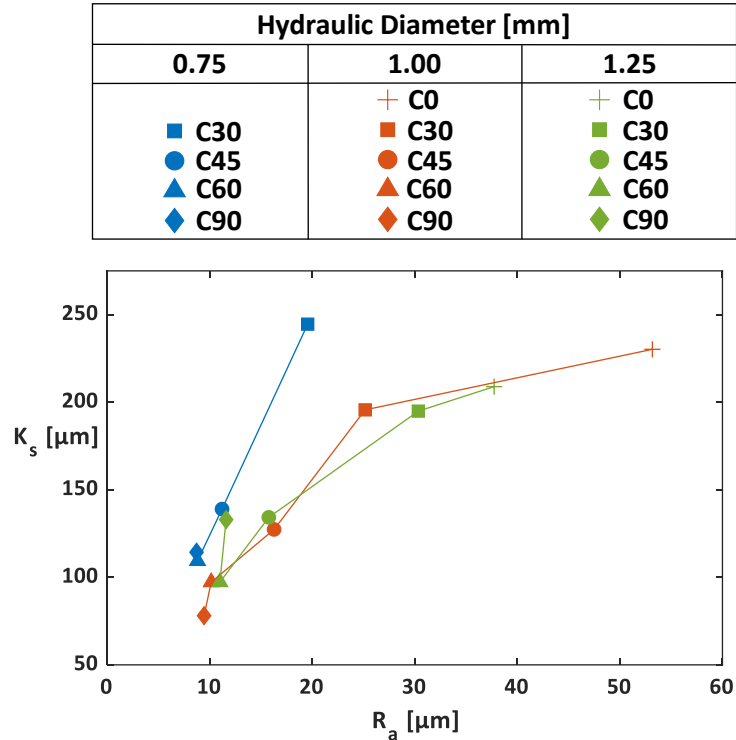
$$\frac{1}{\sqrt{f}} = -2 \log_{10} \left( \frac{K_s}{3.7D_h} + \frac{2.51}{Re\sqrt{f}} \right) \quad (2-3)$$

Results of the sandgrain roughness and arithmetic mean roughness are shown in Figure 2-16, which also shows a decrease in sandgrain roughness as build direction increases. In comparing the data for the 0.75 mm coupons in Figure 2-13 and Figure 2-16, the arithmetic mean roughness ( $R_a$ ) and relative roughness ( $K_s$ ) lead to different observations. For example, the 0.75 mm coupons have the largest  $K_s$  roughness and also have the lowest  $R_a$  roughness. For the 0.75 coupon, the high relative roughness is caused by large protrusions in the flow field created from unsupported downward

facing surfaces, as shown in Figure 2-8(a). These protrusions in the flow act as large turbulators leading to high pressure losses. Coupons with the same diameter built between 60° and 90° share similar surface roughness; however, the 0.75 mm channels contain a 33% (on average) larger sandgrain roughness compared to the 1 mm channels. This results in larger pressure losses for the 0.75 mm coupon at 60° and 90° as seen in Figure 2-15. Larger sandgrain roughness is a result of the deformation of the coupons as indicated by the total runout being larger for the 0.75 mm 60° and 90° coupons compared to the 1 mm coupons.



**Figure 2-15 Cylindrical channel friction factor data of coupons with varying diameters and build directions, along with benchmark data from Stimpson et al. [33].**



**Figure 2-16 Sandgrain roughness calculated using equation (2-3) compared with measured arithmetic mean roughness of coupons.**

### 2.11 Heat Transfer Evaluation

Nusselt number was calculated over a range of Reynolds numbers for each coupon as shown in Figure 2-17. Benchmark Nusselt numbers for a smooth coupon were also collected as shown in Figure 2-17. The small temperature difference between the outlet of the 0.75C30 coupon and wall temperature resulted in unacceptable uncertainties due to a saturation of the coolant temperature. As such, the 0.75C30 coupon is omitted from Figure 2-17.

Similar with the results from Snyder et al. [25], Nusselt number is smallest at the vertical (90°) build direction shown in Figure 2-17. This is supported by the 90° coupons containing the least amount of deformation and surface roughness. Despite the 0° coupons containing the greatest amount of deformation, sandgrain roughness, and  $R_a$  roughness, the 0° coupons showed a lower Nusselt number compared to the 30°, 45°, and 60° coupons. This implies the significance of characterizing the surface morphology which the arithmetic mean roughness does not fully capture in relating Nusselt number. Shown in Figure 2-17, the 0.75 mm diameter channels presented the largest Nusselt numbers which is supported by the coupons also containing the largest sandgrain roughness. These results imply that including smaller diameter channels in cooling designs lead to

higher convective cooling compared with larger channels; however, this comes along with significantly larger pressure losses. Results from Figure 2-17 also indicate that as Reynolds number increases, Nusselt number becomes closer to a smooth channel. As such the heat transfer enhancement decreases with increasing Reynolds number, a similar result is shown by Stimpson et al. [33].

As verified from literature [25,30], using the Gnielinski correlation [45], equation (2-4), for internal AM rough surfaces fails to provide adequate predictions of Nusselt number. As such, Stimpson et al. [30] modified the well-known Gnielinski correlation for internal channels made through AM. Shown in Figure 2-18 for the 0.75C45, 1.00C45, and 1.25C45 coupons, Stimpson's heat transfer correlation reasonably predicts Nusselt numbers with circular AM channels built at 45°. Stimpson's correlation [30], shown in equation (2-5), was within a maximum of 23% of this reports 0.75C45, 1.00C45, 1.25C45 heat transfer data when predicted using friction factor calculated from equation (2-3) with  $K_s/D_h$  measured from experimental data. It is important to note that Stimpson's correlation was developed using rectangular channels built at 45° with a maximum uncertainty of 30%.

$$Nu = \frac{f/8(Re-100)Pr}{1+12.7\sqrt{f/8}(Pr^{2/3}-1)} \quad (2-4)$$

$$Nu = \frac{(Re^{0.5}-29)Pr\sqrt{f/8}}{0.6(1-Pr^{2/3})} \quad (2-5)$$

Hydraulic Diameter [mm]			— Gnielinski $K_s/D_h = 0$ ◆ Benchmark Data [33]
0.75	1.00	1.25	
	+ C0	+ C0	
● C45	■ C30	■ C30	
▲ C60	● C45	● C45	
◆ C90	▲ C60	▲ C60	
	◆ C90	◆ C90	

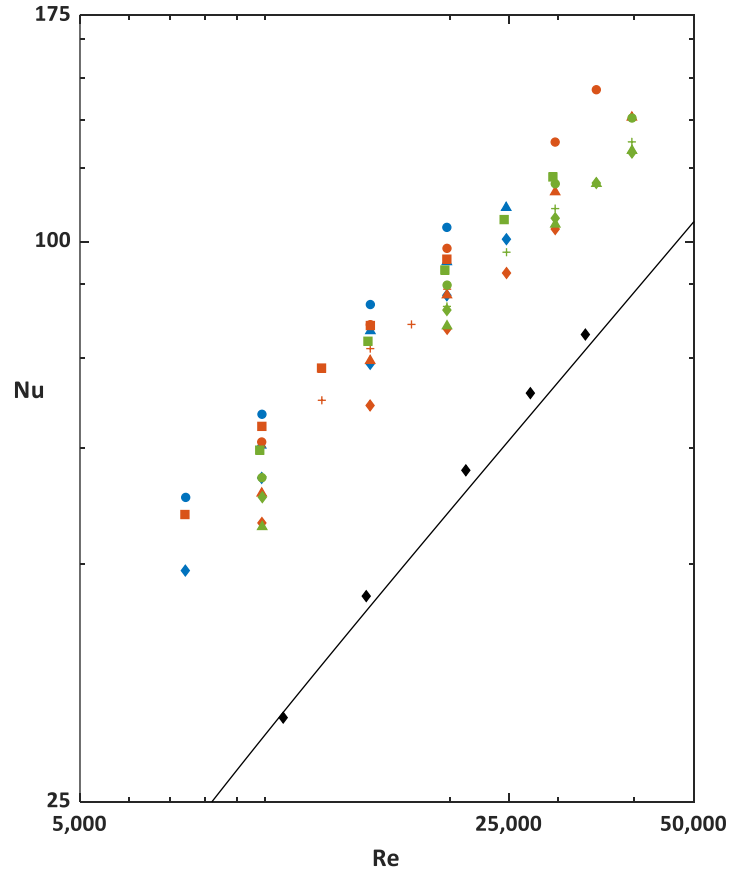
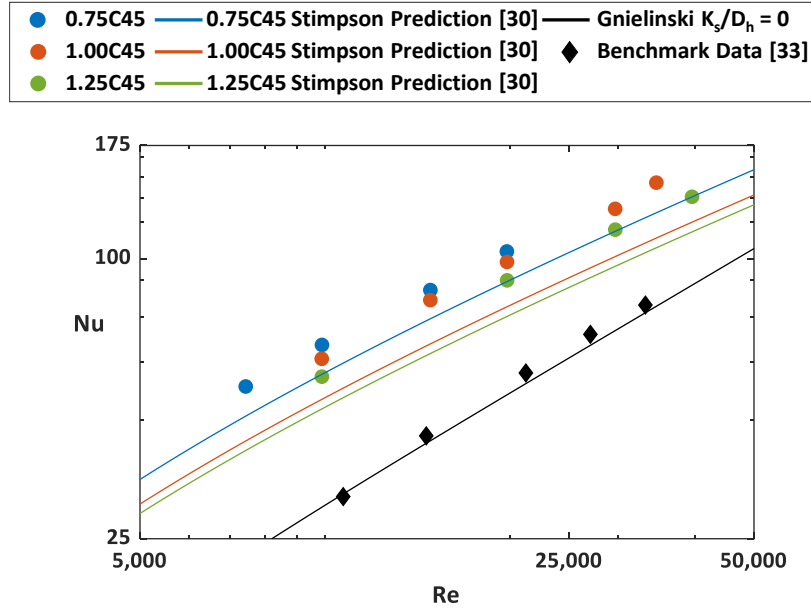


Figure 2-17 Cylindrical channel Nusselt number data with benchmark results from Stimpson et al. [33].



**Figure 2-18 Nusselt number of the 0.75C45, 1.00C45, 1.25C45 coupons with Stimpson et al. [30] correlation calculated using measured friction factor.**

The augmentations of Nusselt number and friction factor are shown in Figure 2-19. The smooth channel friction factor,  $f_0$ , was calculated using equation (2-3) with relative roughness equaling zero. The smooth channel Nusselt number,  $Nu_0$ , was calculated using smooth channel friction factor values from equation (2-3) with Gnielinski's Nusselt number correlation [45], equation (2-4).

In general, Figure 2-19 shows that the  $0^\circ$  build direction increases the friction factor augmentation for the two channels indicated without significantly increasing the heat transfer augmentation. Implementing a channel shape correction at  $0^\circ$  may be able to minimize the large increase in friction factor augmentation with benefits in heat transfer augmentation.

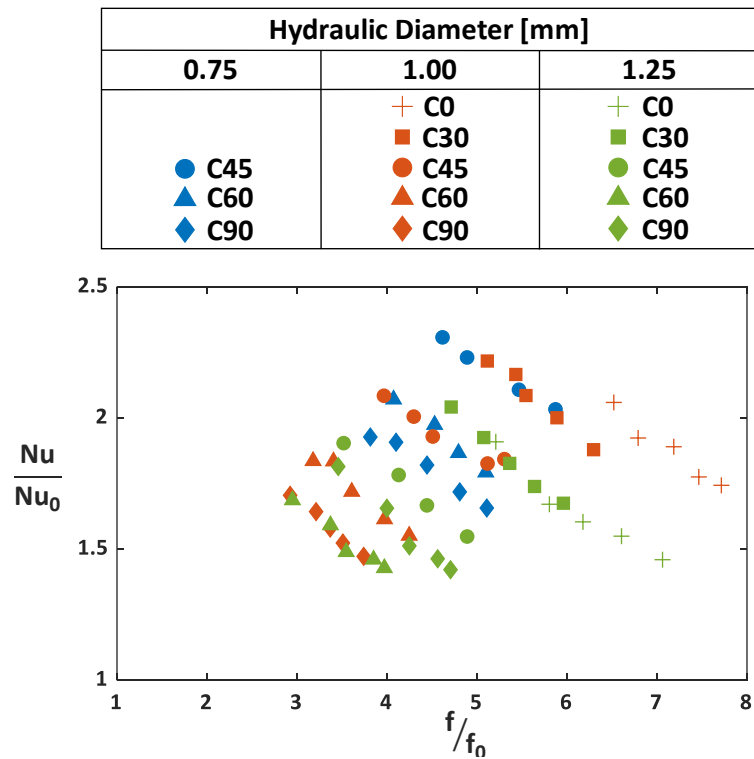
Also, as will be shown in the next graphs, the  $30^\circ$  to  $45^\circ$  channels have higher heat transfer augmentations. For each of the build angles, the smallest channel sizes produced the highest heat transfer augmentation for a given friction factor augmentation.

Augmentations as a function of build angle are shown in Figure 2-20 and Figure 2-21. The augmentations for the friction factor and Nusselt number show very different characteristics. While the friction factor decreases as build angle increases, the heat transfer augmentation peaks between  $30^\circ$  and  $45^\circ$ . Snyder et al. [25] observed the highest heat transfer augmentation at  $45^\circ$  compared to  $0^\circ$  and  $90^\circ$ . As would be anticipated from the roughness values shown in Figure 2-13, which also decrease with build angle, it would be expected that augmentations decrease if it were simply a

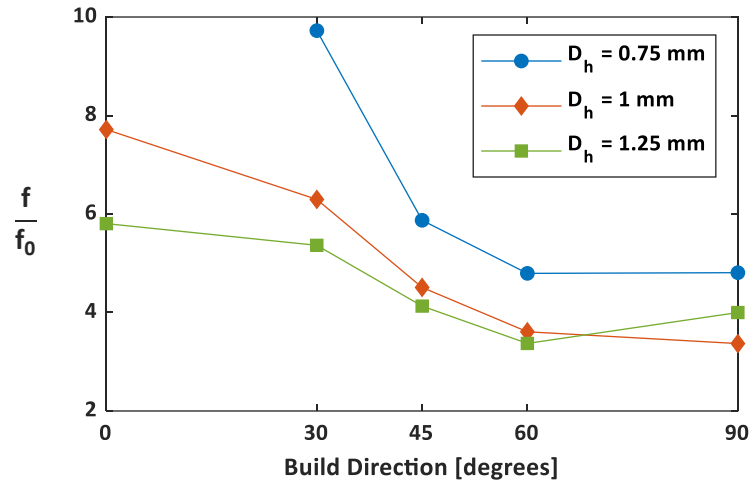


function of roughness. The results in Figure 2-21, however, indicate otherwise for the heat transfer coefficient augmentations that peak between 30° and 45°. These results point to the importance of the surface morphology that results from a particular build angle.

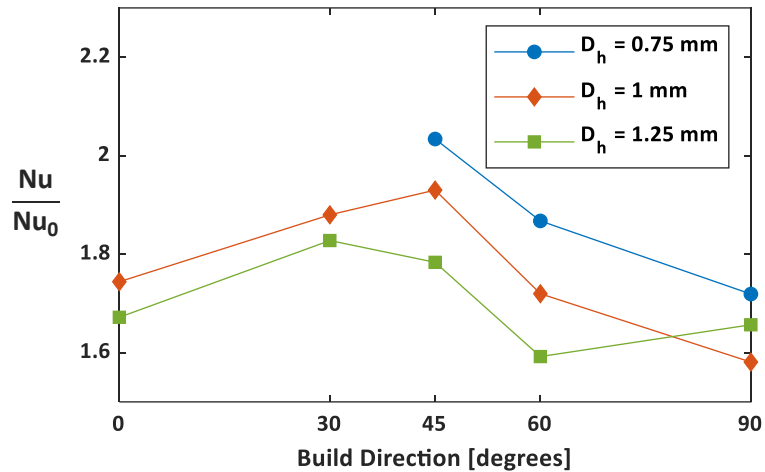
Despite the 60° coupons having similar surface roughness, friction factor augmentations, and geometric tolerances as the 90° coupons. The 60° coupons observed an 8% larger heat transfer augmentation compared to the 90° coupons. From these results, simply by orienting an additive component so a large quantity of 60° channels occur compared to 90° channels result in sizable increases in heat transfer without additional pressure losses.



**Figure 2-19 Nusselt number and friction factor augmentations over a range of Reynolds numbers.**



**Figure 2-20 Friction factor augmentation of coupons across multiple build directions at a shared Reynolds number of 20,000.**



**Figure 2-21 Nusselt number augmentation of coupons across multiple build directions at a shared Reynolds number of 20,000.**

## 2.12 Conclusion

The design freedom allotted through additive manufacturing, specifically DMLS, has the potential to reevaluate current cooling designs that are restrained by traditional manufacturing methods. Turbine designers wanting to implement effective cooling schemes require understanding the impacts the additive process has on the geometric tolerances, surface roughness, pressure losses, and convective cooling of additively produced internal channels.

The results presented in this paper indicated that the build effects on the resulting geometric tolerances of circular channels were quite large. In most cases, build angles below  $60^\circ$  had a

dramatic effect on channel shape and design intent. Build direction contributes greatly to variations in diameter along all of the channel diameters no matter how small. For designers wanting to additively produce circular channels close to their design intent, channel shape modifications are needed at angles below  $60^\circ$ .

Surface roughness changes minimally for channels built between  $60^\circ$  and  $90^\circ$ , regardless of diameter. Just as channel deformation, surface roughness increases as build angle decreases from  $45^\circ$  to  $0^\circ$ . At angles below  $45^\circ$  channel diameter contributes to changes in surface roughness. Applications requiring small additive circular channels with low surface roughness should be built between  $60^\circ$  and  $90^\circ$ .

Circular channels, sharing the same diameter, built between  $60^\circ$  and  $90^\circ$  have similar friction factor augmentations. Relative roughness and friction factor augmentation increases when lowering channel diameter. In contrast, heat transfer augmentation peaks for a build angle between  $30^\circ$  and  $45^\circ$ , regardless of diameter. Decreasing the channel diameter increases both the Nusselt number and friction factor augmentations. These results point to the importance of the surface morphology in which surface roughness does not fully capture.

In summary, the designer using additive manufacturing needs to be made aware of the impacts that build direction, in particular, has on the resulting part. Depending upon the application, it may be necessary to change the channel shape and diameter to achieve the intended design.

## **3 Heat Transfer and Pressure Loss of Additively Manufactured Internal Cooling Channels with Various Shapes<sup>3</sup>**

### **3.1 Abstract**

Additive manufacturing (AM) provides the ability to fabricate highly customized internal cooling passages that are relevant to gas turbine components. This experimental study examines the pressure loss and heat transfer performance of a range of fundamental channel shapes that were produced using direct metal laser sintering. Circular, hexagonal, pentagonal, elliptical, diamond, square, rectangular, trapezoidal, and triangular channel cross-sections were investigated. To maintain the same convective surface area between shapes, the wetted perimeters of the channel cross-sections were kept constant. Parallel computational fluid dynamic simulations were performed to understand the relationships in cooling performance between several channel shapes. Several characteristic length scales were evaluated to scale the pressure loss and heat transfer measurements. Among the channel shapes investigated, the diamond channel showed the lowest Nusselt number and friction factor. The pentagon exhibited a similar Nusselt number as the circular channel despite having a lower friction factor. There was no difference in scaling the friction factor or Nusselt number results of the different channels shapes between using the square root of cross-sectional area compared to hydraulic diameter as the characteristic length scale.

### **3.2 Introduction**

As additive manufacturing (AM) becomes more common in the fabrication of gas turbine components, engineers will begin to better use the added design freedom to construct more complex and higher performing cooling schemes as compared to those that are traditionally investment casted. Prior internal cooling research has looked into the cooling performance of additively made lattice structures [46,47], wavy channels [48], and rectangular/circular [25,30,49] cross-sectional channels. A broader focus on the impact of simplistic polygonal-shaped channels on heat transfer and pressure losses has not been thoroughly investigated. The ability to predict the pressure loss and heat transfer of different channel shapes accurately is important for a range of applications. The channel shape can impact the secondary flows resulting in differences to pressure loss and heat transfer. Several researchers [50–53] have investigated a variety of channels with different cross-sections and saw that using length scales other than hydraulic diameter better scaled cooling performance. The objective of this study is to make use of the additive process to manufacture

---

<sup>3</sup> Wildgoose, A.J. and Thole, K.A., 2022, “Heat Transfer and Pressure Loss of Additively Manufactured Internal Cooling Channels with Various Shapes”, GT2022-82298, will be published in the Journal of Turbomachinery.

various channel shapes to determine how the resulting heat transfer and pressure losses are impacted as well as how to best scale the results.

### **3.3 Literature Review**

Multiple studies have evaluated the pressure loss and heat transfer of various internal channel shapes [50–52,54–56]. As reported by Kays and Crawford [57], hydraulic diameter is predominantly used as a characteristic length to scale the pressure loss and heat transfer of different cross-sectional channel shapes. However, several studies [50,56,58] have found discrepancies when using hydraulic diameter to scale pressure loss for hydraulically smooth cross-sectional shapes. Most notably, Duan et al. [50] showed that when using hydraulic diameter as the length scale for friction factor and Reynolds number, a triangular cross-section can have up to a 30% lower friction factor compared to a circular cross-section thereby indicating that the hydraulic diameter may not be accurately scaling the data. In addition, Jones [58] found that for different aspect ratio rectangular channels the friction factor can be up to 37% higher or 23% lower than a circular channel. These studies emphasize the struggle that hydraulic diameter has as a characteristic length to adequately scale the pressure loss of different channel cross-sections. Consequently, Duan et al. [50] showed that using other length scales, such as the square root of cross-sectional area reduces the scatter in friction factor for various channel shapes compared to hydraulic diameter.

Despite the fewer number of experimental heat transfer measurements relative to pressure loss, studies such as Duan [59] and Leung et al. [56] showed that there can be a range of Nusselt numbers between different channel shapes when using hydraulic diameter as the characteristic length scale. In particular, Leung et al. [60] found that Nusselt number for range of apex angles of triangular ducts can be as much as 29% lower than the Dittus-Boelter Nusselt number correlation. The numerical results from Wang et al. [53] show that the Nusselt number calculated using hydraulic diameter of an equilateral triangle can be 28% different from predictions using traditional Nusselt number correlations developed for circular channels. Similar to the scaling of friction factor, Duan [59] found that using the square root of cross-sectional area scaled Nusselt number for a range of channel shapes better than that of hydraulic diameter. However, due to the lack of available noncircular turbulent heat transfer data the heat transfer results from Duan [59] was generated using the Colburn analogy and not experimental data.

The previous studies mentioned for both pressure loss and heat transfer mainly evaluated a select few of channel shapes such as trapezoidal, rectangular, and triangular cross-sections. The limited amount of noncircular channel shape measurements of pressure loss and heat transfer are possibly a result limited manufacturability. In contrast, AM provides for the fabrication of channel

shapes that were not available for the previous studies. A significant portion of AM channel literature that have fabricated different channel shapes focus more on channel deformation [61–64] rather than pressure losses or convective heat transfer. A comprehensive review from Thole et al. [12] provides an overview of cooling performance of additively made channels. The portion of available AM cooling performance datasets includes a small range of channel shapes such square, rectangular, and circular cross-sections compared to the shapes that have been evaluated in non-AM studies. Subsequently, there is limited knowledge about the scalability of pressure loss or heat transfer using characteristic length scales other than hydraulic diameter.

This study aims to provide additional experimental pressure loss and heat transfer measurements for a range of different channel shapes that have not been evaluated in the literature. Additionally, this paper addresses the scaling of friction factor and Nusselt number results with a characteristic length scale other than hydraulic diameter for polygonal shaped channels. Numerical simulations were performed on select channel shapes to provide a further understanding of the heat transfer performance between channel cross-sections.

### **3.4 Description of Test Coupons**

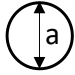
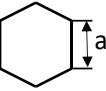
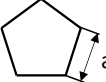
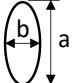
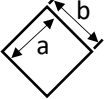
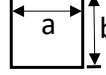
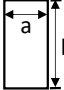
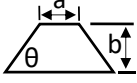
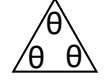
To assess the impact channel shape has on the pressure loss and convective heat transfer, a variety of straight channel shapes were fabricated using direct metal laser sintering (DMLS). Nine channel shapes were selected for evaluation and are specified in Table 3-1. The nine channel shapes were designed to maintain the same cross-sectional perimeter and coupon length to guarantee the same convective heat transfer surface area. The design perimeter for each channel was chosen to match a circular diameter of 1.5 mm giving a perimeter of 4.8 mm.

As seen in Figure 3-1, each test coupon was designed to have nine channels. The channel pitch spacing ( $S$ ), as seen in Figure 3-1, was controlled such that the fin efficiency between channels was greater than 95% to fulfill the constant surface temperature boundary condition during heat transfer measurements. The length-to-hydraulic diameter ratios of the channels were between  $33 < L/D_h < 54$ , which meets fully developed conditions.

The channels were fabricated using a  $90^\circ$  build direction where the streamwise axis of the channel is perpendicular to the surface of the build plate to give the least amount of deformation from their design intent. There were no supports placed inside the channels. Additionally, the channel pitch was designed to limit channel deformation attributed to the proximity of nearby channels. The coupons were fabricated using an EOS-M280 powder bed fusion machine in Inconel 718 (IN718) with a 40-micron layer size. The recycled powder, supplied by EOS, was sieved

through a filter to a nominal 40-micron powder size before use. To lower the chance of particle drag caused by a damaged re-coater blade impacting the coupons, the coupons were angled 3° between their streamwise channel axis and the recoater blade direction as recommend by EOS [34]. Coupons were grouped to limit differences in surface roughness caused by the build location on a substrate as seen in literature [17,25]. To maintain consistency with past literature [25,30,49], all coupons used the recommended EOS processing parameters, outlined in Table 3-2, for a 40-micron layer size in IN718 with wall contouring. The calibration parameters in Table 3-2 were carried out using the manufactures procedures [34]. Loose powder was removed from the internal channels and supports prior to heat treatment. The coupons were solution annealed while attached to the substrate to remove residual stress as recommended by standard EOS heat treatment procedures for Inconel 718 [34]. After heat treatment, a wire electrical discharge machine removed the coupons off the substrate and remove supports.

**Table 3-1. Geometric Specifications for Coupons Sharing a Constant Perimeter ( $P_{des} = 4.79$  mm)**

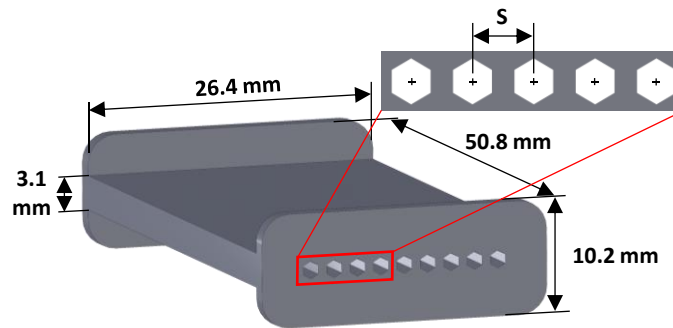
Coupon Name	$D_{h, actual}$ [ $\mu\text{m}$ ]	$A_{actual}$ [ $\mu\text{m}^2$ ] $\cdot 10^7$	$\frac{D_{h, actual}}{D_{h, design}}$	$\frac{p_{actual}}{p_{design}}$	$\frac{A_{actual}}{A_{design}}$	$\frac{S_{design}}{D_{h, design}}$	Area Averaged $R_a$ [ $\mu\text{m}$ ]	Geometry Aspect Ratios [ $\mu\text{m}$ ]
Circle	1590	1.81	1.04	1.06	1.10	1.43	11.82	$a = D_h$ 
Hexagon	1497	1.68	1.08	1.04	1.13	1.57	5.48	$a = 797.96$ 
Pentagon	1428	1.60	1.08	1.04	1.13	1.66	6.85	$a = 957.56$ 
Ellipse	1340	1.51	1.05	1.05	1.09	1.66	6.59	$a/b = 2$ 
Diamond	1314	1.46	1.10	1.03	1.13	1.84	4.91	$a/b = 1$ 
Square	1283	1.50	1.07	1.09	1.17	1.80	17.00	$a/b = 1$ 
Rectangle	1200	1.34	1.13	1.04	1.17	1.99	7.19	$a/b = 2$ 
Trapezoid	1145	1.32	1.11	1.07	1.19	2.16	16.95	$a/b = 0.8$ $\Theta = 60^\circ$ 
Triangle	1047	1.19	1.14	1.05	1.20	2.38	11.90	$\Theta = 60^\circ$ 



### 3.5 Characterization of Channel Shapes

Characterizing the as-built quality and resolving the internal surface morphology are important in evaluating impacts on pressure loss and heat transfer. The coupons were nondestructively evaluated using a computed x-ray tomography (CT scan) method to measure as-built geometries and surface roughness of the channels. To resolve the entire internal surface of all the channels, all coupons were CT scanned at a 35 micron spatial resolution (voxel size). A commercial software [65] was used to capture the internal surface through selectively filtering gray scale values obtained from the volumetric CT scan measurements. Through interpolation the same software is able to resolve  $1/10^{\text{th}}$  of the original voxel size [39].

Channel cross-sectional areas, perimeters, and hydraulic diameters were calculated using an in-house code to analyze 1,200 cross-sectional CT image slices taken along the streamwise axis of the coupon. Pixels in each free space were summed to calculate cross-sectional area while the number of pixels along the border of a channel slice was recorded as the perimeter. Each perimeter and cross-sectional area were averaged to determine a mean hydraulic diameter. Regardless of channel shape, the channel cross-sectional area deviated more from the design intent compared to perimeter as seen in Table 3-1. The cross-sectional area, perimeter, and hydraulic diameter are larger than the design intent for all the channel shapes. This result is similar to previous circular channel literature at the same build direction [25,49].

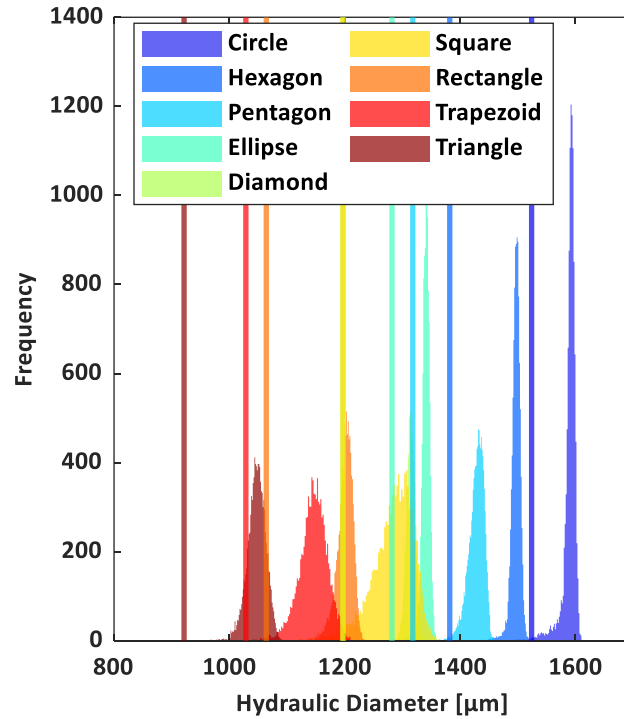


**Figure 3-1. Schematic of coupon dimensions used for experimental testing.**

**Table 3-2. Processing Parameters for AM Coupons**

Parameter	Value
Material	Inconel 718
Layer thickness	0.04 mm
Material setting	IN718 040 211 Performance
Material scaling X	0.12%
Material scaling Y	0.12%
Beam offset	0.12 mm

Even though each channel shape has larger dimensions for the as-built geometry than the design intent, the variation in geometric parameters are different between the channel shapes as seen in Figure 3-2. A histogram for each of the CT slices showing the distribution of hydraulic diameter is shown in Figure 3-2 as compared with the design intent (vertical lines). Clearly seen in Figure 3-2, the as-built diameter is larger than the design intent for all channel shapes. The square, trapezoid, and triangle contain a wider distribution of hydraulic diameter compared to the ellipse, circle and diamond indicating different channel shapes not only deviate from design intent but also contain variations in their geometric dimensions.



**Figure 3-2. Distribution of hydraulic diameter along with design intent calculated from CT scans of the different channel shapes.**

The standard deviations of each channel geometry are shown in Figure 3-3(a-c). Distinct channel shapes exhibit wider distributions in geometric dimensions as seen in the  $3\sigma$  deviations of perimeter, cross-sectional area, and hydraulic diameter. As seen in Figure 3-3(a), the square and trapezoid have the largest variation in hydraulic diameter while the ellipse, diamond, and hexagon contain the smallest variation. There is more variation in perimeter between the different channel shapes as compared to cross-sectional area. As observed in Figure 3-3(b,c), there is a 140% difference between the highest and lowest  $3\sigma$  deviation of perimeter while there is a 53% difference between the highest and lowest  $3\sigma$  deviation of cross-sectional area. The trapezoid, square, and triangle exhibit the largest variation while the ellipse, diamond, hexagon, and circle show the least amount of variation across all geometric dimensions as seen in Figure 3-3(a-c).

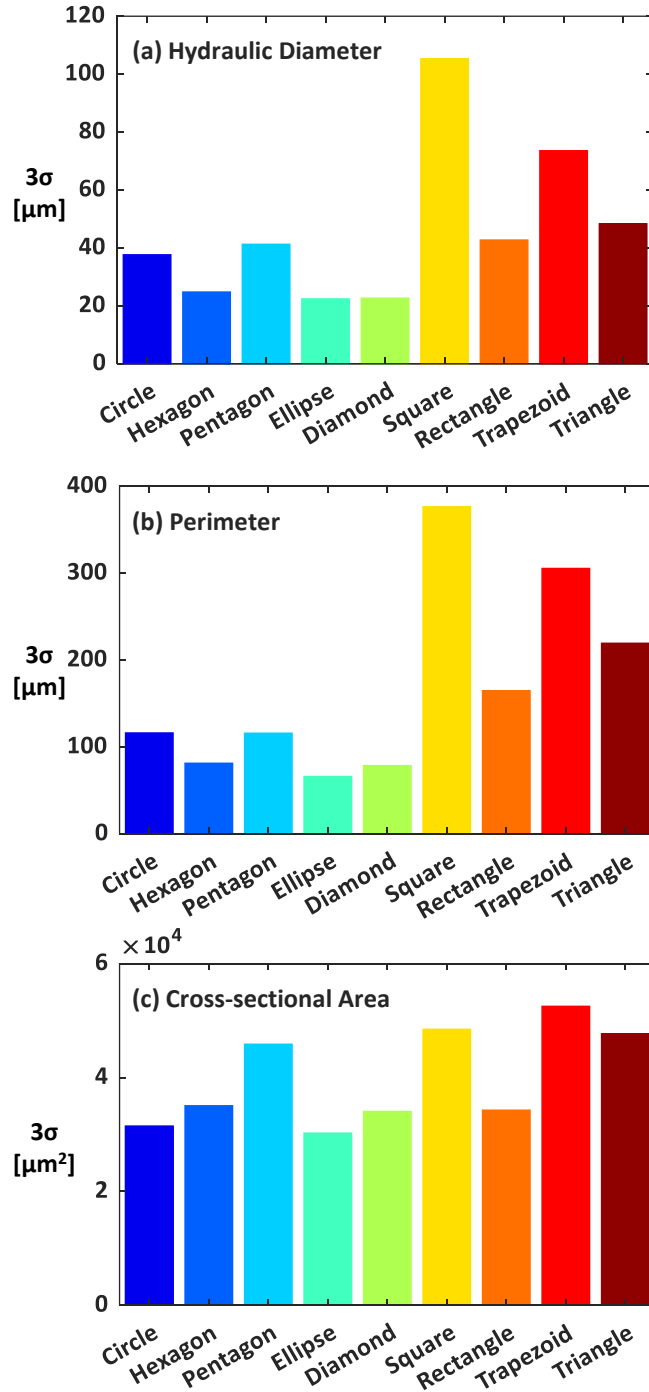


Figure 3-3.  $3\sigma$  deviations of hydraulic diameter (a), perimeter (b), and cross-sectional area (c) of the different channel shapes.

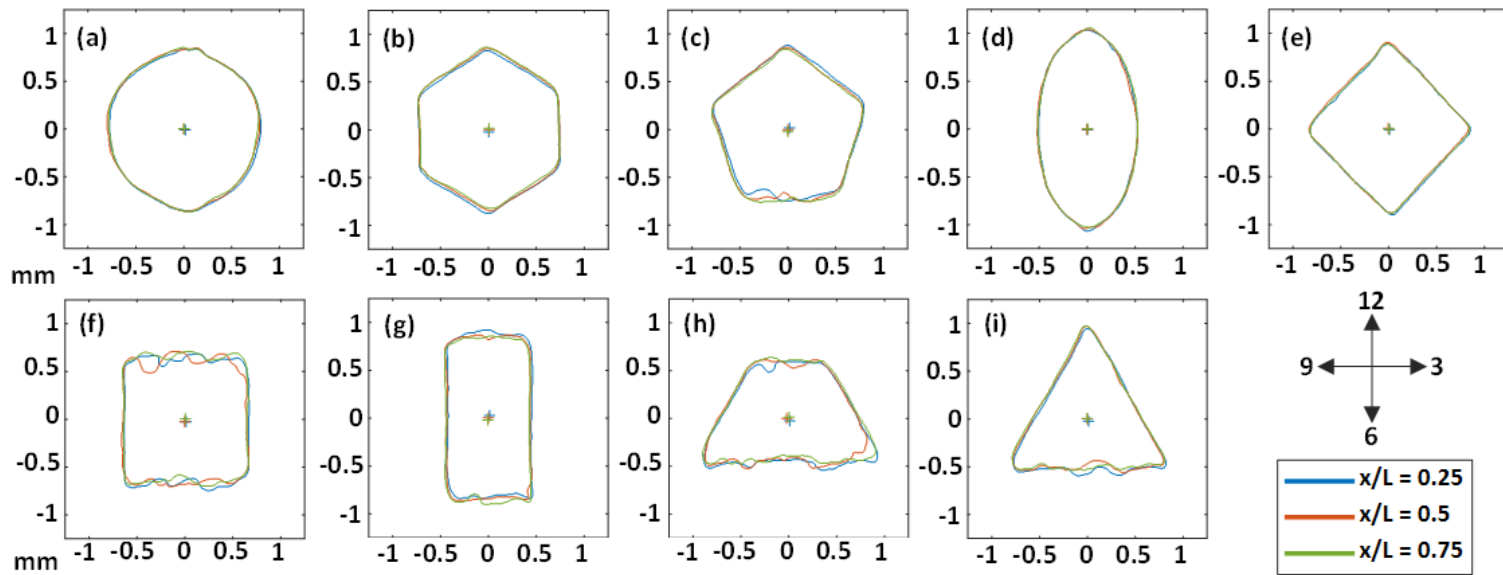


Figure 3-4. Axial slices of channel shapes (circle (a), hexagon (b), pentagon (c), ellipse (d), diamond (e), square (f), rectangle (g), trapezoid (h), and triangle (i) sharing a constant design intent perimeter of 4.79 mm fabricated at the 90° build direction.

The square and diamond channels share the same design intent geometric dimensions with the only difference being the streamwise rotation of the channel. The range of hydraulic diameters is wider for the square as compared to the diamond seen in Figure 3-4(a). Channel cross-sectional slices in Figure 3-4(e,f) show that the square contains more surface deformations relative to the diamond which confirms the variations in hydraulic diameter exhibited in Figure 3(a). Also shown in Figure 3-4(a-i) are channel cross-sections at different axial distances along the streamwise length of the coupon. Centroids at each axial slice, Figure 3-4(a-i), indicate the circle, ellipse, and diamond display the least amount of difference between centroids compared to the square, rectangle, trapezoid, and triangle. The wider spread of centroids of the square, trapezoid, and triangle shapes, seen in Figure 3-4 (f,h,i), are consistent with those same shapes exhibiting larger variations in hydraulic diameter compared to the ellipse, diamond, and circle as shown in Figure 3-3(a).

Accompanied in Figure 3-4 (a-i) is a 12, 3, 6, and 9 o'clock compass which is used to indicate the specific surface orientation within a channel cross-section. As seen in the Figure 3-4 (a-i) slices, surfaces that are at the 12 o'clock and 6 o'clock (horizontal) orientation exhibit sizable surface deformations compared to any other surface orientations. This effect is visibly seen in the slices of the square and diamond, where the square's 12 and 6 o'clock surfaces contain more noticeable surface deformations compared to the diamond surfaces even though both shapes share the same design intent geometry.

Quantitatively when examining the square shape, minimal surface deformations occur at the 3 and 9 o'clock orientation relative to the larger surface deformations seen at the 12 and 6 o'clock surfaces. The reason for these differences in surface roughness has been found by Wildgoose et al. [66] to be a factor of wall thickness and build location.

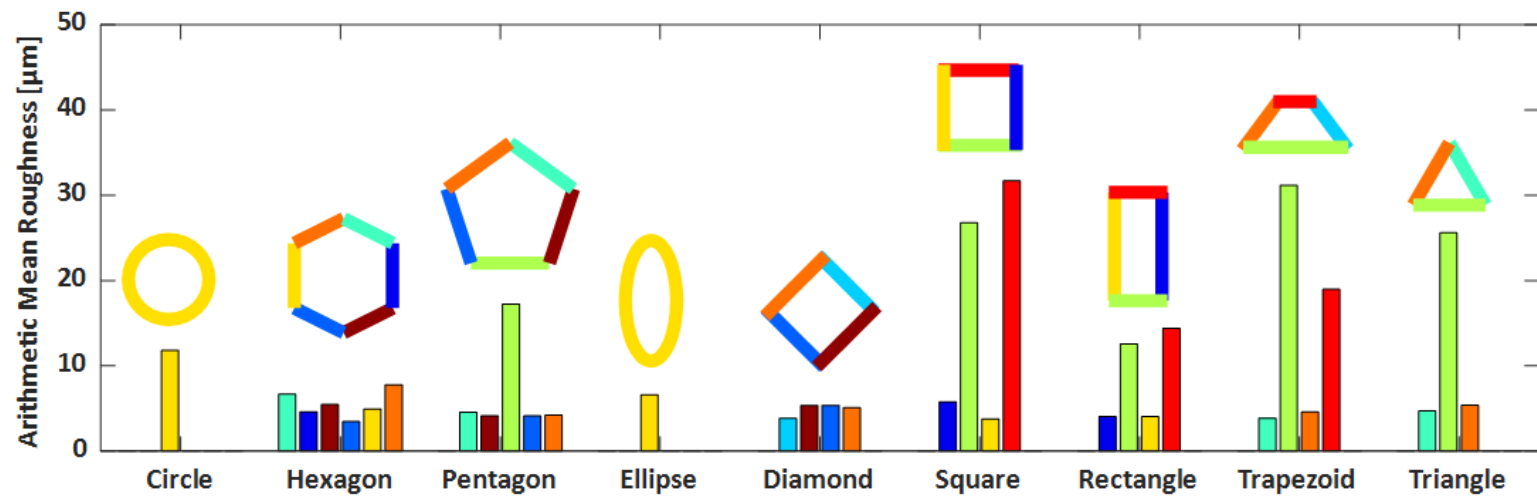


Figure 3-5. Arithmetic mean roughness,  $R_a$ , from CT scan data of multiple surfaces among the different channel shapes which are at the same surface orientation as Figure 4(a-i).

### 3.6 Roughness Quantities

Surface roughness, specifically the arithmetic mean roughness ( $R_a$ ), further characterizes the channel surface. The arithmetic mean roughness provides the average surface deviation from a reference as described in equation (3-1).

$$R_a = \frac{1}{n} \sum_{i=1}^n |Z_{\text{surf}} - Z_{\text{ref}}| \quad (3-1)$$

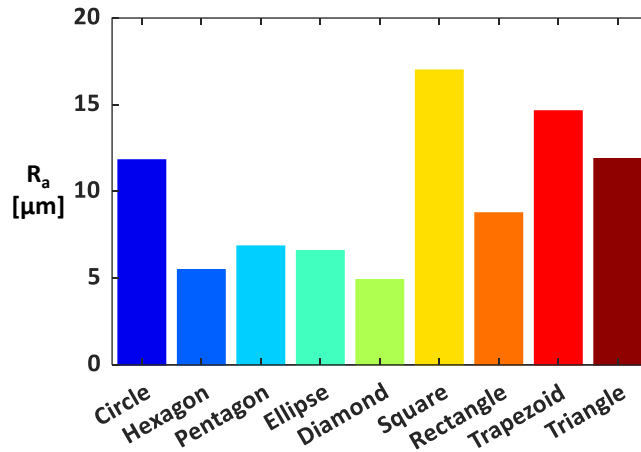
All channel shapes, except for the circle and ellipse due to their inherent surface curvature, used a plane that was fitted to each surface using a Gaussian distribution in order to serve as the reference value,  $Z_{\text{ref}}$ , when calculating the arithmetic mean roughness measurements. The average difference between the plane and the channel surface was recorded as the arithmetic mean roughness. An ellipsoid was fitted using a linear least square regression method to each axial slice to serve as a reference line for the circle and ellipse. This follows a similar procedure outlined in Wildgoose et al. [49] and Klingaa et al. [29].

Shown in Figure 3-5, the arithmetic mean roughness value for the circular channel is consistent with size and magnitude of previous AM circular channel literature [22,29,49,67] despite being larger in hydraulic diameter. In Figure 3-5 channel surfaces are color coded to the individual bars. The arithmetic mean roughness is higher on the 12 and 6 o'clock surfaces compared to all other surface orientations. Nearly all surfaces that are not at the 6 or 12 o'clock orientation contains the same arithmetic mean roughness value.

The 3 and 9 o'clock channel surfaces of the hexagon, square, and rectangular shapes share a similar arithmetic mean roughness. When comparing the rounded channels, both the circle and ellipse contain protrusions at the 6 and 12 o'clock locations seen in Figure 3-4(a,d), with the circle containing the larger deviations.

The arithmetic mean roughness for the surfaces of each channel shape in Figure 3-5 is averaged and displayed in Figure 3-6. The averaged arithmetic mean roughnesses in Figure 3-6 are weighted by the surface area of the channel shapes. Channel shapes that exhibit the least amount of surface area near the 6 and 12 o'clock surface orientations, such as the circle, ellipse, diamond, pentagon, and hexagon show the lowest area averaged arithmetic mean roughness compared to the other channel shapes. As seen in Figure 3-6, the diamond has the lowest value of arithmetic mean roughness resulting from only a small area being exposed to the 12 and 6 o'clock surface orientation.





**Figure 3-6. Area average arithmetic mean roughness of the different channel shape surfaces weighted by the design intent surface area.**

### 3.7 Channel Performance Measurements

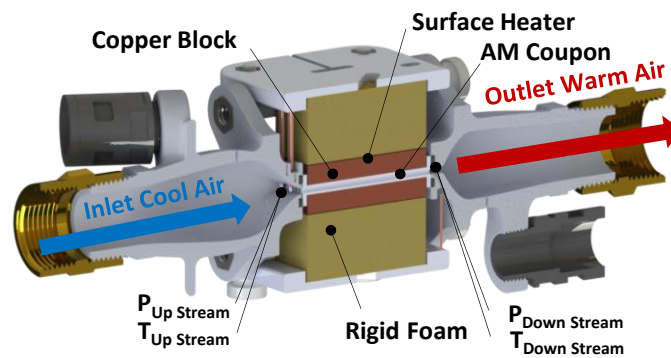
Pressure loss and bulk convection coefficients of the channel shapes were measured over a range of Reynolds numbers using an experimental rig similar to that previously used [25,33,48] as shown in Figure 3-7. The experimental rig has been described in great detail and benchmarked by several investigators [25,33,48].

Darcy friction factor measurements were calculated using measured pressure drops, mass flow rates, and channel geometry dimensions taken from CT scans. During friction factor tests the entrance pressure was set to 689 kPa absolute while the exit pressure ranged from 607 kPa to 661 kPa for the different channel shapes. Inlet loss coefficients were calculated using an area ratio between the channel inlet and plenum inlet while the outlet loss coefficients were one as described by Munson et al. [42]. The mass flow rate was measured upstream of the coupons using a laminar flow element along with pressure and temperature measurements. The friction factor measurements were taken in the incompressible regime where coupon exit Mach numbers were below 0.2. To achieve high Reynolds numbers in the fully turbulent regime, the backflow pressure was regulated to control the exit Mach number ensuring incompressible flow conditions.

Convective heat transfer coefficients were calculated using data measured from the same rig shown in Figure 3-7. A constant channel surface temperature boundary condition was achieved by a copper block being placed between a heater and the coupon surface. During the heat transfer tests the inlet temperature was at 296K while the exit temperatures ranged from 305 K to 322 K for the different

channel shapes. The power supplied by the top and bottom heaters were matched within 2.5%. A detailed description of the heat transfer measurement method is described by Stimpson et al. [30]. The same  $9.77 \pm 0.49$  W/mK thermal conductivity of an additive Inconel 718 material measured by Wildgoose et al. [49] was used for the coupon surface temperature calculation. A one-dimensional conduction analysis using thermocouples placed inside the copper blocks was used to calculate the surface temperature of the coupon channels.

Conduction losses through the rigid foam and plenums were measured and accounted for in the heat transfer measurements. The combined total of conduction losses through the rigid foam and plenums were less than 1% of the total power supplied by both heaters at high and low Reynolds numbers. The difference between the energy supplied by the heaters,  $Q_{\text{heat}}$ , and that transported by the air,  $Q_{\text{air}}$ , after accounting for the conduction losses was within 10.5% for the highest Reynolds numbers and within 5.7% for the lowest Reynolds numbers for all the channel shapes.



**Figure 3-7. Experimental rig used for static pressure drop and bulk convection coefficient measurements.**

### 3.8 Experimental Uncertainty

The propagation of uncertainty method was used to calculate friction factor and heat transfer experimental uncertainty as described by Figliola and Beasley [44]. Hydraulic diameter and pressure drop contributed to friction factor uncertainty the most. The uncertainty in friction factor at high Reynolds numbers was 4% while it was 9% at the lowest Reynolds numbers in the laminar regime. Reynolds number uncertainty was between 3% and 5%. Thermocouple exit temperature and hydraulic diameter were the main contributors to Nusselt number uncertainty. While the experimental uncertainty was 7% for Nusselt number, the repeatability in the measurements for the rectangle and circle was better than 2% across the range of Reynolds numbers evaluated.

### 3.9 Computational Fluid Dynamics Simulations

Computational fluid dynamics (CFD) simulations were conducted on four channel shapes to complement and gain a further understanding of the experimental pressure loss and heat transfer results. The triangle, trapezoid, square, and pentagon channel shapes were selected for evaluation since these shapes show different surface roughness's and experimental pressure loss and heat transfer performances. The single channel steady Reynolds Averaged Navier Stokes (RANS) simulations were completed in ANSYS Fluent [68]. In order to capture the secondary flows of the noncircular channel shapes, the turbulence model was a Baseline Reynolds Stress Model (BSL-RSM). The design intent geometry of the four channel shapes were used for the simulation. The length of the channels matched the length of the experimental coupons. The simulations did not model or include surface roughness since the goal of the simulations are to gain further insights into the cooling performance caused by the shape of the channel without the effect of roughness.

Similar to the experimental heat transfer tests, a constant surface temperature boundary condition was imposed on the surface of the channel. The channel shapes included an inlet mass flow boundary condition and outlet outflow boundary condition. The mass flow inlet was controlled such that the simulations were conducted at a  $Re_{Dh} = 20,000$  and  $Re_{\sqrt{A_c}} = 20,000$  for each channel shape. The Nusselt numbers reported were calculated using the mass averaged mean temperature in the thermally fully developed regime.

The fluid domain of the channels was meshed using tetrahedral elements and inflation layers. The grids were generated with a  $y^+$  value of one in the near wall regions. A grid independence study was performed by varying the number of cells in the fluid domain for the square channel. There was less than a 0.2% difference in Nusselt number of the square channel when going from 10M to 4M cells. The number of cells for each of the channel shapes evaluated were between 10M to 15M cells.

### 3.10 Pressure Loss Measurements

To cover a wide range of Reynolds numbers for each coupon, pressure loss measurements were recorded in the laminar, transitional, and fully turbulent regimes as seen in Figure 3-8. Noncircular hydraulically smooth channel data compiled by Duan et al. [50] is included in Figure 3-8 for hydraulically smooth channels. Also shown in Figure 3-8 is friction factor of a smooth circular channel coupon, created using a non-additive technique, that was used to benchmark the experimental rig. The friction factor of the smooth circular channel coupon agrees with the well-accepted Colebrook friction factor correlation, equation (3-2).

$$\frac{1}{\sqrt{f}} = -2 \log_{10} \left( \frac{K_s}{3.7D_h} + \frac{2.51}{\text{Re}\sqrt{f}} \right) \quad (3-2)$$

Consistent with results for AM internal passages [25,30,48,49], friction factors of the coupons are significantly higher than smooth channels due to surface roughness from the AM process as shown in Figure 3-8. AM coupons transition to turbulence at a much lower Reynolds number than the smooth benchmark coupon. The data in Figure 3-8 indicates that the square channel has a lower critical Reynolds number compared to the diamond, which may not be expected given these are the same shape. However, recall that the square channel contained a significantly higher arithmetic mean roughness compared to the diamond as shown in Figure 3-6. The highest friction factors in Figure 3-8 are observed for channel shapes with more horizontally (6 and 12 o'clock) oriented surfaces, Figure 3-4(f-i), due to 12 and 6 o'clock surfaces containing higher arithmetic mean roughness values compared to 3 and 9 o'clock surfaces as seen in Figure 3-5(a-e).

As another example to that of the square and diamond, consider the comparisons of the friction factors of the hexagon and diamond, it was expected that the hexagon would exhibit a similar or smaller friction factor compared to the diamond because the hexagon has similar variations in geometric dimensions and a larger hydraulic diameter. However, as seen in Figure 3-8 the hexagon contains a higher friction factor relative to the diamond because as seen in Figure 3-5 the arithmetic mean roughness of certain surfaces of the hexagon are two times higher than the diamond surfaces. The surface roughness results from Figure 3-5 and cross-sectional slices from Figure 3-4. also explain the reason the pentagon has a higher friction factor compared to the diamond. The pentagon contains a higher arithmetic mean roughness and a wider spread in centroids compared to the diamond, causing the pentagon's friction factor to be higher.

Similar to the scatter in friction factor measurements of the hydraulically smooth noncircular data from Duan et al. [50], the friction factor of the additive channels varies by as much as 31% at a single Reynolds number. Efforts to scale and reduce the scatter in  $f\text{Re}_{D_h}$  between the channel shapes were made by applying a different characteristic length scale to Reynolds number. It is important to note that the calculation of friction factor still used the hydraulic diameter. Duan et al. [50] observed that using the square root of cross-sectional area as a characteristic length better scales friction factor results across a range of hydraulically smooth channel shapes compared to using hydraulic diameter. Observed in Figure 3-8, the triangular channels from Duan et al. [50] shows a 20% lower  $f\text{Re}_{D_h}$  relative to a circular channel that shares the same hydraulic diameter as the triangle. As seen in Figure 3-9, the scatter of the same two channel shapes (circle and triangle) reduces to 6% when using  $f\text{Re}\sqrt{A_c}$ .

Figure 4-9 shows data for the square, trapezoid, rectangle, and triangle exhibiting a higher  $fRe_{\sqrt{A_c}}$  compared to the circle, hexagon, pentagon, ellipse, and diamond. The friction factor in Figure 3-8 and Figure 4-9 is the same value while the characteristic length for Reynolds number is different. Using the square root of cross-sectional area provides similar scatter as using hydraulic diameter. The difference in  $fRe_{D_h}$  between all the channel shapes at  $Re_{D_h} = 20,000$  is 31% while the difference in  $fRe_{\sqrt{A_c}}$  between all the channel shapes is 32% at  $Re_{\sqrt{A_c}} = 20,000$ . The area scaling parameter proposed by Duan et al. [50] appears to be a better characteristic length in terms of scaling smooth noncircular channels compared to additively made channels as shown in Figure 3-9.

Predicted friction factor CFD results of the square, triangle, trapezoid, and pentagon are shown in Figure 3-8 and Figure 3-9. The predicted friction factor results do not follow the same trends as the experimental results. More specifically, the experimental friction factor was the highest for the square followed by the trapezoid, triangle, and pentagon. While for the predicted friction factor results shown in Figure 3-8 and Figure 3-9, the pentagon exhibits the highest friction factor followed by the square, trapezoid, and triangle. The reason for the difference in order of friction factor trends between the predicted and AM shapes is due to the differences in arithmetic mean roughness present in the AM channel shapes. In contrast to the experimental friction factor results, using the square root of cross-sectional area better scales the predicted friction factor for the square, triangle, trapezoid, pentagon compared to using hydraulic diameter. For the predicted results there is an 7% difference in friction factor between the channel shapes when using hydraulic diameter compared to a 2% difference when using square root of cross-sectional area as the characteristic length scale.

It would be anticipated that the roughness-to-hydraulic diameter ratio,  $R_a/D_h$ , is the cause for the failure to adequately scale the friction factor of the different channel shapes. However, this is not true as seen by the ellipse and circle sharing the same friction factor even though the ellipse contains a 34% lower roughness-to-hydraulic diameter ratio as seen in Table 4-3. Additionally, the rectangle and triangle also share the same friction factor even though the rectangle has a lower roughness-to-hydraulic diameter ratio.

These discrepancies reveal that the roughness-to-hydraulic diameter ratio was not the sole cause for the differences in friction factor. Accordingly, the impact of the ratio of secondary flows to the relative roughness could be one of the leading causes for the failure of hydraulic diameter and square root of cross-sectional area to scale the friction factor data.

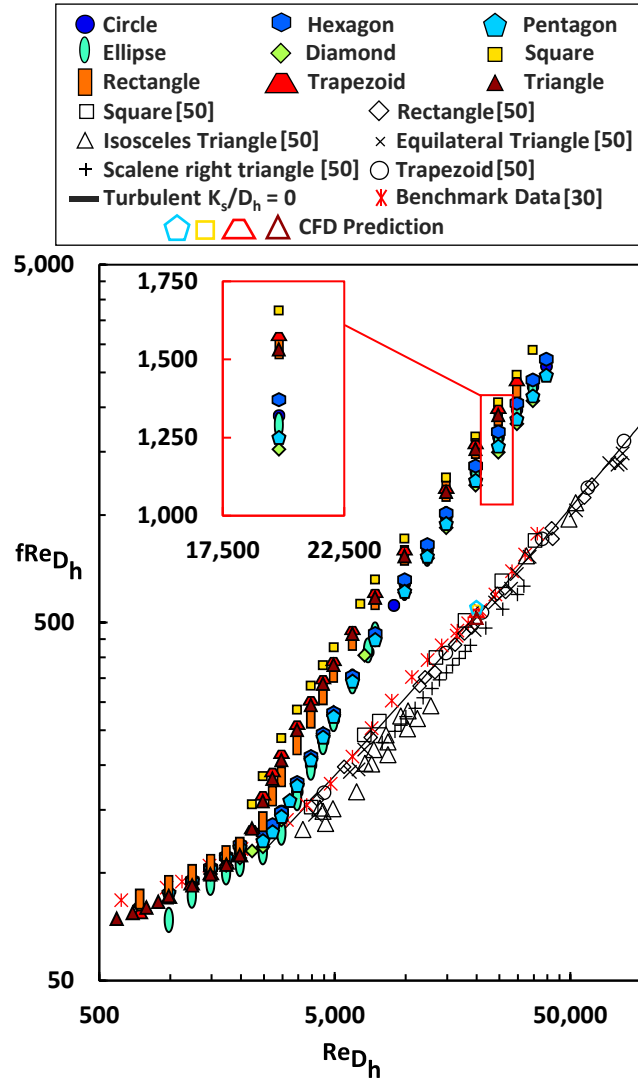


Figure 3-8. Friction factor data over a range of Reynolds numbers calculated using hydraulic diameter with benchmark data from Stimpson et al. [30] and smooth noncircular data compiled by Duan et al. [50].

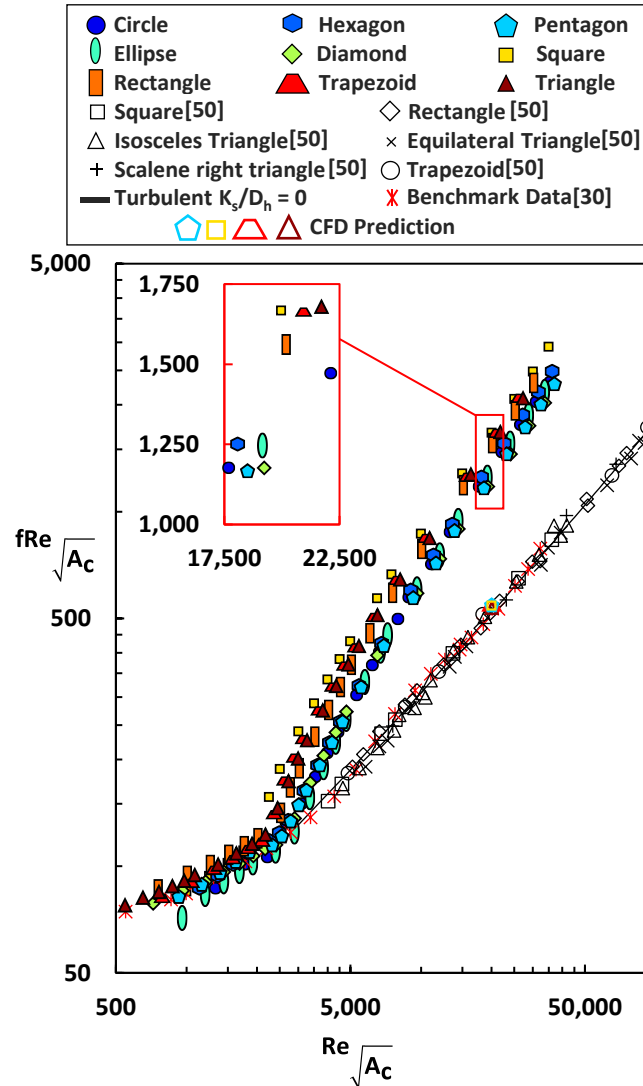


Figure 3-9. Friction factor data over a range of Reynolds numbers calculated using square root of cross-sectional area with benchmark data from Stimpson et al. [30] and smooth noncircular data compiled by Duan et al. [50].

### 3.11 Heat Transfer Evaluation

Similar to pressure losses, the bulk heat transfer was measured over a range of fully turbulent Reynolds numbers as shown in Figure 3-10. Nusselt number and Reynolds number in Figure 3-10 was calculated using hydraulic diameter as the length scale. The same smooth coupon used to benchmark friction factor was also used to benchmark Nusselt number. As seen in Figure 3-10, the smooth benchmark coupon matches Gnielinski's correlation, shown in equation (3-3), for a hydraulically smooth channel.

$$\text{Nu} = \frac{f/8(\text{Re}-1000)\text{Pr}}{1+12.7\sqrt{f/8}(\text{Pr}^{2/3}-1)} \quad (3-3)$$

Of the evaluated channel shapes, the square exhibited the highest Nusselt number and friction factor across the range of Reynolds numbers tested. It was expected that similar to the friction factors, higher surface roughness would result in higher Nusselt numbers; however, this trend was not observed with the triangle and rectangle. Although the triangle and rectangle have higher friction factors compared to the circle, diamond, ellipse, hexagon, and pentagon, the triangle and rectangle's Nusselt numbers were the same value as the mentioned shapes.

For a given Reynolds number there is a 13% difference in Nusselt number across the channel shapes for the experimental results when using hydraulic diameter as the length scale. The numerical results from Wang et al. [53] showed that using hydraulic diameter for a variety of hydraulically smooth polygonal channels lead to large errors in Nusselt number when predicted using correlations such as Gnielinski's correlation developed with circular channel datasets. Similar to the analysis of scaling friction factor results, a comparative analysis was performed between the use of the square root of cross-sectional area and hydraulic diameter for the characteristic length in Reynolds number and Nusselt number.

Like the friction factor trends in Figure 3-8 and Figure 3-9, Figure 3-11 shows that using the square root of cross-sectional area results in a similar spread and scaling for Nusselt number data between all the channel shapes compared to using hydraulic diameter as the length scale in the Reynolds number. In more detail, the difference between the highest and lowest experimental Nusselt number at a shared Reynolds number,  $\text{Re}_{D_h} = 20,000$ , when using hydraulic diameter is 9% while when using the square root of cross-sectional area the largest difference is also 9% at  $\text{Re}_{\sqrt{A_c}} = 20,000$ . The Nusselt number of some channel shapes such as the circle scaled significantly better using the square root of cross-sectional area compared to hydraulic diameter. More specifically, the Nusselt number of the circle using the square root of cross-sectional area, is 2% different than the diamond relative to being 6% different than the diamond when using the hydraulic diameter as the length scale. For both Figure 3-10 and Figure 3-11, the square and trapezoid contain the highest Nusselt numbers compared to the other channel shapes.



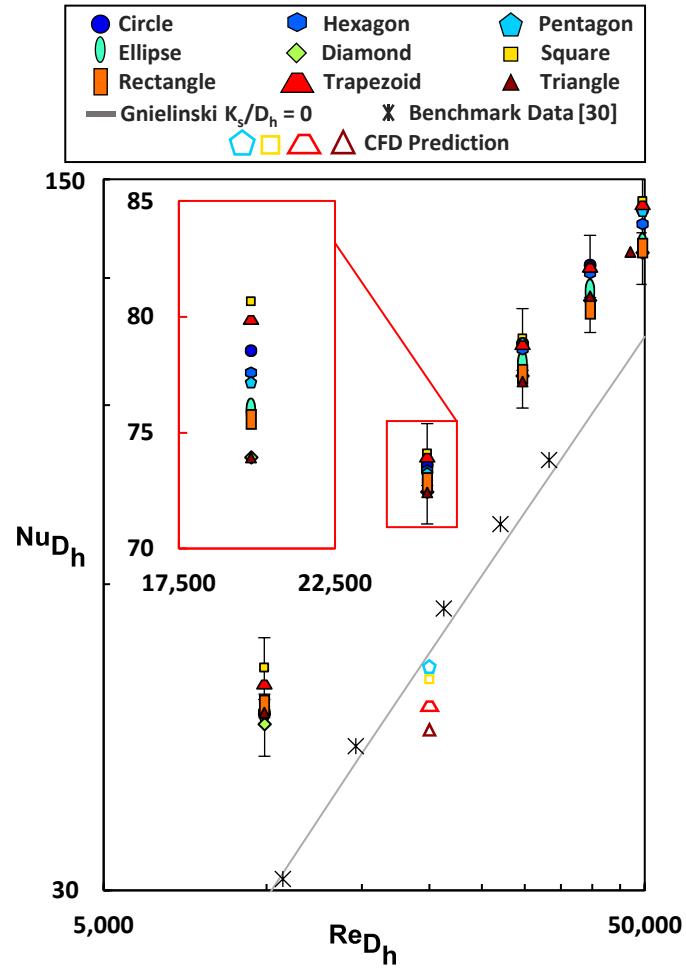
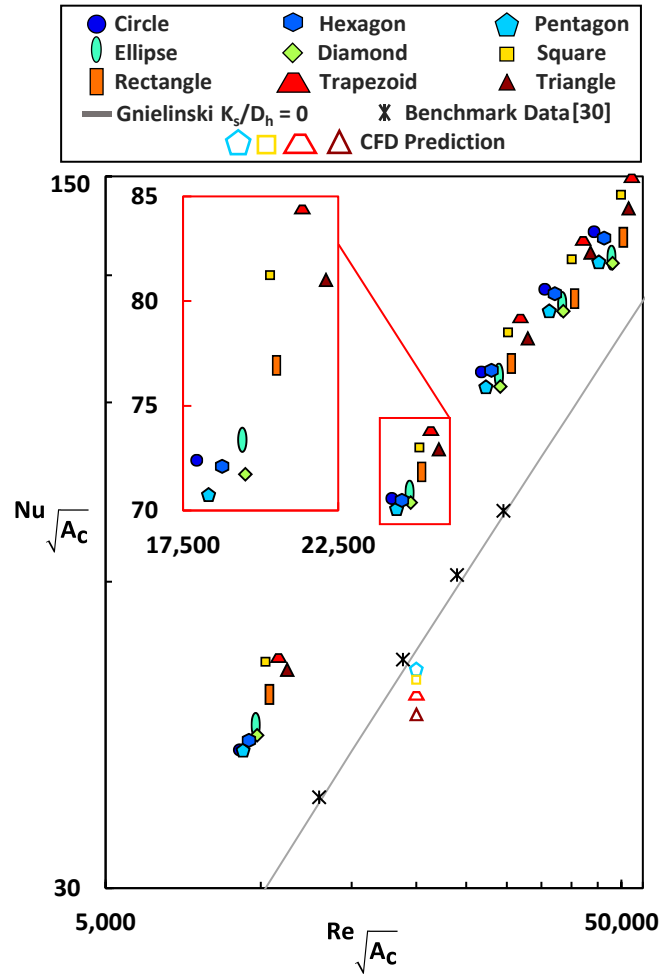


Figure 3-10. Nusselt number data calculated using hydraulic diameter as the characteristic length scale along with numerical data and benchmark results from Stimpson et al. [30].



**Figure 3-11. Nusselt number data calculated using square root of cross-sectional area as the characteristic length scale along with numerical data and benchmark results from Stimpson et al. [30].**

Also shown in Figure 3-10 and Figure 3-11 are the predicted Nusselt number results from the CFD simulations of smooth square, trapezoid, triangle, and pentagon channel shapes. The predictions of the different channel shapes in Figure 3-10 were performed all at the same Reynolds number of  $Re_{D_h} = 20,000$  while in Figure 3-11 the predictions were performed at a shared Reynolds number of  $Re_{\sqrt{A_c}} = 20,000$ .

Similar to the friction factor predictions, the square root of cross-sectional area only slightly better scales the predicted Nusselt number compared to hydraulic diameter. More specifically, the scatter for predicted Nusselt number data when using hydraulic diameter is 14% at  $Re_{D_h} = 20,000$  while when using the square root of cross-sectional area the scatter is reduced to 10% at  $Re_{\sqrt{A_c}} = 20,000$  between the evaluated channel shapes. Matching the predicted friction factor results, the

predicted results in Figure 3-10 and Figure 3-11 show that the pentagon exhibits the highest Nusselt number followed by the square, trapezoid, and triangle. However, the predictions do not fully match experimental trends in Nusselt number. The predicted data shows that the pentagon contains the highest Nusselt number of the four channel shapes while the experimental results show that the pentagon has the third highest Nusselt number out of the four channel shapes. The reason for the discrepancy is a result of the differences in arithmetic mean roughness between the channel shapes that the CFD predictions do not model. The square, trapezoid, and triangle shapes contain roughness levels 40% to 60% higher than the pentagon as seen in Figure 3-6. The higher surface roughness leads to increases in turbulent mixing causing an increase in the Nusselt number for the square, trapezoid, and triangle channel shape's relative to the pentagon. Furthermore, the square, trapezoid, and triangle shapes also contain higher roughness-to-hydraulic diameter ratios as seen in Table 4-3 compared to the pentagon.

Nondimensionalized temperature contours and secondary flow vectors of the numerical data can be seen in Figure 3-12. The temperature is normalized using the surface temperature and mean flow temperature while the secondary flow velocities are nondimensionalized by the mean streamwise velocity. Similar to literature [69,70], Figure 3-12 shows that as the number of sides in a channel increases, there is a higher number of secondary circulation zones and the strength of the circulation zones decrease.

The convective heat transfer near the corners of the channel shapes are lower compared to the area between the corners as a result of a lower velocity at the channel corners. This result agrees with Wang et al. [53], who describes the corners as inducing a blocking effect which lowers the local heat transfer. As the corner angle decreases, such as going from a pentagon to triangle as seen in Figure 3-12, the local heat transfer near the corner reduces. The local heat transfer between the corners increases as the number of sides decrease as seen by the temperature contours in Figure 3-12.

The augmentations of Nusselt number and friction factor relative to smooth correlations, Equation (3), are seen in Figure 3-13. The ellipse, diamond, circle, hexagon, and pentagon exhibited lower friction factor augmentation for an identical Nusselt augmentation compared to the rectangle and triangle. Nusselt number and friction factor augmentations for all the channel shapes are between the square and diamond shapes, signifying that roughness and surface deformations are significant contributors to friction factor and Nusselt number augmentation.

The ellipse, hexagon, circle, diamond, and pentagon contain the same Nusselt number augmentation as the rectangle and triangle for a lower pressure drop penalty at a given Reynolds

number. The pentagon contains the same Nusselt number augmentation as the triangle even though the pentagon has a 21% lower friction factor at the same Reynolds numbers.

As seen in Figure 3-14, Nusselt number and friction factor of the channel shapes are compared to that of the circular channel. The pentagon is the highest performing channel shape relative to the circle, since the pentagon contains a 4% lower friction factor for an equal Nusselt number as the circular channel. The square friction factor augmentation is 25% higher compared to the circle while the square's Nusselt augmentation is only 3% higher at most Reynolds numbers compared to the circle.

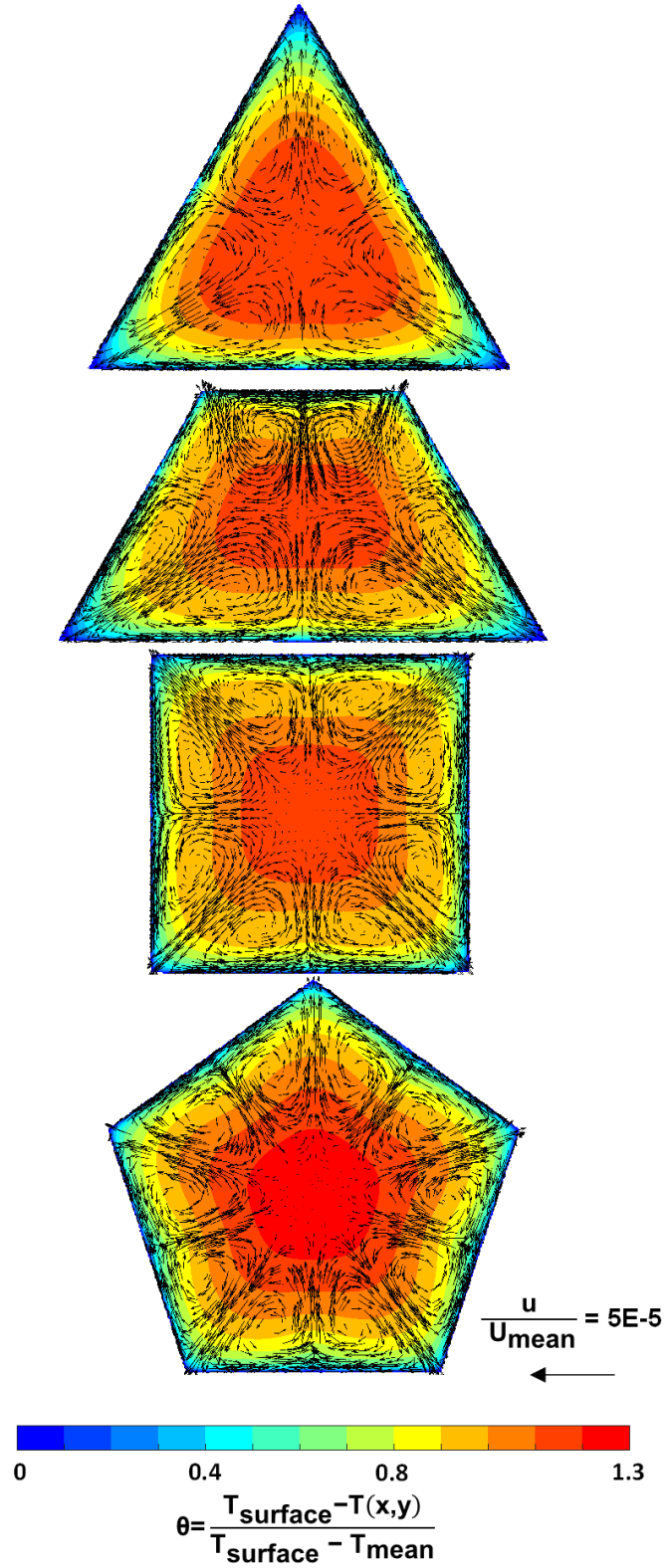


Figure 3-12. Nondimensionalized temperature contours with secondary flow vectors of the triangle, trapezoid, square, and pentagon channel shapes.

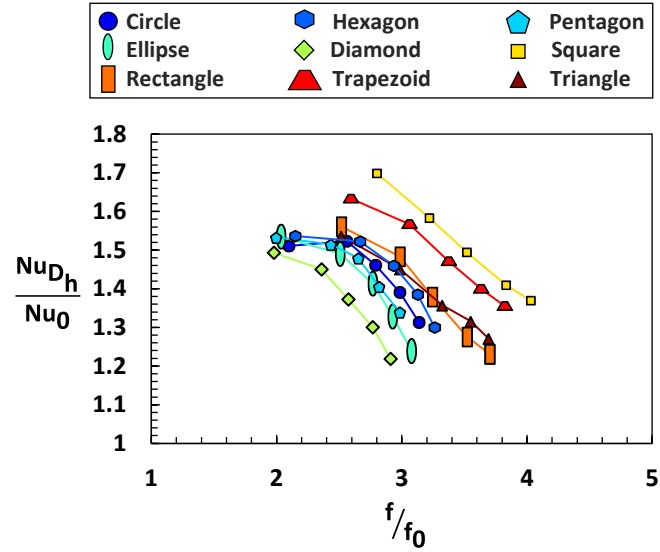


Figure 3-13. Nusselt number and friction factor augmented by a hydraulically smooth channel for the different channel shapes over a range of fully turbulent Reynolds numbers.

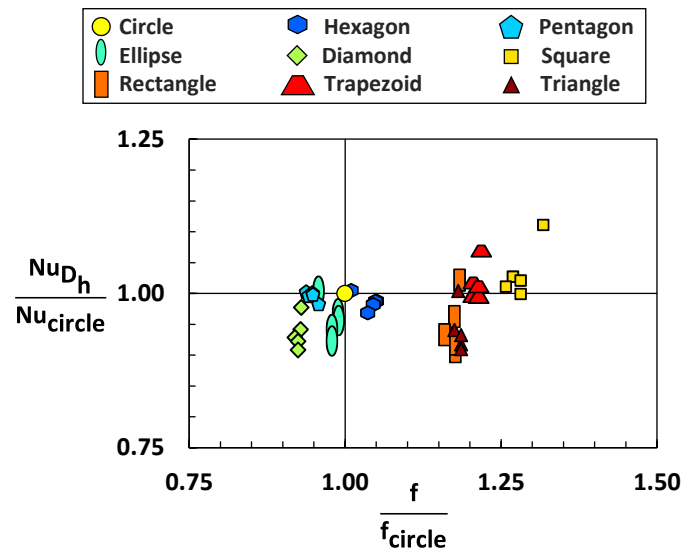


Figure 3-14. Nusselt number and friction factor of channel shapes augmented by the Nusselt number and friction factor of the circular channel shape at the same Reynolds number.

### 3.12 Conclusion

Nine channel shapes (circle, hexagon, pentagon, ellipse, diamond, square, rectangle, trapezoid, and triangle) which shared the same cross-sectional perimeter were manufactured in the 90° (vertical) build orientation using DMLS. The channels were CT scanned to evaluate their geometric dimensions and surface roughness. Pressure loss and heat transfer measurements of the

different channel shapes were evaluated over a range of Reynolds numbers. In addition to the experimental measurements, pressure loss and heat transfer CFD predictions were conducted on the square, trapezoid, pentagon, and triangle channel shapes.

The results presented in this paper show that regardless of channel shape, the as-built channel geometries printed larger than their hydraulic diameter, perimeter, and cross-sectional area design intent. The perimeter of an AM channel is closer to its design intent compared to cross-sectional area regardless of channel shape. There are more variations in a channel's perimeter compared to cross-sectional area.

The square, triangle, trapezoid, and rectangle exhibited the largest deviations in geometry and surface roughness resulting in the highest friction factors. Characteristic length scales such as hydraulic diameter and square root of cross-sectional area were evaluated for both friction factor and Nusselt number. Unlike noncircular hydraulically smooth channels, there was no reduction in the scatter or differences in scaling of friction factor or heat transfer results when using hydraulic diameter or square root of cross-sectional area between the additively made channel shapes. The experimental results reveal that the pentagon showed the best performance between pressure loss and heat transfer compared to the circular channel. The trapezoid and square contained the largest Nusselt number and friction factor augmentations of the evaluated shapes.

Additive manufacturing can be used as a tool to fabricate complex internal passages, however designers using the process need to consider the surface deformation and roughness attributed to the geometry of a passage. There is a fundamental need to address the best scaling parameter of cooling performance for non-conventional shapes, so that the next generation of AM enabled cooling channel designs can be developed and fairly evaluated. Understanding the impact a channel shape has on its pressure losses and convective heat transfer will allow designers to fully utilize the design freedom and added performance when using the additive process.

## **4 Roughness Related to Cooling Performance of Channels Made Through Additive Manufacturing<sup>4</sup>**

### **4.1 Abstract**

The complex surface morphology and multiscale surface features inherent with additively manufactured (AM) components contributes to the overall flow characteristics and heat transfer of cooling passages. As the AM process and cooling data in literature continues to evolve, so does the need for more accurate heat transfer and pressure loss correlations for AM cooling schemes. This study improves the predictability of pressure loss and heat transfer for AM cooling passages by fabricating a range of coupons and investigating samples in literature. Twenty-seven test coupons were manufactured using direct metal laser sintering in an assortment of build directions and build locations that produced a variety of surface morphologies. Nondestructive evaluation, computed tomography scanning, was used to quantify the surface morphology as well as capture the as-built geometric dimensions of the cooling schemes. Friction factor and bulk Nusselt number of the coupons were measured using an experimental rig. Pressure loss and heat transfer correlations in literature were compared with the experimental results from the current coupons and datasets from literature. Arithmetic mean roughness correlations in literature struggled to predict the cooling performance of AM channels since the bulk roughness statistic did not capture the overall form of the surface morphology. A combination of root mean square roughness and skewness of the roughness was able to best predict pressure loss and heat transfer for the present samples and those in literature while being independent of build location, build direction, material, machine, and laser parameters. The maximum absolute error was 25% and average absolute error was 12% for the friction factor correlation. The maximum absolute error was 39% and average absolute error was 8% for the Nusselt Number correlation.

### **4.2 Introduction**

The metal additive manufacturing (AM) process is a key technology that enables quicker development of complex cooling designs such as those seen in gas turbines compared to subtractive or casting fabrication methods. A reduction in part assemblies and overall component weight can also be achieved due to the added design freedom offered through AM relative to traditional fabrication methods. A key characteristic inherent with the AM process, specifically direct metal

---

<sup>4</sup> Wildgoose, A.J., Thole, K.A., Tuneskog, E., and Wang, L., 2023, “4 Roughness Related to Cooling Performance of Channels Made Through Additive Manufacturing”, GT2023-103151, will be submitted for review to Turbo Expo and the Journal of Turbomachinery.



laser sintering (DMLS), is the as-built surface roughness. Several studies [24,30] have shown that surface roughness is one of the main drivers that influences the turbulent mixing and resulting heat transfer enhancement of AM cooling schemes compared to traditionally fabricated designs. The magnitude and size of the roughness features is particularly important in sub-millimeter internal channels, since these features directly influence the overall convective heat transfer.

The rapid development in literature towards the understanding of cooling schemes made through AM means there is significantly more pressure loss and heat transfer data available in literature compared to a few years ago. The predictability of pressure loss or heat transfer of these cooling designs can be improved through additional data and a better understanding of the dominant factors that impact overall cooling performance. This study adds to the available data in literature through the fabrication of cooling samples at a range of AM build conditions (build direction, channel size, and location) and improves on the capabilities for correlations to predict the pressure loss and heat transfer of the present samples and those in literature. By using roughness statistics to correlate pressure loss and heat transfer, the developed correlations can be used regardless of changes to future laser process parameters, materials, and general AM build considerations.

### **4.3 Literature Review**

It is important to characterize the surface roughness since there are a multitude of AM process and build conditions that impact the as-built surface roughness such as changes to build direction [22,24], laser process parameters [13], part geometry [71], and location on the build plate [17,72]. Each of the aforementioned build conditions can change the shape of the roughness features and impact the relationships in cooling performance between samples. More specifically, the range in roughness features can be large droplet elements ranging from 25 to 75  $\mu\text{m}$  [53] to smaller partially sintered particles less than 10  $\mu\text{m}$  [38].

In microchannel cooling schemes, the length scales of the roughness features are the primary drivers of cooling performance [30]. The work by Kandlikar et al. [73], advocates that the roughness features can also be considered as a flow constriction thus limiting the cross-sectional area, which needs to be accounted for in velocity calculations through the use of a constricted flow diameter term. Through the work by Stimpson et al. [30] certain roughness features can act as protruding fins into the flow field. Some roughness features (e.g. partially sintered particles) can have a poor fin efficiency, as result of a high conduction resistance between the roughness feature and AM surface. The results from Stimpson et al. [30] and Kandlikar et al. [73] highlights the importance in evaluating the roughness in order to understand and predict the cooling performance.

The foundational work of Nikuradse [74] used the term equivalent sandgrain roughness,  $k_s$ , as a length scale for roughness in pressure loss (i.e. friction factor) correlations. However, the sand grain roughness is a scaling factor that is not directly measured, instead it is determined through experiments. Since the study of Nikuradse [74], multiple roughness statistics such as arithmetic mean roughness ( $R_a$ ), root mean square roughness ( $R_q$ ), mean roughness depth ( $R_z$ ), skewness ( $R_{sk}$ ), and kurtosis ( $R_{ku}$ ) are now used to describe the form of the surface morphology through destructive and nondestructive evaluation methods that were not previously available. Literature [12,30,73,75–80] uses these statistics along with other forms to correlate the roughness to the sandgrain roughness in order to predict pressure loss and heat transfer in both non-additive and additive cooling schemes. The early predictive work by Sigal and Danberg [81] used other statistical parameters to describe roughness in the form of a density parameter,  $\Lambda_s$ , for uniformly shaped roughness features using surface area ratios of the roughness elements to correlate sandgrain roughness. Van Rij et al. [78] expanded upon this work by using the density parameter with three-dimensional irregular and nonuniform roughness features to predict sandgrain roughness. Taking a different direction, Flack and Schultz showed that a combination of  $R_q$  and  $R_{sk}$  can be used to predict the sandgrain roughness in the form of the Colebrook friction factor correlation with different types of roughness features (ranging from closely packed pyramids to spheres). However, these correlations struggle to predict cooling for AM datasets because the roughness magnitude to channel size ratio of these non-additive studies are lower compared to the roughness nonuniformity and magnitude observed in AM parts.

Stimpson et al. [30] tackled this issue by comparing several roughness correlations in literature to predict the pressure loss and heat transfer using AM coupons from Stimpson et al. [33]. Of the many parameters evaluated, the study found that the arithmetic mean roughness to diameter ratio,  $R_a/D_h$ , best correlated to the relative sandgrain roughness,  $k_s/D_h$ . Furthermore, the study [30] also produced a modified Gnielinski Nusselt correlation exclusively for AM cooling schemes. It is important to note that the correlation was created using square and rectangular channels at a single build direction. Since then, additional data with multiple different channel shapes, build directions, and other AM build parameters have been reported in literature. Several papers [12,30,75,82] have modified the coefficients of a similar form of the Stimpson et al. [30] equation by fitting additional datasets to better predict the relative sandgrain roughness in Colebrook's friction factor equation. In some cases in literature [25,33,49,83], several AM coupons can contain a similar  $R_a/D_h$  ratio but exhibit different friction factors as well as Nusselt Numbers. As a result, using relative roughness correlations that are only a function of  $R_a/D_h$  struggle to predict the pressure loss or heat transfer

for every sample. Goodhand et al. [77] highlights this predicament and states that  $R_a$  is a single roughness statistic that only describes the amplitude of the roughness elements.

A combination of roughness statistics is needed to better describe the relationship between the multi-scale surface features to the pressure loss and heat transfer of AM cooling schemes. Using the additional datasets in literature not present several years ago, the objective of the current study is to more accurately predict the pressure loss and heat transfer of AM cooling schemes. In addition to the data from literature, several samples were fabricated at different build directions, locations, and diameters to be representative of major build parameters that impact cooling performance. The beginning of the paper describes the characterization in roughness and cooling performance and highlights the challenge with  $R_a/D_h$  to predict friction factor and Nusselt number. Towards the end of the paper, both the new data presented and data from literature are used to predict pressure loss and heat transfer for a variety of samples using a combination of roughness statistics.

#### **4.4 Description of Test Coupons**

Twenty-seven cooling coupons, as seen in Table 4-1, were additively manufactured containing a range of different AM build parameters (build direction, build location, and channel size) that represent a variety of typical build and layout considerations of AM cooling schemes. A round channel was chosen for the coupons in Table 4-1 since stress concentrations during the AM process can occur at sharp corners such as square channel shapes leading to warpage. It is well known that the distance a laser is from the part surface can impact both geometry and cooling performance, since the angle between the laser and normal to the surface (laser incidence angle) can impact the melt pool during the AM process [17]. As seen by the build plate of the coupons in Figure 4-1, samples were printed at three specific radial build locations from the laser source ( $R1 = 25$  mm,  $R2 = 58$  mm,  $R3 = 90$  mm) for each quadrant of a four laser direct metal laser sintering EOSM400-4 machine. Even though the laser incidence angle changed as a result of the different radial build locations, literature has shown that the difference in surface roughness of a sample printed at different quadrants of a four laser machine is minimal [66].

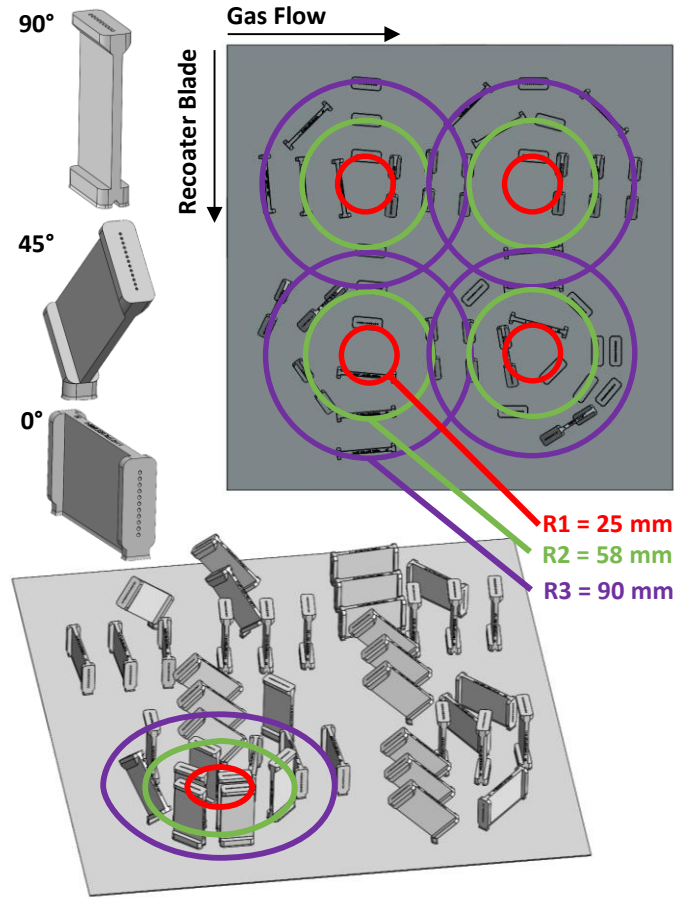
For each radial build location, samples were fabricated at three different build directions ( $0^\circ$ ,  $45^\circ$ , and  $90^\circ$ ), where build direction is defined as the angle between the streamwise axis of the channel to that of the build plate, as seen in Figure 4-1. Additionally, for each build direction the hydraulic diameter of the channel ranged from 0.8 mm to 1.4 mm. Circular channels were chosen for samples built at  $90^\circ$  due to no downward facing surfaces while samples built at a  $45^\circ$  and  $0^\circ$  build direction contained a teardrop correction to mitigate deformation at the downward facing

surface [22,31]. As seen in Figure 4-2, the teardrop shape contained an apex angle of 120°. The samples were fabricated using a STAL15DE [84] material in a 40 micron layer thickness. After fabrication, the samples were solution annealed to reduce residual stress and support removal was performed using a wire electric discharge machine.

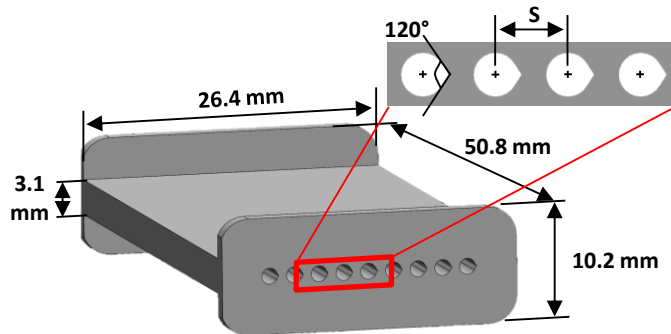
The geometric lengths of the coupons, specifically the channel pitch spacing ( $S$ ) was varied for each hydraulic diameter so that the fin efficiency of the wall between channels during heat transfer measurements is greater than 95% to achieve a constant surface temperature boundary condition. Furthermore, the length-to-hydraulic diameter ratios of the coupons were between  $35 < L/D_h < 61$ , to meet fully developed flow conditions. The overall channel geometry for each coupon is reported in Table 4-1. The naming convention of the coupons in Table 4-1, describes the as-built diameter, channel shape, build direction, and radial build location. For example, as seen in Table 4-1, the 1.1 mm diameter sample containing a circular channel shape built at a 90° build direction at the third radius is named 1.1C90-R3.

**Table 4-1 Geometries for Coupons Built at a Variety of Build Directions, Diameters, and Locations as seen in Figure 4-1.**

Coupon	Radial Location [mm]	$D_{h,meas}$ [ $\mu\text{m}$ ]	Build Direction [deg]	Channel Shape	$D_{h,meas}/D_{h,des}$	$P_{meas}/P_{des}$	$A_{c,meas}/A_{c,des}$	$S/D_{h,des}$	$L/D_{h,des}$
1.4C90-R1	R1 = 25	1405	90	Circle	1.004	1.064	1.068	1.57	35.2
1.4T45-R1	R1 = 25	1393	45	Teardrop	0.995	1.029	1.024	1.57	35.0
1.4T0-R1	R1 = 25	1350	0	Teardrop	0.964	1.019	0.982	1.57	35.0
1.1C90-R1	R1 = 25	1127	90	Circle	1.024	1.073	1.099	1.65	44.6
1.1T45-R1	R1 = 25	1118	45	Teardrop	1.016	1.039	1.056	1.65	44.6
1.1T0-R1	R1 = 25	1069	0	Teardrop	0.971	1.015	0.986	1.65	44.6
0.8C90-R1	R1 = 25	822.1	90	Circle	1.028	1.093	1.123	1.86	61.3
0.8T45-R1	R1 = 25	819.1	45	Teardrop	1.024	1.048	1.074	1.86	61.3
0.8T0-R1	R1 = 25	785.2	0	Teardrop	0.982	1.024	1.005	1.86	61.3
1.4C90-R2	R2 = 58	1438	90	Circle	1.027	1.054	1.083	1.57	35.0
1.4T45-R2	R2 = 58	1432	45	Teardrop	1.023	1.037	1.061	1.57	35.0
1.4T0-R2	R2 = 58	1341	0	Teardrop	0.958	0.988	0.946	1.57	35.0
1.1C90-R2	R2 = 58	1128	90	Circle	1.025	1.065	1.092	1.65	44.5
1.1T45-R2	R2 = 58	1112	45	Teardrop	1.011	1.023	1.034	1.65	44.6
1.1T0-R2	R2 = 58	1057	0	Teardrop	0.961	1.016	0.977	1.65	44.6
0.8C90-R2	R2 = 58	833.1	90	Circle	1.041	1.077	1.121	1.86	61.3
0.8T45-R2	R2 = 58	819.0	45	Teardrop	1.024	1.034	1.059	1.86	61.3
0.8T0-R2	R2 = 58	765.4	0	Teardrop	0.957	1.023	0.979	1.86	61.3
1.4C90-R3	R3 = 90	1415	90	Circle	1.011	1.066	1.078	1.57	35.0
1.4T45-R3	R3 = 90	1396	45	Teardrop	0.997	1.033	1.030	1.57	35.1
1.4T0-R3	R3 = 90	1347	0	Teardrop	0.962	1.017	0.978	1.57	35.0
1.1C90-R3	R3 = 90	1123	90	Circle	1.021	1.075	1.097	1.65	44.6
1.1T45-R3	R3 = 90	1116	45	Teardrop	1.014	1.043	1.058	1.65	44.6
1.1T0-R3	R3 = 90	1057	0	Teardrop	0.961	1.016	0.976	1.65	44.6
0.8C90-R3	R3 = 90	834.8	90	Circle	1.044	1.094	1.142	1.86	61.3
0.8T45-R3	R3 = 90	824.7	45	Teardrop	1.031	1.051	1.084	1.86	61.3
0.8T0-R3	R3 = 90	778.1	0	Teardrop	0.973	1.020	0.992	1.86	61.3



**Figure 4-1** Coupons spanning a range of build directions and diameters fabricated at three distinct radial locations from the four laser EOS M400-4 machine.



**Figure 4-2** Schematic of overall coupon dimensions used for experimental testing.

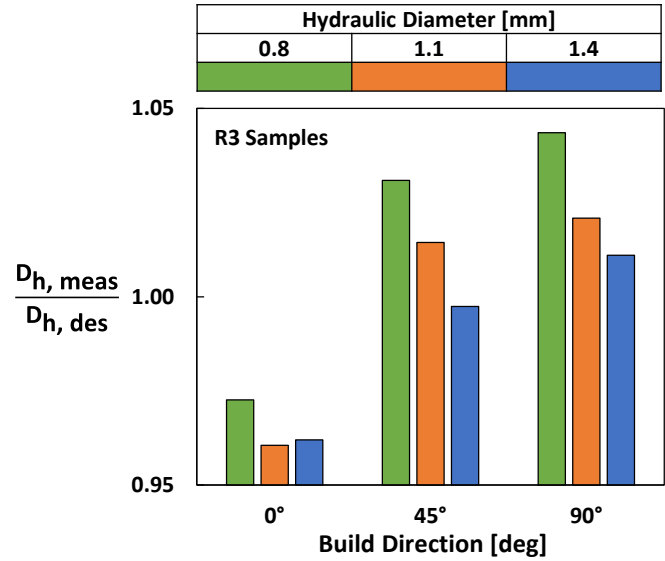
## 4.5 Geometry Characterization

Accurately evaluating the as-built geometry of additively manufactured cooling schemes is important when quantifying pressure loss and heat transfer relations. Additionally, comparison between the design intent and as-built geometry using evaluation methods provides insights into the printability of a design. A nondestructive evaluation method, specifically computed tomography (CT) scanning was used to quantify the internal channel geometries of the coupons in Table 4-1 and check for channel blockages and overall deformation. The entire internal surface of the coupons was CT scanned at a 35 micron voxel resolution. A software was then used to determine the internal surface by filtering the grey scale values from the CT scan measurements [65]. Through interpolation, the CT scan software is capable of resolving one tenth of the original voxel resolution [39].

Geometric dimensions such as hydraulic diameter, cross-sectional area, and perimeter of the channels were averaged and calculated using multiple cross-sectional slices taken from CT scan data along the streamwise axis of the channels. The specific details of this method has been extensively reported in literature [25,49]. All geometric measurements and cooling performance parameters were calculated using CT scan data. The as-built geometric dimensions of the coupons from Figure 4-1 is nondimensionalized by the design intent and is reported in Table 4-1. A graphical representation of the deviation of hydraulic diameter from the design intent is shown in Figure 4-3 for the 3<sup>rd</sup> radius samples.

The majority of the 45° teardrop and 90° circular samples printed larger than their design intent, however the overall deviation from design intent for all the samples regardless of build direction was within 4%. For the 0° teardrop channels, their as-built hydraulic diameter is lower than their design intent. When examining the effect of diameter on deviation from design intent, decreasing diameter results in a higher deviation from the design intent for the 90° and 45° samples. As a result, the smallest channels (0.8 mm) exhibit the highest deviation from design intent at the 45° and 90° build direction relative to the other channel diameters. As seen in Table 4-1, changes to the radial build location of samples did not impact the deviation from design intent for specific diameter or build direction. This result is similar to vertically oriented square channels from Wildgoose et al. [85] fabricated using a single laser machine.

As observed in Table 4-1, the as-built perimeter is on average 4% higher than the design intent for every sample besides the 1.4T0-R2. While for most samples the as-built cross-sectional area follows the same build direction trends as the deviation from hydraulic diameter in Figure 4-3.



**Figure 4-3 Deviation from design intent hydraulic diameter of circular and teardrop channels at a range of build directions.**

#### 4.6 Roughness Characterization

Surface morphology has a direct influence on the amount of turbulent mixing resulting in changes to pressure loss and convective heat transfer. Evaluating surface roughness and its impact to cooling performance aids in the understanding and predictive capabilities of pressure loss and heat transfer in highly rough additive cooling schemes. Surface roughness statistics, such as the arithmetic mean roughness,  $R_a$ , were quantified for the internal surfaces nondestructively using the same CT scan data to calculate channel geometries. The arithmetic mean roughness describes the average deviation of the surface features from a reference value (this is typically the mean roughness height).

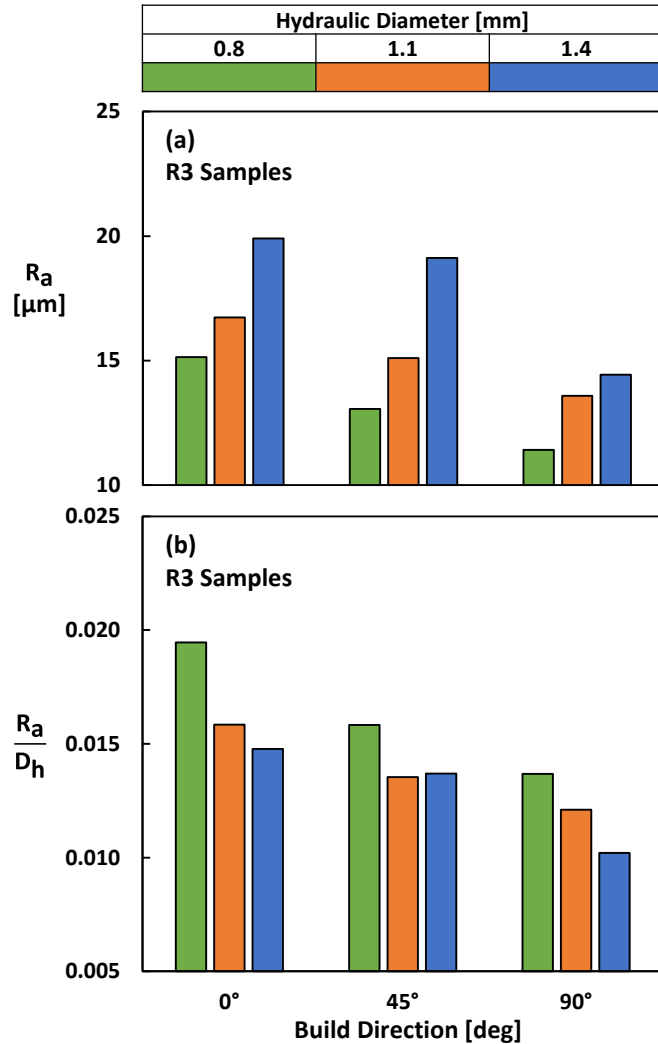
Since the shape of the channels contained curved surfaces (circular and teardrop) an ellipsoid was fitted using a linear least square regression method to each axial cross-sectional slice along the channel length. The average difference from the channel surface to the fitted ellipse was recorded as the arithmetic mean roughness,  $R_a$ . The arithmetic mean roughness values in Figure 4-4 were averaged from multiple channels in each of the coupons in Table 4-1. The method for calculating arithmetic mean roughness is similar to a method used by Klingaa et al. [29] for highly curved channel shapes.

As seen in Figure 4-4 (a), samples fabricated at the 90° build direction show the lowest arithmetic mean roughness level relative to the 45° and 0° orientation. There is no dependence of radial build location on arithmetic mean roughness for any of the build directions. As a result, only



the 3<sup>rd</sup> radius samples from Table 4-1 are shown in Figure 4-4. This result is in contrast to literature [17,66,72]. The cause for no difference in surface roughness as a function of radial location is a factor of the smaller difference in laser incidence angle between the samples fabricated on a four laser machine relative to the samples in literature fabricated on a single laser machine. The change in laser incidence angle is smaller for samples on the four laser machine due to a smaller radial location compared to samples built using a single laser machine in previous literature. At most of the build directions, samples with the highest diameter (1.4 mm) also show the highest arithmetic mean roughness regardless of radial build location.

Nondimensionalizing the arithmetic mean roughness by hydraulic diameter reveals the scale of the roughness features relative to channel size. The results in Figure 4-4 (b) show that as diameter decreases so does the roughness to diameter ratio. The 0.8 mm samples are on average 15% higher in their relative roughness compared to the 1.1 mm and 33% higher compared to the 1.4 mm samples averaged across all build directions and build locations. There is an average 24% increase in roughness to diameter ratio between the 90° and 0° build direction for the 0.8 mm samples. The roughness to diameter ratio is not a function of build location. Additionally, the roughness to diameter ratio increases from the 90° to 0° build direction for a given diameter, which is similar results reported by Snyder et al. [22] and Wildgoose et al. [49]. The cause for this is related to the increasing deformation at the downward facing surfaces.



**Figure 4-4 Arithmetic mean roughness (a) and relative roughness ( $R_a/D_h$ ) (b) of samples for a range of diameters at different build directions and radial build locations.**

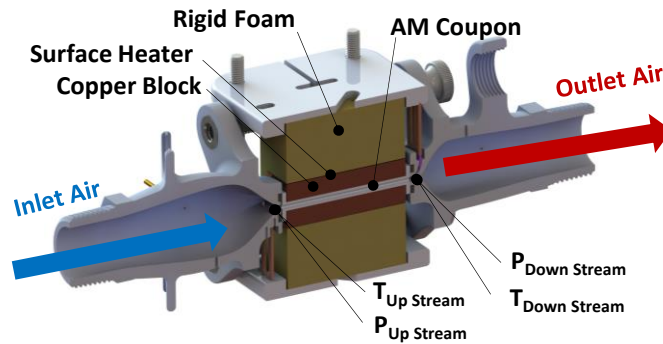
#### 4.7 Channel Performance Measurements

The pressure loss and bulk convective heat transfer of the samples was experimentally measured using a rig, shown in Figure 4-5, that has been extensively reported in literature and benchmarked [30,49]. Friction factor was measured over a range of Reynolds numbers covering the transitional and fully turbulent regime by measuring the static pressure drop between the inlet and outlet of the coupon. Mass flow rate and the geometry of the channels measured from CT scans were accounted for in the friction factor measurement. More specifically, the mass flow rate was measured upstream of the samples using a laminar flow element. The backflow pressure was

regulated downstream of the sample to achieve fully turbulent Reynolds numbers while also being in the incompressible regime (Mach number  $< 0.2$ ). Since the static pressure measurements are upstream of the sample an inlet loss coefficient was calculated using an area ratio (between the plenum inlet and the sample cross-sectional area) while the outlet loss coefficient was one as referenced in Munson et al. [42].

Using the same test rig in Figure 4-5, bulk convection coefficients were measured by imposing a constant surface temperature boundary condition using a heater placed on either side of the coupon with a copper block (imbedded with thermocouples) between the coupon and heater. A one-dimensional conduction circuit using the thermocouples inside the copper block was evaluated to measure the surface temperature of the channels inside the coupon. Stimpson et al. [30] reports a more detailed description of the heat transfer method.

Thermocouples inside the rigid foam and plenums measured conduction losses, and these losses were accounted for in the heat transfer measurements. The total conduction losses were less than 1% of the total power supplied by the heaters across the range of Reynolds numbers evaluated. A separate analysis was performed to account for the losses. The difference between the amount of heat supplied by the heaters,  $Q_{\text{heaters}}$ , to that of the heat transported by the air,  $Q_{\text{air}}$ , after accounting for the conduction losses was 3% at the lowest Reynolds numbers and within 2% at the highest Reynolds number for all the samples evaluated.



**Figure 4-5 Schematic of experimental rig used to measure pressure loss and heat transfer.**

#### 4.8 Experimental Uncertainty

A propagation of uncertainty method following the procedure outlined in Figliola and Beasley [44] was used to determine the experimental uncertainty in friction factor and Nusselt number. The largest contributors towards the uncertainty

in friction factor was the hydraulic diameter and pressure drop. The uncertainty in friction factor was 5% at the lowest Reynolds numbers while it was 4% at the highest Reynolds numbers. The uncertainty in Reynolds number for all the samples was less than 5%. For the heat transfer tests, specifically measuring Nusselt number, the thermocouple exit temperatures and hydraulic diameter contributed most to the uncertainty in Nusselt number. The experimental uncertainty for Nusselt number was 7% across the range of Reynolds numbers evaluated.

#### 4.9 Pressure Loss Measurements

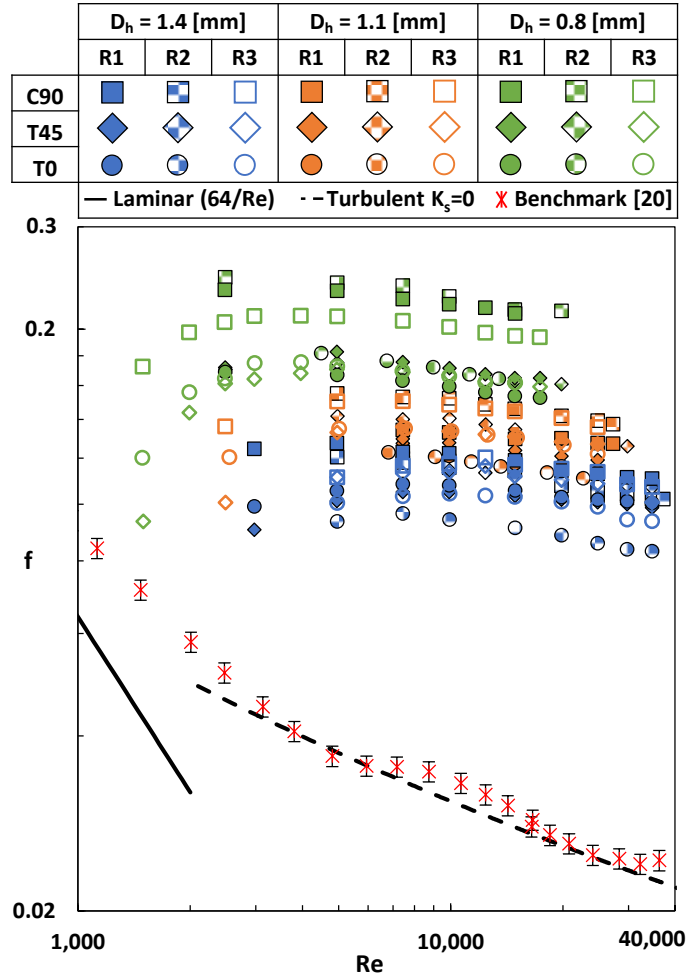
To compare the pressure loss between samples, the nondimensional friction factor was measured over a range of transitional and fully turbulent Reynolds numbers, as shown in Figure 4-6, for all the samples in Table 4-1. Also included in Figure 4-6 is the benchmark data for the experimental rig, where the friction factor of a smooth circular channel coupon agrees with the well-known Colebrook friction factor equation, equation (4-1), at a sandgrain roughness of zero.

$$\frac{1}{\sqrt{f}} = -2 \log_{10} \left( \frac{K_s}{3.7D_h} + \frac{2.51}{Re\sqrt{f}} \right) \quad (4-1)$$

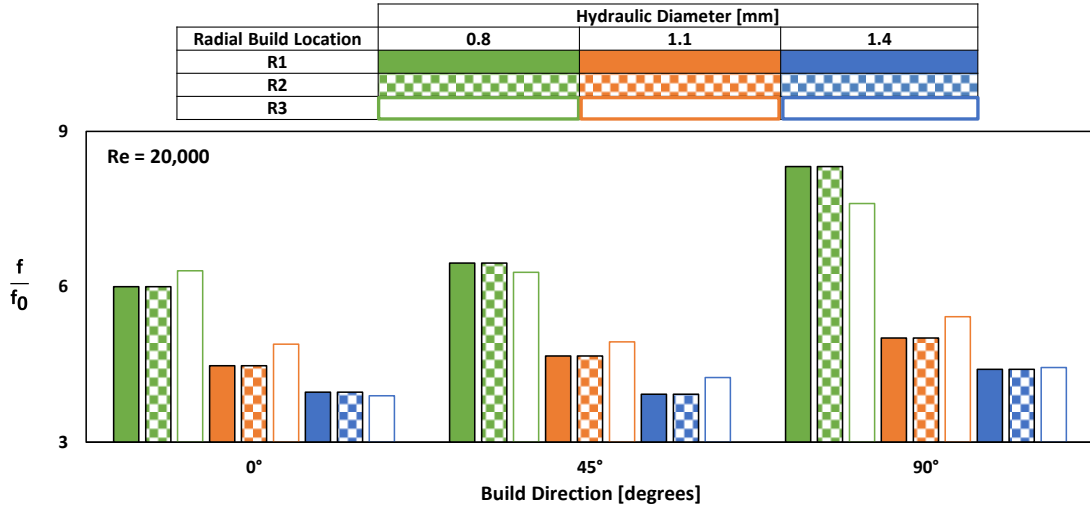
For most of the samples in Figure 4-6, friction factor becomes fully turbulent at around a Reynolds number of 7,500 (critical Reynolds number). As the magnitude of friction factor increases the critical Reynolds number decreases. Similar to the roughness results in Figure 4-4 (a), the friction factor is highest for the smallest diameter channel, which is most likely due to the increase in roughness to diameter ratio as seen in Figure 4-4 (b). The highest level in friction factor was for the 0.8C90-R2 sample, which was 87% different compared to the sample (1.4T0-R2) with the lowest friction factor at a Reynolds number of 10,000. For most of the diameters evaluated, changes to the radial build location did not impact the friction factor. The average difference in friction factor between radial build locations was 7% for the 0.8 mm samples, 10% for the 1.1 mm samples, and 10% for the 1.4 mm samples across all the build directions.

To clearly view trends in friction factor between datasets in Figure 4-6, friction factor augmentation as a function of build direction for the samples in Table 4-1 at a fully turbulent Reynolds number of 20,000 is shown in Figure 4-7, where friction factor is augmented by the friction factor of a hydraulically smooth channel (sandgrain roughness equal to zero) calculated using the Colebrook equation at a shared Reynolds number. For any given diameter, the vertically oriented channels (C90) exhibit the highest friction factor, while in some cases the 0° and 45° channels share a similar friction factor augmentation. Additionally, the lowest diameter (0.8 mm)

samples showed a greater difference in friction factor augmentation between build directions compared to the other diameters. In more detail, the friction factor augmentation of the 90° 0.8 mm channels is 23% higher relative to their 45° and 0° equivalents. The 1.1 mm diameter 90° samples (averaged across all build locations) contained an 11% higher friction factor augmentation compared to their 0° and 45° equivalents. Lastly, the 1.4 mm diameter 90° samples were 9% higher in their friction factor augmentation compared to the 0° and 45° samples.



**Figure 4-6 Friction factor of coupons from Table 4 1 built over a wide range of build directions, build locations, and diameters.**



**Figure 4-7 Friction factor augmented by the friction factor of a hydraulically smooth channel at a Reynolds number of 20,000 for the samples in Table 4 1.**

The friction factor augmentation follows different trends compared to the roughness to diameter ratio in Figure 4-4 (b). While the 90° samples contained the lowest roughness to diameter ratio, their friction factor augmentation was among the highest compared to all other build directions. Consequently, the roughness to diameter ratio struggles to capture the pressure loss trends between samples in Figure 4-7. In a more detailed example, the friction factor augmentation increases 29% for the 0.8 mm samples when going from 45° to the 90° build direction, while the roughness to diameter ratio for the same samples decreases 12% when going from 45° to 90°.

#### 4.10 Heat Transfer Measurements

Similar to the friction factor tests, Nusselt number was measured over a range of fully turbulent Reynolds numbers as seen in Figure 4-8. Also included in the Figure 4-8 is benchmark data from the same hydraulically smooth cylindrical channel coupon as the benchmark data in Figure 4-6. The benchmark data in Figure 4-8 agrees with the well-known Gnielinski Nusselt correlation calculated using a hydraulically smooth friction factor.

The difference in Nusselt number between samples is less than the difference in friction factor. In more detail there is a 23% difference in Nusselt number between the samples at a Reynolds number of 20,000 while for friction factor the difference is 84% at the same Reynolds number. Both the 0.8T0-R2 and 0.8C90-R2 samples showed the highest Nusselt number, while the

1.4C90-R3 and 0.8T45-R1 exhibited the lowest Nusselt number for the range Reynolds numbers. When comparing the heat transfer performance between build locations in Figure 4-8, samples at the 2<sup>nd</sup> radius contain the highest Nusselt augmentation followed by the 3<sup>rd</sup> radius then 1<sup>st</sup> radius across most of the build directions. However the overall trends with build direction and diameter between build location is the same.

To more easily view trends between Nusselt number of the samples in Figure 4-8, Nusselt augmentation of the three radial locations at a shared fully turbulent Reynolds number of 20,000 is shown in Figure 4-9. More specifically, Nusselt number is augmented by the Nusselt number of a hydraulically smooth channel calculated using the Gnielinski correlation with a sandgrain roughness of zero. In contrast to the results from Figure 4-4 and Figure 4-7, Nusselt augmentation does not increase with decreasing channel diameter at any given radial location. Furthermore, the trends in Nusselt number augmentation between samples does not follow friction factor trends. For some samples such as the 0.8T45-R3 coupon, the Nusselt augmentation is the lowest even though the friction factor augmentation in Figure 4-7 was the highest for the 45° samples. Similar results were observed in coupons fabricated over a wide range of build directions by Wildgoose et al. [49]. Where certain roughness elements contributed greatly to pressure loss but contained poor fin efficiencies resulting in a lower Nusselt number relative to friction factor. Samples oriented in the 90° build direction exhibit a similar or lower Nusselt augmentation as samples at the 0° or 45° build direction regardless of diameter or build location.

The arithmetic mean roughness to diameter ratio does not follow the Nusselt augmentation trends in Figure 4-9. When examining the R3 samples, the Nusselt augmentation for the R3 samples at the 45° build direction in Figure 4-9 increases when going from 0.8 mm to 1.4 mm. While for the same R3 samples in Figure 4-4 (b), the roughness to diameter ratio decreases going from 0.8 mm to 1.4 mm. Another example is that both the 1.1T0-R3 and 1.4T0-R3 samples share the same Nusselt augmentation while exhibiting a 27% difference in arithmetic mean roughness to diameter ratio. The differences in trends between Figure 4-8 and Figure 4-4(b) highlights the challenge with using only  $R_a/D_h$  to predict Nusselt number or friction factor.

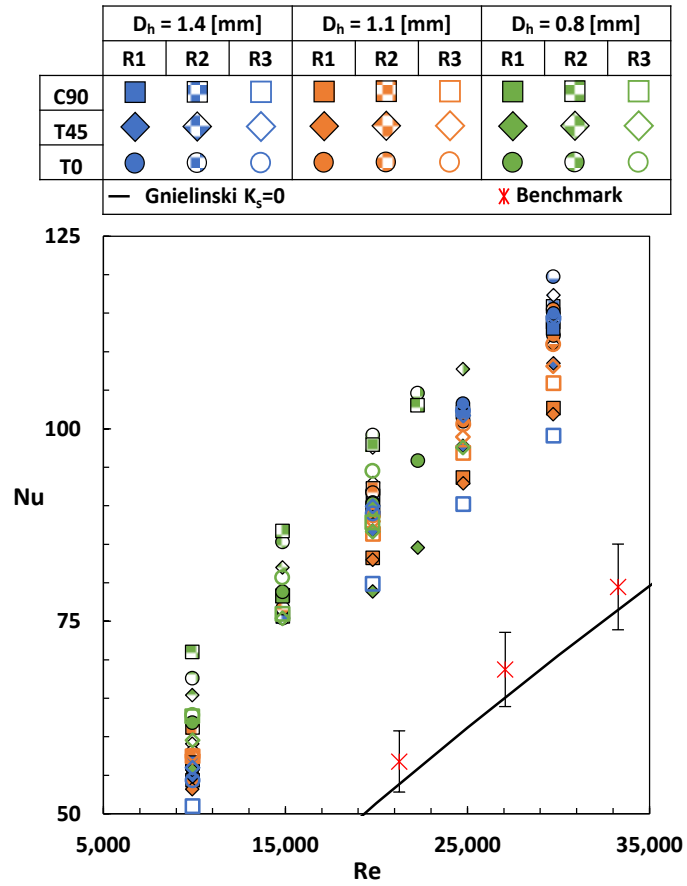
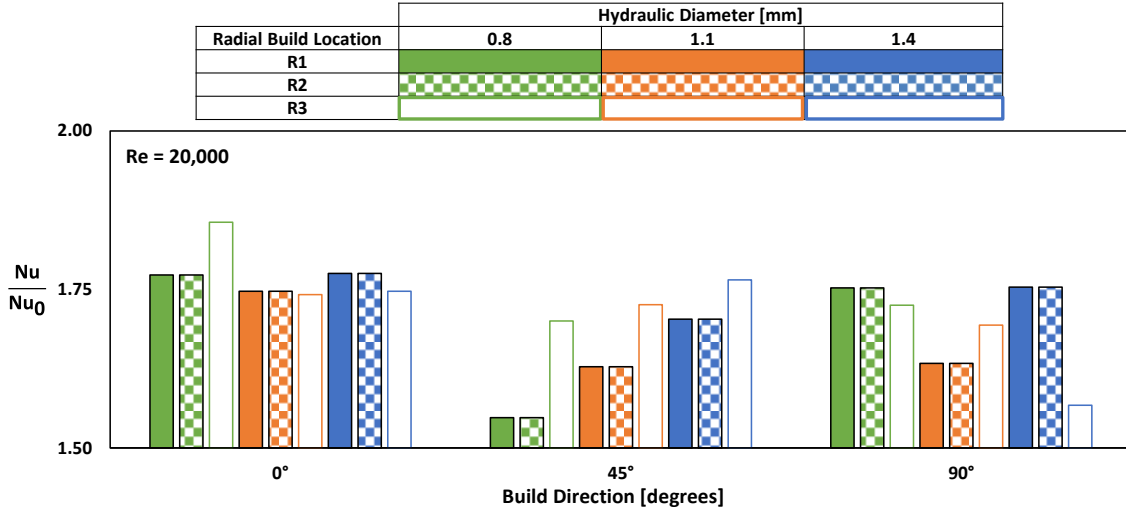


Figure 4-8 Nusselt number of samples (with a variety of build directions, locations, and diameters) from Table 4 1 covering a range of turbulent Reynolds numbers.





**Figure 4-9 Nusselt augmentation of samples fabricated at a variety of build directions and diameters at R1, R2, and R3 at a shared Reynolds number of 20,000.**

#### 4.11 Pressure Loss Correlation

There can be a wide range of friction factor and Nusselt number values for the same arithmetic mean roughness as has been shown in previous sections. Consequently, AM correlations in literature that rely solely on arithmetic mean roughness to diameter ratio struggle to predict friction factor or Nusselt number. To solve this issue, the coupons presented in this paper along with those reported in literature were used to develop a more accurate correlation for heat transfer and pressure loss of internal channels. The test matrix of samples, as seen in Table 4-2, in literature was limited to circular or teardrop channel shapes. Noncircular channel shapes such as square, rectangular, pentagonal, and trapezoidal, can exhibit a range of different roughness's for each side of the channel. Thus, it is difficult for an area averaged roughness statistic to fully capture the surface morphology of the channel. As highlighted by Wildgoose et al. [83], there can also be scaling issues in noncircular channel shapes as result of using hydraulic diameter as the characteristic length in friction factor, Nusselt number, and Reynolds number.

The samples in Table 4-2 includes both circular and teardrop channels built over a range of different build directions, materials, laser process parameters, channel diameters, machines, and different build locations. The present study reanalyzed samples with various roughness statistics from Snyder et al. [25], Wildgoose et al. [83], and Wildgoose et al. [49]. While there were additional samples in literature [86,87] that met the criteria for teardrop and circular channels, only a single roughness statistic such as arithmetic mean roughness was reported. It is important to

**Table 4-2 Samples used for comparing and generating friction factor and Nusselt number correlations**

Channel Shape	$D_h$ [mm]	Build Direction	$R_a/\lambda$	$\Lambda_s$	$R_q/D_h$	$R_{sk}$	# of Samples	Ref
Circular	0.75 - 1.25	0 - 90	0.0026 - 0.1540	32 - 536	0.010-0.072	-0.25-0.46	13	[25]
Circular Teardrop	0.51	45	0.0042-0.0551	25 - 206	0.013-0.048	-0.33-1.18	4	[83]
Circular	1.52	90	0.0844	313	0.009	-0.39	1	[49]
Circular Teardrop	0.80 - 1.40	0 - 90	0.0104- 0.1422	8 - 241	0.013-0.025	-0.6-0.59	27	Current Study

recognize that as the AM cooling field grows so does the need for additional surface roughness statistics to be reported with arithmetic mean roughness.

By focusing on correlating roughness to pressure and heat transfer, the correlations can be used regardless of changes to the machine or process parameters. Several approaches were taken in an effort to correlate the measured surface roughness of the samples in Table 4-2 to predict pressure loss. The first approach followed a similar method to Van Rij et al. [78] and Goodhand et al. [77]. Whereby CT scan data of the samples in Table 4-2 were used to calculate a statistical length parameter using an autocorrelation function (ACF). An ACF used on roughness measurements determines the similarity of a roughness profile. By selectively moving the roughness profile in discretized lengths an ACF is then performed to determine the similarity between roughness elements at a given discretized length (also known as a lag). If values returned from the ACF are near one, then the surface profile is well correlated. While values less than one and even less than zero indicate the surface profile is not very well correlated. Goodhand et al. [77] observed that the minimum discretized length for which the ACF value is at 0.2 results in the roughness profile no longer being correlated and the discretized length is statistically significant. Following a similar procedure as Goodhand et al. [77], the discretized length for when an ACF value is at 0.2 in a channel is known as the correlation length,  $\lambda$ . Several pieces in literature [30,77] have attempted to correlate sandgrain roughness to the correlation length of both additive and nonadditive datasets. A correlation length was evaluated for each of the samples in Table 4-2, using CT scan data. A point cloud of the surface was generated using the cross-sectional slices from the

CT scan data. The point cloud was then organized into multiple axial profile slices going into the channel (similar to a profile obtained by a stylus roughness probe). The ACF was recorded for each lengthwise slice, and the correlation length was calculated.

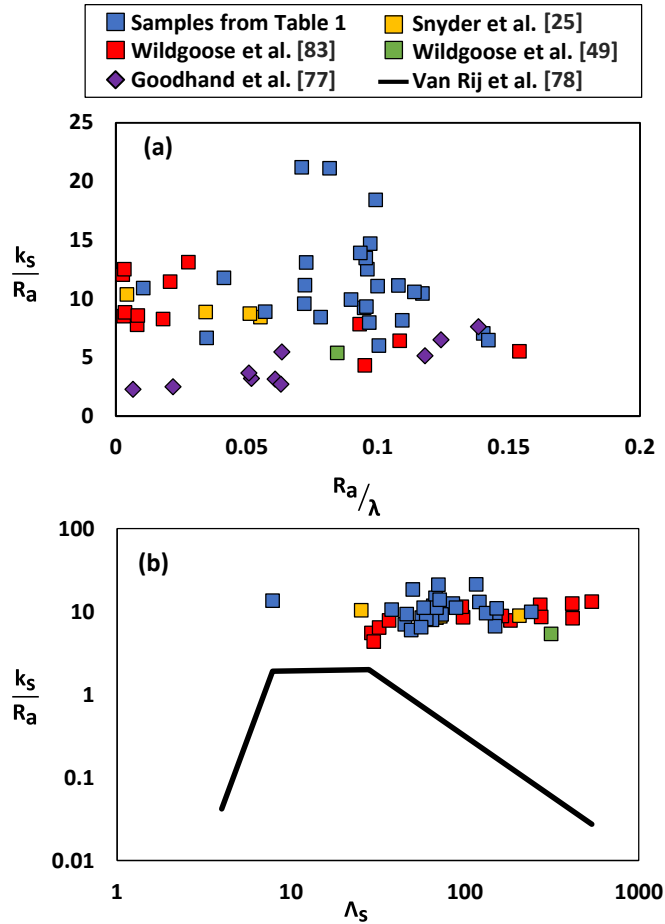
Additionally, the Sigal and Danberg [81] density parameter,  $\Lambda_s$ , was also calculated for all the samples in Table 4-2 since the parameter has seen success in predicting sandgrain roughness in non-additive studies [78,79]. As seen in equation (4-2), the density parameter contains two area ratios. The left area ratio describes the surface area without roughness to that of the summed frontal projected area of the individual roughness elements, while the right area ratio describes the same frontal projected area to the summed total wetted frontal area of the roughness elements.

$$\Lambda_s = \left(\frac{A}{A_f}\right) \left(\frac{A_f}{A_w}\right)^{-1.6} \quad (4-2)$$

Following a similar to procedure to calculate the area ratio as Forooghi et al. [79], a standard tessellation language (STL) of individual channels from samples in Table 4-2 were extracted from CT scan data. Using an in-house code, the STL's were organized where the cross-sections of a channel were placed in the x and y axis while the axial length was the z-axis. For each triangle in the STL file, a normal vector (facing at the interior of the channel) at the centroid of each triangle was determined. The wetted frontal area,  $A_w$ , was calculated by summing the area of all triangles whose normal vector (flow facing triangle) faced the positive z-axis direction. While the frontal area,  $A_f$ , was calculated by taking the area (projected) perpendicular to the flow for each of the flow facing triangles. Normally, the CAD design intent of the channel would be used as the surface area without roughness features, however because the AM process fundamentally changes the shape of the channel, the design intent is not representative of the as-built geometry. Consequently, the surface area without roughness,  $A$ , was calculated by taking the average perimeter from cross-sectional slices and multiplying by the overall channel length.

A range of  $\lambda$  and  $\Lambda_s$  are provided in Table 4-2 for the different samples and shown in Figure 4-10 as a function of sandgrain roughness nondimensionalized by the arithmetic mean roughness calculated from CT scans. Unlike the results from Goodhand et al. [77], the nondimensionalized correlation length struggles to correlate with the nondimensional sandgrain roughness in Figure 4-10 (a). Most notably, there is a wide range in  $k_s/R_a$  between samples for any given  $R_a/\lambda$ . At an  $R_a/\lambda$  value of 0.1, there can be up to a 120% spread in  $k_s/R_a$  between samples. A similar observation in the struggle of  $\lambda$  predicting  $k_s$  is stated by Snyder et al. [30].

The density parameter also struggles to correlate with the nondimensionalized sandgrain roughness as seen in Figure 4-10(b). Accompanied in Figure 4-10 (b) is a piece wise correlation



**Figure 4-10 Comparison of correlation length and density parameters to sandgrain roughness for the samples in Table 4-2.**

developed by Van Rij et al. [78]. When  $\Lambda_s$  is greater than 28, the correlation [78] decreases in  $k_s/R_a$ , however the  $k_s/R_a$  for the AM datasets remain the same regardless of any change to  $\Lambda_s$ . Furthermore, the value of the nondimensionalized sandgrain roughness is higher than the correlation [78].

The second approach to correlate roughness to pressure loss, in this case a nondimensionalized pressure loss known as friction factor, was performed by investigating different forms of bulk roughness statistics, which included  $R_a$ ,  $R_q$ , and  $R_{sk}$ . Bulk roughness statistics require less information of the surface compared to both  $\lambda$  as well as  $\Lambda_s$  and therefore are easier to measure. All basic roughness statistics were calculated using CT scan data with the fitted ellipsoid method. The skewness,  $R_{sk}$ , of the roughness represents the distribution of roughness elements relative to the mean. A positive value of skewness implies that the surface roughness

contains more peaks (surface features are above the mean), while a negative skewness indicates most surface features represents valleys (surface features are below the mean roughness).

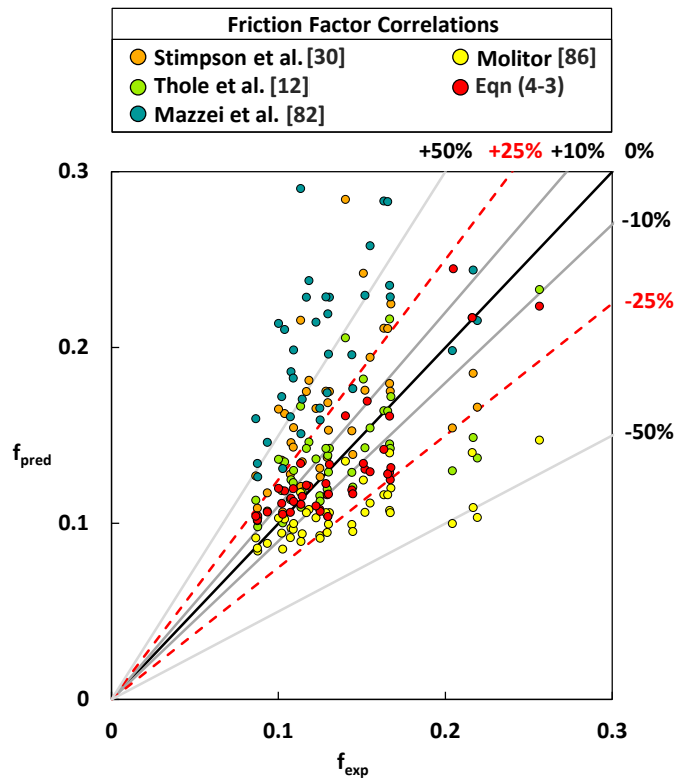
Several friction factor correlations for AM cooling schemes from literature [12,30,82,86] are shown in Table 4-3 and were compared using the datasets from Table 4-2. The mentioned correlations predicted relative sandgrain roughness,  $k_s/D_h$ , using a measured relative arithmetic mean roughness,  $R_a/D_h$ . The predicted friction factor in Figure 4-11 for the correlations by Stimpson et al. [30], Thole et al. [12], Mazzei et al. [82], and Molitor [86] was calculated by calculating the friction factor from Colebrook’s equation, equation (4-1), using the predicted relative sandgrain roughness. Out of the 45 samples in Table 4-2 evaluated for the correlations from literature in Table 4-3, three samples were omitted from the analysis, since the  $R_a/D_h$  ratio was either an extremely high value ( $R_a/D_h > 0.035$ ) such as the case for the 1.25 mm and 1 mm  $0^\circ$  circular coupons from Wildgoose et al. [49] or an extremely low  $R_a/D_h$  value ( $R_a/D_h < 0.007$ ) such as the 1.5 mm circular channel diameter at a  $90^\circ$  build direction from Wildgoose et al. [83].

**Table 4-3 Correlations for Predicting Friction Factor of the Samples in Table 4-2.**

<b>Correlation</b>	<b>Avg</b> [% Error]	<b>Max</b> [% Error]	<b>Ref</b>
$\frac{k_s}{D_h} = 18 \frac{R_a}{D_h} - 0.05$	31%	103%	[30]
$\frac{k_s}{D_h} = 11 \frac{R_a}{D_h}$	15%	47%	[12]
$\frac{k_s}{D_h} = 25.247 \frac{R_a}{D_h} - 0.0822$	68%	186%	[82]
$\frac{k_s}{D_h} = 5.094 \frac{R_a}{D_h} + 0.0258$	21%	53%	[86]
$f = 2.6 \frac{R_q}{D_h} (1 + R_{sk})^{0.3} + 0.074$	12%	25%	Eqn. (4-3)

Figure 4-11 shows the difference from the predicted friction factor ( $f_{pred}$ ) using the correlations in Table 4-3 to the friction factor measured through experiments ( $f_{exp}$ ). More specifically, the Colebrook friction factor equation was used to calculate a predicted friction factor from the relative sandgrain roughness correlations in Table 4-3. As seen in Figure 4-11, there is a wide range between the predicted and experimental friction factor for the correlations from literature. As shown in Table 4-3, the average and maximum absolute percent error was calculated to compare how well the datasets in Table 4-2 were predicted. As seen in Figure 4-11, both Stimpson et al. [30], and Mazzei et al. [82] tend to overpredict friction factor while the correlation

from Molitor underpredicts the friction factor. One of the earliest correlations for AM datasets from Stimpson et al. [30] predicts the friction factor of the samples within an average of 31%, however the maximum error can be up to 103%. Molitor [86] changed the coefficients of the same equation form as Stimpson et al. [30]. With the change in coefficients, the Molitor [86] correlation is able to predict a 21% average absolute percent error and 53% maximum absolute error. By removing the offset term from Stimpson et al. [30], the Thole et al. [12] correlation is able to further reduce the error in predicting friction factor with a 15% average absolute error and 47% maximum absolute error.



**Figure 4-11 Experimental friction factor compared to friction factor predicted using the correlations in Table 4 3 of the datasets in Table 4 2.**

However as was seen in the friction factor augmentation plot of Figure 4-7 and roughness to diameter ratio plot of Figure 4-4(b), several samples can contain the same roughness to diameter ratio while contain different friction factors. . The cause for arithmetic mean roughness to diameter ratio struggling to be related to friction factor or Nusselt number is due to the surface morphology. The work of Stimpson et al. [2], proposes that certain roughness elements can contribute differently to pressure loss and heat transfer. Depending upon how well sintered the roughness element is to

the surface can impact the fin efficiency of the roughness element. Partially sintered particles have poor fin efficiency due to a high conduction resistance between the roughness element and AM surface. The ability to better describe the surface morphology is an ongoing area of research in the community. The use of multiple roughness parameters instead of a single bulk roughness statistic (Ra) that does not fully describe the surface morphology, can help reveal trends in friction factor and Nusselt number. A more accurate prediction in friction factor using roughness terms is challenging to achieve by simply changing the coefficients of a similar form to Stimpson et al. [30].

A different approach was taken to correlate the samples in Table 4-1. Flack and Shultz [80] found that a combination of using the root mean square roughness,  $R_q$ , coupled with skewness,  $R_{sk}$ , resulted in the most effective method to predict sandgrain roughness for non-AM datasets. A similar approach to correlating roughness to pressure loss was taken for the samples in Table 4-2 as Flack and Schultz [80] to generate the correlation, as seen in equation (4-3).

$$f = 2.6 \frac{R_q}{D_h} (1 + R_{sk})^{0.3} + 0.074 \quad (4-3)$$

However, friction factor was correlated instead of sandgrain roughness and to nondimensionalize the equation, the root mean square roughness is normalized by the as-built hydraulic diameter. By calculating friction factor directly, the process of going through a friction factor correlation such as Colebrook is bypassed. Four samples out of the forty-five in Table 4-2 were omitted from the best fit for equation (4-3). Specifically, the 0.8 mm 90° samples built across the different locations from the current study were omitted due to being outliers as result of the highest friction factor relative to other samples. Furthermore the 1.5 mm circular channel from Wildgoose et al. [83] was left out due to a significantly lower  $R_q/D_h$  value relative to the other datasets. As seen in equation (4-3) and Table 4-3, the friction factor correlation is able to predict the data from Table 4-2 within a 12% average absolute error and 25% maximum absolute error. As seen in Figure 4-11, most samples predicted from equation (4-3) are less than 10% error. The use of multiple roughness statistics in equation (4-3) result in half the amount of maximum error as the most accurate  $R_a/D_h$  correlation (from Thole et al. [12]).

The friction factor correlation, equation (4-3), consists of samples fabricated at different AM machines, channel sizes, materials, build directions, and radial build locations. It is important to note that equation (4-3) is only valid for curved channel shapes such as circular and teardrop shapes. Furthermore, the correlation is only valid in the fully turbulent regime where friction factor does not change with Reynolds number.

A comparison of friction factor for several datasets from Table 4-2 and a noncircular channel shape from Wildgoose et al. [83] is shown in Figure 4-12. As seen in Figure 4-12, equation (4-3) is more effective at predicting the friction factor relative to the other correlations in Table 4-2 between the different datasets. However as mentioned, equation (4-3) struggles to predict noncircular channel shapes such as the pentagon in Figure 4-12. The cause is that the positive or negative value of the skewness term is filtered out when performing an area average skewness for each surface of the pentagon channel.

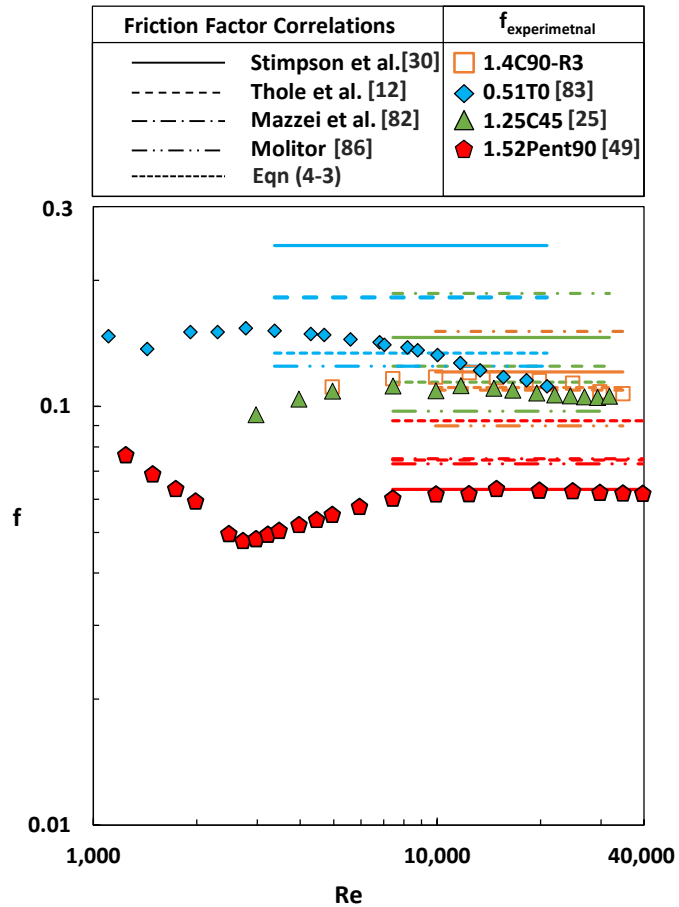


Figure 4-12 Comparison of friction factor correlations of select samples from Table 4 2.

#### 4.12 Heat Transfer Correlation

In addition to correlating friction factor, several Nusselt number correlations for the datasets in Table 4-2 were also investigated. More specifically a modified Gnielinski correlation from Stimpson et al. [30] was compared to another modified form of the Gnielinski correlation, equation (4-4), that was fitted using the data in Table 4-2. The same datasets used to make the



friction factor correlation, equation (4-3), were used to generate the Nusselt number correlation, equation (4-4). Both Nusselt number correlations, in Table 4-4, are functions of Reynolds number, friction factor, and Prandtl number. The predictions of both correlations are presented in Figure 4-13 with two approaches towards calculating the Nusselt number. The first approach assumed that friction factor is known and both Nusselt correlations were calculated using the friction factor measured from experiments, while the second approach assumed friction factor is unknown and is predicted using a friction factor correlation, equation (4-3).

The difference from the predicted Nusselt number ( $Nu_{pred}$ ) using the correlations in Table 4-4 to the Nusselt measured through experiments ( $Nu_{exp}$ ) is shown in Figure 4-13. In more detail, the experimental Nusselt number at a variety of Reynolds numbers for each coupon is compared to a predicted Nusselt number using two different Nusselt number correlations. As seen in Figure 4-13 and Table 4-4, equation (4-4) is more effective at predicting the Nusselt number using the experimental friction factor and predicted friction factor compared to the Stimpson et al. [30] correlation.

$$Nu = \frac{(Re^{0.477}-31)Pr\sqrt{f/8}}{0.38(1-Pr^{2/3})} \quad (4-4)$$

When using equation (4-4), the average absolute error is reduced by half compared to the Stimpson et al. [30] correlation as seen in Table 4-4. As seen in Figure 4-13, the Stimpson et al. [30] correlation underpredicts the Nusselt number when using the experimental friction factor and predicted friction factor. As seen in Table 4-4, there is minimal difference between using the experimental or predicted friction factor for the average and maximum error of the Stimpson et al. [30] correlation. Despite equation (4-4) exhibiting a higher maximum error using the predicted friction factor compared to Stimpson et al [30], there is a single outlier in the data that contributes to the higher maximum error. By removing the outlier (1 mm channel built at the 0° build direction) from Wildgoose et al. [49] in the prediction of equation (4-4), the maximum error of 39% gets reduced to a maximum absolute error of 25% when using the predicted friction factor and 24% when using the experimental friction factor. The cause for the outlier is because the friction factor of the 1 mm channel from Wildgoose et al. [49] exhibited one of the highest friction factor values while the Nusselt number was significantly lower compared to the rest of the samples evaluated. It is important to note that equation (4-4) was created using a total of 41 coupons while the Stimpson et al. [30] correlation was created using a total of 10 coupons.

**Table 4-4 Correlations for Predicting Heat Transfer of the Samples in Table 4-2.**

Correlation	$f_{exp}$		$f_{pred}$ (Eqn 3)		Ref
	Avg   % Error	Max   % Error	Avg   % Error	Max   % Error	
$Nu = \frac{(Re^{0.5} - 29)Pr\sqrt{f/8}}{0.6(1 - Pr^{2/3})}$	14%	31%	16%	32%	[30]
$Nu = \frac{(Re^{0.477} - 31)Pr\sqrt{f/8}}{0.38(1 - Pr^{2/3})}$	8%	27%	8%	39%	Eqn. (4-4)

Similar to Gnielinski correlation, equation (4-4) should only be used in turbulent flows when Reynolds number is greater than 2,300. Since air was the only fluid used to make equation (4-4), fluids where  $Pr \approx 0.7$  should only be used. As result of the datasets used to make equation (4-4), only curved channel shapes such as teardrop and circular designs should be used for the correlation.

A comparison of the same samples from Figure 4-12 are shown in Figure 4-14 for the prediction in Nusselt number using Stimpson et al. [30] and equation (4-4). Equation (4-4) is more effective at predicting Nusselt number when using the experimental friction factor and predicted friction factor from equation (4-3) compared to the correlation from Stimpson et al. [30] for the samples in Figure 4-14. A noncircular channel shape (a pentagon) from Wildgoose et al. [83] is also included in Figure 4-12. The maximum absolute error of the pentagon is 22% when using the experimental friction factor data and 5% when using the friction factor predicted from equation (4-3). Despite a higher error when predicting friction factor using equation (4-3) for pentagon the Nusselt number correlation (equation (4-4)) exhibits a lower error.

Nu Correlations	$f_{\text{experimental}}$	$f_{\text{predicted}}$ (Eqn (4-3))
Stimpson et al.[30]	●	○
Eqn (4-4)	◆	◇

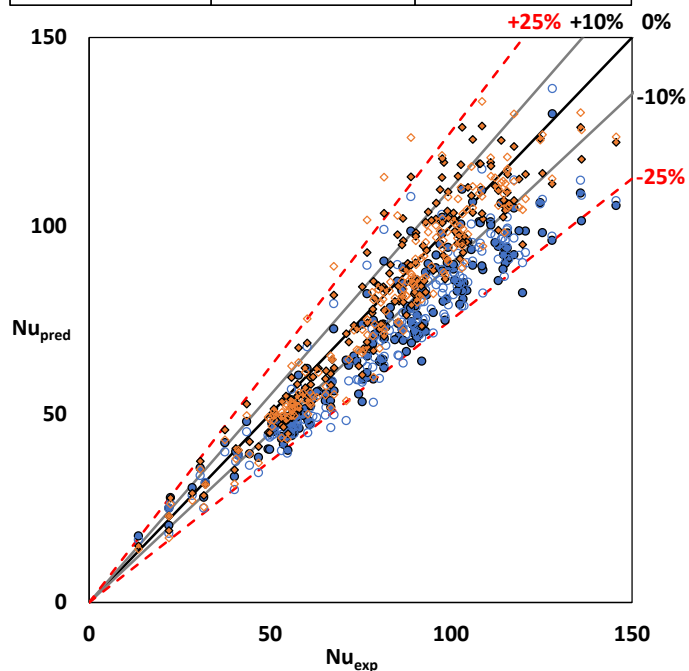
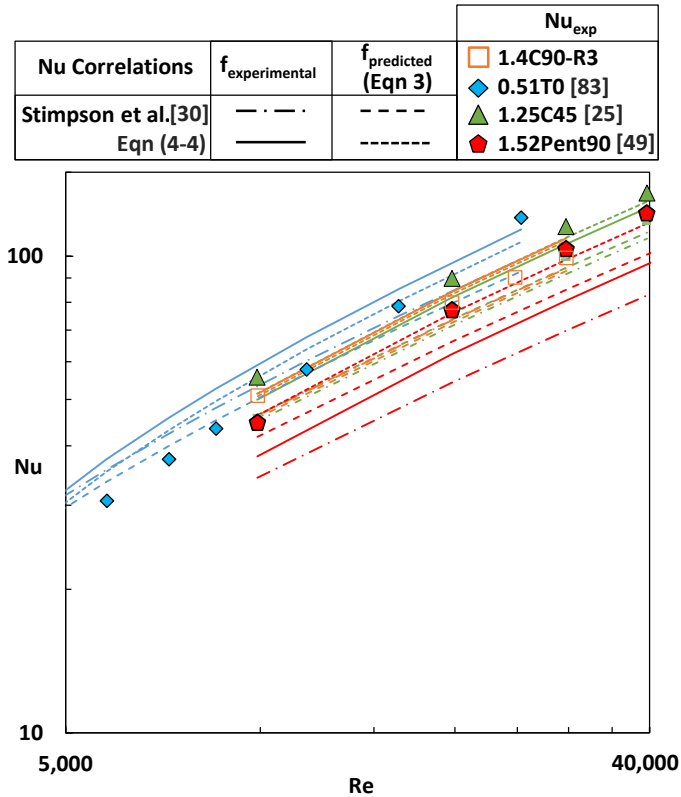


Figure 4-13 Experimental Nusselt number of samples from Table 4 2 compared with the predicted Nusselt number using the experimental friction factor and friction factor predicted using equation (4-3).



**Figure 4-14 Comparison of Nusselt number prediction using equation (4-4) and the Nusselt number correlation from Stimpson et al. [10].**

#### 4.13 Conclusion

Multiple circular and teardrop cooling channel coupons were fabricated over a range of different build considerations (build directions, radial build locations, and channel diameters) using a four laser DMLS machine. Each of the 27 coupons were CT scanned to evaluate their geometric dimensions and internal surface roughness. Pressure loss and heat transfer of the coupons were measured over a range of fully turbulent Reynolds numbers.

For the samples presented in this paper, the hydraulic diameter did not change with radial build location. Channels with teardrop corrections at the 0° build direction contained hydraulic diameters lower than their design intent while teardrop channels at the 45° and circular channels at the 90° build direction had hydraulic diameters higher than their design intent.

Surface roughness, specifically the arithmetic mean roughness, decreased as build direction increased from 0° to 90°. Similar to hydraulic diameter, surface roughness was not a function of build location. The arithmetic mean roughness normalized by hydraulic diameter decreases as build direction increases from 0° to 90°, regardless of diameter or radial build location.

In contrast to the arithmetic mean roughness to diameter ratio, the samples at the 90° build direction contained the highest friction factor relative to the 45° and 0° orientation for any given diameter. As diameter decreased from 1.4 mm to 0.8 mm, the friction factor increased by more than two thirds. Nusselt number followed different trends in build direction compared to the trends of friction factor and surface roughness. Despite the 90° samples exhibiting the highest friction factor, their Nusselt number was equal or lower compared to their 45° and 0° counterparts.

Several correlations from open literature for friction factor and Nusselt number were compared with the coupons from the current study and datasets in literature. A density parameter using area ratios of the roughness elements and a correlation length parameter from an auto correlation function applied to the surface struggled to correlate sandgrain roughness. Bulk roughness correlations from literature such as those using arithmetic mean roughness were unsuccessful in correlating friction factor since samples can contain the same arithmetic mean roughness to diameter ratio, but exhibit different friction factor values. By using a combination of roughness statistics, specifically the root mean square roughness and skewness, a correlation was developed that was able to reduce the error in predicting friction factor by half compared to additive specific roughness correlations in literature. Quantitatively, the presented friction factor correlation was able to predict samples within a maximum absolute error of 25% with an average absolute error of 12%.

A Nusselt number correlation was also created using the datasets for the friction factor correlation. The Nusselt number correlation was able to reduce the average error by half compared to additive specific Nusselt correlations found in literature. In more detail, the presented Nusselt number correlation was able to predict samples within a maximum absolute error of 39% with an average absolute error of 8%.

In summary, friction factor and Nusselt number can be predicted using roughness statistics that are commonly quoted in AM part qualification. The correlations can be used for circular and teardrop channel shapes regardless of changes to machine, material, build direction, build location, and channel size.

## **5 Impacts of The Additive Manufacturing Process on The Roughness of Engine Scale Vanes and Cooling Channels <sup>5</sup>**

### **5.1 Abstract**

By leveraging the additive manufacturing platform, development time and costs for turbine component testing can be reduced relative to traditional investment casting. Surface roughness is a key characteristic of the additive manufacturing process that can impact flow, heat transfer, and mechanical integrity of printed components. There are multiple design and build considerations that result in variability in surface roughness especially when additively fabricating complicated three-dimensional vanes and internal cooling passages. This study characterizes the surface roughness of internal cooling passages, vanes, and flat external surface samples made using additive manufacturing, specifically the direct metal laser sintering process. The samples were manufactured with various wall thicknesses, layer thicknesses, build locations, build directions, and on different AM machines. A combination of computed tomography scanning and optical profilometry were used to evaluate surface roughness levels. The data indicates that the dominate factors in roughness for a given layer thickness are a function of wall thickness, build location, and build direction.

### **5.2 Introduction**

The fabrication guidelines for additive manufacturing (AM), specifically direct metal laser sintering (DMLS) a type of powder bed fusion process, are intrinsically different from traditional subtractive or casting methods. The DMLS process fabricates parts by spreading a layer of metal powder using a re-coater blade on top of a build plate (i.e. substrate). A laser then selectively melts the powder particles following the geometry profile of the part. The layer wise process is then repeated until the part is complete. There are multiple considerations that factor into the AM design and fabrication process of a part such as the printability of part features, the layout of the part on the build plate, and the selection of the AM machine. Each sequence in the fabrication of an AM component influences the deviation from design intent of the part [88]. Characterizing the deviation from design intent in terms of surface roughness is important for AM gas turbine parts since roughness impacts the performance and life cycle of the part.

Understanding the major contributions to the roughness for each step of the build sequence, the process from the design of the part to build layout and then machine selection is important in

---

<sup>5</sup> Wildgoose, A.J., Thole, K.A., Subramanian, R., Kersting, L., and Kulkarni, A., 2022, "Impacts of The Additive Manufacturing Process on The Roughness of Engine Scale Vanes and Cooling Channels," *Journal of Turbomachinery*, vol. **145**(4), pp. 041013.

providing reproducible turbine components made through AM. For example, traditionally fabricated nozzle guide vanes typically have highly engineered curved airfoils and experience a range of wall thicknesses that need to be replicated with tight tolerances. The objective of this study was to provide an overview of influences that the AM build sequence has on the part quality of engine relevant internal cooling channels and vane airfoil geometries. Specifically, the roughness for three different geometries were evaluated that included internal cooling channels, nozzle guide vanes, and flat external surface samples.

### **5.3 Literature Review**

The high surface roughness present in additively manufactured parts is a result of the layer wise process leading to the stair stepping effect as well as multiple effects contributing to changes and instabilities of the melt pool [20]. While it is challenging to fully control the melt pool, several process parameters have been identified in the literature that significantly contribute to surface roughness in AM parts such as changes in heat accumulation due part geometry [71,89], laser parameters [13], angle of part surface with respect to build plate [24,27,28], changes in location on the build plate [17,20,21,72], and layer thickness [90–92]. A combination of these parameters is typically seen in the general build sequence of an AM part, starting from the part design to build plate location to machine parameters.

Multiple studies have found that changes to the geometry of a part can influence the deviation from design intent and surface roughness[71,89]. A study from Jamshidinia et al. [89] showed that decreasing the spacing between 1 mm thick walls showed high roughness as result of partial melting of the Ti-6Al-4V powder particles from increased heat accumulation. Other literature has focused on the minimal feature size and how that affects roughness. Wu et al. [93] showed a lack of fusion between layers at wall thickness below 0.1 mm for Inconel 718. There is an absence of literature, however, concerning the resulting surface roughness over a range of wall thicknesses that occur in turbine components.

When setting up the build layout of samples, consideration is given to the factors that contribute to deviation from design intent such as build direction. It is well known that downward facing surfaces contain higher surface roughness values compared to upward facing surfaces [24,27,28]. The past studies that have evaluated surface roughness levels as a function of build direction do so with mostly non-curved surfaces. Complicated curved surfaces such as airfoils have a range of local surface orientations depending on the airfoil build direction. Studies that have additively fabricated airfoils, either vanes or blades [94,95], have primarily focused on structural

properties. A study by Krewinkel et al. [95] showed that for the particular build direction of the vane, there was a larger deviation from design intent at the midspan of the pressure side compared to the mid-span of the suction side. However, there were no roughness levels reported.

A few studies have shown that part location on a build plate can influence the as-built surface roughness [17,20,21,72]. Laser incidence angle is commonly used to correlate surface roughness dependency on build location. The work from Subramanian et al. [72] and Rott et al. [96] shows that the angle of a surface with respect to the laser source affects the melt pool resulting in increased surface roughness when the part is further from the laser source. The samples used in these studies consist of multi-sided pyramids [17], external surface “chess” pieces [72], and vertically oriented plates [20]. While these studies are thorough in their findings, there is limited knowledge as to whether the same trends are experienced in turbine relevant geometries such as the surfaces of cooling channels and curved surface airfoils.

One of the last build sequence considerations before part removal and heat treatment of an AM part is selecting the appropriate machine and layer thickness. Observations from Subramanian et al. [72] noted that position dependency on roughness followed the same trends for a simple flat surface geometry between single (EOS M290-1) and multi-laser (EOS M400-4) machines. Other machine selection parameters such as layer thickness has been shown to impact the as-built surface roughness and effect material properties [90–92]. A systematic investigation by Bacchewar et al. [90] showed that for upward facing surfaces, roughness increases as layer thickness increases. The same roughness trend was observed for downward facing surfaces angled between 30° and 90°. It is important to note that the different layer thickness evaluated in this study were created using early generation AM machines that resulted in a high (150 to 190 microns) layer thicknesses relative to the layer thickness used in newer generation AM machines (20 to 80 microns).

The goal of this study is to investigate the impact specific sequences in the AM fabrication process has on the surface roughness of engine scale turbine components. This paper analyzes multiple effects on surface roughness including wall thickness, build direction, build location, different AM machine models, and layer sizes for both internal cooling channels and engine scale vane airfoils.

#### **5.4 Description of Samples**

Both internal cooling channels and engine scale vanes were made using AM, specifically DMLS, to evaluate the impact the process and part geometry has on the as-built surface quality of turbine components. As seen by the test matrix in Table 5-1, the scope of samples used for this



study ranged from simple internal cooling channels with a square cross-section to a more complicated engine scale vane to a flat external surface octagonal sample resembling a “chess piece”. The order of samples in Table 5-1 resembles the additive build sequence. Furthermore, a detailed description of the wall thickness ( $t$ ), radial build location ( $r$ ), build direction ( $\Theta$ ), and machine/layer thickness for each of the samples is shown in Table 5-1.

To methodically evaluate the impact of the wall thickness, multiple straight channels were placed in a single coupon as shown in Figure 5-1 and given in Table 5-1. A 12, 3, 6, and 9 o'clock compass is in Figure 5-1 that will be used to specify the specific surface orientation in the cooling channel. The distance between the open channel (12 o'clock surface) and the exterior wall was varied between 0.3 mm and 3.0 mm while the bottom of the square channel maintained the same wall thickness as did the spanwise distance between the channels. The channels were equally spaced 4 mm apart from one another to minimize the effect of channel proximity. As seen in Figure 5-1, the 6 o'clock surface for all the channels was designed with a 2 mm wall thickness to act as a control surface. The particular coupon was placed near the center of the build plate to isolate it from build location effects. The internal channels were fabricated at the  $90^\circ$  (vertical) build direction to limit deformation from the design intent. Build direction is defined as the angle of the surface with respect to the surface of the build plate (i.e. substrate). The internal channel samples in Figure 5-4 were created using an EOS M280-1 machine (single laser) in Inconel 718 (IN718) with a 40-micron layer thickness using standard EOS recommended process parameters [34]. The samples were solution annealed while attached the build plate using standard EOS IN718 recommended heat treatment parameters [34].

The effects of the wall thickness on more complicated curved surfaces were performed on the leading edge (LE) of a vane as seen in Figure 5-2 and Table 5-1. More specifically, the leading edge portion of the National Experimental Turbine (NExT) vane [12]. Similar to the channels, the leading edge vane samples, seen in Figure 5-2, were fabricated at the  $90^\circ$  build direction where build direction for the vane samples is the angle between the radial axis of the leading edge to the surface of the build plate. The LE vane samples included two different wall thicknesses (0.4 mm and 1.4 mm) between the interior and exterior of the vane. The largest thickness of the LE vane is at the leading edge nose while the smallest thickness is near the pressure side of the leading edge region as seen in Figure 5-2. The LE vane samples were manufactured in a 40-micron layer thickness using a single laser EOS M290-1 machine. To investigate build location, the LE vane samples with different wall thicknesses were also manufactured at two different radii (75 mm and 112.5 mm) from the center of the build plate.


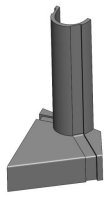
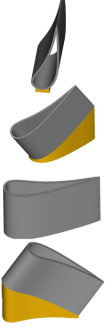

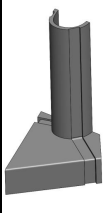
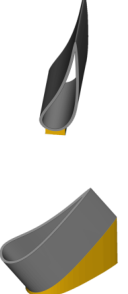
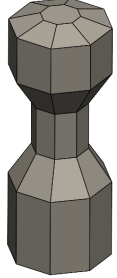
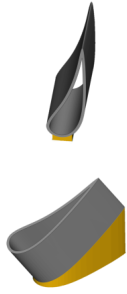
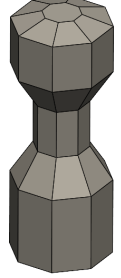

Full, hollow NExT vane samples, shown in Figure 5-3 and highlighted in Table 5-1, containing no internal or external cooling features were made at different build directions. The NExT vane airfoil samples were fabricated at four orientations ( $0^\circ$ ,  $60^\circ$ ,  $90^\circ$ ,  $120^\circ$ ) to characterize the variation in surface roughness across the vane. The full vane airfoil samples at different build directions were made using an EOS M290-1 machine with a 40 micron layer thickness. The distinct build orientations in Figure 5-3 cover a range of airfoil build angles. To minimize the influence of wall thickness on surface roughness, the wall thickness was constant for the full vane samples shown in Figure 5-3. Furthermore, the vane airfoils at different build directions shared a similar radial location from the laser source in order to reduce the impact of build location on the airfoil surface.

Several of the build directions, specifically the  $0^\circ$  and  $60^\circ$  full NExT vanes were also printed using multiple machines, build locations, and in two different layer thickness as outlined in Table 5-1. In more detail, a  $0^\circ$  and  $60^\circ$  full vane was printed at three different radii from the laser source ( $r = 75, 112.5, 187.5$  mm) using the EOS M290-1 machine with a 40 micron layer thickness and also a EOS M400-1 machine with 40 and 80 micron layer thicknesses to understand machine differences.

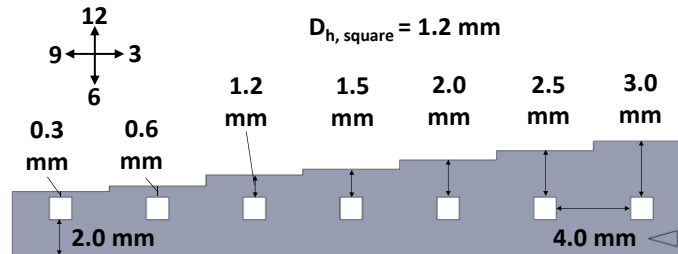
To understand the influence of build location on internal surfaces, several single channel internal cooling samples given in Table 5-1 and shown in Figure 5-4, were fabricated at different radial build locations of 0 mm, 75 mm, and 145 mm. The distances of the samples from the laser source were chosen to cover the printable area of an EOS M280 build plate. All internal cooling samples, wall thickness and build location, were designed with a square cross-section channel with a hydraulic diameter of 1.2 mm and a sample height of 14 mm. Each of the samples had a 2 mm wall thickness with a square cross-section. As seen in Figure 5-4, the single channel samples were fabricated on the same build plate as the channel wall thickness coupon.

To understand the inherent machine related impact on surface roughness, a standard, symmetrical geometry coupon – “octagonal chess piece” – was printed and is shown in Figure 5-5. Each coupon has 33 distinct surfaces: one top horizontal, eight  $20^\circ$  upskin, eight  $60^\circ$  upskin, eight  $90^\circ$  vertical, and eight  $60^\circ$  downskin. The coupons alignment in the build plate was identified by a notch oriented towards the gas flow and the letters aligned from left to right, opposite to the recoater direction. As outlined in Table 5-1, the chess pieces were fabricated using single laser machines (EOS M290-1 and M400-1) and a multi-laser machine (M400-4). The chess pieces were located in each of the print beds at a 75 mm radial location from the laser source. Two layer thickness were investigated – 40 mm and 80 mm (only in M400-1). Siemens Energy proprietary process parameters for IN718 were used in all three machines for the LE vane, full vane, and chess piec

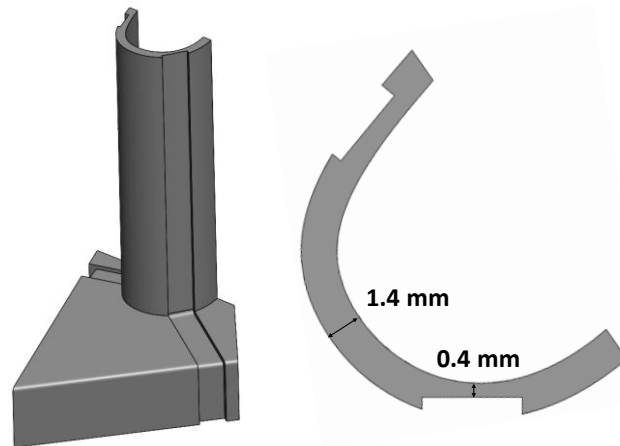
**Table 5-1 Test Matrix of Internal Cooling, Vane, and “Chess Piece” Samples**

Build Sequence	Part Design		Build Layout				Machine Selection			
Parameter Varied	Wall Thickness		Build Direction	Build Location			Layer Thickness		AM Machines	
t [mm]	0.3 - 3.0	0.4 & 1.4	1.4	2	0.4 & 1.4	1.4	-	1.4	-	1.4
r [mm]	15	75 & 112.5	75	0, 75, 145	75 & 112.5	75, 112.5, 187.5	75	75, 112.5, 187.5	75	75
Θ [deg]	90°	90°	0°, 60°, 90°, 120°	90°	90°	0° & 60°	-	0° & 60°	-	0° & 60°
Machine & Layer thickness [μm]	280-1 40	M400-1 40	M290-1 40	M280-1 40	M290-1 40	M400-1 40 & 80	M400-1 40 & 80	M400-1 40 & 80	M290-1 40 M400-4 40 M400-1 40	M290-1 40 M400-1 40
Sample Used										

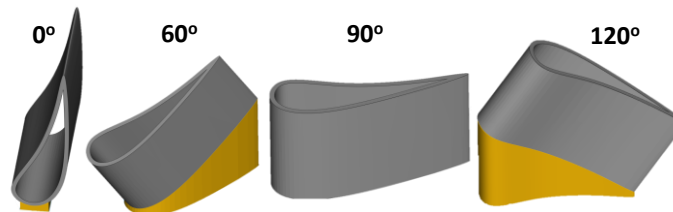
samples. A wire electrical discharge machine was used to remove all the samples in Table 5-1 from their respective build plates. Samples that contained support structures did not have their supports removed.



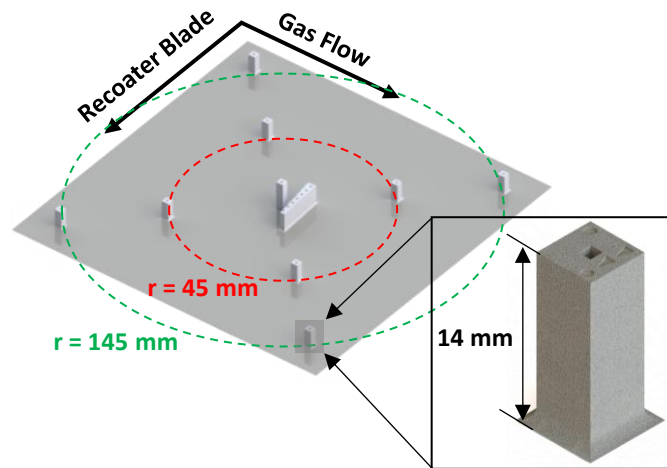
**Figure 5-1. Schematic of vertically oriented sample with square internal cooling channels at different wall thicknesses fabricated close to the center of the build plate.**



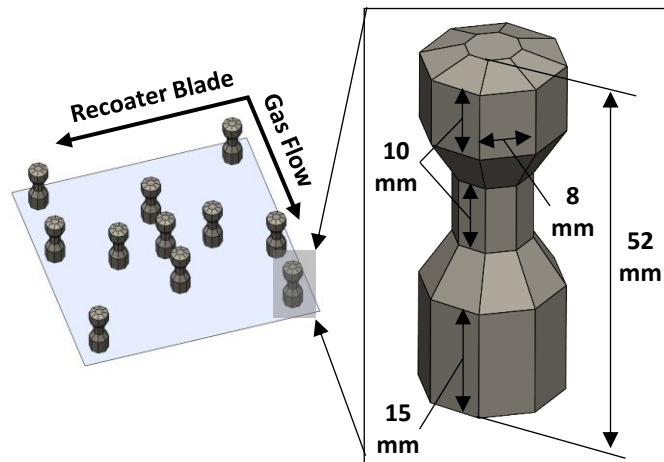
**Figure 5-2. Leading edge NExT vane [97] samples that were fabricated at three different radii from the laser source and contain two different wall thicknesses between the interior and exterior of the leading edge.**



**Figure 5-3. NExT vane airfoils without external and internal cooling fabricated across multiple build directions.**



**Figure 5-4. Schematic of vertically oriented internal cooling square channel samples fabricated on an EOS M280-1 at different radii from the center of the single laser source.**



**Figure 5-5. Build layout of chess piece samples fabricated on different machines using different layer thicknesses.**

### 5.5 Influence of Wall Thickness on Roughness

Evaluating the surface roughness of additively manufactured samples gives insight into the as-built quality of the component and the potential enhancement in heat transfer and pressure loss. The surface of the internal cooling channels in Figure 5-1 were nondestructively evaluated using computed x-ray tomography (CT scans). The surfaces of the channels used for roughness measurements were determined using a commercial software that filters grey scale values obtained from CT scan measurements. The CT scan spatial resolution (i.e. voxel size) of the wall thickness

sample shown in Figure 5-1 was 20 microns. The software is capable of resolving the surface roughness to 1/10<sup>th</sup> of the original voxel size by interpolating the grey scale values [39].

The arithmetic mean roughness, mathematically shown in equation (5-1), was used to characterize the surface roughness for both the internal cooling and vane samples.

$$R_a = \frac{1}{n} \sum_{i=1}^n |z_{\text{surf}} - z_{\text{ref}}| \quad (5-1)$$

The arithmetic mean roughness describes the average deviation of a surface from a reference value. As such, the surface roughness calculated using CT scans was measured by recording the average deviation from the surface relative to a 0.8 mm by 0.8 mm gaussian fitted reference plane. The calculation of arithmetic mean roughness matches the definition for the area averaged arithmetic mean roughness,  $R_a$ . A minimum of five reference planes were fitted to each surface orientation of a cooling channel. The  $R_a$  values of a particular surface orientation (i.e. 6 o'clock) is averaged from using the five planes.

The same five reference planes were also used to calculate the mean roughness depth for the variable wall thickness sample shown in Figure 5-1. The mean roughness depth, mathematically shown in equation (5-2), describes the average difference between the highest and lowest points for the five planes.

$$R_z = \frac{1}{5} \sum_{i=1}^5 (z_{\text{max}} - z_{\text{min}})_i \quad (5-2)$$

Both surface roughness values calculated for each of the channel wall thicknesses shown in Figure 5-1 are reported in Figure 5-6. These results indicate that as wall thickness decreases the arithmetic mean roughness gradually increases. The roughness measurements for a particular surface in Figure 5-6 are accompanied by their 95% confidence interval along with each surface roughness measurement being color matched to the specific surface orientation.

As seen for the 12 o'clock surface in Figure 5-6(a) by changing the wall thickness of a geometry from 3 mm to 0.3 mm, the arithmetic mean roughness increases 231%. In comparison, the 6 o'clock control surface contained a relatively constant surface roughness with a maximum roughness difference of 25% as a result of the constant 2 mm wall thickness. It would be expected that the roughness levels would be similar for the channels in Figure 5-1 since they were all built vertically. However, a higher 12 o'clock surface roughness is observed for the thinner wall channels relative to the channels with thicker walls. The cause for the roughness differences is a result of a higher conduction resistance for the thinner wall channels compared to the thicker wall channels

impacting the heat accumulation causing a disruption to the melt pool leading to more partially melted particles adhering to the solidified surfaces [89]. While the arithmetic mean roughness gradually increases with wall thickness, the increase in surface roughness only begins to become substantial at a thickness below 0.6 mm.

The mean roughness depth,  $R_z$ , for the variable wall thickness sample, Figure 5-6(b), follows similar trends to the arithmetic mean roughness where roughness increases as wall thickness decreases. More specifically, there is a 160% increase in mean roughness depth when changing wall thickness from 3 mm to 0.3 mm. Similar to the arithmetic mean roughness, the 6 o'clock control surface contained a relatively constant mean roughness depth with a maximum roughness difference of 50%.

Also important to note from Figure 5-6 is that there can be a significant difference in arithmetic mean surface roughness for two different walls in a given channel. For example, in channel 1 there is a 77% difference between the 12 o'clock (0.3 mm) and 6 o'clock (3 mm) channel. The amount of variation in surface roughness caused by wall thickness will have a substantial impact to the local convective heat transfer.

The influence of wall thickness on surface roughness for more complicated geometries such as the curved vane leading edge illustrated in Figure 5-2 was also investigated using CT scanning. The same procedure and voxel size for calculating the surface roughness of the internal cooling channel wall thickness sample was used for the roughness measurements of the LE vane samples. More specifically, the same square Gaussian fitted planes as the internal cooling channels were applied along the radial direction of the vane samples in Figure 5-2.

Similar to the results for the channels, the surface roughness increases with decreasing wall thickness for both of the LE vane samples as seen in Figure 5-7. The surface roughness is 51% higher at a wall thickness of 0.4 mm compared to a wall thickness of 1.4 mm for the coupon closest to the laser source. The surface roughness is 30% higher at a wall thickness of 0.4 mm compared to a wall thickness of 1.4 mm for the vane coupon furthest from the laser source. Even though the samples were fabricated at two different build locations, the arithmetic mean roughness measurements show that both samples contain higher roughness levels for the thinner walls.

Investment cast vanes traditionally used in turbines also contain a wide range of wall thickness both between the cooling passages themselves as well as thicknesses of the airfoil. The results from Figure 5-6 and Figure 5-7 suggest that wall thickness can directly impact the as-built surface roughness regardless of surface curvature. These results imply that the surfaces near the trailing edge of a vane, where wall thickness is typically very thin, are expected to have a higher surface roughness compared to other regions of a vane when using AM.

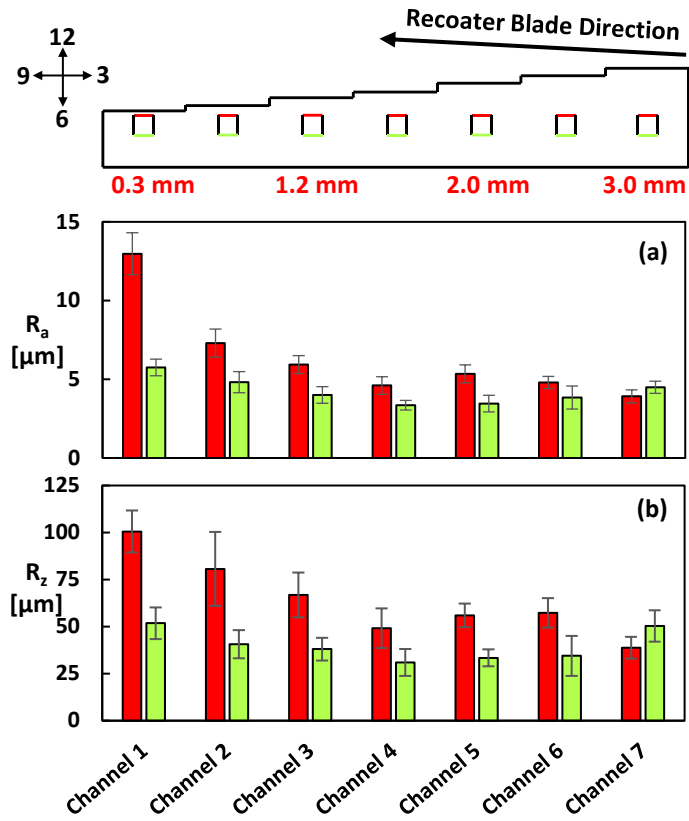
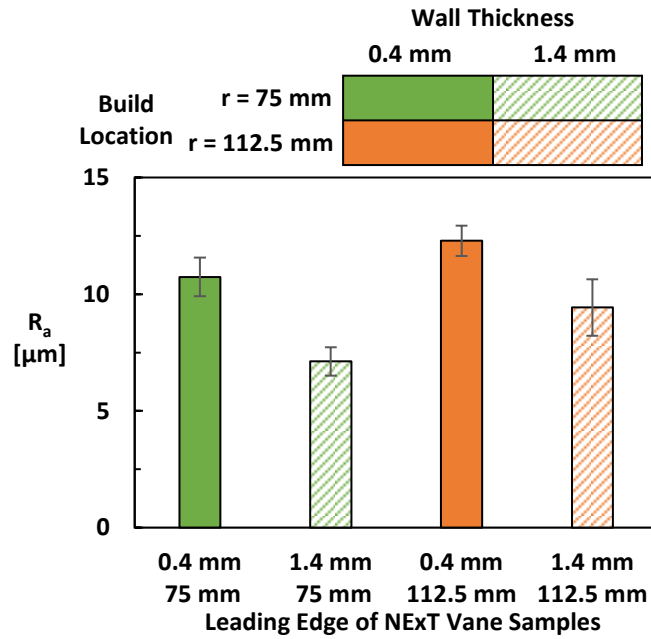


Figure 5-6. Arithmetic mean roughness (6a) and mean roughness depth (6b) of internal wall thickness sample measured from CT scan data of the 6 and 12 o'clock surface orientations.





**Figure 5-7. Arithmetic mean roughness measured using CT scan data of the different wall thickness and build location leading edge NExT vanes samples fabricated on the EOS M290-1 in a 40 micron layer thickness, seen in Figure 5-2.**

### 5.6 Effect of Build Direction on Vane Roughness

The surface roughness, given by equation (5-1), of multiple engine scale vane airfoils printed at multiple build directions was characterized using optical profilometry (OP) to understand the variation in roughness along the length of the curved surfaces of the NExT vanes. Having a direct line of sight to the surface provided the possibility of OP measurements to evaluate the external surface of the vanes in Figure 5-3. OP measurements capture more detail of the surface relative to CT scan measurements because of the higher measurement resolution. When comparing CT scan to OP measurements, Snyder et al. [13] observed that CT measurements show similar trends as OP measurements despite reduced  $R_a$  values using the CT scans. More specifically, CT scans are equivalent to applying a low pass filter to the surface, thus being able to resolve the larger roughness features such as dross compared to the smaller partially melted particles that the OP method is able to resolve.

Multiple 0.8 mm by 0.8 mm sample sizes using OP were taken at 20% span, 50% span, and 80% span of both the suction, leading edge, and pressure side of the NExT vanes. More specifically, the OP measurements were performed using Sensofar S-Neox90, with the focus variation setup. In this measurement mode, an entire Z-range that extends from the lowest valley to the highest peak is scanned. From the scanned images, a 3D image composed of stacked images was compiled and

a 3D image was reconstructed. Images were taken with an objective lens 10X and the surface roughness measurement requirements of 0.8 mm cut-off length, with a L-Gaussian correction was evaluated to meet ISO 4287 standards, after application of a 5x5 median denoising filter.

The  $R_a$  values for the NExT vanes shown in Figure 5-8 indicate that build direction results in as much as a 300% difference depending upon locations on the same vane. The curvature of a vane can result in the local surface containing a range of angles with respect to the build plate. Similar to external and internal surface literature [24,27,30,49], surfaces that are downward facing contain higher roughness levels relative to upward facing surfaces. As the vane orientation increases from  $0^\circ$  to  $120^\circ$ , the roughness of both the leading edge, suction side, and pressure side changes according to the local surface angle with respect to the build plate.

The leading edge portion of the  $0^\circ$  vane in Figure 5-8(a) contains a significantly higher surface roughness compared to the suction side and pressure side of the vane as a result of the downward facing leading edge surface. While not immediately noticeable, the surface roughness of the  $0^\circ$  vane trailing edge suction side is 19% lower compared to the trailing edge pressure side. The cause for the roughness difference is because the surfaces of the suction side trailing edge gradually become upward facing compared to the downward facing surfaces of the pressure side trailing edge due to the curvature of the vane. When comparing the  $0^\circ$  vane to the other orientations in Figure 5-8, the  $0^\circ$  vane has the highest roughness on the leading edge nose. There is minimal difference in roughness on the  $0^\circ$  vane at different span wise locations.

In contrast, the  $60^\circ$  vane in Figure 5-8(b) contains a wide range of roughness levels at different spanwise locations on the suction side and leading edge nose. Surface roughness of the  $60^\circ$  vane is the most non-uniform compared to all other build directions. Surface roughness for the  $60^\circ$  vane is highest at the leading edge nose followed by the suction side then pressure side. The cause for the nonuniformity in surface roughness of the  $60^\circ$  vane is a result of the change in laser incidence angle along the suction side part surface.

Roughness is lowest and most uniform across the airfoil when the leading edge of a vane is parallel to the build direction as seen in Figure 5-8(c). The  $90^\circ$  airfoil contains the lowest surface roughness across the range of build directions evaluated due to the airfoil containing no downward facing surfaces. Since both the external and internal surfaces of the vane share the same  $90^\circ$  build direction, it is speculated that the surface roughness of the interior portion is similar in uniformity as the measured external airfoil surface. The results from Figure 8(c) infer that when all the curved surfaces share the same build direction in this case  $90^\circ$ , the differences in surface roughness are minimal; however, for the build directions other than  $90^\circ$ , the interior surface of the airfoils are different from the exterior. For example, the leading edge external surface roughness of the  $60^\circ$

vane is highest relative to other external locations. While the interior portion of the leading edge 60° vane was not measured, the surface is upward facing which will most likely result in a lower roughness relative to the downward facing external surface of the leading edge airfoil. The exterior surfaces of the vanes in Figure 8 that are upward facing contain interior surfaces that are downfacing.

By orienting the leading edge of a vane to 120° from the build plate, surface roughness increases from the leading edge to the trailing edge of the pressure side and varies little across the spanwise locations as in Figure 5-8(d). The cause for the increase in roughness is attributed to the curvature of the airfoil, more specifically the downward facing surfaces of the pressure side relative to the upward facing surfaces of the leading edge nose and the area near the leading edge of the suction side. The roughness distribution across the airfoils between the 0°, 60°, and 120° samples emphasizes the importance of the local surface angle of a curved surface.

Even though the 90° build for the vane is the most optimal in terms of the lowest external roughness, it is important to note that no cooling features were present in the sample for the data in Figure 5-8. A full additively made vane at the 90° leading edge build direction would most likely require trailing edge cooling passages needing a geometry correction since the cooling passages would be fabricated parallel to the build plate. Furthermore, multiple external supports would be needed to minimize deformation of the fir tree since these features have a high possibility of being built parallel to the build plate when the leading edge is at 90°.

By orienting the vane to 0°, 60°, or 120°, internal passages at the trailing edge are most likely to contain less severe downward facing surfaces and require less geometric corrections relative to the 90° vane. Designers must also consider the orientation of cooling passages at the leading edge and mid region of vanes. A combination of geometry and local surface orientations need to be considered for desired external and internal surface roughness when orienting a curved component.

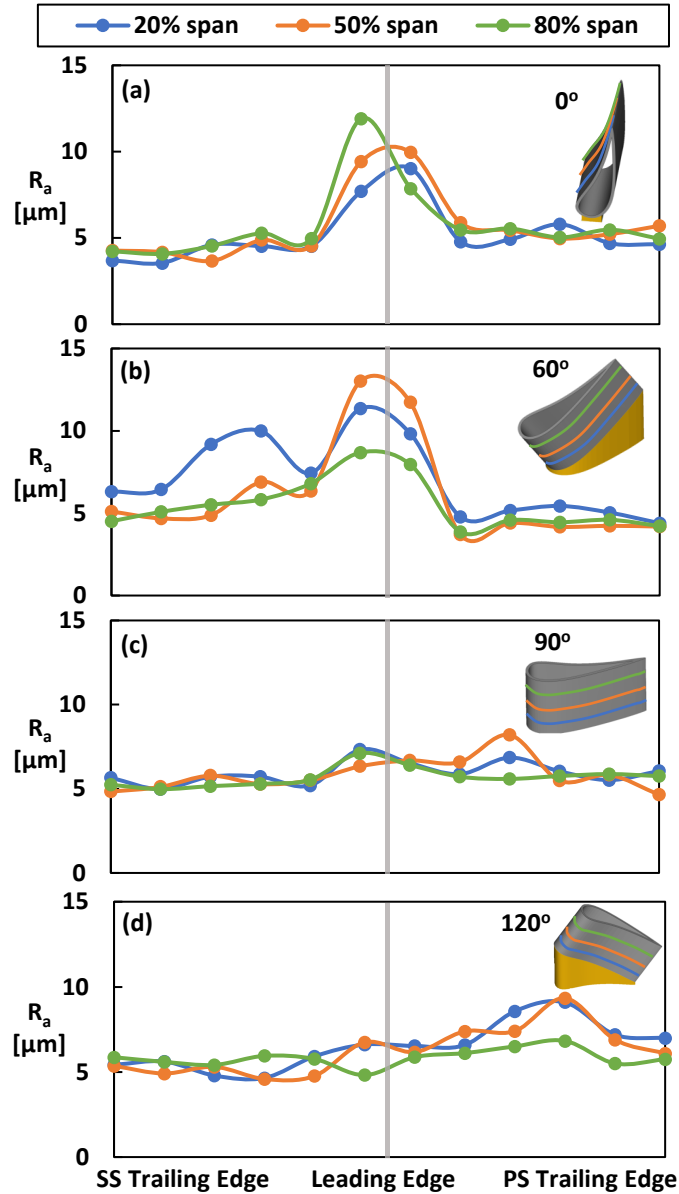


Figure 5-8. Arithmetic mean roughness measured using an optical profilometer across the pressure side, suction side, and leading edge NExT vane airfoils printed at 0° (8a), 60° (8b), 90° (8c), and 120° (8d) on an EOS M290-1 at a 40 micron layer thickness.

### 5.7 Impact of Build Location on Roughness

The roughness values of the internal cooling channel samples at different build locations in Figure 4 were analyzed using the same CT scan roughness procedure outlined for the internal channel wall thickness sample. The voxel resolution for the internal cooling channels at different build directions was lower, 15 microns, compared to the channel wall thickness sample because of a smaller scan area. Contours of  $R_a$ , calculated using equation (5-1), changing with build location

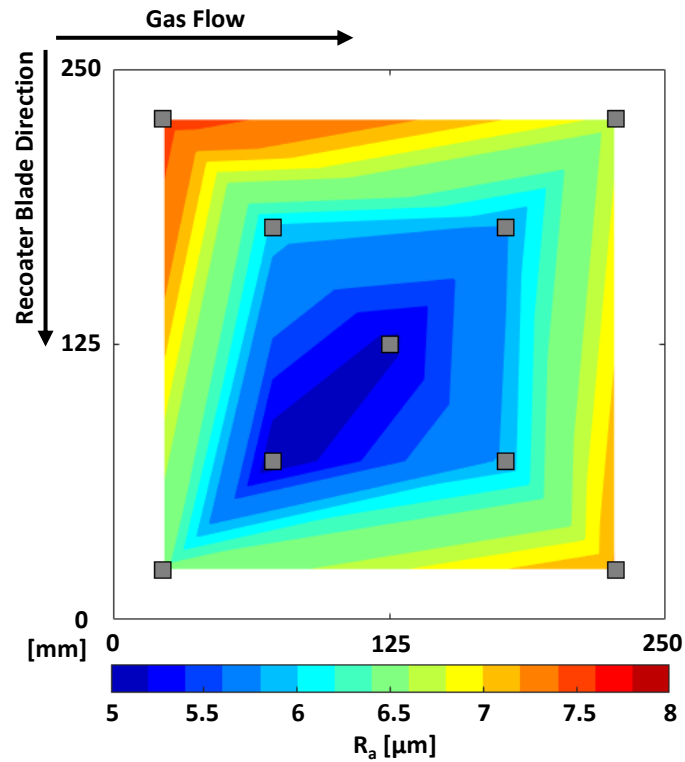
is shown in Figure 5-9. The grey squares in Figure 5-9 represent the exact location and surface orientations of the vertically built square cooling channels on the build plate. The roughness contour is linearly interpolated between the average surface roughness from all surfaces in each of the square internal channels at different build locations. More specifically, the roughness for each sample is averaged using five 0.8 mm by 0.8 mm planes fitted to each side of the square cooling channels.

Similar to external flat surface literature [20,72,96], build location has a considerable impact on the surface roughness for internal surfaces as seen in Figure 5-9 and Figure 5-10. As components are built further from the laser source (i.e. center of build plate for EOS M280-1) the surface roughness increases. Quantitatively, there is a 10% increase in roughness from the center of the build plate to a radial distance of 75 mm. While the roughness is 35% higher from the build plate center to a radial distance of 145 mm. The change in laser incidence angle relative to the part surface causes the melt pool dynamics to change depending on build location resulting in the as-built surface roughness to increase the further the part is from the laser source [17,72]. The results from Figure 5-9 show that it is possible for the surface roughness to become nonuniform for very large parts because of the change in laser incidence angle along the length of the part. The increase in roughness is observed regardless of the proximity the channel is to the origin of the gas flow and beginning of the recoater blade process. With the addition of more samples on the build plate in Figure 5-9, the as-built surface roughness from a particular machine can be recorded.

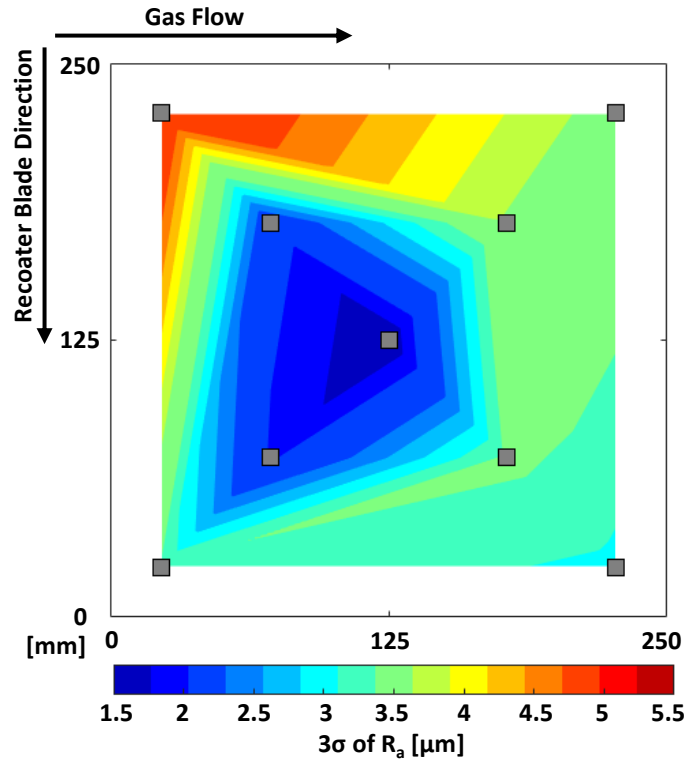
The variation in surface roughness also increases the further a part is from the laser source as seen by the standard deviation contour of arithmetic mean roughness in Figure 5-10. On average there is a 79% increase in the  $3\sigma$  deviation when an internal surface is at the center of the build plate to when the surface is at radial distance of 75 mm from the center. Whereas there is a 142% increase from the center of the build plate to a radial distance of 145 mm. The implications of these results are that internal surfaces are lower in roughness and are more reproducible the closer the part is to the laser source.

The LE vane samples in Figure 5-7 share the same roughness trends of the internal cooling channels in Figure 5-9, where the roughness increases the further the part is from the laser source. It is important to acknowledge that the roughness trends match even though the LE vane and channel samples were built on separate EOS machine models and the geometries of the parts are different. When comparing the two LE vane samples with different wall thickness in Figure 5-7, there is a 14% increase in roughness between the LE vane sample at a radial distance of 75 mm relative to 112.5 mm for the 0.4 wall thickness. Similarly, there is a 32% increase in roughness for the 1.4 mm wall thickness region between 75 mm to 112.5 mm sample location.

Recall that for a given build location of the LE vane samples, surface roughness was still influenced by wall thickness. These results suggest that a combination of wall thickness and changes in build location contributed to the differences in as-built surface roughness of the LE vane samples. For cooling applications using AM, the results from Figure 5-7 and Figure 5-9 show that surface roughness of a component can be altered by changing the build location. The added roughness from moving a part further from the laser source can most likely increase the convective heat transfer with the cost of additional pressure loss for cooling channels. Additionally, the surface of the part will become less uniform the further it is from the laser source.



**Figure 5-9. Build plate contour of average arithmetic mean roughness measured using CT scan data from the four internal surfaces of the square cooling channel.**



**Figure 5-10. Build plate contour of the  $3\sigma$  deviation of arithmetic mean roughness measured using CT scan data from the four internal surfaces of the square cooling channel.**

### 5.8 Effect of Layer Thickness and Machine Type

The surface roughness,  $R_a$ , at multiple surface orientations of the chess piece in Table 5-1 are given by Figure 5-11 using the OP method. Each chess piece that was fabricated at each of the four quadrants (Q1, Q2, Q3, Q4) in the four laser M400-4 are colored coded in Figure 5-11. Each surface roughness bar in Figure 5-11 represents the average roughness of over 80 roughness measurements. In more detail, 11 OP measurements were made for each side (total of eight) of the chess piece sample. The error bars in Figure 5-11 represents the 95% confidence interval of the averaged roughness data.

Results from Figure 5-11 indicate that there is a minimal difference (less than 1 micron) in surface roughness at every surface orientation for the four samples printed using the different lasers in the M400-4 machine. It is important to note that the samples printed at each of the four queens in the M400-4 shared the same radial distance from the laser source.

Similar to layer thickness trends in literature [90], the surface roughness is greater at a 80 micron layer thickness relative to a 40 micron layer thickness as seen in the external surfaces of the chess piece samples in Figure 5-11. On average, the arithmetic mean roughness for the 80 micron layer

thickness is 1 to 13 microns higher compared to the 40 micron layer thickness for all surface orientations, except the downskin 60°, of the chess piece created using the M400-1 machine.

For all the surface orientations evaluated across the chess piece samples that were made using the different machines, surface roughness was typically the highest on the 60° downskin followed by the 20° upskin, 60° upskin, 90° vertical, then 0° horizontal surface orientations. The only machine that did not follow this trend was the M400-1 for an 80 micron layer thickness. The surface roughness of the M400-1 80 micron layer thickness is higher for the 20° upskin surface compared to the 60° downskin surface. After further investigation, the cause is a result of the stair stepping effect, which was exacerbated due to the 80 micron layer thickness relative to a 40 micron layer thickness, that led to an increase in roughness for the 20° upskin surface compared to the 60° downskin surface.

It is clear from the results in Figure 5-11, that the surface roughness across all three machines (M290-1, M400-1, M400-4) for a 40 micron layer thickness are very similar with less than a 5 micron difference. Some surface orientations such as the upskin 20°, upskin 60°, and vertical 90° are less than a 2 micron difference between the 40 micron layer thickness machines. The small difference in roughness level highlights that the machine induced surface roughness variation is minimal on flat surfaces. In comparing the roughness of the single laser machines at a 40 micron layer thickness (M290-1 and M400-1), the roughness is 16-28% lower for the M290-1 compared to the M400-1 for all surface orientations except for the horizontal 0° surface orientation. The surface roughness values across all build orientations were 13-51% higher for the single laser M400-1 chess piece sample compared to the four samples created at the different quadrants using the multi-laser M400-4.

The surface roughness was also evaluated for the 0° and 60° full NExT vane created using different AM machines (M400-1 and M290-1), different radial build locations (75 mm, 112.5 mm, 187.5), and different layer thickness (40 micron for the M290-1 and 40/80 micron for the M400-1). The mid-span OP measurements in Figure 5-12 followed the same measurement method as the vanes in Figure 5-8. The roughness trends from the pressure side to suction side of the airfoil for the 0° and 60° vanes in Figure 5-12 are mostly similar regardless of machine used. Near the leading edge nose for the 0° and 60° vane the surface roughness is highest due to the surface being downfacing compared to the surfaces of the suction side and pressure side. Furthermore, the surface roughness differences between the leading edge and suction and pressure side are due to the complex angles of the laser to the surface and the local scan pattern adjustments done to



accommodate for the local curvature. This effect would require more detail to understand the role of extreme curvature on surface roughness values.

Similar to the internal channel roughness results in Figure 5-9 and the LE vane samples in Figure 5-7, the surface roughness for a vane increases the further it is built from the laser source regardless of build direction and layer thickness as seen in Figure 5-12. These results further support that the distance from the surface to the laser source is a major influence to roughness.

Similar to the flat surface chess piece samples, the surface roughness for the 60° vane with an 80 micron layer is higher compared to its 40 micron equivalent using the M400-1. However, the peak roughness value for the 80 micron layer thickness is near the leading edge pressure side while the peak roughness value for the 40 micron process is near the leading edge suction side. The cause for the discrepancy could be a result of the differences in layer thickness causing a more prominent stair stepping effect to occur. When comparing layer thicknesses for the 0° vane in Figure 5-12(a), the surface roughness is lower for the 80 micron process compared to the 40 micron process of the M400-1. Again, the cause for the result is the difference in layer thickness impacting the stair stepping effect for the specific surface orientation as well as differences in process parameters used for the two layer thicknesses.

Matching the same roughness trend for the M400-1 and M290-1 flat chess pieces surfaces in Figure 5-11, the surface roughness for the 0° and 60° vanes with a 40 micron layer thickness printed at different build locations is higher for the M400-1 compared to the M290-1. For the build plates of the vanes and chess pieces, surface roughness appears to be higher using the M290-1 compared to the M400-1.

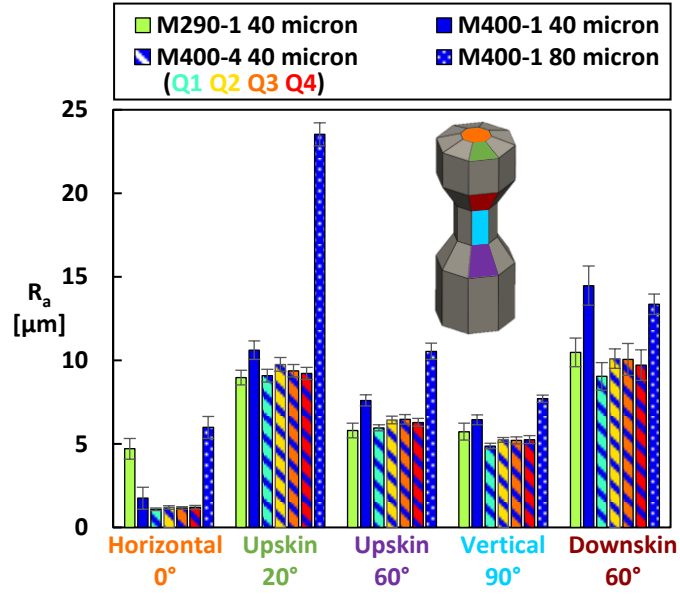
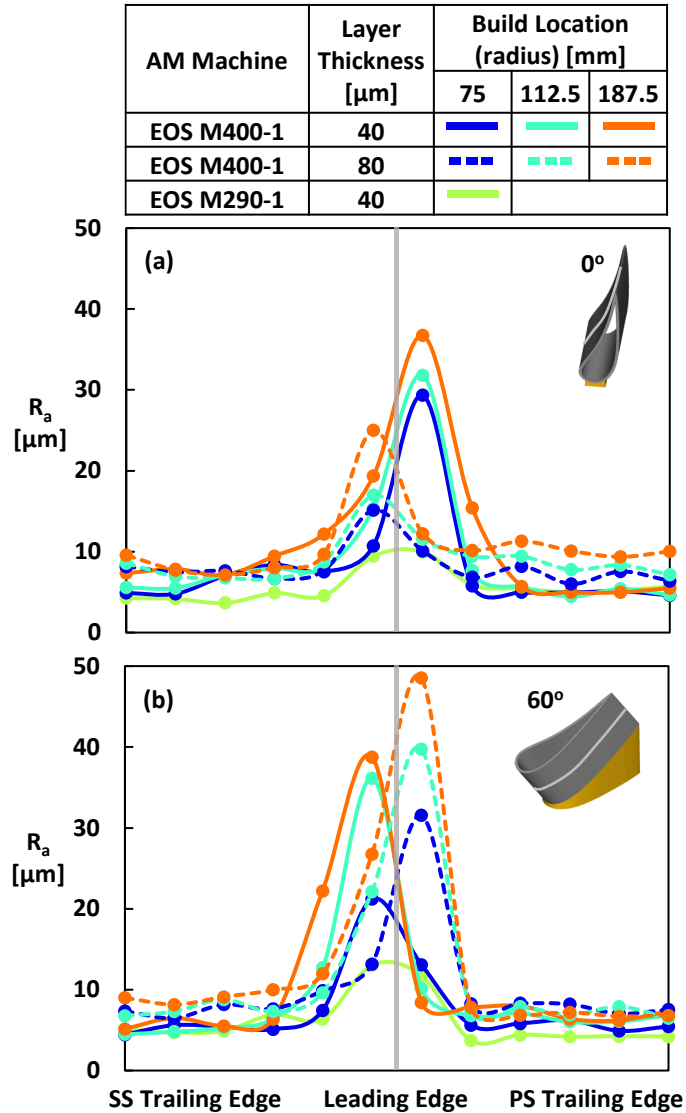


Figure 5-11. Average of 88 arithmetic mean roughness values for each surface of the “chess piece” fabricated using two different single laser machines, two layer thickness, and a four laser machine.



**Figure 5-12. Arithmetic mean roughness using an optical profilometer across the pressure side, suction side, and leading edge of the NExT vane airfoils fabricated at the 0° (12a) and 60° (12b) build direction using different AM machines, build locations, and layer thicknesses.**

### 5.9 Conclusion

Multiple engine relevant samples were fabricated using DMLS to investigate the influence the additive build sequence, spanning part design, build layout and machine selection, has on the as-built surface quality of engine scale vanes, cooling channels, and simple external surface samples. Specifically, the samples were fabricated with a variety of wall thicknesses, build directions, build locations, layer thicknesses, and different AM machines. CT scanning and optical profilometry was

used to measure surface roughness in order to characterize the as-built surface quality of the vane and cooling channel samples.

Roughness results from vanes and cooling channels with varying wall thickness, show that that changes to the geometry of a component, specifically the wall thickness, can impact the surface roughness. As wall thickness decreases the surface roughness increases for both vanes and simple square cross-section channels. The surface roughness of the channels begins to substantially increase at wall thicknesses below 0.6 mm.

The full airfoil of the NExT vane was fabricated across four distinct build directions. The surface roughness was uniform across the spanwise locations for the vanes fabricated with the leading edge at the angle of 0°, 90°, and 120° from the build plate. For several build directions, the curvature of the airfoils resulted in varying levels of surface roughness across the pressure side, suction side, and leading edge of the airfoil. Designers additively fabricating vanes should consider the local surface orientations on the airfoils and the build directions of the internal passages.

The location of samples on the build plate has a direct influence on surface roughness. Both cooling channels, the leading edge portion of the NExT vane, and full NExT vane airfoil were fabricated at different radii from the laser source. For both sets of samples, the surface roughness increases the further the sample is from the laser source. Even with some samples containing changes to wall thickness and build direction, the trend of increasing roughness with increasing distance from the laser source was observed.

Several test samples with external surface resembling a “chess piece” and a full vane at two different build directions were fabricated on different EOS machines using two different layer thickness (40 and 80 microns) along with single and multi-laser setups. Surface roughness was higher in the 80 micron layer thickness relative to the 40 micron layer thickness for most surface orientations of the vanes and the chess piece samples. There were minimal variations in surface roughness between samples fabricated at different quadrants of a four laser EOS M400-4 machine. Roughness for multiple samples was higher for a M400-1 relative to a M290-1 in a 40 micron layer thickness.

Findings from these AM studies and those in the future will continue to advance metal AM to produce repeatable complicated geometries. Understanding the major factors that affect surface roughness for each build sequence in the general AM process is important for the reproducibility and fabrication of vanes and cooling channels. The results from this study indicate that the major influences on surface roughness for flat and curved surface samples at a given layer thickness are build location, build direction, and wall thickness.

## 6 Variability in Additively Manufactured Turbine Cooling Features<sup>6</sup>

### 6.1 Abstract

Additive manufacturing (AM) allows for the rapid fabrication of complex components relative to conventional fabrication methods aiding in the development and testing of advanced turbine cooling methods. The repeatability of printed geometric features in the same part is required to maintain part quality, flow, and heat transfer. It is widely understood as to the impact that the additional roughness of AM provides with regards to part quality, but part variability also leads to differences in performance either locally in considering a single airfoil or globally when considering an entire stage. Previous studies have shown the importance of certain process parameters, build directions, and feature sizes on the part quality when printing a part using AM. As processes have continued to evolve, other artifacts of AM have arisen such as the location on the build plate. This article highlights the progress that has been made on printing commonly used cooling features by either considering simple straight coupons or a curved vane leading edge. Also discussed is the variability that exists and the resulting convective heat transfer and pressure losses. Results indicate that the variation of roughness between components and the part-to-part variations increased the further the component was from the laser source on the build plate. Similarly, the variation and levels in the pressure loss and heat transfer of the cooling channels also increased when samples were placed further from the laser source on the build plate.

### 6.2 Introduction

Advanced manufacturing techniques such as metal additive manufacturing (AM) provide a platform for rapid prototyping and advancing the feasibility of complex designs relative to traditional subtractive or casting fabrication methods. Specifically in this paper, we are referring to parts made through direct metal laser sintering; however, we will use the term AM. AM provides significantly shortened manufacturing times for components and provides opportunities for enhanced design freedom, reduction in part numbers, and reduced development costs relative to conventional fabrication methods. Metal printing techniques, such as direct metal laser sintering, require unique manufacturing and design considerations to produce consistent part tolerances, surface roughness, and overall component quality. The range of geometric tolerances that an additive part can experience becomes an important factor when making turbomachinery components with the goal for rapid prototyping and testing. Consequently, understanding the

---

<sup>6</sup> Wildgoose, A.J., and Thole, K.A., 2023, "Variability in Additively Manufactured Turbine Cooling Features," *Recommended for Journal of Global Power and Propulsion Society*.

amount of variability in overall part design and the effect on the performance of cooling schemes between parts gives insights into the deviation from design intent and overall variability in cooling performance.

This article provides an overview of the state of AM component manufacturing with a focus on turbomachinery components and cooling designs. In more detail, this article examines the: i) manufacturing variation of simple cooling designs; ii) variability and reproducibility of engine scale vanes; and iii) implications of part consistency on convective heat transfer and flow losses. This article pays particular attention to the printability of small-scale cooling features such as film cooling holes and channels over time as technology advancements in the AM process has occurred.

### **6.3 Causes for Geometric Variation of Additively Manufactured Components**

The additive manufacturing process, specifically direct metal laser sintering, is a layer by layer manufacturing process whereby a layer of powder is deposited on to a substrate referred to as a build plate. A laser then selectively melts the powder to form a liquid pool of metal, which then solidifies following the design intent profile of a component. The process is repeated until the component is fully sintered [98]. More detail of each specific process is reported by Frazier [99]. After the part is built, post-processing actions such as heat treatments are performed to reduce residual thermal stresses and alter material properties [11]. Changes and instabilities to the shape of the melt pool directly impacts the magnitude and variation of surface morphology and structural properties within an AM component as described by Feng et al. [100] and Wang et al. [101]. Several factors that contribute to the shape of the melt pool, which in turn affect the surface morphology and deviation from design intent, include surface orientation (build direction), laser processing parameters, support structures, and the distance the part is from the laser source (laser incidence angle) for a given material [17,37,72,102].

Build direction has been reported by many to be a dominating effect on part quality due to additional material being sintered for surfaces that are downward facing [24]. For circular cooling channels, Wildgoose et al. [49] showed that the standard deviation in hydraulic diameter increased by more than 50% when orientating a vertically built channel relative to the horizontal orientation. Similarly, Snyder et al. [22] showed that the circularity, internal surface roughness, and concentricity of a circular channel also changes as a function of build direction.

Data in the literature also shows that when a part shares the same position on different build plates, surface morphology and part geometry can vary between components [103] and [104]. Gradl et al. [105] extensively reported on the part-to-part variation of different geometries including thin walls, holes, hollow and protruding cylinders. Relative geometric error

decreased with increasing feature size, which is similar to results for circular channels from Wildgoose et al. [49]. Regardless of the part geometry, all components from Gradl et al. [105] contained deviations from their design intent.

Variations from the design intent are also present even when multiple samples are built on the same build plate. A contribution to the variation of components within a build plate is related to the location of a part on the build plate. The cause for the positional dependency is a result of the interaction between the angle of the laser beam and powder, this angle is called the laser incidence angle. The work of Kleszczynski et al. [17] highlighted that surface roughness increases the further a sample is from the laser source. Both Sendino et al. [20] and Subramanian et al. [72] support the positional dependency and present relationships between roughness and laser incidence angle through different calibration and benchmark test pieces.

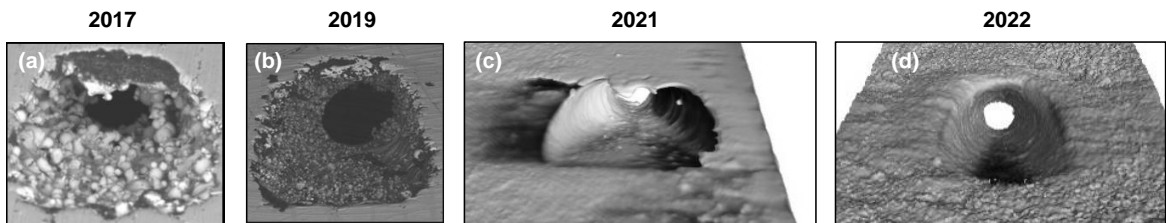
#### **6.4 Progress in Using AM to Manufacture Turbine Cooling Features**

Since the AM process has been embraced by turbine manufactures for rapid development of components, there has been significant progress in the AM technology itself. While this section is not a comprehensive review of all the improvements that have been made to the AM processes, it does focus specifically on how research has improved the printability of geometric features over time. Driving these improvements is the ability required to replicate complex features of hot section components such as vanes, that benefit from the reduced lead time and cost relative to conventional manufacturing methods. Common cooling designs implemented in turbine airfoils include external cooling such as film cooling and internal cooling such as pin fins, ribs, and channels [106]. Within the additive cooling field, there has been considerable research to characterize both traditional internal and external cooling designs as well as designs utilizing the design space offered through AM such as lattice structures [46] and wavy channels in the work of [48,107].

One of the early additive film cooling studies by Vinton et al. [108] and Jackowski et al. [109] showed the ability of AM to produce the millimeter sized features and highlighted the impact of surface roughness from the AM process on overall cooling effectiveness. Stimpson et al. [110] expanded upon the work in terms of characterizing the deviation from design intent as well as an overall cooling effectiveness comparison between AM and traditionally manufactured electric discharged machined film cooling holes. The study reinforced that build direction and hole size are important factors toward hole blockage and printability.

Film cooling holes are especially challenging to fabricate using AM due to the scale of the hole; however, there has been significant advances in AM technology over time as seen in Figure 6-1. Scanning electron microscope images from Stimpson et al. [110] in Figure 6-1 show the

severity of the in-hole roughness and deformation. As AM continued to advance through a better understanding of the interaction between laser parameters and surface roughness, AM vendors have been able to more accurately produce engine-scale film cooling holes as seen from the progression of 2017 to 2022 in Figure 6-1. More specifically, the film cooling holes in Figure 6-1 were fabricated using the same EOS M280-1 machine overall several years. The 2017 hole in Figure 6-1 (a) exhibits the most protrusions in the flow field relative to the other film cooling holes, while the most recent hole Figure 6-1 (d) shows the least amount of protrusions and roughness features. Furthermore, with the improvement in machine parameters several studies such as Gutierrez et al. [111] have shown the ability to produce highly complex adjoint optimized holes on flat coupons. Airfoils, however, remain challenging for AM given the thin walls and wide range of local surface orientations.

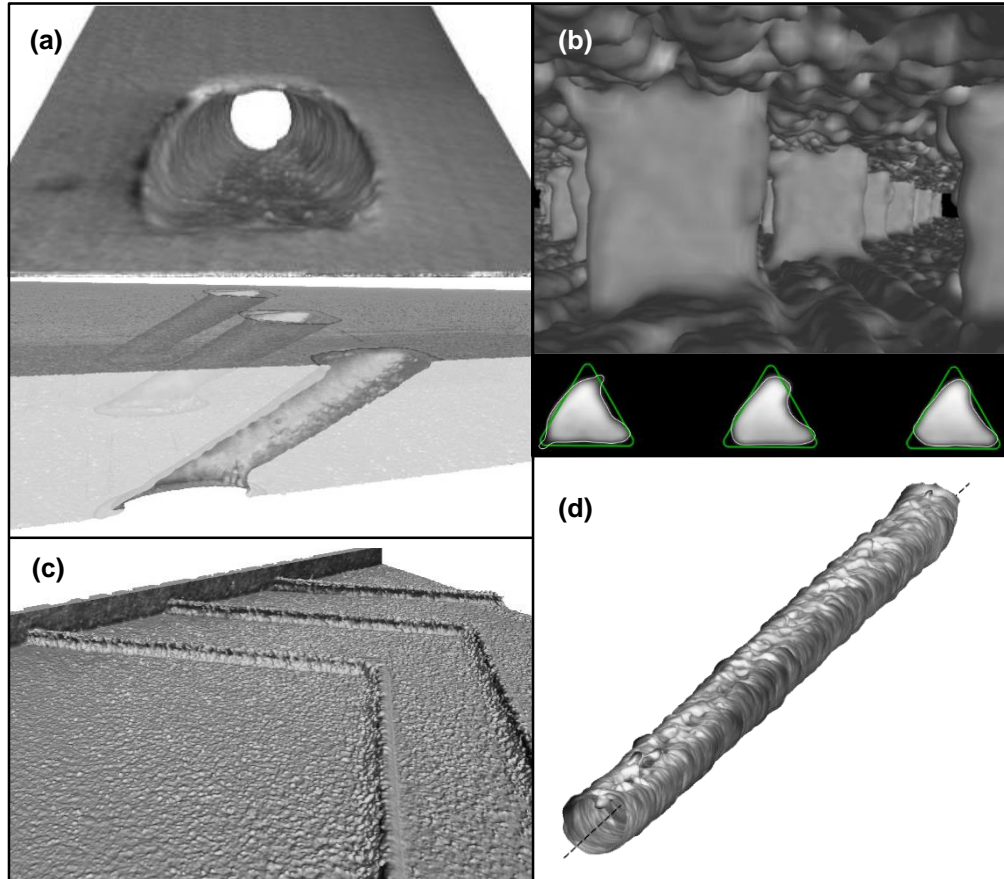


**Figure 6-1 Quality of additively manufactured film cooling holes (a) (Stimpson et al., 2018), (b) (Snyder and Thole, 2019), (c) (Veley et al., 2022), (d) film cooling hole from this study highlighting the improvement in printability over several years.**

As seen from the nondestructive computed tomography (CT) scans in Figure 6-2, there is a range of roughness and deviation from design intent for the external (film cooling hole in Figure 6-2 (a)) and internal cooling designs (pin fins, ribs, and cooling channel in Figure 6-2 (b,c,d)). It is commonly known that the surface deformations in a cooling hole can be reduced by changing the build direction.

For the film cooling hole in Figure 6-2 (a), in-hole roughness is lowest when orienting the metering section of the film cooling hole perpendicular to the build plate [110]. Downward facing surfaces result in unsupported surfaces that cause additional melted material. The additional melted material causes hole blockages and large protrusions in the flow field that reduce the minimum cross-sectional area which ultimately limits the mass flow exiting the cooling hole for a given pressure ratio.





**Figure 6-2 Computed Tomography scans highlighting the print quality of (a) film cooling holes, (b) pin fins from Ferster et al. (Ferster et al. , 2017), (c) ribs , and (d) cooling microchannels from Snyder et al. (Snyder et al., 2015).**

The range of deviation between the design cross-sectional cooling hole area to the minimum cross-sectional area has been reported to be as high as 33% when the hole metering section is aligned perpendicular to the build plate and as high as 75% when the metering section is at a build direction other than being perpendicular to the build plate [110,112]. In some cases, at angles where the film cooling holes are less than 45° between the metering section axis and the build plate the holes have been shown to be completely blocked [110]. When examining the variation from hole to hole for a given part, Veley et al. [112] observed that variation from the design intent between holes depends upon the film cooling hole design.

The same AM build factors that affect the printability of film cooling holes have also been shown to impact the quality of pin fins produced through AM as seen in Figure 6-2(b). The pin fin from Ferster et al. [113], in Figure 6-2(b), shows the severe amount of deformation that can occur for a triangular pin fin that has surfaces downward facing, in this case some surfaces were built parallel to the build plate. When qualitatively observing the variation from pin to pin in Figure

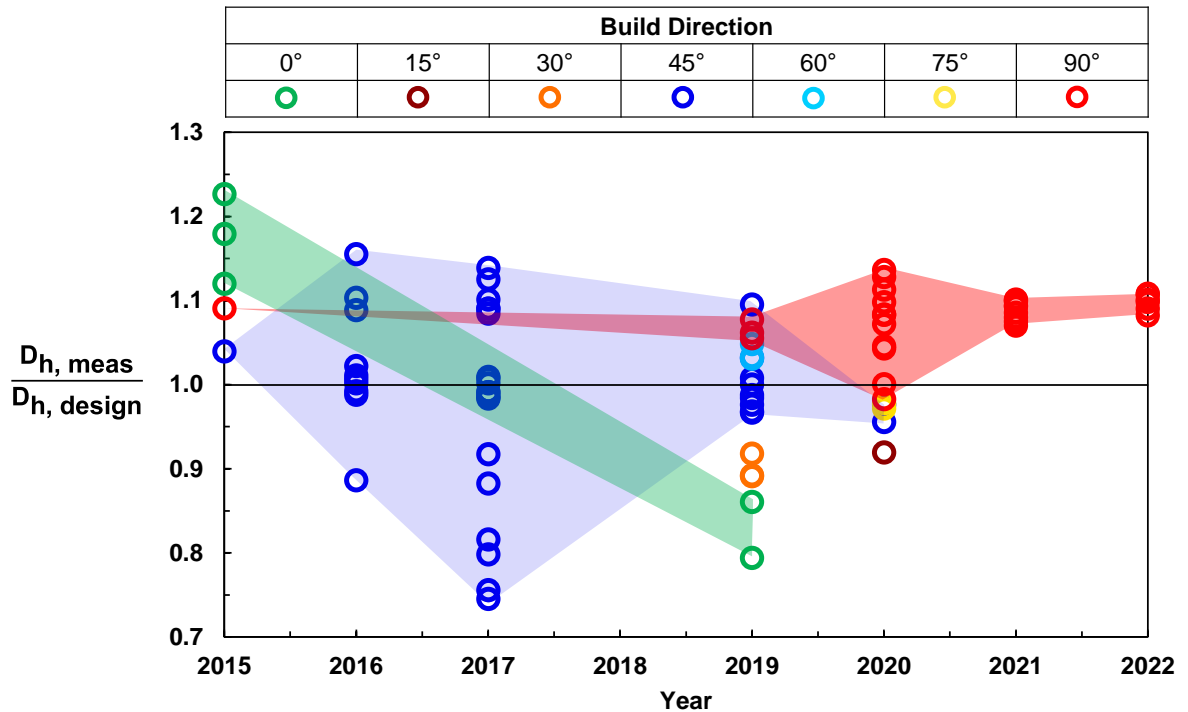
6-2(b) there is not an immediately noticeable difference in cross-section between pin fins. The work of Ferster et al. [113] and [114] showed that changes to geometry of a pin fin, such as going from a circle to a star, can mitigate deformation caused by downward facing surfaces, however similar to the triangular pins in Figure 6-2(b), there is minimal change in tolerances qualitatively between pin fins for a given pin design.

Despite ribs, seen in Figure 6-2(c), being prominent in modern turbine airfoils, there has been little focus toward characterizing the geometric deviations of ribs made through AM. These characterizations continue to be important for turbine applications and more research is needed. The work by Chen et al. [115] investigated the cooling performance of various engine scale rib designs in a two pass rectangular duct, even though AM was used to fabricate the part the rib features were machined to the desired geometry. Searle et al. [116] used the as-built form of the ribs to investigate the cooling performance of ribs and dimple configurations, however the study did not characterize the tolerances or comment on the quality of the ribs.

A significant portion of literature has focused on the deviation from design intent and geometric tolerances for micro-sized channels ranging in diameter from 500 $\mu\text{m}$  to 1250  $\mu\text{m}$  as seen in Figure 6-1(d), more so than other internal features. Similar to the film-cooling hole, the angle at which the channel is relative to the build plate impacts the resulting tolerances and geometry. Snyder et al. [22], Minear et al. [23], Wildgoose et al. [49], Kamat and Pei [31], and Kasperovich et al. [117] showed that cooling channels built perpendicular to the build plate result in the lowest surface roughness and deviation from design intent. Wildgoose et al. [49] showed that for a circular channel fabricated at different build directions, the standard deviation in hydraulic diameter increases 166% when going from a channel built perpendicular to parallel with the build plate. Kasperovich et al. [117] accounted for these differences due to build direction by altering the geometry as well as laser scan parameters to produce favorable tolerances for a range of build directions. Less complex changes to the geometry of the cooling channel such as implementing a teardrop correction for circular channels has also been shown to produce circular channels without severe deformations as in the case of Kamat and Pei [31] and Snyder et al. [22].

Similar to the improvement in film cooling hole printability over time in Figure 6-1, the quality of cooling channels, in terms of replicating the design hydraulic diameter, has also improved over time as indicated in Figure 6-3. Figure 6-3 shows the difference between the measured hydraulic diameter to that of the design intent for cooling channels built using a variety of AM machines (EOS M280-1 and EOS M290-1) at different build directions reported in literature over several years [30,33,49,83,85,102,118]. The samples in Figure 6-3 includes a variety of materials, channel cross-sectional shapes, channel sizes, and laser process parameters. Immediately

noticeable is that the spread in hydraulic diameter for the 45° build direction is less when going from 2015 to 2019. Additionally, the same is true for the 90° channels between 2019 and 2022.



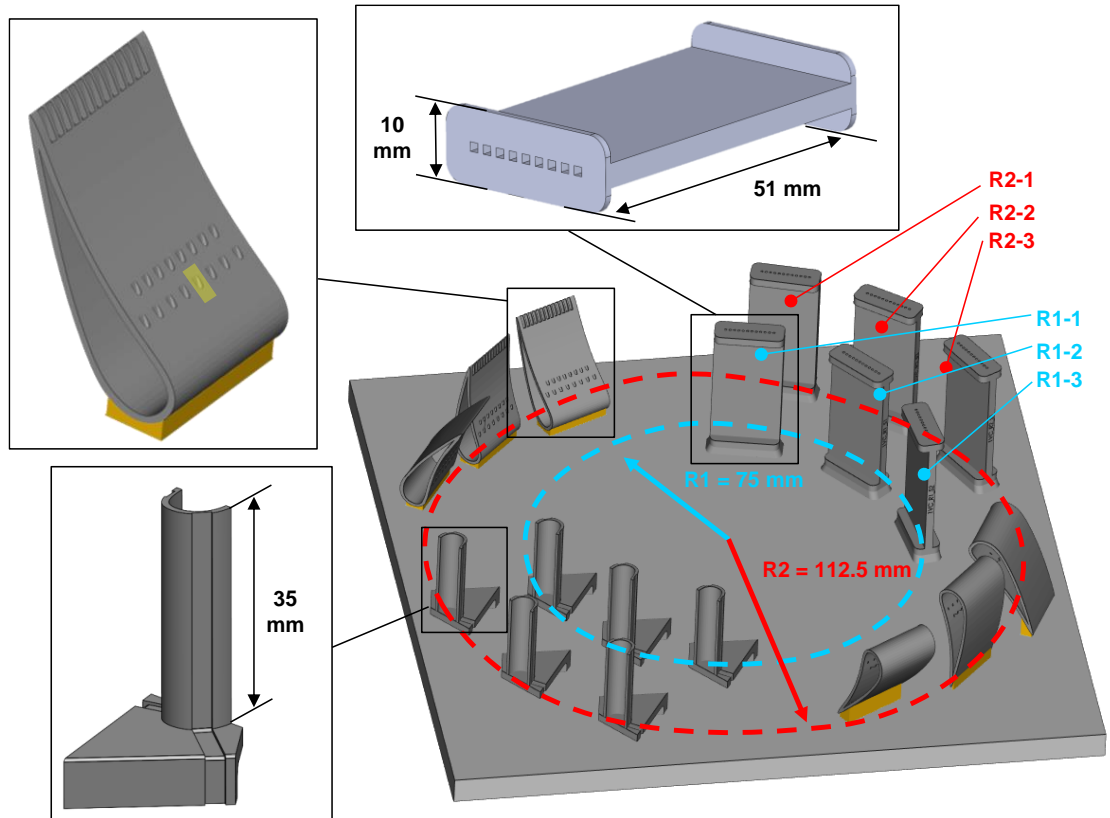
**Figure 6-3 Deviation from design intent hydraulic diameter of microchannels in literature at a variety of build directions (Stimpson et al., 2016c, 2016a; Kirsch et al., 2017; Dahmen et al., 2020b; Wildgoose et al., 2021b, 2022; Alexander J Wildgoose and Thole, 20**

### 6.5 Roughness and Geometry Variability of Simple Channels due to Build Plate Location

As the AM technology has continued to evolve over time, research has gone beyond identifying the most primary effects on as-built geometry such as feature size and build direction, new issues have evolved such as part reproducibility. Especially since part reproducibility is critical in turbine components to ensure expected flow distributions and part temperatures. As a result, several cooling channel coupons were fabricated to investigate the variability in geometry and roughness at different build plate locations. More specifically, square microchannel coupons with a  $D_h = 1.25$  mm were fabricated multiple times on a build plate at two different radial build plate locations, as seen in Figure 6-4. The coupons were made using Inconel 718 with a 40 micron layer thickness. The coupons were fabricated at a radial distance of  $R1 = 75$  mm and  $R2 = 112.5$  mm from the center of the build plate (laser source) as seen in Figure 6-4. Each leading edge vane and microchannel sample design was printed three times at each of the radial build locations in Figure

6-4. To mitigate surface deformation caused by build direction, the channels were fabricated with their streamwise axis perpendicular to the build plate. The samples were fabricated using standard manufactured recommended laser process parameters on a single laser EOS M290-1 machine and with EOS recommended post processing heat treatment parameters [34]. Furthermore, the Inconel 718 powder was sieved through a filter to a 40-micron nominal powder size.

Hydraulic diameter was characterized for the cooling coupons in Figure 6-4 using computed tomography scanning. The deviation from design intent hydraulic diameter for each square channel samples at the two radii's is shown in Figure 6-5(a). The naming convention of for each of the samples lists the radius they were fabricated at and then the sample number (i.e. R1-1), as shown in Figure 6-4. As seen by the data in Figure 6-5(a), there is little difference in hydraulic diameter for the square channels even with changes to build location. For the square samples at both radii, 75 and 112.5 mm, there is a 2% difference in hydraulic diameter between the three samples. While there is minimal difference in the as-built hydraulic diameter between the samples at different locations, the standard deviation in hydraulic diameter, specifically  $3\sigma$  variation in hydraulic diameter, for a sample does change with build location. There is a greater variation in hydraulic diameter for samples built at the 112.5 mm radius compared to the closer radius as seen in Figure 6-5(b) for the square coupons. The average variation in hydraulic diameter of the 112.5 mm radius group for the square channels is 37% higher compared to the smaller radius.



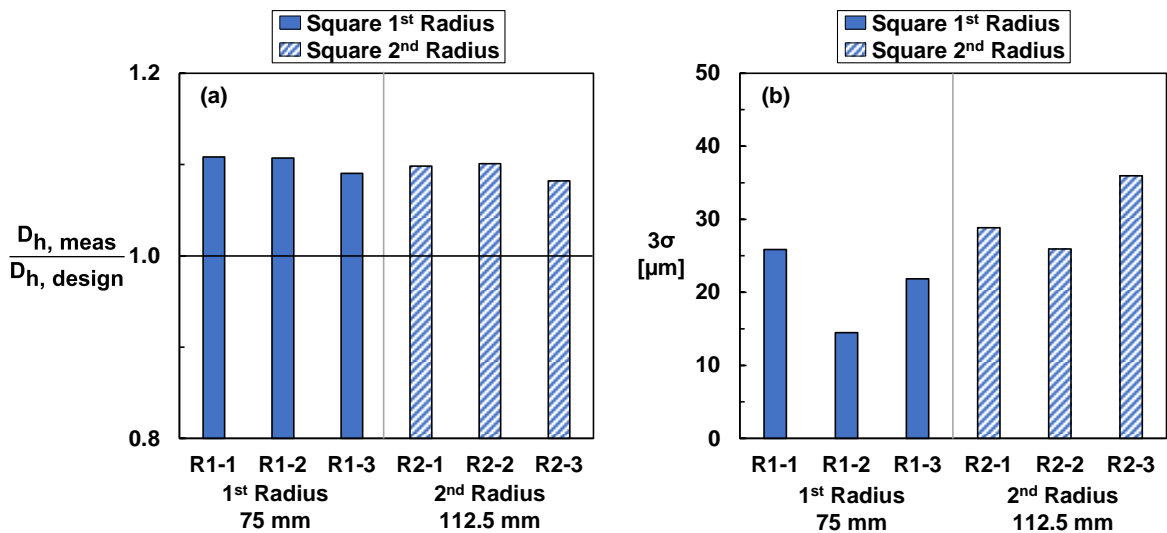
**Figure 6-4 Layout of build plate to evaluate the variability of cooling channels and cooled NExT vanes on an EOS M290-1.**

In addition to characterizing the geometry of the coupon, surface arithmetic mean roughness values were quantified for each sample. The arithmetic mean roughness describes the average deviation from a surface to a datum value. In this case, multiple planes were fitted for each surface of the channel to act as a reference value and the difference between the surface and the planes were recorded as the arithmetic mean roughness. The specific details of this method have been described by Wildgoose et al. [49] and Snyder et al. [22]. The arithmetic mean roughness for each surface of the square channels (as defined by the clock shown in the legend) were averaged and given by Figure 6-6(a) while the area average arithmetic mean roughness in Figure 6-6(b) is averaged between all channel surfaces for a given coupon and is weighted by the design intent surface area.

Regardless of surface orientation in the square channel, samples that were produced further from the laser source exhibit a higher arithmetic mean roughness relative to samples built closer to the laser source as seen in Figure 6-6(a). The positional dependency on roughness exhibited by the square channels is similar to literature [20,66,72]. Even though multiple parts can be built on a

build plate, there can still be differences in surface roughness between parts as result of changes to the radial build location. As seen in Figure 6-4, the 6 and 12 o'clock surfaces of the square cooling passages are perpendicular to the laser source (center of the build plate). Most surface orientations, such as 3 o'clock, 9 o'clock, and 12 o'clock in Figure 6-6(a) have a similar arithmetic mean roughness between samples for a given build location. However, the 6 o'clock direction has the highest variation in arithmetic mean roughness between samples for both build locations relative to other surface orientations. The result infers that some surfaces within a channel, despite all sharing the same local surface orientation with respect to the build plate, can differ between samples. Even though the square cooling channels were all built vertically, the 6 o'clock and 12 o'clock orientations contain higher roughness levels relative to the 3 and 9 o'clock surfaces. The reason for the differences was found to be a factor of wall thickness [66].

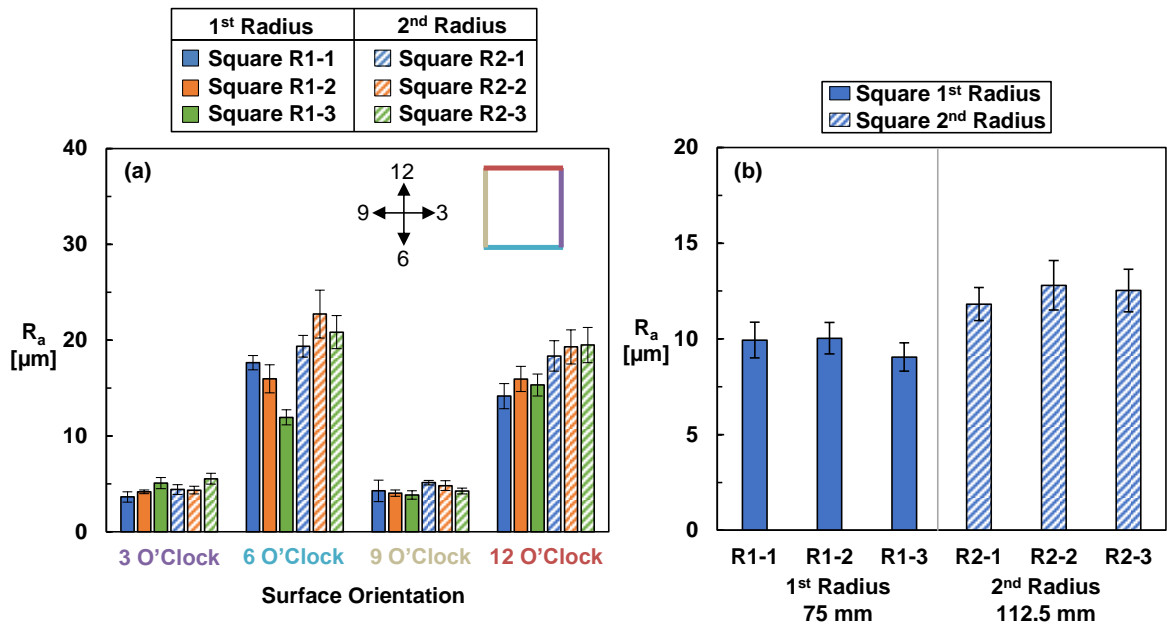
The area averaged arithmetic mean roughness in Figure 6-6(b) show an average 28% increase in surface roughness for the 112.5 mm radial position relative to the smaller radial build location. Figure 6(b) also indicates little difference in surface roughness between samples for a given radial build location. Samples fabricated at the larger radius have a difference of 6% in arithmetic mean roughness while samples fabricated at the smaller radius have a 10% difference in roughness. These results indicate that cooling channels built further from the laser source exhibit more variation and higher surface roughness compared to samples built closer to the laser source.



**Figure 6-5 Average hydraulic diameter of square and hexagonal channels, built across two different build locations, measured from CT scans (a) along with each of the coupons  $3\sigma$  (b) variation in hydraulic diameter.**

## 6.6 Part-to-part Variability of Features on Turbine Components due to Build Plate Location

The inherent complexity of cooling schemes implemented in turbine vanes highlights the challenges additive manufacturing faces to both resolve and fabricate the tight tolerances required for predictable cooling performance between parts. Few studies have investigated the printability of vane external or internal cooling features as well as the overall deviation from design intent. Hossain et al. [119] evaluated the overall cooling effectiveness of nozzle guide vanes with different film cooling holes designs. To adequately resolve a complex cooling hole, [120] and [119] increased the diameter of the film cooling hole by 30% to ensure minimal blockage. Kirollos and Povey [121] also oversized film cooling holes to reduce shrinkage effects during manufacturing of a nozzle guide vane produced through AM. While the Kirollos and Povey [121] study primary focus was on cooling performance of the AM vane relative to a traditionally casted vane, there was a standard deviation of  $\pm 0.15$  mm from the design intent of the AM vane.

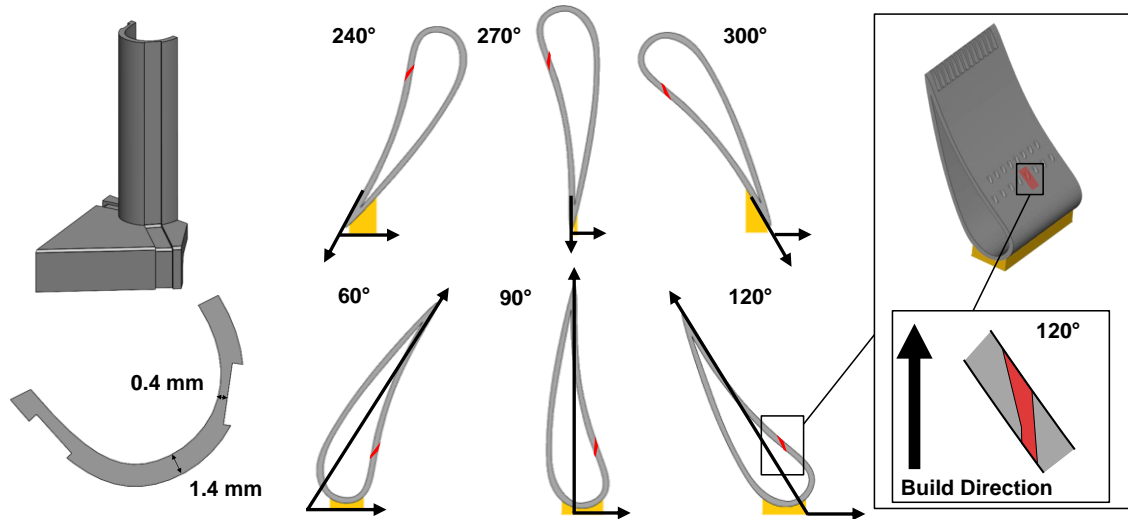


**Figure 6-6 Arithmetic mean roughness form CT scan data of each surface for the square cooling channels (a) along with area average arithmetic mean roughness (b) of the same square channels weighted by the design intent surface area.**

Wildgoose et al. [66] focused on the impact of the vane geometry and AM build parameters on the resulting surface quality of vane airfoils. Their results showed the importance of the overall build direction given the many features in a vane giving way to differences in surface uniformity between the pressure and suction sides. Their study also investigated positional effects on a vane

airfoil and showed that the surface roughness of airfoils increased by 25% as the part location on the build plate went from 75 mm to 187.5 mm. Additionally, differences were observed between different machines and layer thicknesses. Airfoils fabricated using an 80 micron layer thickness contained higher levels of surface roughness relative to 40 microns. Additionally, the surface roughness of the airfoils was lower when fabricated on an EOS M290-1 compared to an EOS M400-1. However, there were no cooling features, either internal or external, included in their printed vane coupons.

It would be expected that the variations from design intent from part-to-part of cooling channels would be amplified when fabricating the higher complexity of vanes with cooling features. To further understand the effect of part-to-part variation and printability of cooling features in vanes, several coupon sections from Penn State’s National Experimental Turbine (NExT) vane [122], shown in Figure 6-7, were fabricated using an EOS M290-1 with a 40 micron layer thickness using standard EOS recommended process parameters. The sample designs in Figure 6-7 serve as an illustration of the leading-edge vane with variable wall thicknesses (0.4 mm and 1.4 mm) as well as a full vane airfoil with pressure side film cooling holes at different build directions. Wildgoose et al. [66]



**Figure 6-7** Leading edge NExT vane that were fabricated at different build locations as well as the full NExT vane with highlighted first row film cooling holes fabricated at different build directions (300°, 270°, 240°, 60°, 90°, 120°).

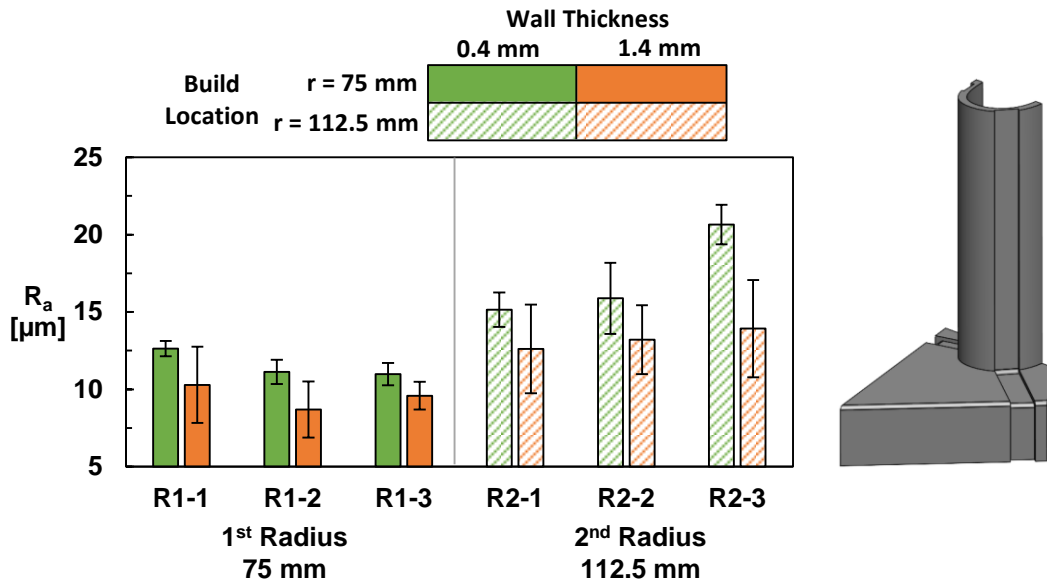
showed that wall thickness below 0.6 mm influences the surface roughness as result of instabilities to the melt pool caused by the change in conduction resistance due to the geometry.



In printing the NExT vanes, the first objective was to evaluate the part-to-part variation of the airfoil shape, specifically the leading edge, while the second objective was to investigate a feasible build direction to resolve cooling features for a cooled AM vane. The focus of this was primarily on the film-cooling features. As seen in Figure 4, the leading edge (LE) portion of the NExT vane airfoil was printed multiple times at two different radial build locations to investigate part-to-part variation of a vane airfoil with no cooling features. Additionally, the mid-span region of a full vane airfoil with internal cooling features including the ribs and film-cooling holes was fabricated at six different build directions. All of the six build directions maintained the same radial build and were placed on the build plate shown in Figure 6-4.

The LE vane samples included two wall thicknesses to observe this affect for the airfoil. The leading edge of the vane samples was fabricated perpendicular to the build plate resulting in minimal impact of build direction on surface quality due to no downward facing surfaces. The arithmetic mean roughness was evaluated for the interior portion of the LE vane samples for the two different wall thickness as given in Figure 6-7. Even with the added complexity of the curved vane surface compared to the cooling channels without surface curvature, the arithmetic mean roughness of the LE vanes in Figure 6-8 follow similar relationships as the channels in Figure 6-6. For both wall thicknesses, the arithmetic mean roughness is higher for a part this is located further from the laser source. Quantitatively, there was an average 49% increase in surface roughness for the 0.4 mm wall thickness when increasing the radial location from 75 mm to 112.5 mm. There was a 39% increase in arithmetic mean roughness for the 1.4 mm wall thickness when comparing the 1<sup>st</sup> and 2<sup>nd</sup> radial build locations. The roughness dependency on position agrees with literature, [17,72] where the change in roughness is attributed to the laser incidence angle. Following Subramanian et al. [72], the laser incidence angle is the angle between the vector normal to the surface being sintered to that of the vector from the laser source to the surface.

Matching prior results, [66], the arithmetic mean roughness for both build locations increased at the lower 0.4 mm wall thickness relative to the 1.4 mm wall thickness. On average, there was a 22% increase in surface roughness from the 1.4 mm to the 0.4 mm wall thickness for the smaller radius while the increase for the larger radius was 30%. The implications of roughness being impacted by wall thickness highlights the potential influence of thin walled features such as the trailing edge of an AM vane or thin walled features of a fin heat exchanger having higher surface roughness relative to other regions of the part.



**Figure 6-8 Arithmetic mean roughness measured from CT scan data of the different wall thickness and build location of the leading edge NExT vane samples seen in Figure 7.**

When investigating the part variability, there is a higher variation in roughness between samples for the larger radius which is consistent with the previously reported results. For a given build location such as the 1<sup>st</sup> radius, the difference in roughness between the three samples is 14% at the 0.4 mm wall thickness. While the roughness is 17% different for the samples containing a wall thickness of 1.4 mm. The percent difference in roughness between the different wall thicknesses increases the further a sample is from the laser source. The difference in roughness between the three samples for the larger radius (2<sup>nd</sup> radius) is at 31% for the 0.4 mm wall thickness while it is 48% for the 1.4 mm wall thickness. The results from Figure 6-5, Figure 6-6, and Figure 6-8 infer that regardless of part geometry, there is less variation in surface quality between parts when samples are closer to the laser source.

The ability to fabricate film cooling holes on a turbine airfoil using AM can save significant time and costs since the part would not need to go through an additional post-printing step. The producibility of film cooling holes on vanes was evaluated using the NExT vanes with film cooling holes on the pressure side for different build directions from the build plate. To cover a range of build directions, the vane was fabricated with the leading edge facing upwards (60°, 90°, and 120°) and with the leading edge facing downwards (300°, 270°, and 240°).

The midspan first row film cooling hole on the vane pressure side as seen in the highlighted region in Figure 6-4 and Figure 6-7 for the 120° vane was selected for evaluation due to the importance in the ability to resolve the cooling feature because of the high heat load of the pressure

side relative to the suction side. For this location, highlighted in the yellow region in Figure 4, the 7-7-7 film-cooling hole was the geometry of choice [123]. The meter section diameter of the 7-7-7 hole was 0.53 mm while the thickness of the wall on the airfoil was 1.4 mm. The local surface orientation of the first row film cooling hole on the 120° vane is enlarged in Figure 6-7. Support structures were used in the internal cavities of the vane to prevent a build failure in the internal cavities of the vane. As opposed to cooled vanes in literature, the 7-7-7 film cooling holes were not scaled for the 40-micron Inconel 718 process.

The CT scans of the vane were fit to the design intent of the vane with cooling features and the deviation from design intent of the evaluated film cooling hole is recorded in Figure 6-9. Note that positive values of the color bar in Figure 6-9 indicate the surface was overbuilt meaning material is present when there was no intended material from the design while negative values in the color bar infer the surface was underbuilt. Also accompanied in Figure 6-9 are labels of the surfaces before the film cooling hole (windward direction) as well as after the film cooling hole (leeward direction).

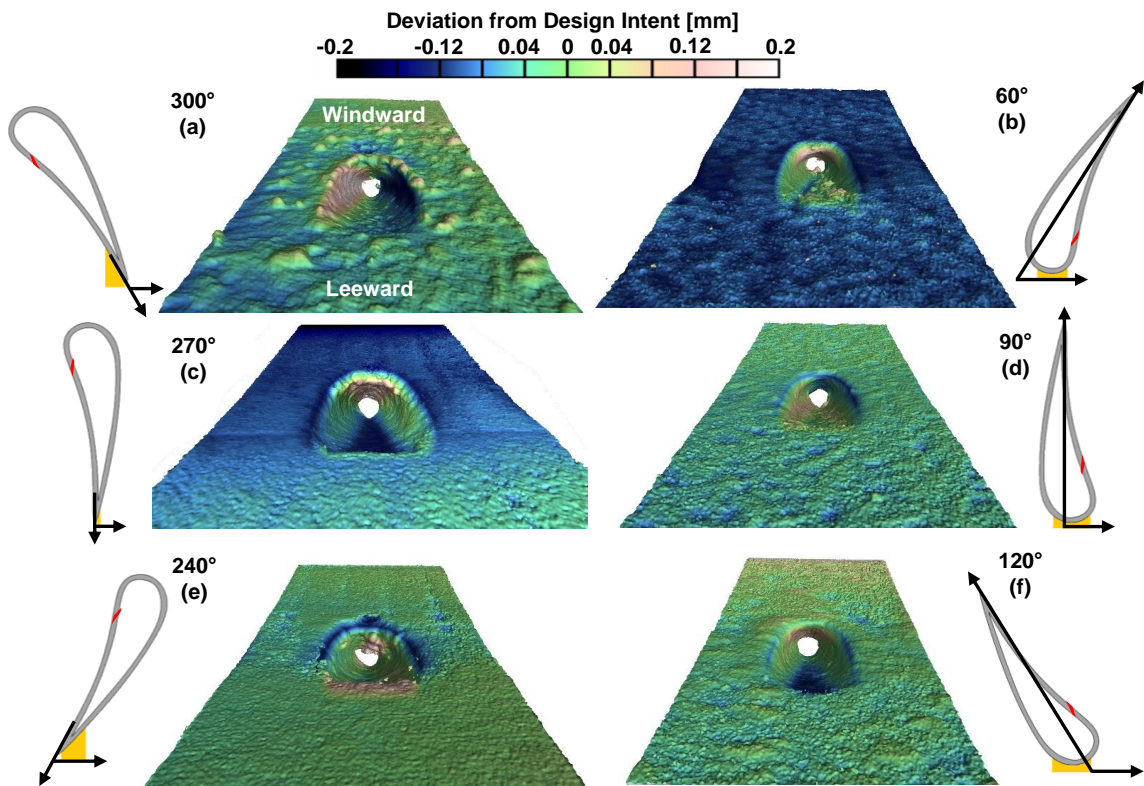
There is a wide range of deviations from design intent and differences in film cooling hole quality for the range of build directions evaluated. Pressure side surfaces that contained downward facing areas such as the 300° and 60° samples, showed the most variability in PS surface quality compared to all other build directions. As seen in the 60° sample, there are differences in the roughness of the pressure side as well as the roughness inside the 7-7-7 film cooling hole as a result of the local surface orientations being different between the hole and PS surface. The in-hole roughness of the 60° and 240° samples are highest compared to all other build directions due to local surface orientations within the holes being built closest to parallel with the build plate. Upon further investigation of the 60° sample, several film cooling holes on the first row were in some cases completely or partially blocked.

In contrast, despite the high surface variability in the 300° sample, the PS surface built closer to the design intent compared to the 60° sample. The surface quality on the PS is worst for the 300° sample compared to all other build directions, most likely due to the 300° sample containing the most severe downward facing surface.

Both the 270° and 90° build directions were able to resolve the entrance of the cooling hole better relative to the 300° and 60° samples. The downward facing windward side of the 270° hole contains more deviations from the design as seen by the different roughness features in Figure 6-9(c). When comparing the printability of the 7-7-7 hole between the 270° and 90° build direction, the 90° contains less surface roughness within the hole since the metering axis of the cooling hole was greater than 45°. However as seen in Figure 6-6(c and d), the entrance region of the hole differs

from the circular design intent. There are also significant roughness features at the leeward side of the 240° sample, seen in Figure 6-9(e), since the metering section axis was built less than 45° from the build plate.

The build direction that best resolved the film cooling hole and printed closest to the design intent was the 120° sample, as seen in Figure 6-9(f), compared to all other build directions. Not only did the entrance of the film cooling hole print closest to the circular design intent but the PS surface contained minimal amounts of surface roughness relative to the other samples. In addition, both the leeward and windward sides of the film cooling hole were resolved and showed similar surface variations. Furthermore, there was no observable blockage in any of the other first row film cooling holes of the 120° sample.



**Figure 6-9 CT scans of the mid span first row 7-7-7 film cooling hole at the pressure side of the NExT vane fabricated at six different build directions.**

### 6.7 Pressure loss and Heat transfer resulting from Build Plate Location

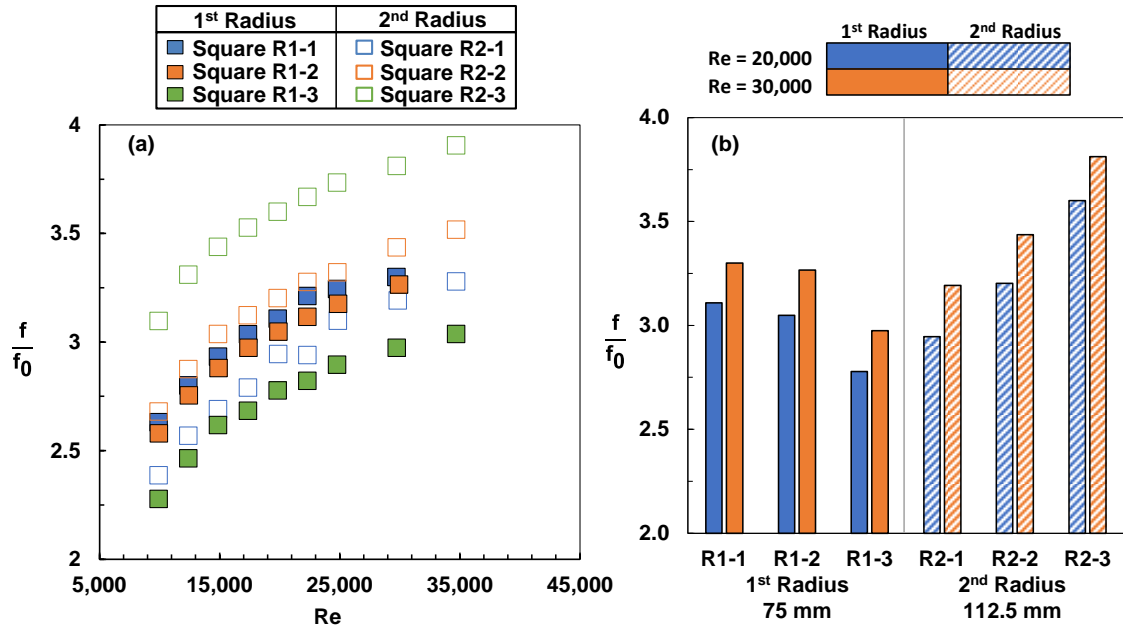
The AM process not only affects part quality and tolerances, but for cooling applications convective heat transfer and pressure loss are impacted. There has been extensive work in literature,

summarized by Thole et al. [12], to show the impact of the surface roughness from AM on the heat transfer and pressure loss of cooling schemes. Effects of AM build parameters such as build direction can cause as much as a 78% difference in friction factor as seen in the work by Wildgoose et al. [49] and Stimpson et al. [33]. Apart from the work of Kirsch et al. [118] few studies have investigated part-to-part differences in cooling performance of channels. Kirsch et al. [118] found that different materials can cause friction factor to vary by as much as three times between samples that share the same design intent. When investigating the difference in cooling performance from part-to-part in other studies, the work of Stimpson et al. [33] stated that there was minimal difference in friction factor or Nusselt number between three test samples, however no statistical quantity was mentioned.

Experimental pressure loss and heat transfer test were performed on the cooling channel samples in Figure 6-4 to bring insight into the amount of variation in cooling performance between samples for each of the different locations on the build plate. Augmentations relative to smooth channels were calculated using the well-known Colebrook [124] correlation for the friction factor and Gnielinski [45] correlation for heat transfer.

The results in Figure 6-10 indicate that the friction factor augmentation increases as the samples are built further from the laser source. For a given fully turbulent Reynolds number, such as 20,000 as seen in Figure 6-10(b), there is on average a 9% increase in friction factor from the 75 mm radial build location to the 112.5 mm build location. There is not only an increase in friction factor when changing build locations but the difference in friction factors between samples at a given location increases the further a sample is from the laser source. More specifically, there is a 11% difference in friction factor between data at a Reynolds number of 20,000 for the 75 mm radial build location. The friction factor difference between samples increases to a 20% difference for samples built at the 112.5 mm build location. Similarly at a Reynolds number of 30,000, as seen in Figure 6-10(b), the friction factor difference between data points is 10% at the 75 mm radial build location while there is an 18% difference for samples built at the 112.5 mm radial build location.

Despite being built at the 2<sup>nd</sup> radius, the R2-1 sample shows a lower friction factor relative to the R1-1 and R1-2 sample in Figure 6-10. This result emphasizes that there can be a range of friction factor observed even when samples share the radial build location



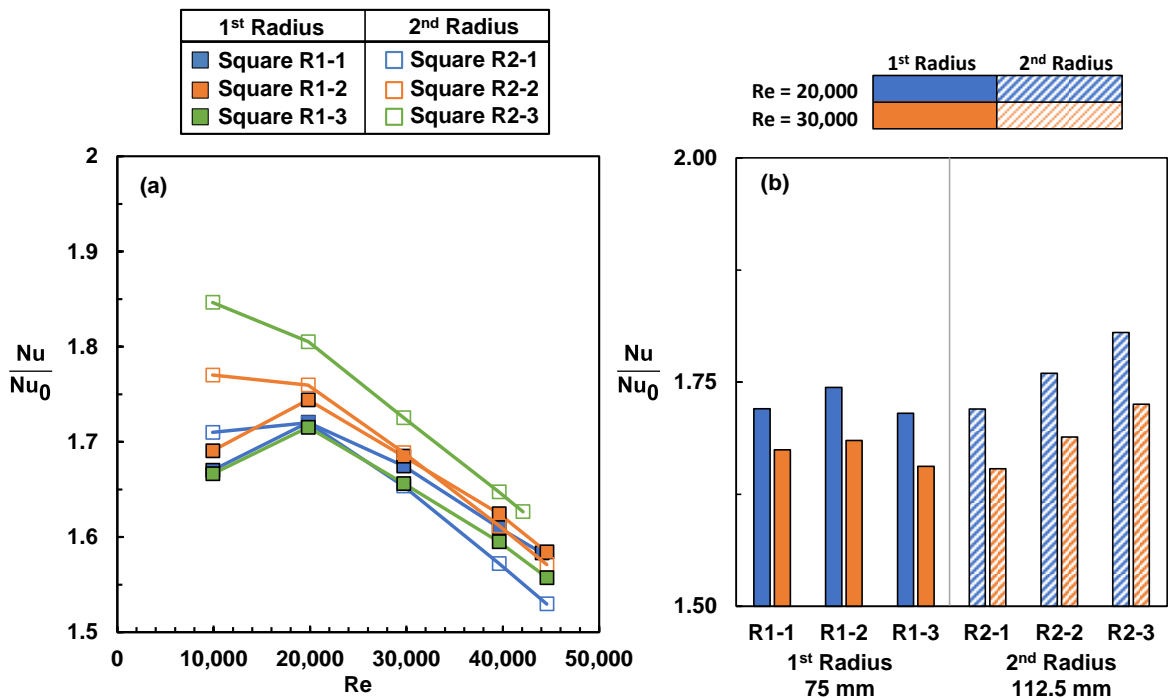
**Figure 6-10 Friction factor augmentation of square cooling channel samples across various Reynolds numbers (a) as well as friction factor augmentation of the channels at a Reynolds number of 20,000 and 30,000 (b).**

and design intent. Overall, there is a 26% difference in friction factor between all the samples on the build plate at a Reynolds number of 20,000 and a 27% difference in friction factor between all the samples on the build plate at a Reynolds number of 30,000. As a result, there can be a wide variation in pressure loss between channels in complicated multi-channel cooling schemes that cover a large area on a build plate.

In addition to evaluating friction factor, the same experimental test rig measured bulk convection coefficients for the samples in Figure 6-10 in order to calculate a bulk Nusselt number using several heaters and thermocouples. Nusselt number was calculated using the hydraulic diameter measured from CT scans. Further detail regarding the specific convection heat transfer measurement technique is reported in Stimpson et al. [33]. Nusselt number in Figure 6-11 is nondimensionalized by the Nusselt number of a hydraulically smooth channel, which was calculating using the Gnielinski's correlation using the friction factor from the Colebrook correlation with a sandgrain roughness of zero. Following the propagation of uncertainty analysis specified by Figliola and Beasley (Figliola and Beasley, 2005) the uncertainty for Nusselt number was less than 7% across the range of Reynolds numbers evaluated.

Comparable to the friction factor results, there can be a range of Nusselt numbers between samples on a build plate as seen in the 5% difference in Nusselt number between all the samples at Reynolds number of 20,000 as seen in Figure 6-11. The Nusselt number is on average 2% higher

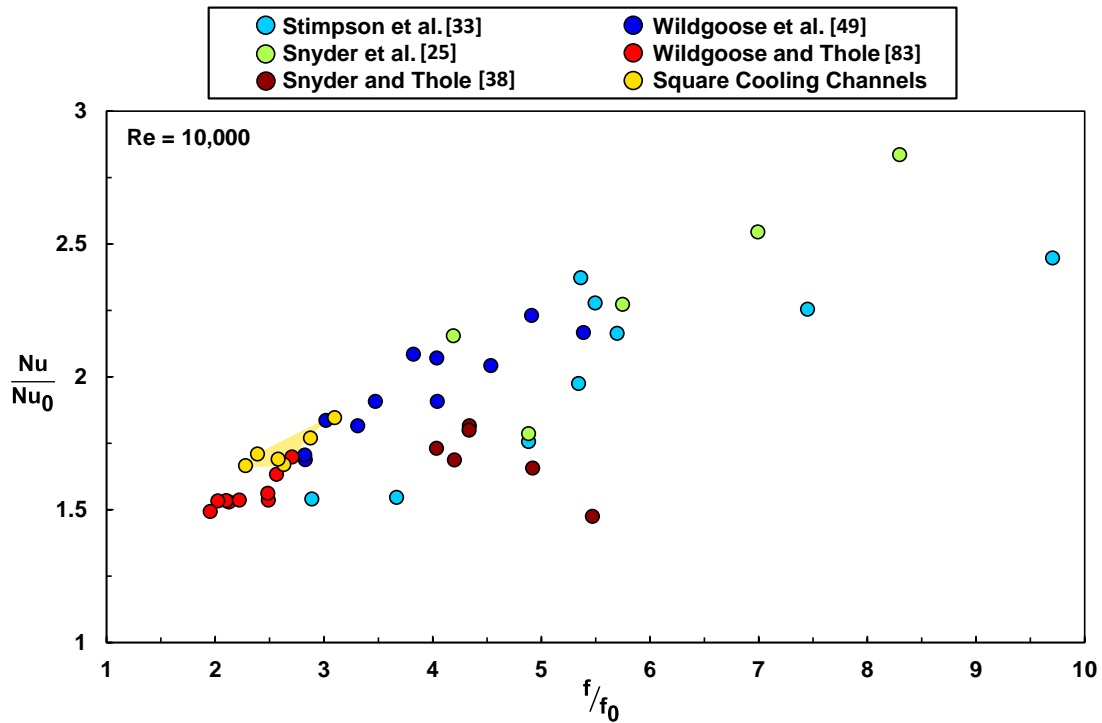
for samples at the 2<sup>nd</sup> radial build location relative to samples at the 1<sup>st</sup> radial build location. There is more variation in Nusselt number for samples built further from the laser source which is similar to: the friction factor, variation in hydraulic diameter, and area average arithmetic mean roughness results. The amount of difference in Nusselt number between samples doubled when going from the 1<sup>st</sup> radius to the 2<sup>nd</sup> radius for the two Reynolds numbers in Figure 6-11(b). The spread in friction factor and Nusselt number of the 2<sup>nd</sup> radius samples is significant enough that some samples such as the R2-1, have friction factor and Nusselt number values that are equal to some of the 1<sup>st</sup> radius samples. When comparing the spread in friction factor values to Nusselt number values the relationships between samples are similar to Kirsch et al. [118], where there is a greater spread in the value of friction factor relative to Nusselt number for all the samples on the build plate. Quantitatively, there is a 26% difference in friction factor while there is a 5% difference in Nusselt number for all the samples on the build plate.



**Figure 6-11 Nusselt number augmentation of square cooling channel samples across various Reynolds numbers (a) as well as Nusselt number augmentation of the channels at a Reynolds number of 20,000 and 30,000 (b).**

In an effort to compare the repeatability in cooling performance of the square cooling channels to AM channel literature, Figure 6-12 highlights the distribution in friction factor augmentation and Nusselt augmentation of the square cooling channels relative to several AM

channels from literature at a Reynolds number of 10,000. The samples from literature include: square and rectangular samples built at different sizes [33], circular channels built at different build directions [25] and [83], rectangular channels made with varying laser processing parameters [38], and samples with different cross-sectional shapes [83]. It is important to note that the square cooling channels in Figure 6-12 are the only samples which all share the same design intent and build direction for evaluating part-to-part variation on the build plate. The square cooling channels from Figure 6-4 are shown with a yellow area giving importance to the amount of variation in friction factor and Nusselt number on a build plate for a shared channel design. For a given Reynolds number there is more variation in friction factor compared to Nusselt number for the square cooling channels, as seen by the shape of the highlighted yellow area in Figure 6-12. In more detail, there is a 30% difference in friction factor augmentation for the square cooling channels relative to a 10% difference in Nusselt number augmentation. The part-to-part differences in cooling performance of the square cooling channels emulates the possible differences in cooling performance for the samples in public literature.



**Figure 6-12 Friction factor and Nusselt number augmentation of cooling channels built at different build directions, channel cross-sections, laser parameters, and diameters at a Re = 10,000.**



## 6.8 Conclusion

There can be significant variability in geometry and surface quality for components that have been additively manufactured as result of the complex interaction between the laser and powder in the additive manufacturing process. The metal additive process enables the rapid prototyping and testing of turbine components. The reproducibility of a part is imperative for turbine components to guarantee expected part temperature and flow properties. The better understanding and development of AM process parameters over the years has improved the producibility and minimized blockages of internal and external vane cooling features such as film cooling holes and micro-sized channels. Even with the improved sets of process parameters over the years, hole blockages, particularly in engine scale film cooling holes are still present depending upon the hole orientation.

This paper has also explored the variability in geometry and part quality of engine scale cooled vanes as well as the variability in heat transfer and pressure loss from part-to-part of simple cooling channels. To assess variability in cooling channel designs, several cooling channel coupons were fabricated multiple times at two different build plate locations. The hydraulic diameter of the cooling channels was found to varied minimally between samples even at different build locations. In contrast, the standard deviation of hydraulic diameter increased the further the part was built from the laser source. Similar to the variation in diameter, the internal surface roughness of the square cooling channels increased the further the part was built from the laser source.

Experimental friction factor and Nusselt number tests were measured for the cooling channels printed multiple times on a build plate. Both the magnitude and differences in friction factor and Nusselt number between parts increased the further the samples were built from the laser source.

Turbine relevant geometries such as the leading edge portion of a vane airfoil was fabricated at the same build locations and multiple times as the cooling coupons. The leading edge samples also contained variable wall thicknesses that resulted in a higher surface roughness for surfaces built with a thin wall compared to surfaces built with a thicker wall. The surface roughness magnitude and variation in roughness of the leading edge vane samples increased the further the sample was from the laser source.

Full vane airfoils with internal and external cooling features were fabricated across multiple different build directions to investigate the printability of the pressure side film cooling holes as well as surface quality. Certain build directions such as orientating the leading edge of a vane 120° from the top of a build plate produced film cooling holes closest to their design intent while also producing the lowest variability in pressure side surface quality. The print quality of the

overall component and its cooling features depends upon the local surface orientation of the features and airfoil.

Examining the variability in geometry and cooling performance of additively manufactured vanes and cooling channels provides insight and foundational development to enabling rapid prototyping and testing of AM turbine components. Positional effects on the build plate and local surface orientations within a part contribute to the printability and geometric variability of AM components.

## 7 CONCLUSIONS

The research reported in this dissertation has advanced the understanding of AM build process impacts on the tolerances and convective heat transfer of cooling channels and has laid out the foundational work to fabricate favorable geometry of turbine relevant components such as guide vanes for use in rapid prototyping during the traditional design and development process of a vane or blade. More specifically, the previous chapters have highlighted the impact the AM process has on internal cooling features as well as the as-built surface quality of external vane features like film cooling holes and airfoil shape. Designers can use this work to improve the part-to-part consistency, internal cooling performance predictability, and build quality of engine components for rapid prototyping. A direct application of this work is seen in the Steady Thermal Aero Research Turbine (START) lab at the Pennsylvania State University, where the AM process is used to rapidly test cooling design effectiveness and the impact of vane/blade dimensions on engine efficiency significantly quicker and less costly than using traditionally casted components.

The following section summarizes the key findings from this dissertation that include: (i) the influence of the AM process on the tolerances and surface quality of internal cooling passages, (ii) highlighting relationships between surface roughness and the overall cooling performance of cooling passages, (iii) build considerations of the AM process for fabricating consistent and desired tolerances of gas turbine components. The final section provides recommendations for future work to improve the capability in using AM to rapidly fabricate advance cooling designs at reduced costs and project time relative to traditionally casted components.

### 7.1 Influence of the AM process on the build quality of internal cooling passages

Changes to the additive build process can influence the resulting geometric tolerances and surface quality of components. The impact of those effects are magnified when examining small scale features such as cooling passages. To make consistent internal cooling schemes, particularly when rapid prototyping AM turbine components, it is useful to understand how the part accuracy of the internal component geometry is affected by the build process. In more detail, the term build process covers common AM part considerations such as how to design the component containing downfacing surfaces to where the component is placed on the build plate. Consequently, the geometric tolerances were evaluated for multiple engine scale internal cooling channels that were fabricated at a variety of build considerations.

The direction at which the cooling channels are fabricated relative to the build plate impacts the as-built quality of cooling passages. The geometric tolerances of cooling passages such as

deviation from the design intent hydraulic diameter decreases when orienting the streamline axis of a cooling passage from vertical ( $90^\circ$ ) to horizontal ( $0^\circ$ ) with respect to the build plate. The variation, specifically the standard deviation, in the as-built hydraulic diameter nonlinearly increases when orienting a cooling channel from the vertical to horizontal orientation. With changes to the channel size, there is minimal difference in the deviation from design intent and standard deviation in hydraulic diameter for a given build direction. The internal surface roughness of cooling channels, in particular the arithmetic mean roughness, nonlinearly increased when changing the orientation of a channel from vertical to horizontal to the build plate. At certain build directions, channel corrections such as a teardrop shapes are needed (at around a  $60^\circ$  build direction for circular channels) to mitigate hole blockage and prevent severe cooling passage deformation.

A common step during the additive process is the choice of where to place the part on the build plate before printing. This dissertation revealed the impact build location has on the placement of internal cooling passages. The angle at which the laser melts the powder of the surface (laser incidence angle) can cause disruptions to the melt pool leading to differences in surface quality of components. Surface roughness and overall deviation from geometric design intent was found to increase the further the cooling passage is from the laser source, regardless if it is a single or multi-laser machine. There is a 35% increase in roughness when changing the radial build location of a cooling passage from 0 mm to 145 mm from the laser source. Furthermore, the variation in surface roughness and variation in geometric tolerances for cooling passages similarly increases the further the part is from the laser source.

Changes to the cross-sectional shape of a cooling channel were found to cause differences in surface roughness due to changes in heat accumulation during the AM process. Through the use of nondestructive evaluation (CT scanning), a range in the magnitude of internal surface roughness was observed depending upon the shape of the channel. There was a three times difference in surface roughness between the diamond and square channel shape. After further investigation, wall thickness was found to be the cause for the difference in roughness among the various channel shapes. More specifically, surface roughness was found to increase as the wall thickness decreased below 0.6 mm of the cooling passage.

To emulate large scale production of AM components for rapid prototyping purposes, multiple cooling passage components were fabricated on a build plate. For the first time in open literature, the amount of variation in geometric tolerances for the same design intent part printed multiple times on a build plate (design repeatability) was quantitatively characterized for cooling passages. Despite printing the samples with the same design intent, build direction, and radial build location, the surface roughness of the internal cooling passages varied by 10% between

components. The work in this dissertation highlights the design choices designers must consider to fabricate internal cooling passages consistently.

## **7.2 Pressure loss and Convective Heat Transfer relationships of AM cooling schemes**

An investigation in surface roughness and geometric tolerancing of cooling channels is important in order to explain relationships in pressure loss and heat transfer of cooling passages made through AM. The work in this dissertation investigated the impact of the AM process on the cooling performance of channels as well as leveraged the design freedom offered through AM to examine the scaling of pressure loss and heat transfer in non-circular channel shapes so cooling designs can be fairly compared. The build direction of a channel passage was shown to have a strong impact on the pressure loss (friction factor) and heat transfer (Nusselt Number) of circular cooling channels. Friction factor followed the same nonlinear increase trend as surface roughness when orientating a channel from 90° to 0°. In contrast, the Nusselt number peaked between the 30° and 45° build direction and decreased from 30° to 0°. As channel diameter decreases the roughness to diameter ratio increases causing the friction factor and Nusselt number to increase. Changes to the location of a component on the build plate subsequently impacted the friction factor and Nusselt number. More specifically, the friction factor increased 9% while the Nusselt number increased 5% when changing the radial build location of a cooling coupon from 75 mm to 112.5 mm with respect to the laser source.

The ability to produce consistent friction factor or Nusselt number of a cooling design printed multiple times is important for scaling production of AM components. As such, the variability in friction factor and Nusselt number of a cooling channel was evaluated. There can be as much as an 18% difference in friction factor and 5% difference in Nusselt number for a cooling sample printing multiple times on a build plate at a shared radial build location.

The design freedom AM offers allows novel cooling passages to be created that would be challenging or costly to produce using traditional manufacturing methods. With the ability to fabricate novel cooling designs there brings a need to select the appropriate characteristic length scales for cooling relations to allow for fair comparisons between designs. Consequently, different length scales for friction factor and Nusselt number were analyzed to scale the experimental results for a variety of noncircular channel shapes. Results showed that both the surface roughness and cross-sectional shape of a channel influences the resulting pressure loss and heat transfer causing the characteristic length scales, such as hydraulic diameter and square root of cross-sectional area, evaluated to struggle with collapsing the data.

Since the beginning of the research for this dissertation there has been a substantial increase in the amount of experimental AM cooling data available. Additionally, literature has proposed several correlations to predict both friction factor and Nusselt number using measured surface roughness. Pressure loss and heat transfer correlations in literature were found to struggle to predict the cooling performance of the new data available. The cause was found to be a result of the bulk roughness statistic parameter (arithmetic mean roughness). The arithmetic mean roughness is a general roughness statistic that was found to not fully capture the relationship between cooling performance and surface morphology. A combination of roughness statistics such as the root mean square roughness and skewness was used to create an improved correlation for friction factor, which was found to reduce the average absolute error by half compared to previous correlations. Furthermore, a Nusselt correlation was developed using datasets from previous authored papers as well as those found in literature to reduce the error by half compared to the correlations available in literature. The friction factor correlation is able to predict pressure loss data within a maximum error of 25% while the Nusselt correlation is able to predict heat transfer within a maximum error of 39%.

### **7.3 Impact of the AM process on the Build Quality of External features of Turbine Parts**

Additive manufacturing provides the ability to fabricate complicated components such as turbine vanes and blades, which are expensive and challenging to make using traditional investment casting methods. More specifically, the additive process can be used as tool in the rapid development of complex cooling designs during the component design process. The work in this dissertation documents design choices designers must consider when using the additive process for the fabrication of gas turbine components, in particular guide vanes. In more detail, the impact of build direction, build location, differences between AM machines, and wall thickness was evaluated for external features such as the airfoil and film cooling holes of a vane, in this case the National Experimental Turbine (NExT) vane [122].

The magnitude in surface roughness of a leading-edge uncooled vane was found to increase 49% when placing the component from 75 mm to 112.5 mm from the center of the laser source. Additionally, the same sample also contained two different wall thicknesses to investigate the effect of changes to geometry on the airfoil. Similar to the internal passages, surfaces with a low wall thickness (0.4 mm) exhibited a 30% higher roughness compared to surfaces with a higher wall thickness (1.4 mm) of the airfoil. A full vane airfoil without cooling was printed at different build directions, locations, on various AM machines, and at two different wall thicknesses. As result of

the local surface orientation on an airfoil, build direction was found to cause nonuniformities in surface quality between the suction side and pressure side of the airfoil. The most uniform roughness along the airfoil and least amount of first row film cooling hole deformation occurs when the leading edge of a vane is angled  $120^\circ$  with respect to the build plate. The stair stepping effect caused differences in roughness between the pressure side and suction side of the airfoil when going from a 40 micron layer thickness to an 80 micron layer thickness.

Several NExT vanes containing both internal and external cooling features were fabricated to investigate which build orientation is most optimal to resolve the external cooling features. Using CT scans, the first-row film cooling holes at the pressure side were resolved and deviation from design intent was found to be a strong function of local surface orientation. Depending on the airfoil orientation, the film cooling holes can exhibit both smooth and rough surfaces such as the  $60^\circ$  and  $240^\circ$  leading edge orientation. Orientating the airfoil of a vane  $120^\circ$  with respect to the build plate, results in the least amount of deformation within the film cooling hole as well as lowest variability in surface roughness of the pressure and suction side. Understanding the causes for differences in roughness are important to quantify since these differences influence the overall cooling effectiveness of a vane and part to part consistency.

#### **7.4 Recommendations for Future Work**

The research presented in this dissertation expands the understanding of how the complex AM process influences both the cooling performance of passages and tolerances of engine scale gas turbine components. To fully unlock the potential of AM in heat transfer applications, more research is needed in several key areas of AM process control and the understanding of fundamental interactions between surface roughness and cooling performance.

Being able to control the melt pool during the metal AM process allows for the control of geometric tolerances and surface quality of components, regardless of complexity. More specifically, further research into the interaction between the powder and the laser along with in-situ processing can allow for dynamic laser control to mitigate keyhole formations, dross features, and overall part shrinkage. The addition of in-situ processing, specifically pictorial information, can bring quantitative evidence for the blockage of cooling holes during the build process as well as provide a feedback platform to manipulate laser parameters to achieve desired part tolerances. Currently it is common to evaluate cooling passage blockage through flow testing or nondestructive and destructive evaluation methods such as direct line of sight or CT scanning. Implementing in-situ monitoring on the geometric quality of the part can bypass post-build part qualification

processes, such that it improves the time to development of advanced cooling schemes. However, these concepts require additional research in complex systems control as well as laser parameter and software development.

To harness the full potential of the AM process for heat transfer applications, the influence of surface roughness on convective heat transfer at the fundamental interaction level requires additional development. In more detail, a better understanding of which roughness features contribute to high convective heat transfer and which roughness features cause low convective heat transfer can allow for cooling trends between samples to be more easily identifiable. A similar concept can be applied to the pressure loss of certain features. Combining the understanding of the AM laser parameters on roughness and roughness on cooling performance, can permit engineers to selectively tailor heat transfer or pressure loss for individual surfaces. The opportunities for tailoring cooling performance at different locations in the part can expand the current implementation of using AM for heat transfer cooling schemes.

Lastly, investigating different forms of roughness statistics used to describe the nonuniformity of AM surfaces can allow for more detailed surface qualification for the AM community. A combination of future areas of investigation and the research presented in this dissertation serves as a pipeline toward understanding the factors causing deviation from design intent and cooling effectiveness such that additive manufacturing can be used towards the rapid development and testing of advance cooling designs.



## REFERENCES

- [1] Bunker, R. S., 2017, "Evolution of Turbine Cooling," Proc. ASME Turbo Expo, **1**.
- [2] Bunker, R. S., 2006, "Cooling Design Analysis," *The Gas Turbine Handbook*, , R. A. Dennis, ed., Department of Energy, National Energy Technology Laboratory.
- [3] Bunker, R. S., 2013, "Gas Turbine Cooling: Moving from Macro to Micro Cooling," *Proceedings of the ASME Turbo Expo*.
- [4] Takeishi, K., 2022, "Evolution of Turbine Cooled Vanes and Blades Applied for Large Industrial Gas Turbines and Its Trend toward Carbon Neutrality," *Energies* 2022, Vol. 15, Page 8935, **15**(23), p. 8935.
- [5] Bales, D. A., Klucha, A., and Dolansky, G. M., 2014, "Uber-Cooled Turbine Section Component Made by Additive Manufacturing," p. US 2014/0169981 A1.
- [6] ASTM, 2013, "Standard Terminology for Additive Manufacturing Technologies," F2792 - 12a.
- [7] Gradl, P. R., Greene, S. E., Protz, C., Bullard, B., Buzzell, J., Garcia, C., Wood, J., Cooper, K., Hulka, J., and Osborne, R., 2018, "Additive Manufacturing of Liquid Rocket Engine Combustion Devices: A Summary of Process Developments and Hot-Fire Testing Results," *2018 Joint Propulsion Conference*, American Institute of Aeronautics and Astronautics Inc, AIAA.
- [8] Badiru, A., Valencia, V., and Liu, D., 2017, *Additive Manufacturing Handbook: Product Development for the Defense Industry*, CRC Press.
- [9] Shipley, H., McDonnell, D., Culleton, M., Coull, R., Lupoi, R., O'Donnell, G., and Trimble, D., 2018, "Optimisation of Process Parameters to Address Fundamental Challenges during Selective Laser Melting of Ti-6Al-4V: A Review," *Int. J. Mach. Tools Manuf.*, **128**, pp. 1–20.
- [10] Ahmed, F., Ali, U., Sarker, D., Marzbanrad, E., Choi, K., Mahmoodkhani, Y., and Toyserkani, E., 2020, "Study of Powder Recycling and Its Effect on Printed Parts during Laser Powder-Bed Fusion of 17-4 PH Stainless Steel," *J. Mater. Process. Technol.*, **278**.
- [11] DebRoy, T., Wei, H. L., Zuback, J. S., Mukherjee, T., Elmer, J. W., Milewski, J. O., Beese, A. M., Wilson-Heid, A., De, A., and Zhang, W., 2018, "Additive Manufacturing of Metallic Components – Process, Structure and Properties," *Prog. Mater. Sci.*, **92**, pp. 112–224.
- [12] Thole, K. A., Lynch, S., and Wildgoose, A. J., 2021, "Review of Advances in Convective Heat Transfer Developed through Additive Manufacturing," *Adv. Heat Transf.*, **53**.
- [13] Snyder, J. C., and Thole, K. A., 2020, "Tailoring Surface Roughness Using Additive

- Manufacturing to Improve Internal Cooling,” *J. Turbomach.*, **142**(7), p. 071004.
- [14] Yadroitsev, I., and Smurov, I., 2011, “Surface Morphology in Selective Laser Melting of Metal Powders,” *Physics Procedia*, Elsevier B.V., pp. 264–270.
- [15] Wang, D., Liu, Y., Yang, Y., and Xiao, D., 2016, “Theoretical and Experimental Study on Surface Roughness of 316L Stainless Steel Metal Parts Obtained through Selective Laser Melting,” *Rapid Prototyp. J.*, **22**(4), pp. 706–716.
- [16] Teng, C., Gong, H., Szabo, A., Dilip, J. J. S., Ashby, K., Zhang, S., Patil, N., Pal, D., and Stucker, B., 2017, “Simulating Melt Pool Shape and Lack of Fusion Porosity for Selective Laser Melting of Cobalt Chromium Components,” *J. Manuf. Sci. Eng. Trans. ASME*, **139**(1).
- [17] Kleszczynski, S., Ladewig, A., Friedberger, K., Jacobsmuhlen, J. zur, Merhof, D., and G, W., 2015, “Position Dependency of Surface Roughness in Parts From Laser Beam,” *SFF Symp. Proc.*, pp. 360–370.
- [18] Chen, Z., Wu, X., Tomus, D., and Davies, C. H. J., 2018, “Surface Roughness of Selective Laser Melted Ti-6Al-4V Alloy Components,” *Addit. Manuf.*, **21**, pp. 91–103.
- [19] Oter, Z. C., Coskun, M., and Koc, E., 2020, “Effect of Building Platform Position on the Surface Quality, Dimensional Accuracy, and Geometrical Precision of Direct Metal Laser Sintering (DMLS) Parts,” *Euro PM 2018 Congress and Exhibition*, European Powder Metallurgy Association (EPMA).
- [20] Sendino, S., Martinez, S., Lamikiz, A., Lartategui, F., Gardon, M., and Gonzalez, J. J., 2021, “Analytical Study of the Melt Pool Distortion in the Laser Powder Bed Fusion Process Caused by the Angle of Incidence of the Laser and Its Effect on the Surface Finish of the Part,” *IOP Conf. Ser. Mater. Sci. Eng.*, **1193**(1), p. 012010.
- [21] Oter, Z. C., Coskun, M., Akca, Y., Surmen, O., Yilmaz, M. S., Ozer, G., Tarakci, G., Khan, H. M., and Koc, E., 2019, “Support Optimization for Overhanging Parts in Direct Metal Laser Sintering,” *Optik (Stuttg.)*, **181**, pp. 575–581.
- [22] Snyder, J. C., Stimpson, C. K., Thole, K. A., and Mongillo, D. J., 2015, “Build Direction Effects on Microchannel Tolerance and Surface Roughness,” *J. Mech. Des. Trans. ASME*, **137**(11), p. 111411.
- [23] Mingear, J., Zhang, B., Hartl, D., and Elwany, A., 2019, “Effect of Process Parameters and Electropolishing on the Surface Roughness of Interior Channels in Additively Manufactured Nickel-Titanium Shape Memory Alloy Actuators,” *Addit. Manuf.*, **27**, pp. 565–575.
- [24] Ventola, L., Robotti, F., Dialameh, M., Calignano, F., Manfredi, D., Chiavazzo, E., and

- Asinari, P., 2014, "Rough Surfaces with Enhanced Heat Transfer for Electronics Cooling by Direct Metal Laser Sintering," *Int. J. Heat Mass Transf.*, **75**, pp. 58–74.
- [25] Snyder, J. C., Stimpson, C. K., Thole, K. A., and Mongillo, D., 2016, "Build Direction Effects on Additively Manufactured Channels," *J. Turbomach.*, **138**(5), p. 051006.
- [26] Morel, C., Cioca, V. V., Lavernhe, S., Jardini, A. L., and Conte, E., 2018, "Part Surface Roughness on Laser Sintering and Milling of Maraging Steel 300," *High Speed Mach. Product. Qual. Digit.*, (1), pp. 3–6.
- [27] Pakkanen, J., Calignano, F., Trevisan, F., Lorusso, M., Ambrosio, E. P., Manfredi, D., and Fino, P., 2016, "Study of Internal Channel Surface Roughnesses Manufactured by Selective Laser Melting in Aluminum and Titanium Alloys," *Metall. Mater. Trans. A Phys. Metall. Mater. Sci.*, **47**(8), pp. 3837–3844.
- [28] Tian, Y., Tomus, D., Rometsch, P., and Wu, X., 2016, "Influences of Processing Parameters on Surface Roughness of Hastelloy X Produced by Selective Laser Melting," *Addit. Manuf.*, **13**, pp. 103–112.
- [29] Klingaa, C. G., Bjerre, M. K., Baier, S., De Chiffre, L., Mohanty, S., and Hattel, J. H., 2019, "Roughness Investigation of SLM Manufactured Conformal Cooling Channels Using X-Ray Computed Tomography," *9th Conference on Industrial Computer Tomography*.
- [30] Stimpson, C. K., Snyder, J. C., Thole, K. A., and Mongillo, D., 2016, "Scaling Roughness Effects on Pressure Loss and Heat Transfer of Additively Manufactured Channels," *J. Turbomach.*, **139**(2), p. 021003.
- [31] Kamat, A. M., and Pei, Y., 2019, "An Analytical Method to Predict and Compensate for Residual Stress-Induced Deformation in Overhanging Regions of Internal Channels Fabricated Using Powder Bed Fusion," *Addit. Manuf.*, **29**, p. 100796.
- [32] Parbat, S. N., Yang, L., Min, Z., and Chyu, M. K., 2019, "Experimental and Numerical Analysis of Additively Manufactured Coupons with Parallel Channels and Inline Wall Jets," *J. Turbomach.*, **141**(6).
- [33] Stimpson, C. K., Snyder, J. C., Thole, K. A., and Mongillo, D., 2016, "Roughness Effects on Flow and Heat Transfer for Additively Manufactured Channels," *J. Turbomach.*, **138**(5), p. 051008.
- [34] EOS, 2011, *Technical Description EOSINT M 280*.
- [35] Snyder, J. C., 2019, "IMPROVING TURBINE COOLING THROUGH CONTROL OF SURFACE ROUGHNESS IN THE ADDITIVE MANUFACTURING PROCESS," The Pennsylvania State University.
- [36] Fox, J. C., Moylan, S. P., and Lane, B. M., 2016, "Effect of Process Parameters on the

- Surface Roughness of Overhanging Structures in Laser Powder Bed Fusion Additive Manufacturing,” *Procedia CIRP*, pp. 131–134.
- [37] Calignano, F., Manfredi, D., Ambrosio, E. P., Iuliano, L., and Fino, P., 2013, “Influence of Process Parameters on Surface Roughness of Aluminum Parts Produced by DMLS,” *Int. J. Adv. Manuf. Technol.*, **67**(9–12), pp. 2743–2751.
- [38] Snyder, J. C., and Thole, K. A., 2020, “Effect of Additive Manufacturing Process Parameters on Turbine Cooling,” *J. Turbomach.*, **142**(5).
- [39] Reinhart, C., 2011, *Industrial CT & Precision*, Volume Graphics GmbH, Heidelberg, Germany.
- [40] Stimpson, C. K., Snyder, J. C., Thole, K. A., and Mongillo, D., 2018, “Effectiveness Measurements of Additively Manufactured Film Cooling Holes,” *J. Turbomach.*, **140**(1).
- [41] Ealy, B., Calderon, L., Wang, W., Valentin, R., Mingareev, I., Richardson, M., and Kapat, J., 2017, “Characterization of Laser Additive Manufacturing-Fabricated Porous Superalloys for Turbine Components,” *J. Eng. Gas Turbines Power*, **139**(10).
- [42] Munson, R. B., Young, D. F., and Okiishi, T. H., 1990, *Fundamentals of Fluid Mechanics*, Wiley & Sons, Hoboken, NJ.
- [43] Sweet, J. N., Roth, E. P., and Moss, M., 1987, “Thermal Conductivity of Inconel 718 and 304 Stainless Steel,” *Int. J. Thermophys.*, **8**(5), pp. 593–606.
- [44] Figliola, R. S., and Beasley, D. E., 2005, *Theory and Design for Mechanical Measurements*, Wiley & Sons, Hoboken, Nj.
- [45] Gnielinski, 1976, “New Equations for Heat and Mass Transfer in Turbulent Pipe and Channel Flow,” *Int. Chem. Eng.*, **16**(2), pp. 359–368.
- [46] Liang, D., He, G., Chen, W., Chen, Y., and Chyu, M. K., 2022, “Fluid Flow and Heat Transfer Performance for Micro-Lattice Structures Fabricated by Selective Laser Melting,” *Int. J. Therm. Sci.*, **172**, p. 107312.
- [47] Parbat, S., Min, Z., Yang, L., and Chyu, M., 2020, “Experimental and Numerical Analysis of Additively Manufactured Inconel 718 Coupons with Lattice Structure,” *J. Turbomach.*, **142**(6).
- [48] Kirsch, K. L., and Thole, K. A., 2018, “Experimental Investigation of Numerically Optimized Wavy Microchannels Created through Additive Manufacturing,” *J. Turbomach.*, **140**(2).
- [49] Wildgoose, A. J., Thole, K. A., Sanders, P., and Wang, L., 2021, “Impact of Additive Manufacturing on Internal Cooling Channels with Varying Diameters and Build Directions,” *J. Turbomach.*, **143**(7).

- [50] Duan, Z., Yovanovich, M. M., and Muzychka, Y. S., 2012, “Pressure Drop for Fully Developed Turbulent Flow in Circular and Noncircular Ducts,” *J. Fluids Eng. Trans. ASME*, **134**(6).
- [51] Sarmiento, A. P. C., Soares, V. H. T., Milanez, F. H., and Mantelli, M. B. H., 2020, “Heat Transfer Correlation for Circular and Non-Circular Ducts in the Transition Regime,” *Int. J. Heat Mass Transf.*, **149**, p. 119165.
- [52] McHale, J. P., and Garimella, S. V., 2010, “Heat Transfer in Trapezoidal Microchannels of Various Aspect Ratios,” *Int. J. Heat Mass Transf.*, **53**(1–3), pp. 365–375.
- [53] Wang, P., Yang, M., Wang, Z., and Zhang, Y., 2014, “A New Heat Transfer Correlation for Turbulent Flow of Air with Variable Properties in Noncircular Ducts,” *J. Heat Transfer*, **136**(10).
- [54] Muzychka, Y. S., and Yovanovich, M. M., 2009, “Pressure Drop in Laminar Developing Flow in Noncircular Ducts: A Scaling and Modeling Approach,” *J. Fluids Eng. Trans. ASME*, **131**(11), pp. 1111051–11110511.
- [55] Nikuradse, J., 1926, “Untersuchungen Über Die Geschwindigkeitsverteilung in Turbulenten Stromungen,” *VDI-Forschungsheft*, **No. 281**.
- [56] Leung, C. W., and Probert, S. D., 1997, “Forced-Convective Turbulent-Flows through Horizontal Ducts with Isosceles-Triangular Internal Cross-Sections,” *Appl. Energy*, **57**(1), pp. 13–24.
- [57] Oertel, H., 2010, “Convective Heat and Mass Transfer,” *Applied Mathematical Sciences (Switzerland)*, McGraw-Hill, Boston, pp. 409–453.
- [58] Jones, O. C., 1976, “An Improvement in the Calculation of Turbulent Friction in Rectangular Ducts,” *J. Fluids Eng.*
- [59] Duan, Z., 2012, “New Correlative Models for Fully Developed Turbulent Heat and Mass Transfer in Circular and Noncircular Ducts,” *J. Heat Transfer*, **134**(1).
- [60] Leung, C. W., Wong, T. T., and Kang, H. J., 1998, “Forced Convection of Turbulent Flow in Triangular Ducts with Different Angles and Surface Roughnesses,” *Heat Mass Transf. und Stoffuebertragung*, **34**(1), pp. 63–68.
- [61] Snyder, J. C., Stimpson, C. K., Thole, K. A., and Mongillo, D. J., 2015, “Build Direction Effects on Microchannel Tolerance and Surface Roughness,” *J. Mech. Des. Trans. ASME*, **137**(11), p. 111411.
- [62] Klingaa, C. G., Bjerre, M. K., Baier, S., De Chiffre, L., Mohanty, S., and Hattel, J. H., 2019, “Roughness Investigation of SLM Manufactured Conformal Cooling Channels Using X-Ray Computed Tomography,” *9th Conference on Industrial Computer Tomography*.

- [63] Zhang, B., Li, L., and Anand, S., 2020, “Distortion Prediction and NURBS Based Geometry Compensation for Reducing Part Errors in Additive Manufacturing,” *Procedia Manuf.*, **48**, pp. 706–717.
- [64] Kamat, A. M., and Pei, Y., 2019, “An Analytical Method to Predict and Compensate for Residual Stress-Induced Deformation in Overhanging Regions of Internal Channels Fabricated Using Powder Bed Fusion,” *Addit. Manuf.*
- [65] Volume Graphics, 2021, “VGStudio MAX.”
- [66] Wildgoose, A. J., Thole, K. A., Subramanian, R., Kerating, L., and Kulkarni, A., 2022, “Impacts of the Additive Manufacturing Process on the Roughness of Engine Scale Vanes and Cooling Channels,” *Under Rev. Proc. ASME Turbo Expo*, GT2022-82298.
- [67] Klingaa, C. G., Dahmen, T., Baier-Stegmaier, S., Mohanty, S., and Hattel, J. H., 2020, “Investigation of the Roughness Variation along the Length of LPBF Manufactured Straight Channels,” *Nondestruct. Test. Eval.*, **35**(3), pp. 304–314.
- [68] ANSYS, 2020, *ANSYS FLUENT*, Canonsburg, PA.
- [69] Deprati, F., 2021, “Direct Numerical Simulation of Flow and Heat Transfer in Complex Ducts,” *Aerotec. Missili Spaz.*, **100**, pp. 263–276.
- [70] Li, Y. K., Zheng, Z. Y., Zhang, H. N., Li, F. C., Qian, S., Joo, S. W., and Kulagina, L. V., 2017, “Numerical Study on Secondary Flows of Viscoelastic Fluids in Straight Ducts: Origin Analysis and Parametric Effects,” *Comput. Fluids*, **152**, pp. 57–73.
- [71] Yeung, H., Lane, B., and Fox, J., 2019, “Part Geometry and Conduction-Based Laser Power Control for Powder Bed Fusion Additive Manufacturing,” *Addit. Manuf.*, **30**, p. 100844.
- [72] Subramanian, R., Rule, D., and Nazik, O., 2021, “Dependence of LPBF Surface Roughness on Laser Incidence Angle and Component Build Orientation,” *Proceedings of the ASME Turbo Expo*, American Society of Mechanical Engineers Digital Collection.
- [73] Kandlikar, S. G., Schmitt, D., Carrano, A. L., and Taylor, J. B., 2005, “Characterization of Surface Roughness Effects on Pressure Drop in Single-Phase Flow in Minichannels,” *Phys. Fluids*, **17**(10), p. 100606.
- [74] Nikuradse, J., 1950, “Laws of Flow in Rough Pipes,” *J. Appl. Phys.*, **3**(November), p. 399.
- [75] Mazzei, L., Da Soghe, R., and Bianchini, C., 2022, “Calibration of a CFD Methodology for the Simulation of Additively Manufactured Components Accounting for the Effects of Diameter and Printing Direction on Friction and Heat Transfer,” *Proceedings of the ASME Turbo Expo*, American Society of Mechanical Engineers Digital Collection.
- [76] Zhou, L., Zhu, Y., Liu, H., He, T., Zhang, C., and Yang, H., 2021, “A Comprehensive Model to Predict Friction Factors of Fluid Channels Fabricated Using Laser Powder Bed Fusion

- Additive Manufacturing,” *Addit. Manuf.*, **47**, p. 102212.
- [77] Goodhand, M. N., Walton, K., Blunt, L., Lung, H. W., Miller, R. J., and Marsden, R., 2016, “The Limitations of Using ‘Ra’ to Describe Surface Roughness,” *J. Turbomach.*, **138**(10).
- [78] Van Rij, J. A., Belnap, B. J., and Ligrani, P. M., 2002, “Analysis and Experiments on Three-Dimensional, Irregular Surface Roughness,” *J. Fluids Eng. Trans. ASME*, **124**(3), pp. 671–677.
- [79] Forooghi, P., Stroh, A., Magagnato, F., Jakirlić, S., and Frohnepfel, B., 2017, “Toward a Universal Roughness Correlation,” *J. Fluids Eng. Trans. ASME*, **139**(12).
- [80] Flack, K. A., and Schultz, M. P., 2010, “Review of Hydraulic Roughness Scales in the Fully Rough Regime,” *J. Fluids Eng. Trans. ASME*, **132**(4), pp. 0412031–04120310.
- [81] Sigal, A., and Danberg, J. E., 1990, “New Correlation of Roughness Density Effect on the Turbulent Boundary Layer,” *AIAA J.*, **28**(3), pp. 554–556.
- [82] Mazzei, L., Da Soghe, R., and Bianchini, C., 2022, “Calibration of a Computational Fluid Dynamics Methodology for the Simulation of Roughness Effects on Friction and Heat Transfer in Additive Manufactured Components,” *J. Turbomach.*, **144**(8).
- [83] Wildgoose, A. J., and Thole, K. A., 2022, “Heat Transfer and Pressure Loss of Additively Manufactured Internal Cooling Channels with Various Shapes,” *Proceedings of the ASME Turbo Expo*, pp. GT2022-82298.
- [84] Segersäll, M., 2013, “Nickel-Based Single-Crystal Superalloys - the Crystal Orientation Influence on High Temperature Properties.”
- [85] Wildgoose, A. J., and Thole, K. A., 2022, “Variability in Additively Manufactured Turbine Cooling Features,” *J. Glob. Power Propuls. Soc.*
- [86] Molitor, V. D., 2018, “Experimental Study on Pressure Losses in Additive Manufactured Channels,” RWTH, Aachen.
- [87] Nambisan, J., “Experimental Study on Pressure Losses in Additively Manufactured and Machined Orifices,” Linköping University.
- [88] Rehme, O., 2010, *Cellular Design for Laser Freeform Fabrication*, Cuvillier Verlag.
- [89] Jamshidinia, M., and Kovacevic, R., 2015, “The Influence of Heat Accumulation on the Surface Roughness in Powder-Bed Additive Manufacturing,” *Surf. Topogr. Metrol. Prop.*, **3**(1), p. 014003.
- [90] Bacchewar, P. B., Singhal, S. K., and Pandey, P. M., 2007, “Statistical Modelling and Optimization of Surface Roughness in the Selective Laser Sintering Process,” *Proc. Inst. Mech. Eng. Part B J. Eng. Manuf.*, **221**(1), pp. 35–52.
- [91] Wegner, A., and Witt, G., 2012, “Correlation of Process Parameters and Part Properties in

- Laser Sintering Using Response Surface Modeling,” *Physics Procedia*, pp. 480–490.
- [92] Strano, G., Hao, L., Everson, R. M., and Evans, K. E., 2013, “Surface Roughness Analysis, Modelling and Prediction in Selective Laser Melting,” *J. Mater. Process. Technol.*, **213**(4), pp. 589–597.
- [93] Wu, Z., Narra, S. P., and Rollett, A., 2020, “Exploring the Fabrication Limits of Thin-Wall Structures in a Laser Powder Bed Fusion Process,” *Int. J. Adv. Manuf. Technol.*, **110**(1–2), pp. 191–207.
- [94] Kaplanskii, Y. Y., Levashov, E. A., Korotitskiy, A. V., Loginov, P. A., Sentyurina, Z. A., and Mazalov, A. B., 2020, “Influence of Aging and HIP Treatment on the Structure and Properties of NiAl-Based Turbine Blades Manufactured by Laser Powder Bed Fusion,” *Addit. Manuf.*, **31**.
- [95] Krewinkel, R., Such, A., de la Torre, A. O., Wiedermann, A., Castillo, D., Rodriguez, S. A., Schleifenbaum, J. H., and Blaswich, M., 2020, “Design and Characterization of Additively Manufactured NGVs Operated in a Small Industrial Gas Turbine,” *Int. J. Gas Turbine, Propuls. Power Syst.*, **11**(4).
- [96] Rott, S., Ladewig, A., Friedberger, K., Casper, J., Full, M., and Schleifenbaum, J. H., 2020, “Surface Roughness in Laser Powder Bed Fusion – Interdependency of Surface Orientation and Laser Incidence,” *Addit. Manuf.*, **36**, p. 101437.
- [97] Thole, K. A., Barringer, M. D., Berdanier, R. A., Fishbone, S., Wagner, J. H., Dennis, R., Black, J., Burke, P., Straub, D., O’neill, F., Stimpson, C. K., Riahi, A., Aggarwala, A., Bradshaw, S., Kohli, A., Mongillo, D., Praisner, T., Rodriguez, J., Fox, M., and Kim, Y. W., 2021, “Defining a Testbed for the U.S. Turbine Industry: The National Experimental Turbine (NExT),” *AIAA Propulsion and Energy Forum, 2021*, American Institute of Aeronautics and Astronautics (AIAA).
- [98] King, W. E., Anderson, A. T., Ferencz, R. M., Hodge, N. E., Kamath, C., Khairallah, S. A., and Rubenchik, A. M., 2015, “Laser Powder Bed Fusion Additive Manufacturing of Metals; Physics, Computational, and Materials Challenges,” *Appl. Phys. Rev.*, **2**(4), p. 041304.
- [99] Frazier, W. E., 2014, “Metal Additive Manufacturing: A Review,” *J. Mater. Eng. Perform.*, **23**(6), pp. 1917–1928.
- [100] Feng, S., Kamat, A. M., Sabooni, S., and Pei, Y., 2021, “Experimental and Numerical Investigation of the Origin of Surface Roughness in Laser Powder Bed Fused Overhang Regions,” *Virtual Phys. Prototyp.*, **16**(S1), pp. S66–S84.
- [101] Wang, D., Yang, Y., Yi, Z., and Su, X., 2013, “Research on the Fabricating Quality Optimization of the Overhanging Surface in SLM Process,” *Int. J. Adv. Manuf. Technol.*,



65(9–12), pp. 1471–1484.

- [102] Dahmen, T., Klingaa, C. G., Baier-Stegmaier, S., Lapina, A., Pedersen, D. B., and Hattel, J. H., 2020, “Characterization of Channels Made by Laser Powder Bed Fusion and Binder Jetting Using X-Ray CT and Image Analysis,” *Addit. Manuf.*, **36**.
- [103] Fox, J. C., 2019, “Variation of Surface Topography in Laser Powder Bed Fusion Additive Manufacturing of Nickel Super Alloy 625,” *J. Res. Natl. Inst. Stand. Technol.*, **124**(124023), p. 124023.
- [104] Dowling, L., Kennedy, J., O’Shaughnessy, S., and Trimble, D., 2020, “A Review of Critical Repeatability and Reproducibility Issues in Powder Bed Fusion,” *Mater. Des.*, **186**, p. 108346.
- [105] Gradl, P. R., Tinker, D. C., Ivester, J., Skinner, S. W., Teasley, T., and Bili, J. L., 2021, “Geometric Feature Reproducibility for Laser Powder Bed Fusion (L-PBF) Additive Manufacturing with Inconel 718,” *Addit. Manuf.*, **47**, p. 102305.
- [106] Han, J. C., Dutta, S., and Ekkad, S., 2012, *Gas Turbine Heat Transfer and Cooling Technology*, CRC Press/Taylor & Francis.
- [107] Corbett, T., Thole, K. A., and Bollapragada, S., 2022, “AMPLITUDE AND WAVELENGTH EFFECTS FOR WAVY CHANNELS,” *J. Turbomach.*, pp. 1–28.
- [108] Vinton, K. R., Nahang-Toudeshki, S., Wright, L. M., and Carter, A., 2016, “Full Coverage Film Cooling Performance for Combustor Cooling Manufactured Using DMLS,” *Proceedings of the ASME Turbo Expo*, American Society of Mechanical Engineers Digital Collection.
- [109] Jackowski, T., Schulz, A., Bauer, H. J., Gerendás, M., and Behrendt, T., 2016, “Effusion Cooled Combustor Liner Tiles with Modern Cooling Concepts: A Comparative Experimental Study,” *Proceedings of the ASME Turbo Expo*, American Society of Mechanical Engineers Digital Collection.
- [110] Stimpson, C. K., Snyder, J. C., Thole, K. A., and Mongillo, D., 2018, “Effects of Coolant Feed Direction on Additively Manufactured Film Cooling Holes,” *J. Turbomach.*, **140**(11).
- [111] Gutierrez, D., Yoon, C., Furgeson, M. T., Veley, E. M., Bogard, D. G., and Thole, K. A., 2022, “Evaluation of Adjoint Optimized Holes - Part I Baseline Performance,” pp. 1–14.
- [112] Veley, E. M., Thole, K. A., Furgeson, M. T., and Bogard, D. G., 2022, “Printability and Overall Cooling Performance of Additively Manufactured Holes With Inlet And Exit Rounding,” *ASME T Urbo Expo 2022*, pp. GT2022-83313.
- [113] Ferster, K. K., Kirsch, K. L., and Thole, K. A., 2017, “Effects of Geometry, Spacing, and Number of Pin Fins in Additively Manufactured Microchannel Pin Fin Arrays,” *J.*

- Turbomach., **5C**(1).
- [114] Corbett, T. M., and Thole, K. A., 2022, “Impacts of Pin Fin Shape and Spacing on Heat Transfer and Pressure Losses,” *GT2022-82673*.
- [115] Chen, A. F., Shiau, C. C., Han, J. C., and Krewinkel, R., 2019, “Heat Transfer in a Rotating Two-Pass Rectangular Channel Featuring a Converging Tip Turn with Various 45 Deg Rib Coverage Designs,” *J. Therm. Sci. Eng. Appl.*, **11**(6).
- [116] Searle, M., Roy, A., Black, J., Straub, D., and Ramesh, S., 2022, “Investigating Gas Turbine Internal Cooling Using Supercritical CO<sub>2</sub> at Higher Reynolds Numbers for Direct Fired Cycle Applications,” *J. Turbomach.*, **144**(1).
- [117] Kasperovich, G., Becker, R., Artzt, K., Barriobero-Vila, P., Requena, G., and Haubrich, J., 2021, “The Effect of Build Direction and Geometric Optimization in Laser Powder Bed Fusion of Inconel 718 Structures with Internal Channels,” *Mater. Des.*, **207**.
- [118] Kirsch, K. L., Snyder, J. C., Stimpson, C. K., Thole, K. A., and Mongillo, D., 2017, “Repeatability in Performance of Micro Cooling Geometries Manufactured with Laser Powder Bed Fusion,” *53rd AIAA/SAE/ASEE Joint Propulsion Conference, 2017*, American Institute of Aeronautics and Astronautics Inc, AIAA.
- [119] Hossain, M. A., Ameri, A., Gregory, J. W., and Bons, J. P., 2021, “Experimental Investigation of Innovative Cooling Schemes on an Additively Manufactured Engine Scale Turbine Nozzle Guide Vane,” *J. Turbomach.*, **143**(5).
- [120] Hossain, M. A., Prenter, R., Lundgreen, R. K., Ameri, A., Gregory, J. W., and Bons, J. P., 2018, “Experimental and Numerical Investigation of Sweeping Jet Film Cooling,” *J. Turbomach.*, **140**(3).
- [121] Kirolos, B., and Povey, T., 2017, “Laboratory Infrared Thermal Assessment of Laser-Sintered High-Pressure Nozzle Guide Vanes to Derisk Engine Design Programs,” *J. Turbomach.*, **139**(4).
- [122] Thole, K. A., Barringer, M. D., Berdanier, R. A., Fishbone, S., Wagner, J. H., Dennis, R., Black, J., Burke, P., Straub, D., O’neill, F., Stimpson, C. K., Riahi, A., Aggarwala, A., Bradshaw, S., Kohli, A., Mongillo, D., Praisner, T., Rodriguez, J., Fox, M., and Kim, Y. W., 2021, “Defining a Testbed for the U.S. Turbine Industry: The National Experimental Turbine (NExT),” *AIAA Propuls. Energy Forum*, 2021.
- [123] Schroeder, R. P., and Thole, K. A., 2022, “Adiabatic Effectiveness Measurements for a Baseline Shaped Film Cooling Hole,” *J. Turbomach.*, **144**(12).
- [124] Zigrang, D. J., and Sylvester, N. D., 1985, “A Review of Explicit Friction Factor Equations,” *J. Energy Resour. Technol.*, **107**(2), pp. 280–283.

## Appendix A: Uncertainty Analysis

### Nomenclature

$A_c$	cross-sectional flow area
$A_{cu}$	cross-sectional area of copper block
$D_h$	hydraulic diameter, $4A_c/\text{perim}$
$f$	Darcy friction factor, $f = \Delta P \frac{D_h}{L} \frac{2}{\rho u^2}$
$h$	convective heat transfer coefficient, $h = \frac{Q_{in,heater} - \sum Q_{loss}}{A_s \Delta T_{lm}}$
$k$	thermal conductivity
$k_{air}$	thermal conductivity of air
$k_{cu}$	thermal conductivity of copper
$k_{paste}$	thermal conductivity of thermal paste
$L$	channel length
$\dot{m}$	mass flowrate
$Nu$	Nusselt number, $hD_h/k_{air}$
$\text{Perim}$	channel perimeter
$P_i$	static pressure at inlet
$P_o$	static pressure at outlet
$Re$	Reynolds number, $uD_h/\nu$
$t_{cu}$	thickness of copper block
$t_{paste}$	thickness of paste
$t_{wall}$	thickness of coupon wall
$T_i$	inlet temperature
$T_o$	outlet temperature
$T_s$	surface temperature
$T_{LM}$	log-mean temperature, $\Delta T_{LM} = \frac{(\Delta T_{in} - \Delta T_{out})}{\ln\left(\frac{T_s - T_{in}}{T_s - T_{out}}\right)}$

### Greek

$\nu$	kinematic viscosity
$\mu$	viscosity

An uncertainty analysis was performed on the Reynolds number (Re), measured friction factor (f), and Nusselt number (Nu) using the propagation of uncertainty method by Figliola and Beasley [44]. The equation for Reynolds number, friction factor, and Nusselt number is shown in Equation A.1, Equation A.2, and Equation A.3. The calculation for the convection coefficient (h) in Equation A.3 is shown in Equation A.4.

$$\text{Re} = \frac{4 \cdot \dot{m}}{\mu \cdot \text{Perim}} \quad (\text{A.1})$$

$$f = \frac{D_h \cdot \Delta P \cdot (\rho_{in} + \rho_{out}) \cdot A_c^2}{L \cdot \dot{m}^2} \quad (\text{A.2})$$

$$\text{Nu} = \frac{h \cdot D_h}{k_{air}} \quad (\text{A.3})$$

$$h = \frac{Q_{total}}{A_s \cdot \Delta T_{LM}} \quad (\text{A.4})$$

### Reynolds Number Uncertainty

The propagation of uncertainty method described by Figliola and Beasley [1] uses a partial derivative technique to describe individual parameter uncertainties and relate them to the overall uncertainty of the desired calculated value. As seen in Equation A.5, the uncertainty of Reynolds number is calculated through the partial derivatives of the individual terms used in Equation A.1 to calculate Reynolds number.

$$u_{\text{Re}} = \sqrt{\left(\frac{\partial \text{Re}}{\partial \dot{m}} u_{\dot{m}}\right)^2 + \left(\frac{\partial \text{Re}}{\partial D_h} u_{D_h}\right)^2 + \left(\frac{\partial \text{Re}}{\partial A_c} u_{A_c}\right)^2 + \left(\frac{\partial \text{Re}}{\partial \mu} u_{\mu}\right)^2} \quad (\text{A.5})$$

The mass flow rate in equation A.1 is measured using a laminar flow element upstream of the coupon. While the hydraulic diameter and cross-sectional area of the coupon channels is measured from computed tomography scan data. Table A.1 and Table A.2 show the uncertainty calculation of the square sample from Wildgoose et al. [2] at a Reynolds number of 10,000 and

20,000. The individual contributions to the overall uncertainty of the Reynolds number are also shown in Table A.1 and Table A.2.

**Table A. 1. Reynolds number Uncertainty of Square Sample (Re = 9.91E3)**

Partial Derivative Term	Value	Uncertainty	Contribution to Overall uncertainty
$\dot{m}$ [kg/s]	2.15E-03	1.97E-04	100
Perim [ $\mu\text{m}$ ]	4.68E+04	35	0.00
$A_c$ [ $\text{mm}^2$ ]	15.023	0.036	0.00
$\mu$	1.85E-05	8.86E-07	0.00
$U_{Re}$ (%)	<b>4.60</b>		

**Table A. 2. Reynolds number Uncertainty of Square Sample (Re = 1.98E4)**

Partial Derivative Term	Value	Uncertainty	Contribution to Overall uncertainty
$\dot{m}$ [kg/s]	4.30E-03	1.97E-04	99.95
Perim [ $\mu\text{m}$ ]	4.68E+04	35	0.01
$A_c$ [ $\text{mm}^2$ ]	15.023	0.036	0
$\mu$	1.85E-05	8.86E-07	0.04
$U_{Re}$ (%)	<b>5.00</b>		

### Friction Factor Uncertainty

As seen in Equation A.6, the uncertainty of the friction factor is calculated through the partial derivatives of the uncertainty terms used to measure friction factor in Equation A.2.

$$u_f = \sqrt{\left(\frac{\partial f}{\partial D_h} u_{D_h}\right)^2 + \left(\frac{\partial f}{\partial \Delta P} u_{\Delta P}\right)^2 + \left(\frac{\partial f}{\partial \rho_{in}} u_{\rho_{in}}\right)^2 + \dots + \left(\frac{\partial f}{\partial \rho_{out}} u_{\rho_{out}}\right)^2 + \left(\frac{\partial f}{\partial A_c} u_{A_c}\right)^2 + \left(\frac{\partial f}{\partial L} u_L\right)^2 + \left(\frac{\partial f}{\partial \dot{m}} u_{\dot{m}}\right)^2} \quad (\text{A.6})$$

The density at the inlet and outlet were calculated using ideal gas law using thermocouples and pressure taps at the upstream and downstream of the coupons. The ideal gas law equation for upstream density is shown in Equation A.7. The uncertainty calculation for the upstream density is shown in Equation A.8. The same calculation for upstream density was also completed for the downstream density.

$$\rho_i = \frac{P_i}{R_s T_i} \quad (\text{A.7})$$

$$u_{\rho_i} = \sqrt{\left(\frac{\partial \rho_i}{\partial P_i} u_{P_i}\right)^2 + \left(\frac{\partial \rho_i}{\partial R_s} u_{R_s}\right)^2 + \left(\frac{\partial \rho_i}{\partial T_i} u_{T_i}\right)^2} \quad (\text{A.8})$$

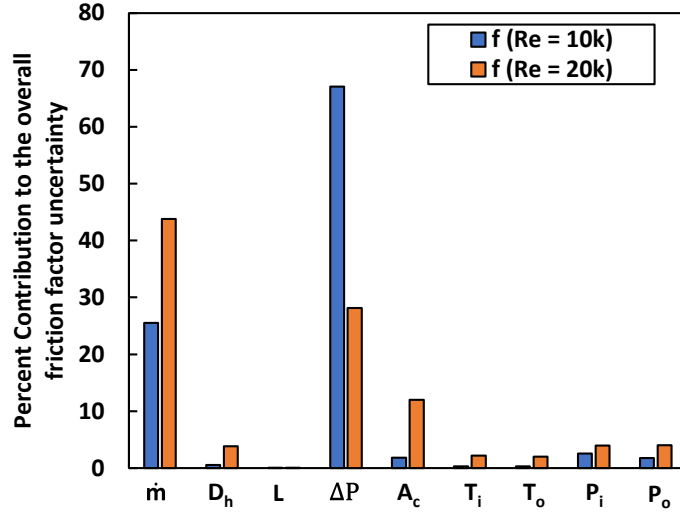
Table A.3 and Table A.4 show the uncertainty calculation with specific values at two different Reynolds number of the square channel coupon from Wildgoose et al. [83]. The individual percent contributions of each uncertainty towards friction factor is seen in Figure A.1.

**Table A. 3. Friction Factor Uncertainty of Square Sample (Re = 9.91E3)**

Partial Derivative Term	Value	Uncertainty	Contribution to Overall uncertainty
$\dot{m}$ [kg/s]	0.002153	1.973E-04	25.52
$D_h$ [μm]	1283.00	35.00	0.58
$L$ [mm]	495.00	0.035	0.01
$\Delta P$ [Pa]	1.18E+04	352.8	67.06
$A_c$ [mm <sup>2</sup> ]	15.023	0.03604	1.81
$T_i$ [K]	296.3	1.185	0.33
$T_o$ [K]	295.1	1.181	0.30
$P_i$ [Pa]	256216	2649	2.59
$P_o$ [Pa]	244457	2649	1.80
$U_f$ (%)	<b>4.00</b>		

**Table A. 4. Friction Factor Uncertainty of Square Sample (Re = 1.98E4)**

Partial Derivative Term	Value	Uncertainty	Contribution to Overall uncertainty
$\dot{m}$ [kg/s]	0.004303	1.973E-04	43.79
$D_h$ [μm]	1283.00	35.00	3.87
$L$ [mm]	495.00	0.035	0.02
$\Delta P$ [Pa]	2.34E+04	172.4	28.15
$A_c$ [mm <sup>2</sup> ]	15.023	0.03604	11.98
$T_i$ [K]	296	1.184	2.18
$T_o$ [K]	294.8	1.179	1.99
$P_i$ [Pa]	490412	2654	3.99
$P_o$ [Pa]	466695	2649	4.03
$U_f$ (%)	<b>5.03</b>		



**Figure A.1** Parameter percent contribution to the friction factor uncertainty.

### Heat Transfer Uncertainty:

The same propagation of uncertainty method for Reynolds number and friction factor was used in the uncertainty analysis of Nusselt number. As seen in Equation A.9, the uncertainty of the Nusselt number is calculated through the partial derivative of the uncertainties from the terms used in to calculate Nusselt number in Equation A.3.

$$u_{Nu} = \sqrt{\left(\frac{\partial Nu}{\partial h} u_h\right)^2 + \left(\frac{\partial Nu}{\partial k_{air}} u_{k_{air}}\right)^2 + \left(\frac{\partial Nu}{\partial D_h} u_{D_h}\right)^2} \quad (A.9)$$

The uncertainty of the convection coefficient in Equation A.3 is shown in Equation A.10. Where  $Q_{net}$  is the total power of the heaters minus the loss to the surroundings (through conduction in the foam and plenums). The log mean temperature term in equation A.4 is shown in Equation A.11. The uncertainty calculation for log mean temperature is shown in Equation A.12. The coupon surface temperature in Equation A.11 is calculated using a conduction resistance network as seen in Equation A.13. The uncertainty of the coupon surface temperature is calculated using the propagation of uncertainty method as seen by Equation A.14.

$$u_h = \sqrt{\left(\frac{\partial h}{\partial Q_{net}} u_{Q_{net}}\right)^2 + \left(\frac{\partial h}{\partial A_s} u_{A_s}\right)^2 + \left(\frac{\partial h}{\partial \Delta T_{LM}} u_{\Delta T_{LM}}\right)^2} \quad (A.10)$$

$$\Delta T_{LM} = \frac{(T_s - T_{out}) - (T_s - T_{in})}{\ln\left(\frac{T_s - T_{out}}{T_s - T_{in}}\right)} \quad (A.11)$$

$$u_{\Delta T_{LM}} = \sqrt{\left(\frac{\partial \Delta T_{LM}}{\partial T_s} u_{T_s}\right)^2 + \left(\frac{\partial \Delta T_{LM}}{\partial T_{in}} u_{T_{in}}\right)^2 + \left(\frac{\partial \Delta T_{LM}}{\partial T_{out}} u_{T_{out}}\right)^2} \quad (\text{A.12})$$

$$T_s = T_{Copper} - \frac{Q_{net}}{A_{copper}} \left( \frac{t_{Copper}}{k_{Copper}} + \frac{t_{paste}}{k_{paste}} + \frac{t_{coupon}}{k_{coupon}} \right) \quad (\text{A.13})$$

$$u_{T_s} = \sqrt{\left(\frac{\partial T_s}{\partial Q_{net}} u_{Q_{net}}\right)^2 + \left(\frac{\partial T_s}{\partial T_{copper}} u_{T_{copper}}\right)^2 + \left(\frac{\partial T_s}{\partial A_{copper}} u_{A_{copper}}\right)^2 + \dots} \quad (\text{A.14})$$

$$+ \left(\frac{\partial T_s}{\partial t_{copper}} u_{t_{copper}}\right)^2 + \left(\frac{\partial T_s}{\partial t_{paste}} u_{t_{paste}}\right)^2 + \left(\frac{\partial T_s}{\partial t_{coupon}} u_{t_{coupon}}\right)^2 + \dots$$

$$+ \left(\frac{\partial T_s}{\partial k_{copper}} u_{k_{copper}}\right)^2 + \left(\frac{\partial T_s}{\partial k_{paste}} u_{k_{paste}}\right)^2 + \left(\frac{\partial T_s}{\partial k_{coupon}} u_{k_{coupon}}\right)^2$$

Table A.5 and Table A.6 show the uncertainty calculation for Nusselt number at two different Reynolds numbers of the square coupon from Wildgoose et al. [2]. The individual percent contributions of each Nusselt number uncertainty is shown in Figure A.2.

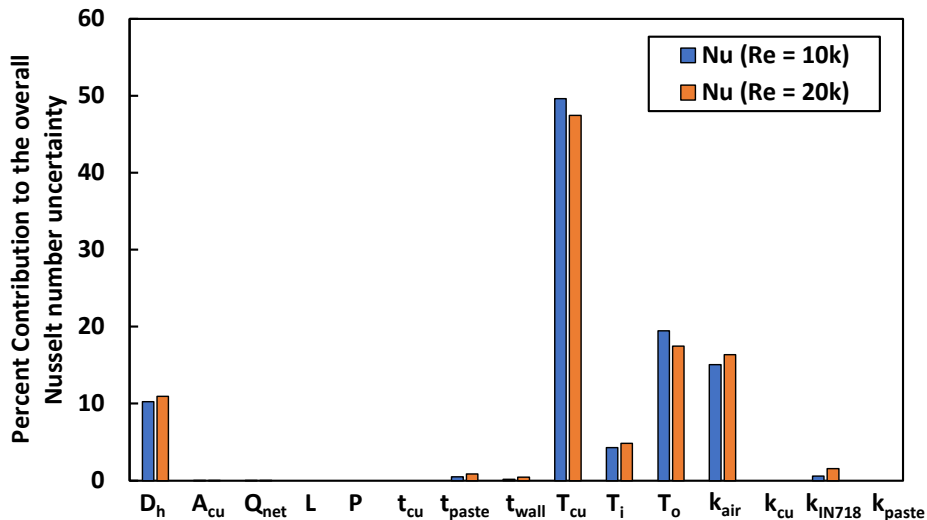
**Table A.5. Nusselt Number Uncertainty of Square Sample (Re = 9.90E3)**

Partial Derivative Term	Value	Uncertainty	Contribution to Overall uncertainty
D <sub>h</sub> [μm]	1283	35.00	10.24
A <sub>cu</sub> [mm <sup>2</sup> ]	1212.6	0.010	0.01
Q <sub>net</sub> [W]	53.62	0.089	0.04
L [mm]	495.0	0.035	0.00
Perim [mm]	46.83	0.035	0.00
t <sub>cu</sub> [mm]	6.36	0.010	0.00
t <sub>paste</sub> [mm]	2.54	0.010	0.50
t <sub>wall</sub> [mm]	0.830	0.035	0.17
T <sub>cu</sub> [K]	338.2	1.353	49.65
T <sub>i</sub> [K]	295.8	1.197	4.28
T <sub>o</sub> [K]	321.5	1.269	19.46
k <sub>air</sub> [W/mK]	0.027	0.00089	15.05
k <sub>cu</sub> [W/mK]	385.0	3.850	0.00
k <sub>IN718</sub> [W/mK]	9.77	0.770	0.60
k <sub>paste</sub> [W/mK]	2.31	0.023	0.00
U <sub>Nu</sub> (%)	<b>8.52</b>		



**Table A.6. Nusselt Number Uncertainty of Square Sample (Re = 1.98E4)**

Partial Derivative Term	Value	Uncertainty	Contribution to Overall uncertainty
$D_h$ [ $\mu\text{m}$ ]	1283.0	35.00	10.96
$A_{cu}$ [ $\text{mm}^2$ ]	1212.6	0.01	0.04
$Q_{net}$ [W]	88.68	0.089	0.02
$L$ [mm]	495.0	0.035	0.00
Perim [mm]	46.83	0.035	0.00
$t_{cu}$ [mm]	6.360	0.01	0.00
$t_{paste}$ [mm]	2.540	0.01	0.85
$t_{wall}$ [mm]	0.830	0.035	0.44
$T_{cu}$ [K]	338.2	1.353	47.47
$T_i$ [K]	296.0	1.197	4.84
$T_o$ [K]	317.6	1.269	17.47
$k_{air}$ [W/mK]	0.027	0.00089	16.35
$k_{cu}$ [W/mK]	385.0	3.85	0.00
$k_{IN718}$ [W/mK]	9.770	0.77	1.56
$k_{paste}$ [W/mK]	2.310	0.0231	0.00
$U_{Nu}$ (%)	<b>8.24</b>		



**Figure A.2 Parameter percent contribution to the Nusselt number uncertainty.**

**References**

- [1] Figliola, R. S., and Beasley, D. E., 2005, *Theory and Design for Mechanical Measurements*, Wiley & Sons, Hoboken, Nj.
- [2] Wildgoose, A. J., and Thole, K. A., 2022, "Heat Transfer and Pressure Loss of Additively Manufactured Internal Cooling Channels with Various Shapes," *Proceedings of the ASME Turbo Expo*, pp. GT2022-82298.

## VITA

### **Alexander J. Wildgoose**

Alexander Wildgoose was born in Germany and grew up in Montgomery New Jersey, where he graduated from Montgomery High School in 2014. Mr. Wildgoose received his BS in Mechanical Engineering at Rowan University. During his undergraduate studies he pursued an interest in engineering education, research in energy harvesters, and microfluidics. Consequently, he published several pieces of work during his undergraduate studies through ASME IMECE and IEEE FIE. During his Junior year, he was given the opportunity to perform research on energy harvesters at Pennsylvania State University under a National Science Foundation Research Experience for Undergraduates.

Directly following his undergraduate studies, Alexander pursued a Ph.D at the Steady Thermal Aero Research (START) Lab at Pennsylvania State University under the guidance of Dr. Karen Thole in 2018. He received his MS in Mechanical Engineering at Pennsylvania State University in 2021. At the Pennsylvania State University, he studied additive manufacturing and heat transfer for applications in gas turbines. Mr. Wildgoose is proud to be a member of ASME and in particular the gas turbine community. He has served as a Student Advisory Committee liaison for the heat transfer and education committee as well as reviewed several papers for ASME Turbo Expo, Journal of Turbomachinery, and the Journal of Thermophysics and Heat Transfer.

During his university studies, Mr. Wildgoose has received several accolades for academic achievements and research. He has been awarded the Tirupathi Reddy Chandrupatla Award for Excellence in Mechanical Engineering from Rowan University in 2018, the Gabon Family Graduate Fellowship in Mechanical Engineering from Pennsylvania State University in 2018, the NASA Pennsylvania Space Grant Consortium Graduate Fellowship in 2019, the Pennsylvania State University Graduate Student Summer Fellowship in 2022, and a travel award from ASME IGTI in 2022. Upon graduation, Alexander will join General Electric Aerospace as a Lead Engineer developing advanced cooling designs for gas turbine components.